Predictions to all orders in perturbative quantum chromodynamics for high energy collider experiments

Dissertation
for the award of the degree
"Doctor rerum naturalium" (Dr. rer. nat.)
of the Georg-August-Universität Göttingen

within the doctoral program Physik
of the Georg-August University School of Science (GAUSS)

submitted by

Daniel Reichelt

from Dresden

Göttingen, 2021

Thesis-Committee

Prof. Dr. Steffen Schumann,
Institut für Theoretische Physik, Georg-August-Universität Göttingen

Prof. Laura Covi, PhD,
Institut für Theoretische Physik, Georg-August-Universität Göttingen

Prof. Dr. Matthias Krüger,
Institut für Theoretische Physik, Georg-August-Universität Göttingen

Members of the Examination Board

Reviewer: Prof. Dr. Steffen Schumann
Institut für Theoretische Physik,
Georg-August-Universität Göttingen

Second Reviewer: Prof. Laura Covi, PhD
Institut für Theoretische Physik,
Georg-August-Universität Göttingen

Additional Reviewer: Dr. Andrea Banfi
Department of Physics and Astronomy,
University of Sussex

Further members of the Examination Board:

Prof. Dr. Matthias Krüger
Institut für Theoretische Physik, Georg-August-Universität Göttingen

apl. Prof. Dr. Karl-Henning Rehren
Institut für Theoretische Physik, Georg-August-Universität Göttingen

Prof. Dr. Arnulf Quadt
II. Physikalisches Institut, Georg-August-Universität Göttingen

Prof. Dr. Stan Lai
II. Physikalisches Institut, Georg-August-Universität Göttingen

Date of the oral examination: 13. October 2021

Abstract

This thesis discusses an implementation of automated all orders calculations in perturbative quantum chromodynamics and its application to measurements at recent collider experiments. It is realised as a plugin to the SHERPA event generator framework. The theoretical basis is provided by the well established CAESAR formalism. This allows one to take into account the leading and next-to-leading logarithmic enhanced terms. NLO+NLL′ accuracy is achieved by matching the resulting expressions to calculations at next-to-leading order in the strong coupling constant. Non-perturbative corrections are transferred from Monte Carlo simulations to the all orders distributions. Going beyond the original CAESAR formalism, soft drop groomed observables as well as jet substructure variables are discussed in the same framework. Use cases are illustrated with various examples. In electron positron annihilation, the resummation of high multiplicity jet rates is presented, as well as an analysis of the potential of soft drop grooming, applied to the thrust observable, to improve fits of the strong coupling constant. Relevant to the currently operating Large Hadron Collider are the phenomenological studies of soft drop groomed global event shapes in proton proton collisions and predictions for jet substructure observables. The latter are compared to recent measurements by the CMS experiment.

Authorship

The original research presented in this thesis has been worked on and published in collaboration with the respective co-authors in the peer-reviewed publications

[I]   **Fitting the Strong Coupling Constant
        with Soft-Drop Thrust**
        by Simone Marzani, Daniel Reichelt, Steffen Schumann,
        Gregory Soyez, and Vincent Theeuwes
        published in JHEP **11** (2019), 179
        e-print available at [arXiv:1906.10504] [InSPIRE]

[II]   **Resummed predictions for jet-resolution scales in
        multijet production in e^+e^- annihilation**
        by Nick Baberuxki, Christian Preuss, Daniel Reichelt,
        and Steffen Schumann
        published in JHEP **04** (2020), 112
        e-print available at [arXiv:1912.09396] [InSPIRE]

[III]   **Soft-drop grooming for hadronic event shapes**
        by Jeremy Baron, Daniel Reichelt, Steffen Schumann,
        Niklas Schwanemann, and Vincent Theeuwes
        published in JHEP **08** (2021), 142
        e-print available at [arXiv:2012.09574] [InSPIRE]

[IV]   **Jet Angularities in Z+jet production at the LHC**
        by Simone Caletti, Oleh Fedkevych, Simone Marzani,
        Daniel Reichelt, Steffen Schumann, Gregory Soyez,
        and Vincent Theeuwes
        published in JHEP **08** (2021), 76
        e-print available at [arXiv:2104.06920] [InSPIRE]

and the pre-print

[V]   **Tagging the initial-state gluon**
        by Simone Caletti, Oleh Fedkevych, Simone Marzani,
        and Daniel Reichelt
        e-print available at [arXiv:2108.10024] [InSPIRE]

This work and my personal education in the various topics are also based on collaborative work with other researchers. This has led to the additional peer-reviewed publications

[VI]   **Numerical resummation at subleading color**
         in the strongly ordered soft gluon limit
         by Stefan Höche and Daniel Reichelt
         published in Phys. Rev. D **104** (2021), 034006
         e-print available at [arXiv:2001.11492] [InSPIRE]

[VII]   **Momentum conservation and unitarity in parton showers**
         and NLL resummation
         by Stefan Höche, Daniel Reichelt and Frank Siegert
         published in JHEP **01** (2018), 118
         e-print available at [arXiv:1711.03497] [InSPIRE]

[VIII]   **Improving the Simulation of Quark and Gluon Jets**
         with Herwig 7
         by Daniel Reichelt, Peter Richardson and Andrzej Siodmok
         published in Eur. Phys. J. C **77** (2017), no. 12, 876
         e-print available at [arXiv:1708.01491] [InSPIRE]

and the contribution to conference proceedings

[IX]   **Colour Reconnections in Quark and Gluon Jets in Herwig 7**
         by Daniel Reichelt, Peter Richardson and Andrzej Siodmok
         published in Acta Phys. Polon. B **48** (2017), 1167-1173 [InSPIRE]

Contents

Introduction

The development of high energy particle colliders started with the first proposals to collide two beams of fast moving particles [1, 2] in the 1950's [3]. Since then, a large number of facilities have been built to perform this kind of experiment, at ever increasing energies and using various types of particles in the colliding beams. Fig. 1.1 shows an overview of the experiments performed over the last decades. The first examples are colliders working with beams of electrons and positrons at energy scales below and around 1 GeV [4–12]. An early example for a proton-proton collider are the Intersecting Storage Rings (ISR) [13, 14] at the European Organisation for Nuclear Research (CERN). Truly high energy experiments with electrons were performed at the Stanford Linear Accelerator (SLAC) [15].

The latest series of experiments to have finished include the HERA collider at DESY collecting data from electron proton collisions, at the four experiments H1 [16], ZEUS [17], HERMES [16] and HERA-B [18]. Experiments with proton-antiproton collisions at high energies were most recently performed by the D0 [19] and CDF [20] collaborations at the Tevatron collider at Fermilab reaching energies of almost 2 TeV. The highest energies in electron-positron collisions, up to 209 GeV, were achieved by the Large Electron Positron collider (LEP), again at CERN. The four experiments ALEPH [21], DELPHI [22], OPAL [23] and L3 [24] also collected a large amount of data at lower energies, in particular at the Z-pole around 91.2 GeV.

LEP was replaced by the currently operating Large Hadron Collider (LHC). It is collecting data at the ATLAS [25], CMS [26], LHCb [27] and Alice [28] experiments. Most collisions were recorded at energies of 7 TeV and 13 TeV with proton beams. The LHC is also performing runs with heavy ions like lead, and similarly the dedicated Relativistic Heavy Ion Collider (RHIC) [14], is another example for a current experiment collecting data from proton collisions. The exploration of electron-positron annihilation continues currently at lower energies for example at the KEK facilities, with Belle II [29] being the latest experiment dedicated to the study of B-hadron physics at the $\mathcal{O}(10$ GeV$)$ scale.

The discoveries made at those experiments at increasing energies were met by developments in the theoretical understanding of the fundamental components of matter surrounding us and the interactions between them. This is summarised in the standard model (SM) of particle physics. A key role is played by the strong interactions governing the physics of hadrons. Their understanding has played a major role in the past and current collider experiments, either with the setup being dedicated to their study, or as a main contributor of background noise to the actual physics goals.

The study of the standard model has gone from a quest for qualitative explanations of the observed effects towards precision calculations of specific quantities. The following thesis will provide a framework for such calculations in perturbative quantum chromodynamics at all orders, in an automated fashion. This will be put into context over the next chapter, dedicated to reviewing key topics of the SM and the theory of strong interactions in particular. The third chapter will introduce necessary phenomenological tools and techniques, followed by a summary of the CAESAR formalism used to achieve the precision aimed for here. The fifth chapter documents details of the approach to this formalism within the SHERPA framework. The final chapter is dedicated to illustrating use cases of this implementation.
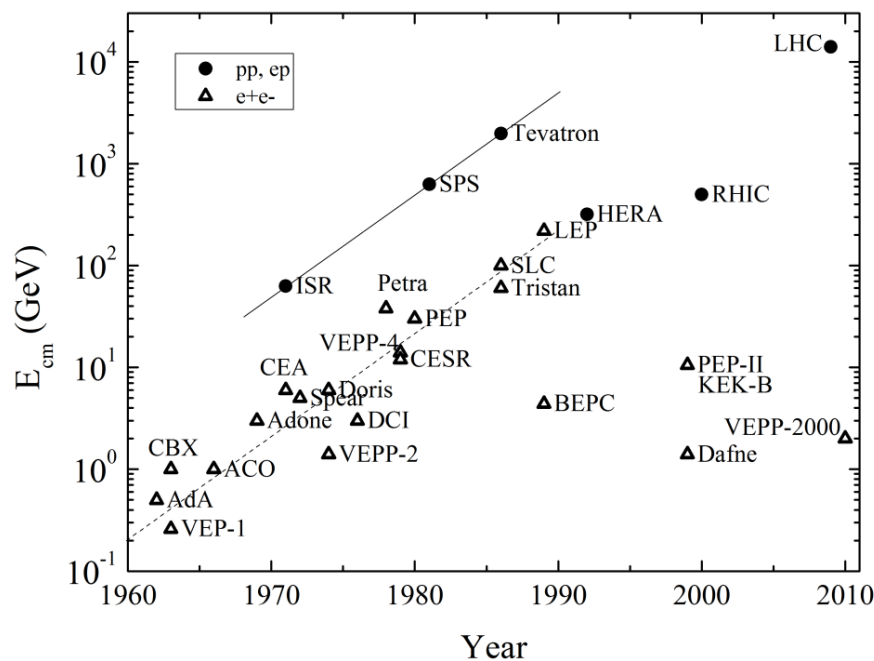

Figure 1.1: Colliders over the decades.
Figure and caption taken from Ref. [3].

$$\frac{dN_{\text{exp}}}{dt} = L \cdot \sigma_{\text{int}}$$

$$L = f \frac{N_1 N_2}{A}$$

Quantum chromodynamics and the standard model of particle physics

The modern formulation of the standard model of particle physics is in terms of a local relativistic quantum field theory. It contains all degrees of freedom known to date to be necessary to collectively describe in particular data from collider experiments. The progress of the field is regularly reviewed by the particle data group, and the latest edition of this review, [30], is to be regarded as the principal reference for factual statements and concrete parameters in the following, if no other reference is given.

This chapter is mostly meant to set the frame for the original work presented later by introducing known results within the SM, as they are discussed in advanced but standard text books, e.g. [31–39], but with no particular claim of completeness regarding tangential topics. In addition to the textbooks, relevant review articles are [40, 41] for the physics discussions and [3, 42] for the historical developments. The following also serves to establish the notation employed in the later chapters of this thesis.

The final section of this chapter focuses on Quantum Chromodynamics (QCD) and mainly the necessary developments to perform calculations within the framework of perturbation theory. Ultimately, this is what is needed to introduce the concepts reflected in the CAESAR formalism explained later. Of course, approaches like lattice gauge theory to QCD, for example [43–45], are also very important. On the one hand they provide numerical calculations that would not be available in perturbation theory. On the other hand, they underline the concepts and ideas that arise from the perturbative study of QCD but can not yet be proven rigorously on a mathematical basis.

2.1 The standard model

The matter content of the SM consists of 12 fermionic degrees of freedom, distinguished by their masses and participation in the various interactions. All known interactions are described by gauge theories, and are separated into an electroweak part, described as a $SU(2) \times U(1)$ gauge theory [46–48] broken by the Higgs mechanism [49–53], and QCD. For the latter, the appropriate gauge group is $SU(3)$.

At relatively low energies, $\approx \mathcal{O}(100 \text{ MeV}) - \mathcal{O}(10 \text{ GeV})$, QCD is argued to exhibit effective degrees of freedoms called hadrons. The most well known probably are protons and neutrons at masses of ≈ 1 GeV that make up the nuclei of all atoms comprising everyday matter. Experimentally however, one observes a full zoo of shorter lived mesons and baryons in this energy range. The symmetry patterns [54, 55] observed in those historically led to the postulate that hadrons are in fact bound states composed of the more fundamental quarks [56, 57]. At the same energy scale, only one of the four bosons implied by the $SU(2) \times U(1)$ gauge symmetry remains massless after electroweak symmetry breaking. It is identified with the photon of quantum electrodynamics (QED), while the Z boson ($M_Z \approx 91.2$ GeV) and the oppositely charged W bosons ($M_W \approx 80$ GeV) are associated with much higher mass scales. The picture at low energies is then that of a spectrum of hadrons at their respective energies, that can be electrically charged or neutral and correspondingly interact and decay due to both QED and strong interactions. Effective four point interactions, historically named after Fermi [58], and nowadays derived from the exchange of the massive gauge bosons, also play a role. They however are suppressed by factors of $\mathcal{O}(1/M_Z^2) \approx \mathcal{O}(1/M_W^2)$, and usually are only significant when the other interactions are absent due to some symmetry and corresponding conservation law. Yet lower energies are associated with larger time scales, such that only the stable or very long lived hadrons remain available. These are mostly protons and neutrons, which themselves form bound states via effective strong interactions and lead to nuclear physics with binding energies of $\approx 1 - 10$ MeV. One eventually arrives at the QED picture of electrons, protons/nuclei and photons which governs atomic and molecular physics in various non-relativistic approximations.

The work in this thesis is however on collider phenomenology at higher energy scales, or at the very least in the range of hadronic physics at $1 - 10$ GeV. Relevant additional energy scales are set by the W and Z bosons mentioned before, the scalar Higgs boson, the last of the SM particles to be confirmed experimentally [59, 60], with $M_H \approx 125$ GeV and the top quark at $m_t \approx 173$ GeV. These will in the following be relevant to determine the physical values of the energy scales and for kinematic restrictions to the phase space of collision products. The physical effects associated with them will however not be discussed in detail. In fact, only the last one, the top

quark, actually corresponds to a degree of freedom appearing in QCD. The majority of experiments performed so far were not able to produce top quarks due to their lower collision energy (an energy of $2m_t \approx 350$ GeV would be necessary to produce a pair of top quarks, exceeding even the highest energies reached at LEP). They are only studied at the latest two hadron colliders, the Tevatron where they were discovered [61, 62], and the LHC. Even there however, the effective center of mass energies are rarely high enough to neglect the top mass. The main effects taken into account here are suppressed for quarks with a significant mass relative to the overall energy scale. Hence top quarks will not play a major role in the following. The other quark masses are at or below the scales of hadronic physics. The lightest three, the up, down and strange quark, have masses well below 1 GeV, and can be regarded as massless for all practical purposes in the following. The charm and bottom quarks have masses of $m_c \approx 1.28$ GeV and $m_b \approx 4.8$ GeV, making corrections associated with them worth considering in some cases. Nevertheless, the main theory used in the following will be that of QCD with 5 exactly massless quarks.

The idea that hadrons are effectively bound states of quarks is further supported by experiments examining scattering of leptons off nuclei like protons [63–65]. At sufficiently high energies, when the proton is destroyed in the process ("deep inelastic scattering", DIS), one observes that the interaction, mediated by the photons of QED, indeed appears to effectively be with smaller charged constituents inside the proton. This can be formalised as a particular scaling behaviour of the so called structure functions effectively describing the deviation of nuclei from point-like particles [66]. Further developments lead to the parton model [67, 68]. The picture is that of hadrons containing valence quarks of the various types, matching their overall quantum numbers and each carrying a fraction x of the momentum of the respective hadrons. One then works with distributions $f_q^{\text{hadron}}(x)$, describing the probability to find a parton of type q with momentum fraction x of the hadron momentum inside the hadron. In addition there might be quark-antiquark pairs with cancelling quantum numbers, and one can relate properties O_{hadron} of a given hadron to the equivalent property of its quark constituents O_{parton}, schematically

$$O_{\text{hadron}} = \sum_{q,\bar{q}} \int_0^1 dx \, f_q^{\text{hadron}}(x, Q^2) O_{\text{parton}}(x) \; . \tag{2.1}$$

The actual distribution functions $f(x, Q^2)$ need to be determined from experiments. An energy scale Q^2 is added as a second dependence, anticipating that Bjorken scaling is not exact. This approach needs to be extended to not only quarks but also electrically neutral gluons [69] to explain the interactions between the quarks, guided and confirmed by further experimental observations in DIS [70, 71]. It can later be justified in the context of lowest order approximations in full QCD.

2.2   Quantum chromodynamics as a gauge theory

The most complete formulation of the strong interaction in terms of a quantum field theory we know of is as a Yang-Mills theory [72]. This is a gauge theory with a non-abelian gauge group. The massless[1] Yang-Mills Lagrangian density is given by

$$\mathcal{L} = -\frac{1}{4}F_{\mu\nu}^a F^{a,\mu\nu} + \sum_{n_F} \bar{q}_i \left(\gamma^\mu \partial_\mu + ig\gamma^\mu t_{ij}^a A_\mu^a \right) q_j \ , \qquad (2.2)$$

$$\text{with} \quad F_{\mu\nu}^a = \partial_\mu A_\nu^a - \partial_\nu A_\mu^a - gf^{abc}A_\mu^b A_\nu^c \ . \qquad (2.3)$$

Here, the spinors q_i represent the quarks, which occur in n_F identical copies called flavours. The field strength tensor $F_{\mu\nu}^a$ is build from the gluon fields A_μ^a. The quark fields carry a fundamental representation of the gauge group, indicated by the index i, while the gluons are associated with the adjoint representation. The coupling between them is explicitly proportional to the generators t^a of the fundamental representation,

$$\left[t^a, t^b \right] \equiv if^{abc}t^c \ , \qquad (2.4)$$

while the gluon self coupling, the third term in Eq. (2.3), is proportional to the structure constants f^{abc} of the gauge group. For QCD, the relevant group is $SU(N_c)$. The physical "number of colours" is $N_c = 3$, but it is convenient to leave this open for now. The commutator in Eq. (2.4) does not define the t^a in a completely unique way. One might thus choose to work in a basis where

$$t_{ij}^a t_{ji}^b = T_R \delta_{ab} \ . \qquad (2.5)$$

An explicit example fulfilling this for the fundamental representation is provided by the so called Gell-Mann matrices. The normalisation T_R is a matter of convention. A typical choice is $T_R = 1/2$. With a basis like this it is possible to eliminate the structure constants, since

$$-\frac{i}{T_R} \left(t_{ij}^a t_{jk}^b - t_{ij}^b t_{jk}^a \right) t_{ki}^c = \frac{1}{T_R} f^{abd} t_{ik}^d t_{ki}^c = f^{abc} \ , \qquad (2.6)$$

with the middle equality being a direct application of the definition Eq. (2.4). A useful relation in practical calculations involving these operators is

$$t_{ij}^a t_{kl}^a = T_R \left(\delta_{jk}\delta_{il} - \frac{1}{N_c}\delta_{ij}\delta_{kl} \right) \ , \qquad (2.7)$$

known as Fierz identity. It allows one to express any product of colour matrices t^a, and via Eq. (2.6) also structure constants f^{abc}, as a product of δ_{ij}'s that are 1 if $i = j$

---

[1]Nothing is preventing the introduction of a standard mass term for the q fields here, but as argued in the previous section, the focus here shall be strictly on massless QCD.

and 0 otherwise, rendering the numerical evaluation straightforward (though of course possibly time consuming if many terms are involved). Note that the indices of the fundamental representation run from $i = 1 \ldots N_c$, such that $\delta_{ii} = N_c$. With these identities at hand it is for example easy to evaluate the quadratic Casimir invariants of the fundamental and adjoint representations

$$t_{ij}^a t_{jk}^a = T_R \left(N_c \delta_{ik} - \frac{1}{N_c} \delta_{ij} \delta_{jk} \right) = T_R \frac{N_c^2 - 1}{N_C} \delta_{ik} \equiv C_F \delta_{ik} \tag{2.8}$$

$$f^{abc} f^{abd} = \left(\frac{-i}{T_R} \right)^2 \left(t_{ij}^a t_{jk}^b - t_{ij}^b t_{jk}^a \right) \left(t_{lm}^a t_{mn}^b - t_{lm}^b t_{mn}^a \right) t_{ki}^c t_{nl}^d \tag{2.9}$$

$$= 2 \left(\frac{-i}{T_R} \right)^2 \left(t_{ij}^a t_{lm}^a t_{jk}^b t_{mn}^b - t_{ij}^a t_{mn}^a t_{jk}^b t_{lm}^b \right) t_{ki}^c t_{nl}^d$$

$$= -2 \left(\left(\delta_{jl} \delta_{im} - \frac{1}{N_c} \delta_{ij} \delta_{lm} \right) \left(\delta_{km} \delta_{jn} - \frac{1}{N_c} \delta_{jk} \delta_{mn} \right) \right.$$

$$\left. - \left(\delta_{jm} \delta_{in} - \frac{1}{N_c} \delta_{ij} \delta_{mn} \right) \left(\delta_{kl} \delta_{jm} - \frac{1}{N_c} \delta_{jk} \delta_{lm} \right) \right) t_{ki}^c t_{nl}^d$$

$$= -2 \left(\left(\delta_{nl} \delta_{ik} - \frac{2}{N_c} \delta_{in} \delta_{lk} + \frac{1}{N_c^2} \delta_{ik} \delta_{ln} \right) \right.$$

$$\left. - \left(N_c \delta_{in} \delta_{kl} - \frac{2}{N_c} \delta_{in} \delta_{kl} + \frac{1}{N_c^2} \delta_{ik} \delta_{nl} \right) \right) t_{ki}^c t_{nl}^d$$

$$= 2 N_c t_{kn}^c t_{nl}^d = 2 T_R N_c \delta_{cd} \equiv C_A \delta_{cd} \ .$$

Note that multiplying out the two brackets in the first line in Eq. (2.9) leads to four terms that are pairwise equal after renaming indices. The terms in the second to last line that do not cancel between the two brackets are of the form $\delta_{ij} t_{ij}^a$, apart from the one that equals the final result. As the t^a are generators of $SU(N_c)$, and hence their trace is zero, those terms vanish. With $T_R = 1/2$ and for $N_c = 3$ one has $C_F = 4/3$ and $C_A = 3$.

To make contact with collider experiments, the principal quantities of interest are scattering cross-sections,

$$\Sigma\left(\Theta\right) = \sum_{\mathcal{C}} \int d\mathcal{C} \langle \mathcal{C} | \mathcal{C} \rangle \Theta(\mathcal{C}) \ . \tag{2.10}$$

Here $\mathcal{C} = \mathcal{C}_{\text{in}} \cup \mathcal{C}_{\text{out}}$ is the collection of all particles, *i.e.* the set of momenta and flavours, in the initial and final state of a collision, and the sum is in principle over all possible

configurations. The notation will be simplified to treat this just as a set of momenta or flavours if appropriate for the context in the following. For example, the integral over $d\mathcal{C}$ represents the integration over the kinematic variables of the final state. It contains all the momentum conserving delta functions and associated factors to make it the fully Lorentz invariant phase space element. The object $|\mathcal{C}\rangle$ appearing in the cross section is the amplitude for scattering from the initial state $\mathcal{C}_{\mathrm{in}}$ to the final state $\mathcal{C}_{\mathrm{out}}$. As is implied by the notation, it can usually be viewed as a vector in a space of adequate quantum numbers, and the average and sum over those is understood to be implied by the product between the amplitude and its conjugate, $\langle\cdot|\cdot\rangle$. This squared matrix element is related to the probability of a scattering from the initial to the final state. The cross section Σ depends on the various cuts made in an experiment, represented by Θ. It is indeed usually in the form of a collection of θ functions,

$$\theta(x) = \begin{cases} 1 & \text{if} \quad x > 0 \\ 0 & \text{else,} \end{cases} \tag{2.11}$$

depending on variables calculated from $\mathcal{C}$. Typically, the initial state $\mathcal{C}_{\mathrm{in}}$ does not vary within a given experiment, so conditions on it will be omitted in the Θ function. A typical example is an inclusive cross-section, *i.e.* without a kinematic cut and with some final state particle required, say for the sake of concreteness a Z boson and fix the initial state to two protons. This can be expressed as

$$\Theta(\mathcal{C}) = \begin{cases} 1 \text{ if } Z \in \mathcal{C}_{\mathrm{out}} \\ 0 \text{ else} \end{cases} \tag{2.12}$$

$$\sigma^{\mathrm{DY}} \equiv \Sigma^{\mathrm{DY}} = \int d\mathcal{C}(Q^2, y)\langle pp \to Z | pp \to Z\rangle \tag{2.13}$$

$$+ \sum_X \int dX \, d\mathcal{C}(Q^2, y)\langle pp \to Z + X | pp \to Z + X\rangle \ .$$

As the notation suggests, this is an example of a Drell-Yan (DY) process. It has been made explicit that the kinematics of the Z boson can be parametrised by its virtuality Q^2 and its rapidity y, and the sum has been separated into a term where the final state only consists of the Z boson, and one where the sum over an additional collection of arbitrary final state particles X is executed. Another important example is the case where a single number $V(\mathcal{C})$ is calculated from all momenta of the final state particles, and a cut v on this number is placed:

$$\Theta(\mathcal{C}) = \theta(v - V(\mathcal{C})) \tag{2.14}$$

$$\Sigma(v) = \sum_{\mathcal{C}} \int d\mathcal{C}\langle\mathcal{C}|\mathcal{C}\rangle\theta(v - V(\mathcal{C})) \ . \tag{2.15}$$

At the end of the day this, might be combined with additional requirements on $\mathcal{C}$. Note that, from the knowledge of Σ as a function of v, one can reconstruct a differential cross-section

$$\frac{d\sigma}{dv} \equiv \frac{d\Sigma}{dv} = \sum_{\mathcal{C}} \int d\mathcal{C} \langle \mathcal{C}|\mathcal{C}\rangle \delta\left(v - V\left(\mathcal{C}\right)\right) \ . \tag{2.16}$$

A problem that has not been addressed so far is that experiments are performed with hadrons in the initial state, and are also observed to always produce hadrons as final states, but QCD is formulated in terms of quarks and gluons. If one accepts the parton model, with the quarks and gluons of QCD as partons, this connection is a straightforward application of the concept expressed in Eq. (2.1). Taking again the Drell-Yan cross section as an example, one writes

$$\sigma^{\mathsf{DY}} = \sum_{a,b=q,\bar{q},g} \int_0^1 dx_a\, dx_b\, f_a^{\mathsf{proton}}(x_a, \mu_F^2) f_b^{\mathsf{proton}}(x_b, \mu_F^2) \tag{2.17}$$

$$\times\, \Sigma\left(\{a, x_a p_1\}, \{b, x_b p_2\}; Z + X\right)$$

$$= \sum_{a,b=q,\bar{q},g} \int_0^1 dx_a\, dx_b\, f_a^{\mathsf{proton}}(x_a, \mu_F^2) f_b^{\mathsf{proton}}(x_b, \mu_F^2)$$

$$\times \int d\mathcal{C}(Q^2, y)\langle ab \to Z|ab \to Z\rangle + \dots \ .$$

Here the dots represent the sum over additional final state particles similar to the second line in Eq. (2.13). The partonic initial state in the first line represents partons a and b, with respective four momenta $x_a p_1$, $x_b p_2$, p_1 and p_2 being the momenta of the initial state protons. Note that the sum contains gluons as initial states. At leading order this contribution is of course absent since there is no fundamental $gg \to Z$ interaction. At higher orders a Z can be produced with one or two gluons in the initial state however.

This approach can be applied to all kinds of hadronic processes, like the DIS process introduced earlier or proton-(anti-)proton collisions with different final states, within the parton model. Careful analyses can justify it in the form of rigorous factorization theorems within QCD, typically validating it up to power corrections $\mathcal{O}(1/Q^2)$ for some relevant energy scale Q^2, see for example Ref. [73]. The precise formulation of those theorems is omitted here, and the focus will be on performing precise calculations for the partonic part within QCD.

An analogous approach is available if one is for example interested in a particular hadron in the final state, $\mathcal{C} = h + X$. Here the partonic calculation is carried out for all possible partonic final states and then convoluted with fragmentation functions $f_h^{\mathsf{parton}}(x)$, empirically representing the probability to produce hadron h with energy fraction x from a specific parton. Alternatively, one might attempt to directly apply

the final state cuts in Θ to the partonic final state. This is certainly justified if one considers inclusive hadron production, $\Theta = 1$. The same might be done conceptually if Θ contains cuts that are mainly measuring the overall energy distribution of the final state, an assumption known as parton-hadron duality. Typically however, there is some modelling input required in those cases to match actual experimental data.

2.3 Perturbative quantum chromodynamics

In the previous section, it was assumed that one just knows the amplitudes once the field theory is fixed by the Lagrangian density. Indeed, following textbook treatment such as [74], the LSZ reduction formula [75] provides the link between scattering amplitudes from asymptotic free incoming to free outgoing states [76, 77] and n-point functions of the quantum field theory. The main approach to calculating those, at least taken here, is that of perturbation theory. That is, they are calculated as a series in the coupling parameter g present in the interaction terms in Eq. (2.2) and Eq. (2.3).

$$|\mathcal{C}\rangle = \sum_{n=0} \frac{g^{2n}}{(4\pi)^n} |\mathcal{C}^{(n)}\rangle \ , \tag{2.18}$$
$$|\mathcal{C}^{(n)}\rangle = g^{n_{\mathsf{Born}}} |\mathcal{C}_n\rangle \ .$$

Note that it has been anticipated that only corrections with an even power of g are appearing in practise. Because of this, it is useful to introduce the notation

$$\alpha_{\mathsf{s}} \equiv \frac{g^2}{4\pi} \ . \tag{2.19}$$

The inclusion of the factor of 4π is purely conventional at this point and just modifies the definition of the coefficient $|\mathcal{C}^{(n)}\rangle$. Depending on the cuts in $\Theta(\mathcal{C})$ there will be a lowest order n_{born} at which amplitudes contribute, those will be called Born level amplitudes. Note that the superscript (n) in $|\mathcal{C}^{(n)}\rangle$ denotes the orders additional to n_{Born}, as indicated in the second line of Eq. (2.18). Higher order corrections for the same amplitude add internal lines and are called virtual corrections. They lead to a "loop" topology, *cf.* the example in the left of Fig. 2.1, with an additional loop per non-vanishing order in g^2, hence e.g. the first order corrections are also called one-loop amplitudes.

Note that the sum over $\mathcal{C}$ in Eq. (2.10) includes final states where the Born level is at different orders if this is permitted by the measurement function Θ, such that the contributions to a cross section Σ at a given order in g can mix virtual and Born type corrections. In that sense the leading order amplitude for an observable is given by the lowest order amplitude where that observable is non-zero in a non trivial way, while higher order corrections with additional particles in $\mathcal{C}$ are referred to as "real" corrections for that observable.

The practical calculation of the amplitudes at a given order proceeds via the well known Feynman diagram calculus. Additional to the external momenta specified by $\mathcal{C}$, the loops appearing at higher orders contain internal momenta. Those need to be integrated over. It is well known that these integrals are not necessarily finite in the physical 4

spacetime dimensions. In the following it will be assumed that they are regularised in dimensional regularisation. This means that integrals are calculated in $D = 4 - 2\epsilon$ dimensions.

Consider e.g. the quark self energy in Fig. 2.1, which can be evaluated to[2]

$$i\Sigma(p) = \mu^{2\epsilon} \int \frac{d^D k}{(4\pi^D)} (-ig)^2 t_{il}^a t_{lj}^a \gamma^\mu \frac{i(k_\alpha \gamma^\alpha + p_\alpha \gamma^\alpha)}{(k+p)^2} \gamma^\nu \frac{-ig_{\mu\nu}}{k^2} \ . \tag{2.20}$$

See any standard textbook mentioned at the beginning of this section for the necessary Feynman rules, for concreteness the convention used corresponds to Ref. [36] and all expressions are given in the Feynman gauge. Note the introduction of the energy scale μ to preserve the dimension of the integral measure.

The necessary colour factor equals $t_{il}^a t_{lj}^a = C_F \delta_{ij}$ as shown in Eq. (2.8). A lot of standard techniques exist to deal with integrals at one loop. One example is the Passarino-Veltman decomposition [78], reducing vector and tensor valued integrals to scalar ones. This explicitly exposes the divergence as 4 spacetime dimensions are approached from the general $D = 4 - 2\epsilon$ as poles $1/\epsilon$. These can be dealt with using multiplicative renormalisation. One shifts all parameters of the Lagrangian according to

$$q \to Z_q^{1/2} q \sim \left(1 + \delta_q/2\right) q \ , \tag{2.21}$$

$$A^\mu \to Z_A^{1/2} A^\mu \sim \left(1 + \delta_A/2\right) A^\mu \ , \tag{2.22}$$

$$g \to Z_g \mu^\epsilon g \sim (1 + \delta_g)\mu^\epsilon g \ . \tag{2.23}$$

The expansion of the factors Z_i in terms of δ_i at one loop lead to the addition of counter term diagrams as shown on the right of Fig. 2.1. One determines the δ coefficients by requiring finite results for physical observables. The final result for the quark self energy is, *cf.* for example [36]

$$i\Sigma(p) = ip_\alpha \gamma^\alpha \left[\frac{g^2}{16\pi^2} \frac{2C_F}{\epsilon} + \text{finite} + \delta_q \right] \ . \tag{2.24}$$

Note the part that is finite for $\epsilon \to 0$ is ignored here. The pole in ϵ can be absorbed by setting

$$\delta_q = -\frac{\alpha_\mathsf{s} C_F}{4\pi} \frac{2}{\epsilon} \ . \tag{2.25}$$

---

[2]Note the doubling of the symbol Σ here in order to follow conventional notation. In later chapters, Σ will exclusively refer to cross sections.
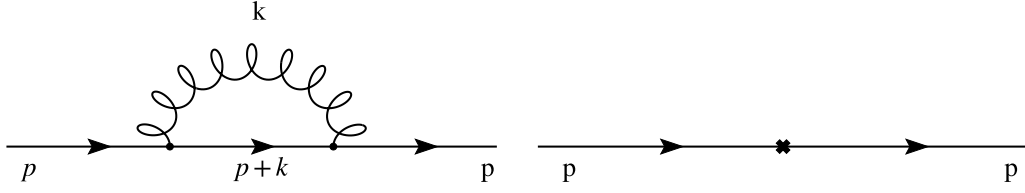
Figure 2.1: Feynman diagram and counter term contributing to the quark self energy at one loop order.

The analogous result for the gluon self energy implies

$$\delta_A = \frac{\alpha_{\mathsf{s}}}{4\pi} \left(\frac{5}{3} C_A - \frac{4}{3} T_R n_f \right) \frac{2}{\epsilon} \, . \tag{2.26}$$

The corrections to the three-point function depends on all three renormalisation parameters,

$$\delta_g + \delta_q + \delta_A/2 = -\frac{\alpha_{\mathsf{s}}}{4\pi} (C_A + C_F) \frac{2}{\epsilon} \tag{2.27}$$

$$\Rightarrow \delta_g = \frac{\alpha_{\mathsf{s}}}{4\pi} \left(-\frac{11}{6} C_A + \frac{2}{3} T_R n_f \right) \frac{2}{\epsilon} \, . \tag{2.28}$$

Note how the shift of g in Eq. (2.23) depends on the scale μ introduced earlier. This dependence can be absorbed into the physical coupling constant $g_{\text{phys}} \equiv Z_g \mu^\epsilon g$. Since μ is an arbitrary scale, physical results should not depend on it. This can be guaranteed by requiring that,

$$0 = \frac{dg_{\text{phys}}^2}{d \ln \mu^2} \equiv \epsilon \mu^{2\epsilon} Z_g^2 g^2 + \mu^{2\epsilon} \beta(\alpha_{\mathsf{s}}) \frac{dZ_g^2 g^2}{d\alpha_{\mathsf{s}}} \, , \tag{2.29}$$

where the second term on the right hand side defines the function $\beta(\alpha_{\mathsf{s}}) = d\alpha_{\mathsf{s}} \, / \, d \ln \mu^2$. Note that the derivative of the coupling squared has been taken, and with respect to the log of the scale μ. Those are choices, the only point being that independence is expressed by the fact that the derivative is zero. The dependence of Z_g on α_{s} is via δ_g in Eq. (2.28). The β function can be determined order by order in α_{s}

$$\frac{d\alpha_{\mathsf{s}} \left(\mu^2 \right)}{d \ln \mu^2} = -\beta_0 \alpha_{\mathsf{s}}^2 - \beta_1 \alpha_{\mathsf{s}}^3 + \mathcal{O}(\alpha_{\mathsf{s}}^4) \, , \tag{2.30}$$

with [79, 80]

$$\beta_0 = \frac{11C_A - 2n_f}{12\pi} \; , \tag{2.31}$$

$$\beta_1 = \frac{17C_A^2 - 5C_A n_f - 3C_F n_f}{24\pi^2} \; . \tag{2.32}$$

This renormalisation group equation relates the strong coupling at a reference scale, a typical choice is the Z mass M_Z^2 with $\alpha_s(M_Z^2) \approx 0.118$, to an arbitrary scale,

$$\alpha_s^{1L}\left(\mu^2\right) = \frac{\alpha_s\left(M_Z^2\right)}{1 + \alpha_s\left(M_Z^2\right)\beta_0 \ln \mu^2/M_Z^2} \; . \tag{2.33}$$

The "1L" superscript indicates that the running has been computed at one-loop accuracy. Including the β_1 coefficient in Eq. (2.30), one obtains

$$\alpha_s\left(\mu^2\right) = \alpha_s^{1L}\left(\mu^2\right) + \alpha_s^{2L}\left(\mu^2\right) \; , \tag{2.34}$$

with the two loop part of the running of the strong coupling given by

$$\alpha_s^{2L}\left(\mu^2\right) = \alpha_s^2\left(M_Z^2\right)\frac{\beta_1}{\beta_0}\frac{\ln\left(1 + \alpha_s\left(M_Z^2\right)\beta_0 \ln \mu^2/M_Z^2\right)}{1 + \alpha_s\left(M_Z^2\right)\beta_0 \ln \mu^2/M_Z^2} \; . \tag{2.35}$$

Historically, the realisation that the β function is negative[3] was an important step in establishing QCD as the underlying fundamental theory of the strong interaction. As can be seen from Eq. (2.33), it leads to a decrease of α_s with the energy scale, $\alpha_s\left(\mu^2 \to \infty\right) \to 0$. This supports the parton model picture, where partons are strongly bound and confined to hadrons at low energies, but are weakly bound and asymptotic free at higher energies. This observation is known as asymptotic freedom. Investigating the low energy behaviour, the one loop running exhibits the so-called Landau pole, approached when the denominator in Eq. (2.33) is zero. At one loop, this happens when μ^2 equals

$$\Lambda_{\text{QCD}}^2 = M_Z^2 e^{-1/\alpha_s\left(M_Z^2\right)\beta_0} \; . \tag{2.36}$$

If one uses realistic values for M_Z and $\alpha_s\left(M_Z^2\right)$, this is at very low energies $\Lambda_{\text{QCD}} < 100$ MeV. However, higher order corrections heavily modify this, as well as the energy thresholds corresponding to the heavier b and c quarks. Realistically, the Landau pole sets an energy scale of $\approx 100 - 400$ MeV [32].

The poles in ϵ discussed so far were all associated to the high energy behaviour of the amplitudes (in analogy to electromagnetic radiation, this is referred to as the ultra-violet (UV) regime). It can be traced to the fact that the nominator in integrals does not
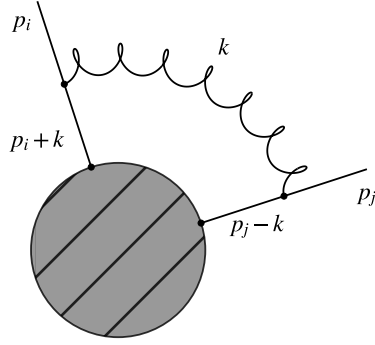
Figure 2.2: Example diagram giving rise to collinear divergencies if k is on-shell $k^2 = 0$ and collinear to either p_i or p_j, and to a soft divergence if $k \to 0$.

vanish quick enough for $k \to \infty$, relative to the denominator build from the propagators involved in the loop.

Equivalently, one might expect problems when $k \to 0$, if the powers of k in the numerator are smaller than in the denominator and the integrand hence potentially diverges. Those are known as infrared (IR) divergences. They correspond to configurations where the internal propagator lines of a loop correction are on their mass shell, $l_i^2 = 0$. As an example consider the insertion of a gluon between two final state legs $\{p_i, p_j\} \subset \mathcal{C}$ of an amplitude as shown in Fig. 2.2. The product of propagators will be of the form

$$\propto \frac{1}{k^2 (p_i + k)^2 (p_j - k)^2} \ . \tag{2.37}$$

This is naively divergent if

$$k^\mu \to 0 \Rightarrow k^2 \to 0, \tag{2.38}$$

corresponding to a soft gluon, and the cases where the gluon momentum is collinear to leg i or j,

$$k^\mu \to z_i p_i^\mu \Rightarrow (p_i + k)^2 \to (1 + z_i)^2 p_i^2 = 0 \ , \tag{2.39}$$
$$k^\mu \to z_j p_j^\mu \Rightarrow (p_j - k)^2 \to (1 - z_j)^2 p_j^2 = 0 \ , \tag{2.40}$$

for some proportionality constant

$$0 < z_i, z_j < 1 \ . \tag{2.41}$$

---

[3]The obvious caveat to this statement is that n_f can not be too large, which is no problem at the physical $n_f \le 6$, well established at the experimentally relevant energies.

Note that in principle, those zeros in the denominator do not necessarily lead to actual divergencies of the integrals, and of course there could be more that are missed here. A careful analysis of this [34, 40] leads to more precise conditions called Landau equations [81]. They confirm this is the general structure appearing also at higher order, *i.e.* with more virtual gluons (or quark loops, in principle) inserted. In general, IR divergences occur whenever all the loop momenta that are on-shell are either collinear to one of the external legs, $k_i \to p_i$ or are zero $k_i \to 0$. Possible off shell momenta can be ignored for this purpose. The physics picture emerging from this discussion is that of collimated jets of gluons, along the directions given by the hard legs in the amplitude, accompanied by clusters of additional soft gluons. To analyse the situation
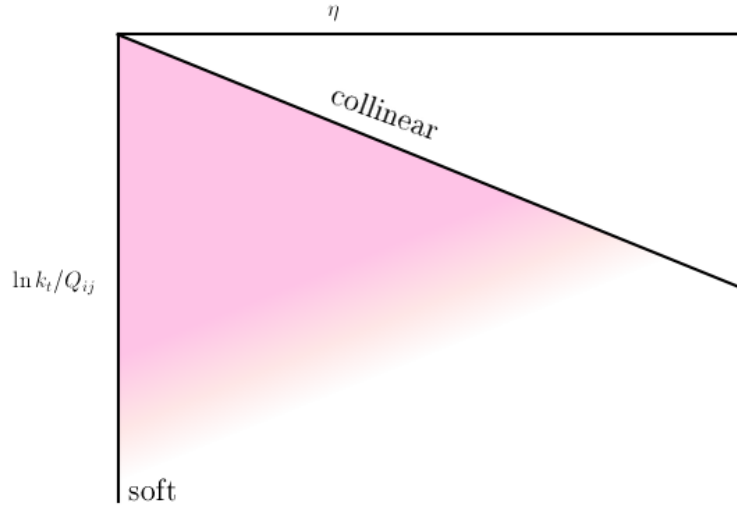

Figure 2.3: Lund plane illustrating the collinear and soft phase space of the ij dipole for $\eta > 0$.

in Fig. 2.2 more closely, it is practical to introduce the so called Sudakov decomposition of k in terms of p_i and p_j,

$$k = z_i p_i + z_j p_j + k_\perp \ , \tag{2.42}$$

where $k_\perp$ is a four momentum with $k_\perp \cdot p_i = 0 = k_\perp \cdot p_j$ and $k_\perp^2 = -k_t^2$ is the transverse momentum of k with respect to the ij dipole,

$$k_t^2 \equiv \frac{(k \cdot p_i)(p_j \cdot k)}{p_i \cdot p_j} \tag{2.43}$$

$$= z_i z_j Q_{ij}^2 \ . \tag{2.44}$$

The center-of-mass energy of the radiating dipole is given by

$$Q_{ij}^2 = 2p_i \cdot p_j \ . \tag{2.45}$$

The equality $-k_t^2 = k_\perp^2$ is implied by the masslessnes of the gluon momentum k, *i.e.* $k^2 = 0$. This leaves one degree of freedom for $k_\perp$, corresponding to the azimuthal orientation ϕ of the transverse momentum in the plane perpendicular to p_i and p_j. To construct it one picks two independent directions transverse to the reference momenta to define a plane and chooses a vector in this plane in polar coordinates using ϕ as the angle. This detail can be ignored for the moment. The Sudakov components z_i, z_j are also referred as light-cone momentum fractions. Their ratio defines a further useful quantity, the rapidity of k relative to the ij dipole,

$$\eta = \frac{1}{2} \ln \frac{z_i}{z_j} \ . \tag{2.46}$$

Taking Eq. (2.43) and Eq. (2.46) together, the Sudakov decomposition Eq. (2.42) can also be cast as

$$k = \frac{k_t}{Q_{ij}} \left(e^\eta p_i + e^{-\eta} p_j - Q_{ij} n_\perp \right) \tag{2.47}$$

with

$$n_\perp = \frac{k_\perp}{k_t} \ . \tag{2.48}$$

Now, the soft limit, where all components of the four momentum k approach 0, corresponds to a vanishing k_t or

$$\ln \frac{k_t}{Q_{ij}} \to -\infty \ . \tag{2.49}$$

The collinear limits, $z_i, z_j \to 0$ are reflected by arbitrarily large positive or negative rapidity. The condition from Eq. (2.41) however limits

$$\ln \frac{k_t}{Q_{ij}} < \eta < - \ln \frac{k_t}{Q_{ij}} \ . \tag{2.50}$$

Solutions here of course only exist if $k_t < Q_{ij}$. This situation can be illustrated in so called Lund plane diagrams [82, 83]. An example is depicted in Fig. 2.3. It is cut at $\eta = 0$, the negative η part would be mirrored but otherwise identical. The diagonal line marks the boundary given by Eq. (2.50), and the red fill is the area valid for k. It fades out towards the soft and soft-collinear limit, where the divergences identified here are located. In practice, it is often useful to choose a coordinate system where the

reference momenta are back-to-back, and their spatial momenta are along the positive and negative z-direction, for p_i and p_j respectively,

$$p_{i/j} = \frac{Q_{ij}}{2} \left(1, 0, 0, \pm 1\right) \ .$$

(2.51)

In this frame, components of the gluon momentum from Eq. (2.47) can be expressed as

$$k = k_t \left(\cosh \eta, \sin \phi, \cos \phi, \sinh \eta\right) \ .$$
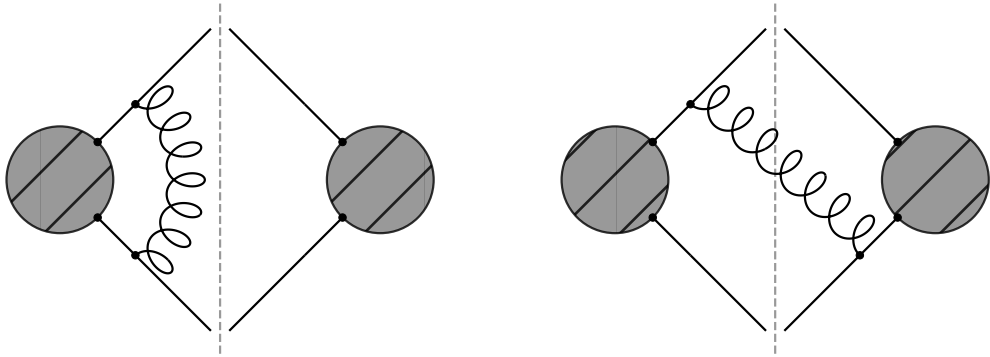
(2.52)

Figure 2.4: Examples of cut diagrams correlated by soft and collinear divergencies.

The Kinoshita-Lee-Nauenberg theorem [84, 85], a general version of the Bloch-Nordsieck theorem [86], guarantees that those divergences cancel between real and virtual corrections. They rely on the unitarity of the quantum field theory. This can be formalised in the so called cut rules [87]. A cut diagram is obtained by setting a loop momentum in a virtual correction on its mass shell and replacing the loop integral by a phase space integral. Unitarity of the theory then allows sums over all cuts in a diagram to be calculated by generalised versions of the optical theorem, relating them to a forward scattering cross section that can be argued to be finite on physical grounds. Fig. 2.4 shows an example of virtual and real amplitudes that are related by unitarity. Note there are more diagrams contributing, with a similar topology but for example with the gluon connecting the left lower to the right upper leg and alike.

The implication is that the sum over final states $\mathcal{C}$ in *e.g.* Eq. (2.10) needs to be such that this cancellation is not broken. This is a requirement on the $\Theta\left(\mathcal{C}\right)$. Whenever a

momentum $k \in \mathcal{C} = \{p_1, \ldots, p_n, k\}$ becomes soft, $k \to 0$, one needs to be able to remove it without changing Θ. Likewise, if k approaches the collinear limit of one of the other particles p_i, those can be combined with no effect on Θ. Formally this can be expressed as

$$\lim_{k \to 0} \Theta(\{p_1, \ldots, p_n, k\}) = \Theta(\{p_1, \ldots, p_n\}) \ , \tag{2.53}$$

$$\lim_{k \to z p_i} \Theta(\{p_1, \ldots, p_n, k\}) = \Theta(\{p_1, \ldots, p_i + k, p_n\}) \ . \tag{2.54}$$

This requirement is referred to as infrared and collinear safety (IRC safety). In the example of the virtual insertion from Fig. 2.2, this implies that the real and virtual corrections illustrated in Fig. 2.4 always need to be considered together.

The scope of this work ultimately is the calculation of cross sections of the type in Eq. (2.15). The relevant observables $V(\{p\})$ will typically be non-zero from some final state multiplicity $(n + 1)$ on, and hence measure the deviation from the Born multiplicity n. It will from now on be assumed that the function Θ includes additional limits that, in an IR safe way, imply that the n Born momenta are all well separated and significantly non-zero. At Born order the sum over final states $\mathcal{C}$ is over the different channels δ,

$$\Sigma(v) = \sum_{\delta} \Sigma^{\delta}(v) \ , \tag{2.55}$$

where the δ mark a particular assignment of flavours to the n Born partons. In the following, the final states $\mathcal{C}$ corresponding to the Born final states for the observable in question will hence be referred to as $\mathcal{B}^{\delta}$. At this order the observable is trivial $V(\mathcal{B}) = 0$, so the cross section is constant

$$\Sigma^{\delta,(0)}(v) = \int d\mathcal{B}^{\delta} \langle \mathcal{B}^{\delta} | \mathcal{B}^{\delta} \rangle = \sigma^{(0)} \ . \tag{2.56}$$

Note that the different orders of Σ will be denoted by

$$\Sigma = \Sigma^{(0)} + \Sigma^{(1)} + \Sigma^{(2)} + \mathcal{O}(\alpha_s^{n_{\mathrm{Born}}} \alpha_s^3) \ . \tag{2.57}$$

At first order, according to the discussion above, one has to add the one-loop correction, integrated over the loop momentum k, and the cut diagrams, integrated over the phase space of $n + 1$ particles $\mathcal{B}^{\delta} \cup \{k\}$:

$$\Sigma^{\delta,(1)}(v) = \int \frac{d^D k}{(4\pi^D)} 2 \operatorname{Re}\left(\langle \mathcal{B}^{\delta,(1)} | \mathcal{B}^{\delta} \rangle \right) \tag{2.58}$$

$$+ \int d(\mathcal{B}^{\delta} \cup \{k\}) \langle \mathcal{B}^{\delta} \cup \{k\} | \mathcal{B}^{\delta} \cup \{k\} \rangle \theta\left(v - V(\mathcal{B}^{\delta}, k) \right) \ .$$

Note how the loop correction $|\mathcal{B}^{\delta,(1)}\rangle$ contributes via interference with the Born level amplitude, since both correspond to the same configuration of partons. The θ function cutting on V is hence still trivial for them. It however affects the real corrections, disturbing the cancellation between uncut and cut diagrams. To make it more explicit, use

$$1 = \theta\left(v - V(\mathcal{B}^{\delta}, k)\right) + \theta\left(V(\mathcal{B}^{\delta}, k) - v\right) \,, \tag{2.59}$$

to rewrite the θ function,

$$
\begin{aligned}
\Sigma^{\delta,(1)}(v) = \; & \int d\mathcal{B}^{\delta} \int \frac{d^D k}{(4\pi^D)} 2\operatorname{Re}\left(\langle \mathcal{B}^{\delta,(1)}|\mathcal{B}^{\delta}\rangle\right) \\
& + \int d(\mathcal{B}^{\delta} \cup \{k\})\langle \mathcal{B}^{\delta} \cup \{k\}|\mathcal{B}^{\delta} \cup \{k\}\rangle \\
& - \int d(\mathcal{B}^{\delta} \cup \{k\})\langle \mathcal{B}^{\delta} \cup \{k\}|\mathcal{B}^{\delta} \cup \{k\}\rangle \theta\left(V(\mathcal{B}^{\delta}, k) - v\right) \,.
\end{aligned}
\tag{2.60}
$$

The focus will now be on the insertion of gluons approaching the soft limit, $k \to 0$. IR safety requires that in this limits, the first and second line cancel. The real contribution in the third line factorises in the same limit as

$$\langle \mathcal{B} \cup \{k\}|\mathcal{B} \cup \{k\}\rangle \sim g^2 \sum_{I,J \in \mathcal{B}} \frac{p_I \cdot p_J}{(p_I \cdot k)(k \cdot p_J)}\langle \mathcal{B}|\mathbf{T}_I \mathbf{T}_J|\mathcal{B}\rangle \,. \tag{2.61}$$

Here the $\mathbf{T}_I$ denote colour insertion operators that map the colour structures of the $\mathcal{B}$ configuration to the appropriate one for the amplitude with an additional gluon attached at leg J in the amplitude and at leg I in the conjugate amplitude. The phase space factorises similarly, and the integration over the soft collinear gluon momentum k will be expressed in the Sudakov components relative to the dipoles. The third line of Eq. (2.60) can now be written as

$$
\begin{aligned}
\Sigma^{\delta,(1)}(v) \sim & \sum_{I \neq J} \int d\mathcal{B}^{\delta} \int dk_t^2 \, d\eta \, \frac{d\phi}{2\pi} \frac{\alpha_s}{\pi} \frac{p_I \cdot p_J}{(p_I \cdot k)(k \cdot p_J)}\langle \mathcal{B}^{\delta}|\mathbf{T}_I \mathbf{T}_J|\mathcal{B}^{\delta}\rangle \\
& \times \theta\left(V(\mathcal{B}^{\delta}, k) - v\right) \,,
\end{aligned}
\tag{2.62}
$$

$$\equiv \sum_{I \neq J} \int d\mathcal{B}^{\delta} \langle \mathcal{B}^{\delta}|R_{IJ}^{\mathcal{B}^{\delta}}|\mathcal{B}^{\delta}\rangle \,. \tag{2.63}$$

Note that the integral over k only covers a region away from the soft collinear divergencies, as long as v is finite $v > 0$, and can hence after UV renormalisation it can directly

be performed in 4 dimensions. The integration boundaries are given by Fig. 2.3 and the additional θ function in Eq. (2.62).

To explore it further, assume that the function $V(\mathcal{B}, k)$ can, in some arbitrary frame, be parametrised with coefficients a_l, b_l, d_l as, *cf.* Ref. [88],

$$V(\mathcal{B}, k) = d_l \left(\frac{k_t^{(l)}}{\mu_Q} \right)^{a_l} e^{-b_l \eta^{(l)}} \tag{2.64}$$

when k approaches the $l = I, J$ collinear limit. Here $k_t^{(l)}$ and $\eta^{(l)}$ are the transverse momentum and rapidity with respect to l. They can be identified with the ones defined in terms of the dipole IJ earlier in the center of mass frame of the dipole,

$$k_t^{(I)} = k_t \tag{2.65}$$

while η^l in a general frame is obtained from the invariant introduced earlier by

$$\eta^{(I)} = \eta + \ln \frac{2E_I}{Q_{IJ}} \ . \tag{2.66}$$

The energy scale μ_Q is introduced to arrive at a dimensionless V.

The idea is now to use this approximation with $l = I$ for $\ln k_t/Q_{IJ} < \eta < \eta_{\mathsf{min}}$ and with $l = J$ for $\eta_{\mathsf{min}} < \eta < -\ln k_t/Q_{IJ}$. The usual choice for $\eta_{\mathsf{min}} = 0$ splits the dipole into two parts, corresponding to the I and J collinear region. For one of those one obtains, after carrying out the ϕ integration that is assumed to be trivial for simplicity,

$$R_{IJ}^{\mathcal{B}} = \mathbf{T}_I \mathbf{T}_J \left(R_{I;J}^{\mathcal{B}} + R_{J;I}^{\mathcal{B}} \right) \ , \tag{2.67}$$

$$R_{J;I}^{\mathcal{B}} = \int \frac{dk_t^2}{k_t^2} \int_{\eta_{\mathsf{min}}}^{\ln Q_{IJ}/k_t} d\eta \frac{\alpha_{\mathsf{s}}}{\pi} \theta \left(d_J \left(\frac{k_t^J}{\mu_Q} \right)^{a_J} e^{-b_J \eta^{(J)}} - v \right) \ . \tag{2.68}$$

The interplay between the η integration limits and the θ function can be analysed by visualising the integration boundaries in the Lund plane. This is shown in Fig. 2.5 for $b = 1$. The θ function implies the red line. The dashed line marks $k_t/\mu_Q = v^{1/(a+b)}$. It separates the k_t integral into a region where k_t is larger than this, where the θ function is trivial, and a region where the θ function is determining the upper η limit alone.
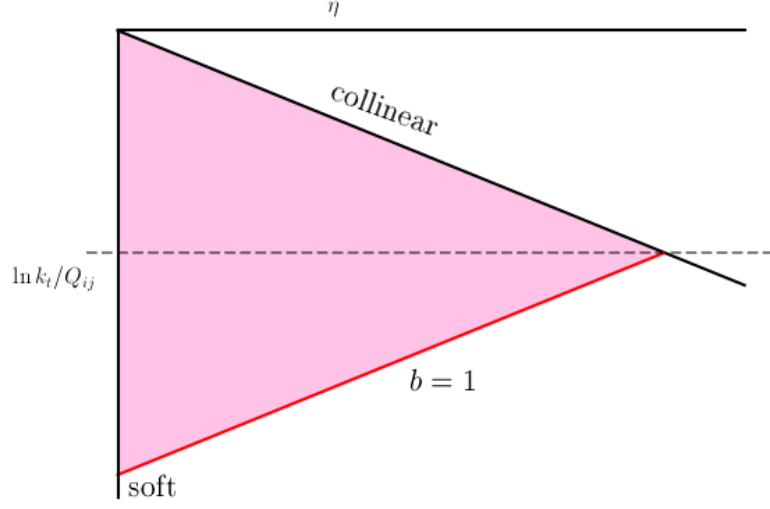
Figure 2.5: Lund plane illustrating the integration boundary for $b = 1$ and the separation between the two integration regions, see text for details.

The integrand, apart from the θ function, at this level of approximation is independent of η, so

$$R^{\mathcal{B}}_{J;I} = \int_{\mu_Q^2 v^{2/(a+b)}}^{\mu_Q^2} \frac{dk_t^2}{k_t^2} \frac{\alpha_s}{\pi} \left(-\ln \frac{k_t}{Q_{IJ}} - \eta_{\min} \right) \tag{2.69}$$

$$+ \int_{\mu_Q^2 v^{2/a}}^{\mu_Q^2 v^{2/(a+b)}} \frac{dk_t^2}{k_t^2} \frac{\alpha_s}{\pi} \left(\frac{1}{b} \ln \left[\frac{d}{v} \left(\frac{k_t}{\mu_Q} \right)^a \right] - \ln \frac{2E_J}{Q_{IJ}} - \eta_{\min} \right),$$

$$= \int_{\mu_Q^2 v^{2/(a+b)}}^{\mu_Q^2} \frac{dk_t^2}{k_t^2} \frac{\alpha_s}{\pi} \left(-\ln \frac{k_t}{\mu_Q} - \eta_{\min} \right) \tag{2.70}$$

$$+ \int_{\mu_Q^2 v^{2/a}}^{\mu_Q^2 v^{2/(a+b)}} \frac{dk_t^2}{k_t^2} \frac{\alpha_s}{\pi} \left(\frac{1}{b} \ln \left[\frac{d}{v} \left(\frac{k_t}{\mu_Q} \right)^a \right] - \ln \frac{2E_J}{\mu_Q} - \eta_{\min} \right)$$

$$+ \int_{\mu_Q^2 v^{2/a}}^{\mu_Q^2 v^{2/(a+b)}} \frac{dk_t^2}{k_t^2} \frac{\alpha_s}{\pi} \ln \frac{\mu_Q}{Q_{\text{soft}}} - \int_{\mu_Q^2 v^{2/a}}^{\mu_Q^2} \frac{dk_t^2}{k_t^2} \frac{\alpha_s}{\pi} \ln \frac{Q_{IJ}}{Q_{\text{soft}}}.$$

In the second step, the dependence on the dipole mass Q_{IJ} has been isolated, allowing

to define a function r_J equal to the first two lines and the first terms in the third line that truly only depend on J. Note that the auxiliary scale Q_{soft} was introduced, to keep all dependence on μ_Q in r_J. However, at this step it is obvious that the full expression is exactly independent of this scale. Using the fixed coupling approximation, $\alpha_{\mathsf{s}} = \text{const.}$, the new r_J can be given in terms of the logarithm $L \equiv -\ln v$

$$r_J^{\mathcal{B}} = \frac{2}{a(a+b_J)} \left(\frac{\alpha_{\mathsf{s}}}{2\pi} L^2 + \frac{\alpha_{\mathsf{s}}}{2\pi} L \left(\ln d_J - b_J \ln \frac{2E_J}{\mu_Q} \right) \right) . \tag{2.71}$$

Now the radiator function for the full IJ dipole looks like

$$R_{IJ}^{\mathcal{B}} = \mathbf{T}_I \mathbf{T}_J r_J^{\mathcal{B}} + \mathbf{T}_I \mathbf{T}_J r_I^{\mathcal{B}} + 2\mathbf{T}_I \mathbf{T}_J T_{\text{f.c.}}(L/a) \ln \frac{Q_{IJ}}{Q_{\text{soft}}} , \tag{2.72}$$

with the function

$$T_{\text{f.c.}}(L) = \int_{\mu_Q^2 e^{-2L}}^{\mu_Q^2} \frac{dk_t^2}{k_t^2} \frac{\alpha_{\mathsf{s}}}{\pi}. \tag{2.73}$$

Note the subscript f.c. indicating the fixed coupling approximation, since a similar function will later be introduced including the running of α_{s}.

Some more tidying up is in order. The sum over all dipoles can be rearranged into a sum over the individual legs and an additional piece containing the correlations between them

$$\sum_{I \neq J} R_{IJ}^{\mathcal{B}} = \sum_I \sum_{J \neq I} \mathbf{T}_I \mathbf{T}_J r_I^{\mathcal{B}} + T_{\text{f.c.}}(L/a) \sum_{I \neq J} \mathbf{T}_I \mathbf{T}_J \ln \frac{Q_{IJ}}{Q_{\text{soft}}} \tag{2.74}$$

$$\equiv \sum_I R_I^{\mathcal{B}} + T_{\text{f.c.}}(L/a) \Gamma \tag{2.75}$$

with

$$R_I^{\mathcal{B}} \equiv \mathbf{T_I} \left(\sum_{J \neq I} \mathbf{T}_J \right) r_I^{\mathcal{B}} , \tag{2.76}$$

$$\Gamma \equiv \sum_{I \neq J} \mathbf{T}_I \mathbf{T}_J \ln \frac{Q_{IJ}}{Q_{\text{soft}}} . \tag{2.77}$$

The Born amplitudes $\mathcal{B}$ are necessarily colour singlets, implying

$$\sum_{J \in \mathcal{B}} \mathbf{T}_J |\mathcal{B}\rangle = 0 , \tag{2.78}$$

$$\Rightarrow \sum_{J \neq I} \mathbf{T}_J |\mathcal{B}\rangle = -\mathbf{T}_I |\mathcal{B}\rangle , \tag{2.79}$$

and the radiator function can be simplified to

$$R_I^{\mathcal{B}} = -\mathbf{T}_I^2 r_I^{\mathcal{B}} = -C_I r_I \ , \tag{2.80}$$

with the Casimir factor C_I corresponding to the flavour of leg I, C_A for a gluon and C_F for a quark. The main point here is the general structure of the first order cross section in the small v, large L limit. As is revealed in Eq. (2.71), the leading term in that limit is $\propto \alpha_{\mathsf{s}} L^2$. It should be noted that the analysis is based on the eikonal approximation in Eq. (2.61), which indeed reproduces this term correctly. It originates from the phase space where the gluon is both soft $k \to 0$ *and* collinear to one of the external lines. There are additional terms $\propto \alpha_{\mathsf{s}} L$ that are non-vanishing in the $L \to \infty$ limit but are subleading with respect to the L^2 terms. The eikonal approximation is appropriate in the soft limit, where the gluon is not necessarily collinear. This is referred to as the soft wide-angle part of phase space. Another effect comes from configurations that are collinear to say parton I, but are not soft, hence called hard-collinear region. In this limit the eikonal approximation is not correct. The correct limit in this case is given by the Altarelli-Parisi splitting functions [89–92], in terms of the Sudakov component z of the emitted gluon in terms of the emitter I,

$$P_{qq}(z) = C_F \left[\frac{2}{1-z} - (1+z) \right] \ , \tag{2.81}$$

$$P_{gg}(z) = C_A \left[\frac{z}{1-z} + \frac{1-z}{z} + z(1-z) \right] \ , \tag{2.82}$$

$$P_{gq}(z) = T_R \left[z^2 + (1-z)^2 \right] \ . \tag{2.83}$$

The factorisation in terms of those is valid in the hard- and the soft collinear regions. To avoid double counting, the collinear limit of the eikonal approximation has to be subtracted, leaving only the terms that are finite for $z \to 1$. The coefficients of the single logarithmic terms are then obtained by integrating over z

$$2C_F B_q \equiv -C_F \int_0^1 dz(1+z) = -\frac{3}{2} C_F \tag{2.84}$$

which is applicable if I is a quark. For gluons, one needs to take into account the case where a gluon splits into a pair of collinear quarks Eq. (2.83), with n_f flavour options, as well as into two collinear gluons represented by Eq. (2.82). The result is

$$2C_A B_g \equiv -\frac{11C_A - 4T_R n_f}{12C_A} \ . \tag{2.85}$$

The coefficients B_l are also referred to as collinear anomalous dimensions. Since their effects are relevant in the hard region only, they contribute to r_I with a term

$$\propto C_I B_I T_{\mathsf{f.c.}} \left(\frac{L}{a+b_I} \right) \ . \tag{2.86}$$

This completes the single logarithmic terms at order α_{s}. The remaining contributions to Eq. (2.60) are either constants or vanish in the $v \to 0$ limit. Analysing higher orders, this structure repeats, in the sense that there are always logarithms with up to twice the powers as α_{s}. The full structure at all orders is of the form

$$\Sigma(v) \sim \sigma^{(0)} \Big[1 + \tag{2.87}$$
$$\left(\frac{\alpha_{\mathsf{s}}}{2\pi} \right) \left(D_1(v) + C_1 + G_{11}L + G_{12}L^2 \right) +$$
$$\left(\frac{\alpha_{\mathsf{s}}}{2\pi} \right)^2 \left(D_2(v) + C_2 + G_{21}L + G_{22}L^2 + G_{23}L^3 + G_{24}L^4) \right) +$$
$$\left(\frac{\alpha_{\mathsf{s}}}{2\pi} \right)^3 \left(D_3(v) + C_3 + G_{31}L + G_{32}L^2 + G_{33}L^3 + G_{34}L^4 + G_{35}L^5 + G_{36}L^6) \right)$$
$$+ \dots \Big] .$$

The functions D_i vanish in the small observable limit,

$$D_i(v) \to 0 \qquad \text{as} \qquad v \to 0 . \tag{2.88}$$

All other coefficients are just constants that can in principle be calculated, *e.g.* G_{12} and G_{22} can be read off from Eq. (2.71). The individual rows in Eq. (2.87) correspond to a computation order by order in normal perturbation theory, *i.e.* as an expansion in α_{s}. The goal of all orders statements is to first take into account the most important terms from each line in the $v \to 0$ limit. This is literately re-summing Eq. (2.87), by first adding up all terms at the end of each line, then all second to last terms, and so on. This is simplified for suitable observables, which will be specified later, for which the re-summed cross section has the structure [88]

$$\Sigma(v) \propto \left(1 + C(\alpha_{\mathsf{s}}) \right) \exp \left[L g_1(\alpha_{\mathsf{s}}L) + g_2(\alpha_{\mathsf{s}}L) + \alpha_{\mathsf{s}}g_3(\alpha_{\mathsf{s}}L) \dots \right] \tag{2.89}$$

with the g_i being power series in $\alpha_{\mathsf{s}}L$. This means that the first expression, including the L in front, contains terms of the form $\alpha_{\mathsf{s}}^n L^{n+1}$ and the second one, g_2, contains terms with equal powers in α_{s} and L. The C in Eq. (2.89) is also a power series in α_{s}. It is clear that, for such an observable, knowing g_1 and g_2 allows one to obtain the leading and a lot of the subleading terms in Eq. (2.87). The focus here will be on observables where this structure holds. By convention, expressions for Σ are called LL correct if they contain all terms generated by g_1, and NLL correct if they contain the terms obtained from g_2 in Eq. (2.89). Notice however that there is a term $\propto \alpha_{\mathsf{s}}$ generated from the first order expansion of C in Eq. (2.89), combined with the $\alpha_{\mathsf{s}}L^2$ term generated from $L g_1(\alpha_{\mathsf{s}}L)$ in the series expansion of the $\exp$ function, that contributes to $G_{22}\alpha_{\mathsf{s}}^2 L^2$ in Eq. (2.87). It is thus not sufficient to know g_2 to correctly obtain this term. The accuracy where the C is included to order α_{s}, and the g_1 and g_2 functions are included to reach NLL accuracy, is referred to as NLL$'$ accuracy in the following.

Tools and techniques for theory and phenomenology

Over the last decades of experiments researching QCD, or dealing with QCD contributions as dominant backgrounds, several techniques have emerged and proven useful in phenomenological studies. At the same time, a huge set of tools is available nowadays to perform and check calculations. With an involved subject like QCD, those two are never completely separate, with tools being constructed to meet the requirements in phenomenology and experiments, and at the same time studies being designed to make best use of the available tools. The following section is dedicated to a more detailed introduction to those tools and techniques.

The main goal of the first two sections is to introduce specific examples for observables V that are suitable to be used in the calculation of cross sections of the form Eq. (2.15). The first section introduces examples of global event shapes. Those include the standard examples to which the formalism, specified precisely later in Ch. 4, is natively applicable. The second section describes the formal definition of jets, introducing resolution scales as another standard example. Additional observables arise from the substructure of jets. For those, the final result still takes a similar structure to Eq. (2.89), but the details differ. In the third section, the soft drop technique to remove non-perturbative contributions from final states is introduced.

The remainder of the chapter describes the tools used in order to perform practical one-loop calculations, and reviews the literature on so called general purpose Monte Carlo generators. This refers to tools meant to give a complete account of collider events, by combining insight into perturbative calculations with models of hadronisation and the effects associated with hadronic initial states.

3.1   Global event shapes

The simplest thing to do if one wishes to study QCD experimentally is to define a function of all the momenta in the final state and measure the cross section differential in that. The general picture one has in mind is that of a hard born configuration with n hard legs and a function of the final momenta that vanishes if only n particles are present $V(\{p\}) = 0$. The observable defined by that function can then be said to measure the deviation from the n particle configuration. A standard example here is thrust [93] in hadron production from lepton-lepton collisions. It is defined by considering

$$T\left(\{p\}\right) \equiv \max_{n} \frac{\sum_{p_i \in \{p\}} |\vec{n} \cdot \vec{p_i}|}{|\vec{p}|^{\text{event}}} \quad \text{with} \quad |\vec{p}|^{\text{event}} \equiv \sum_{p_i \in \{p\}} |\vec{p_i}| \qquad (3.1)$$

$$V_{\text{Thrust}}\left(\{p\}\right) = \tau \equiv 1 - T\left(\{p\}\right) \ , \qquad (3.2)$$

where T is the historical thrust observable while τ is actually vanishing in the two particle limit. Many recent calculations involving thrust prefer to work with τ instead of T. The vector $\vec{n}_T$ that maximises the sum in Eq. (3.1) defines the so called thrust axis. In an event with only two outgoing particles, which are necessarily on one axis ($\vec{p_1} = -\vec{p_2}$) in the lab frame due to momentum conservation, $\vec{n}_T$ is parallel to this axis and $T = 1, \tau = 0$. For events with three particles, it can be shown that the thrust axis is along the direction of largest momentum. The following will assume this is p_1, $\vec{n}_T = \vec{p_1}/|\vec{p_1}|$. Thrust is in this case given by

$$\tau |\vec{p}|^{\text{event}} = |\vec{p}|^{\text{event}} - \left(\frac{|\vec{p_1} \cdot \vec{p_2}|}{|\vec{p_1}|} + \frac{|\vec{p_1} \cdot \vec{p_3}|}{|\vec{p_1}|} + \frac{|\vec{p_1}|^2}{|\vec{p_1}|} \right) \qquad (3.3)$$

$$|\vec{p}|^{\text{event}} = |\vec{p_1}| + |\vec{p_2}| + |\vec{p_3}| \ . \qquad (3.4)$$

Taking p_3 to represent a soft gluon momentum, expressed like in Eq. (2.52) with p_1 and p_2 as the references, and ignoring the recoil of the additional gluon,

$$\vec{p_1} = |\vec{p}|(0,0,-1) \ , \qquad \vec{p_2} = |\vec{p}|(0,0,1) \ , \qquad (3.5)$$

$$\vec{p_3} = k_t(\cos\phi, \sin\phi, \sinh\eta) \ , \qquad (3.6)$$

one can calculate

$$|\vec{p_1} \cdot \vec{p_2}| = |\vec{p}|^2 = |\vec{p_1}|^2 = |\vec{p_2}|^2 \qquad (3.7)$$

$$|\vec{p_3} \cdot \vec{p_1}| = |\vec{p}|k_t \sinh\eta \ , \qquad |\vec{p_3}|^2 = k_t^2(1 + \sinh^2\eta) = k_t^2 \cosh^2\eta \ . \qquad (3.8)$$

Inserting this into Eq. (3.3), thrust is given by

$$\tau |\vec{p}|^{\text{event}} = k_t(\cosh\eta - \sinh\eta) = k_t e^{-\eta} \ . \qquad (3.9)$$

Comparing to Eq. (2.64), thrust corresponds to coefficients $a = 1$ and $b = 1$. The parameters are equal for both legs, hence the indices are suppressed.

Note that momentum conservation forces all three particles into a common plane. As a next step, one might want to define observables measuring the deviation from those planar configurations. This can again be done based on the construction of thrust. First, project the momenta in the event into the plane perpendicular to the thrust axis $\vec{n}_T$. Then perform the same maximisation procedure as for thrust on those projections to define the thrust major axis $\vec{n}_M$,

$$V_{\text{Thrust-Major}}\left(\{p\}\right) = T_M\left(\{p\}\right) \equiv \max_{n \perp n_T} \frac{\sum_{p_i \in p} |\vec{n} \cdot p_i|}{|\vec{p}|^{\text{event}}} \ . \tag{3.10}$$

Thrust major is an example of an observable that does not scale with η. in terms of Eq. (2.64) this is expressed by $a = 1$ and $b = 0$. Finally, one can define the thrust minor as

$$V_{\text{Thrust-Minor}}\left(\{p\}\right) = T_m\left(\{p\}\right) \equiv \frac{\sum_{p_i \in p} |\vec{n}_m \cdot p_i|}{|\vec{p}|^{\text{event}}} \tag{3.11}$$

$$\vec{n}_m \equiv \vec{n}_T \times \vec{n}_M \ , \tag{3.12}$$

with the trust minor axis $\vec{n}_m$. Thrust major, as thrust itself, is non-zero for events with three particles, and hence referred to as an example of three-jet observables. Thrust minor on the other hand is a four-jet observable that is measuring the deviation from planar three-jet events.

The thrust axis conveniently allows to split the final state $\mathcal{C}$ into two hemispheres, according to the sign of $\vec{n}_T \cdot \vec{p}_i$

$$\mathcal{H}_L = \left\{i \in \mathcal{C} \middle| \vec{n}_T \cdot \vec{p}_i < 0\right\} \ , \tag{3.13}$$

$$\mathcal{H}_R = \left\{i \in \mathcal{C} \middle| \vec{n}_T \cdot \vec{p}_i > 0\right\} \ , \tag{3.14}$$

where the indices L, R label the left and right hemisphere (what is labelled as "left" and "right" depends on the chosen coordinate system and is ultimately meaningless, the point is that every event is split into two hemispheres in a unique way). These can be used to define observables that measure properties of those hemispheres instead of the full event. Examples are the masses

$$m_L^2 = \frac{\left(\sum_{p_i \in \mathcal{H}_L} p_i\right)^2}{|\vec{p}|^{\text{event}}} \ , \qquad m_R^2 = \frac{\left(\sum_{p_i \in \mathcal{H}_R} p_i\right)^2}{|\vec{p}|^{\text{event}}} \ , \tag{3.15}$$

$$V_{\text{Heavy Mass}}\left(\{p\}\right) = m_H^2 = \max\left(\{m_L^2, m_R^2\}\right) \ . \tag{3.16}$$

For a single soft emission, the scaling of the heavy hemisphere mass m_H in terms of Eq. (2.64) is the same as for thrust. Another example for a scaling proportional to the relative transverse momentum only, $b = 0$, is the wide hemisphere broadening B_W, that can be defined as

$$B_L = \frac{\sum_{p_i \in \mathcal{H}_L} |\vec{p}_i \times \vec{n}_T|}{|\vec{p}|^{\text{event}}} \ , \qquad B_R = \frac{\sum_{p_i \in \mathcal{H}_R} |\vec{p}_i \times \vec{n}_T|}{|\vec{p}|^{\text{event}}} \qquad (3.17)$$

$$V_{\text{Wide Broadening}} \left(\{p\}\right) = B_W = \max \left(\{B_L, B_R\}\right) \ . \qquad (3.18)$$

A similar approach is available in hadron-hadron collisions. As explained before, the physics picture for such interactions is that of two partons, one from each of the colliding hadrons, interact with each other. Those partons will only have a fraction of the hadronic momentum, hence the overall center of mass frame is unknown. Since they are still collinear to the hadron directions however, the sums of the transverse momenta cancel in the laboratory frame. Observables for hadronic collisions are hence usually defined only referring to the transverse components of the particle momenta. The hadronic version of thrust, called transverse thrust in the following, can be defined as

$$V_{\text{Transverse Thrust}} \left(\{p\}\right) = \tau_\perp \equiv 1 - \max_{\vec{n}_\perp} \left(\frac{\sum_i |\vec{p}_{T,i} \cdot \vec{n}_\perp|}{\left(p_{T,\text{tot}}\right)^{\text{event}}} \right) \ , \qquad (3.19)$$

$$\left(p_{T,\text{tot}}\right)^{\text{event}} = \sum_i p_{T,i} \ . \qquad (3.20)$$

As in the lepton collider version, transverse thrust by definition vanishes in the limit of 2 *final state* particles. Note that this means 4 coloured legs are involved in the Born events, including the initial state. Eq. (3.19) again implicitly defines the transverse thrust axis. This similarly divides the event into two hemispheres. Based on those, one can define the same kinds of event shapes as in the e^+e^- case above.

3.2 Jet algorithms and jet substructure

In the preceding section, the word "jet" has been used to loosely mean a collimated bunch of particles. As the earlier analysis suggests, this is in fact a typical occurrence in hadron production events. To gather a quantitative description of jets, it is necessary to formalise their definition. Early attempts on this were based on first defining a jet as all particles within a geometrical cone around some direction [94]. Stable cones are then defined by iteratively using the sum of the particle momenta inside the cones as new directions, see e.g. [95] for a review. Out of the several versions of these definitions, only the latest iterations, like the one in Ref. [96] are IRC safe.

A second class of jet algorithms are the so called sequential clustering algorithms [97, 98]. They usually depend on some distance measure between two final state particles d_{ij} and between a final state particle and the beam d_{iB}, and on some stopping criterion. The procedure is as follows:

0. Start with the list $\mathcal{O}$ of all final state objects that enter the clustering, the beams B and $\bar{B}$, and the list of clustered jets $\mathcal{J}$.

1. Check if the stopping criterion is met. If yes, add all remaining objects in $\mathcal{O}$ to $\mathcal{J}$ and terminate the algorithm. The list $\mathcal{J}$ contains the jets.

2. Determine the pair $\{i, j\} \in \mathcal{O}$ that minimises some distance measure d_{ij}, and the object k that minimises the beam distance measure d_{kB}.

3. The next step is determined by $d = \min\left(d_{ij}, d_{kB}\right)$:

   (a) If $d = d_{ij}$, update $\mathcal{O}$ by removing objects i and j and adding a new object with four momentum $p_i + p_j$.

   (b) If $d = d_{kB}$, update $\mathcal{O}$ and $\mathcal{J}$ by moving object k from $\mathcal{O}$ to $\mathcal{J}$.

   Go back to step 1.

In this form, jets will be defined throughout this thesis. Some relevant variations that exist in the literature include

Different combination schemes: If two final state objects i and j are combined, the four momentum of the new object might be determined from the original p_i and p_j in other ways than by simply adding them. Common variations are ones where the combined object remains massless, which can for example be achieved

by explicitly setting the energy to the magnitude of the spatial momentum component, $\vec{p}_{i+j} = \vec{p}_i + \vec{p}_j, p_{i+j} = \left(|\vec{p}_{i+j}|, \vec{p}_{i+j}\right)$.

Inclusive and exclusive algorithms In cases where the minimal distance is d_{kB}, i.e. a distance with respect to the beam, instead of adding k to $\mathcal{J}$ it might just be dropped. This might for example be the appropriate procedure in cases where those objects are supposed to be interpreted as radiation from the beam particles.

Different sequential combination algorithms are distinguished by the definition of the distance measures, and by the stopping criterion. In the case of colour singlet initial states, the beam distance measures are usually ignored, note this might formally be incorporated in the above scheme by setting d_{iB} to infinity. The usual stopping criteria are:

In cases d_{iB} is calculated, and i is moved to $\mathcal{J}$ if d_{iB} is the minimal measure, the algorithm can just be run until $\mathcal{O}$ is empty. This shall be the default choice here for hadronic initial states.

The algorithm can terminate if the distances between all particles are larger than some d_{cut}. In general, the distance measure used for terminating the algorithm might be different from the one used to determine which clustering is to happen next. Nevertheless, placing a cut in the same distance measure as is used in the algorithm will be the default choice for lepton-lepton collisions.

A very general class of algorithms, depending on a parameter p is specified by the distance measure

$$d_{iB} = k_{t,i}^{2p} \tag{3.21}$$

$$d_{ij} = \min(k_{t,i}^{2p}, k_{t,j}^{2p})\left(\frac{\Delta R_{ij}}{R}\right)^2 \tag{3.22}$$

where k_t is the transverse momentum relative to the beam. The angular distance ΔR_{ij} is given by

$$\Delta R_{ij}^2 = \left(y_i - y_j\right)^2 + \left(\phi_i - \phi_j\right)^2 \tag{3.23}$$

with the rapidity y_i and azimuthal angle ϕ_i of particle i, again relative to the beam axis. Note that ambiguities in choosing the coordinate system, like which of the two beams is in forward, $y > 0$ direction and where the $\phi = 0$ reference is located, are dropping out of this distance. The parameter R can be used to set the intended radius of the jet.

In addition, it is often convenient to define dimensionless versions of the distance measures

$$y_{ij} = \frac{d_{ij}}{Q^2} \qquad (3.24)$$

with some relevant physical energy scale Q^2. This is in particular the usual procedure for measurements in e^+e^- annihilation, where Q^2 is taken to be the center of mass energy of the collision. In this case it is more conventional to work with a distance measure of the form

$$y_{ij} = \frac{2\min(E_i^{2p}, E_j^{2p})}{Q^2}(1 - \cos\theta_{ij}) \,, \qquad (3.25)$$

where this time θ_{ij} is the absolute angle between the momenta,

$$\cos\theta_{ij} = \frac{\vec{p}_i \cdot \vec{p}_j}{|\vec{p}_i||\vec{p}_j|} \,, \qquad (3.26)$$

and E_i labels the energy of particle i, both defined in the center of mass frame of the collision. Note again that no beam distance measure is defined or needed in this case.

In both the hadron and lepton collider version, p is most commonly taken to be $p = 1$ (Durham or k_t algorithm, *cf.* [99–101] for lepton and [102, 103] for hadron colliders), $p = 0$ (Cambridge-Aachen (C/A) algorithm, *cf.* [104, 105]) or $p = -1$ (anti-k_t algorithm, *cf.* [106]). Those three names will in the following be used to refer to both distance measures, Eq. (3.21) and Eq. (3.25), with the corresponding values of p, understanding that the one appropriate for the collider type being discussed is meant. The FASTJET [107] package will be used in the following to access the various clustering algorithms.

A first important class of observables that can be defined based on these jet algorithms are jet resolution scales at which a new jet emerges. For the sake of simplicity, consider the Durham measure in e^+e^- annihilation. If the algorithm is run in the default version, i.e. until all remaining $y_{ij} > y_{\text{cut}}$, then y_n is defined to be the minimal value y_{cut} can be set to such that the list $\mathcal{J}$ at the end consists of at least n objects. In practice, it can be determined by running the algorithm, and terminating it when n objects are left in $\mathcal{O}$. Then calculate the distance measures once more, the smallest one is y_n. As the name suggests, the distance measure in the k_t algorithm corresponds to the relative transverse momentum squared between the two particles in the soft-collinear limit. This observable can hence be parametrised in terms of Eq. (2.64) by the parameters $a = 2$ and $b = 0$.

It is also possible to look at observables measuring properties and substructure of a given jet, in complete analogy to the properties of the hemispheres in the last section.

With the normalisation most common in the literature, e.g. the jet mass reads

$$V_{\text{Mass}}\left(\mathcal{J}\right) = \rho = \frac{\left(\sum_{i\in\mathcal{J}} p_i\right)^2}{R p_T^2} \ . \tag{3.27}$$

The mass of jets produced in hadron collisions has been studied extensively, both in theory [108–114] and experiment [115–120] , *cf.* [121–123] for reviews. A class of observables is summarised by the so called angularities [124], depending on a parameter α:

$$V_{\text{Angularity}}\left(\mathcal{J}\right) = \lambda_\alpha = \sum_{i\in\mathcal{J}} \frac{p_{T,i}}{p_{T,\text{tot}}} \left(\frac{\Delta R_{iJ}}{R}\right)^\alpha \ . \tag{3.28}$$

Here ΔR_{iJ} denotes the angular distance between jet constituent i and the overall jet axis associated with $\mathcal{J}$, calculated according to Eq. (3.23). There is a choice possible for what exact axis is associated with the jet. Here, the definition will follow Ref. [IV], taking the jet axis as the sum of the jet momenta for $\alpha > 1$. For $\alpha \leq 1$, it is defined to be the Winner-Take-All (WTA) axis [125] as defined in Ref. [126]. This avoids additional sensitivity of the observable to collinear recoil [127, 128]. Relevant calculations for this observable in various setups have been performed in [129–133]. In terms of Eq. (2.64), the angularities are parametrised for a soft gluon collinear to the jet axis by $a = 1$ and $b = \alpha - 1$. For $\alpha = 2$, this is the same scaling as for the jet mass, Eq. (3.27). Note that sometimes a yet more general version is defined where the transverse momentum fraction of each particle in the jet also enters with a variable power κ. The usually studied parameter variations $\kappa = 0$, $\alpha = 0$ (note in this case the sum in Eq. (3.28) just counts the particles) and $\kappa = 2$, $\alpha = 0$, are not IRC safe however, and will hence not be further discussed here.

3.3 Soft drop grooming

The general approach to predictions here is perturbation theory. However, there are important effects outside of its scope. Next to modelling those non-perturbative effects, it is well motivated to try and define observables that are as insensitive to them as possible. While perturbative corrections are predominantly associated with the directions of the hard legs in the process, other effects tend to be uncorrelated, and hence dominate the (soft) physics at wide angles.

An array of methods is based on attempts to clean up a given jet, or even a full event, from such contributions, *cf.* the reviews in [39, 134]. An example, that will be used here, is the soft drop grooming procedure. It was originally proposed in the context of hadron-hadron collisions [135]. For lepton-lepton collisions slight modifications [136], similar to the differences in cluster algorithms, are conventional. The structure of the algorithm is given by the following steps:

    0. Start with the list $\mathcal{O}$ of all objects that shall be subject to the grooming procedure.

    1. Run the C/A cluster algorithm on $\mathcal{O}$ until it contains only one object.

    2. Undo the last combination to obtain two objects $\{I \cup J\} = \mathcal{O}$. Calculate the soft drop condition:

$$\text{for the hadron-like algorithm} \quad \frac{\min\left(p_{T,I}, p_{T,J}\right)}{p_{T,I} + p_{T,J}} > z_{\mathsf{cut}} \left(\frac{\Delta R_{IJ}}{R}\right)^{\beta} , \quad (3.29)$$

$$\text{for the lepton-like algorithm} \quad \frac{\min\left(E_I, E_J\right)}{E_I + E_J} > z_{\mathsf{cut}} \left(\frac{1 - \cos\theta_{IJ}}{1 - \cos R}\right)^{\beta/2} . \quad (3.30)$$

    3. If the soft drop condition is true, terminate the algorithm. The groomed object $\mathcal{O}'$ consists of all particles in the single object in $\mathcal{O}$.

    4. Otherwise, remove the softer of I, J, where "softer" here refers to the object with smaller transverse momentum p_T (energy E) for the hadron-like (lepton-like) algorithm. After this, $\mathcal{O}$ consists of the harder of I, J alone.
       Go back to step 2.

The adjustable parameters are $z_{\mathsf{cut}}, \beta \geq 0$. With the requirement $\beta \geq 0$, the discussion here is restricted to what is referred to as "grooming mode", and excludes the "tagging mode" $\beta < 0$, see e.g. [135]. The $\beta = 0$ case coincides with the modified mass drop

tagger, which was introduces in the literature earlier [137]. The soft drop condition technically also contains a radius parameter R, but note that a change in it can always be absorbed into a redefinition of z_{cut}. A typical choice for the parameters is $z_{\text{cut}} \approx 0.1$ and $\beta = 0, 1, 2, \ldots$, *cf.* for example Ref. [III].

The original application is to jets, in which case R would be set to the radius of the jet, i.e. to the maximal angular distance two particles inside the jet can be apart. The technique has been applied to more global event shapes in e^+e^- annihilation [136, 138] by using the hemispheres defined by the thrust axis as inputs to the soft drop algorithm. The groomed hemispheres $\mathcal{H}'_X$ with $X = L, R$ then contain all particles of the original hemispheres that are not removed by the grooming algorithm.

The same approach is taken in Ref. [III] to groom the full final state at hadron colliders. Having cleaned the event in this way, one can calculate just the same observables on the groomed final state object, either a jet or the two hemispheres, in principle. Some care has to be taken in the precise definition of those observables however, to avoid IRC unsafety that might in particular enter via the normalisation of the observable, *cf.* Ref. [I], in particular App. A.

For concreteness, a definition of thrust after soft drop in e^+e^- annihilation, *cf.* Ref. [I] is given by

$$\tau_{\text{SD}} \equiv \left(1 - \frac{\sum_{i \in \mathcal{H}'_L} \left| \vec{n}'_L \cdot \vec{p}_i \right|}{\left(|\vec{p}| \right)^{\text{event}}} + \frac{\sum_{i \in \mathcal{H}'_R} \left| \vec{n}'_R \cdot \vec{p}_i \right|}{\left(|\vec{p}| \right)^{\text{event}}} \right) \frac{\left(|\vec{p}| \right)^{\text{groomed}}}{\left(|\vec{p}| \right)^{\text{event}}} \, , \tag{3.31}$$

with

$$\vec{n}'_X = \frac{\sum_{i \in \mathcal{H}'_X} \vec{p}_i}{\left| \sum_{i \in \mathcal{H}'_X} \vec{p}_i \right|} \, , \quad \text{and} \quad \left(|\vec{p}| \right)^{\text{groomed}} = \sum_{i \in \mathcal{H}'_L} |\vec{p}_i| + \sum_{i \in \mathcal{H}'_R} |\vec{p}_i| \, . \tag{3.32}$$

Similarly, the proposed hadron collider version of transverse thrust from Ref. [III] is formulated as

$$\tau_{\perp}^{\text{SD}} \equiv \left(1 - \frac{\sum_{i \in \mathcal{H}'_L} |\vec{p}_{T,i} \cdot \vec{n}'_{\perp,L}|}{\left(p_{T,\text{tot}} \right)^{\text{groomed}}} - \frac{\sum_{i \in \mathcal{H}'_R} |\vec{p}_{T,i} \cdot \vec{n}'_{\perp,R}|}{\left(p_{T,\text{tot}} \right)^{\text{groomed}}} \right) \frac{\left(p_{T,\text{tot}} \right)^{\text{groomed}}}{\left(p_{T,\text{tot}} \right)^{\text{event}}} \tag{3.33}$$

with

$$\vec{n}'_{\perp,X} = \frac{\sum_{i \in \mathcal{H}'_X} \vec{p}_{T,i}}{\left| \sum_{i \in \mathcal{H}'_X} \vec{p}_{T,i} \right|}, \quad \text{and} \quad \left(p_{T,\text{tot}} \right)^{\text{groomed}} = \sum_{i \in \mathcal{H}'_L} \left| \vec{p}_{T,i} \right| + \sum_{i \in \mathcal{H}'_R} \left| \vec{p}_{T,i} \right| \, . \tag{3.34}$$

In both cases, the relevant axes in both hemispheres are redefined in a way to ensure that the observables vanish if there are only two partons *that survive grooming*. With similar reasoning, one could in principle also define soft drop groomed versions for the other event shapes mentioned in Sec. 3.1.

A particularly well studied example is the groomed version of the jet mass introduced in the last section [112, 119, 120, 136, 139–143]. Likewise, the angularities as defined in Eq. (3.28) can be measured on a jet after grooming. See [144, 145] for measurements and [146] for relevant calculations besides those mentioned earlier for the plain angularities. Similar considerations apply to the normalisation. For example, the transverse momentum p_T of a jet after grooming is not an IRC safe observable in itself. So dividing by it, as is done in many definitions of jet observables since it represents the typical physical scale of relevance, is problematic. See Ref. [142] for a detailed discussion concerning the use of the groomed jet p_T. The definition given in Eq. (3.28) can however directly be applied to a jet after grooming. Note that there the normalisation is given by the scalar sum of the transverse momenta of the jet constituents.

To arrive at an interpretation of soft drop grooming in the Lund plane introduced earlier, note that the condition in Eq. (3.29) can be rewritten in terms of the Sudakov composition of a gluon momentum soft-collinear to a final state leg l by using, *cf.* Ref. [III],

$$p_{T,k} = k_t^{(l)} \frac{e^{\eta^{(l)}}}{2} \sin\theta \,, \qquad p_{T,l} = E_l \sin\theta \,, \tag{3.35}$$

$$|\Delta y| = \frac{2e^{-\eta^{(l)}} \cos\phi}{\sin\theta} \,, \qquad |\Delta\phi| = \frac{2e^{-\eta^{(l)}} \sin\phi}{\sin\theta} \,. \tag{3.36}$$

If the gluon is not groomed, its momentum has to obey the condition

$$\frac{k_t^{(l)} e^{(1+\beta)\eta^{(l)}}}{2E_l} \geq z_{\text{cut}} \left(\frac{R\sin\theta}{2} \right)^{-\beta} \equiv z'_{\text{cut}} \,. \tag{3.37}$$

Note that here the effective soft drop parameter z'_{cut} was defined, consistent with the earlier comment that a change in R can be absorbed into the definition of z_{cut}. The corresponding Lund plane picture is shown in Fig. 3.1. The blue area illustrates the region of phase space where a gluon is groomed away that would otherwise contribute to an observable with $b_l = 1$ and $a = 1$. The solid blue area is groomed for $\beta = 0$, while the hatched area is removed if $\beta = 1$. The effect of choosing a larger β is to suppress grooming in the more collinear region, as is evidenced by the behaviour of the blue dashed boundary of the $\beta = 1$ area relative to the $\beta = 0$ case. Comparing to Eq. (3.29) and noting that the angular distance is positive $\Delta R_{IJ} > 0$, grooming is completely inactive in the $\beta \to \infty$ limit.
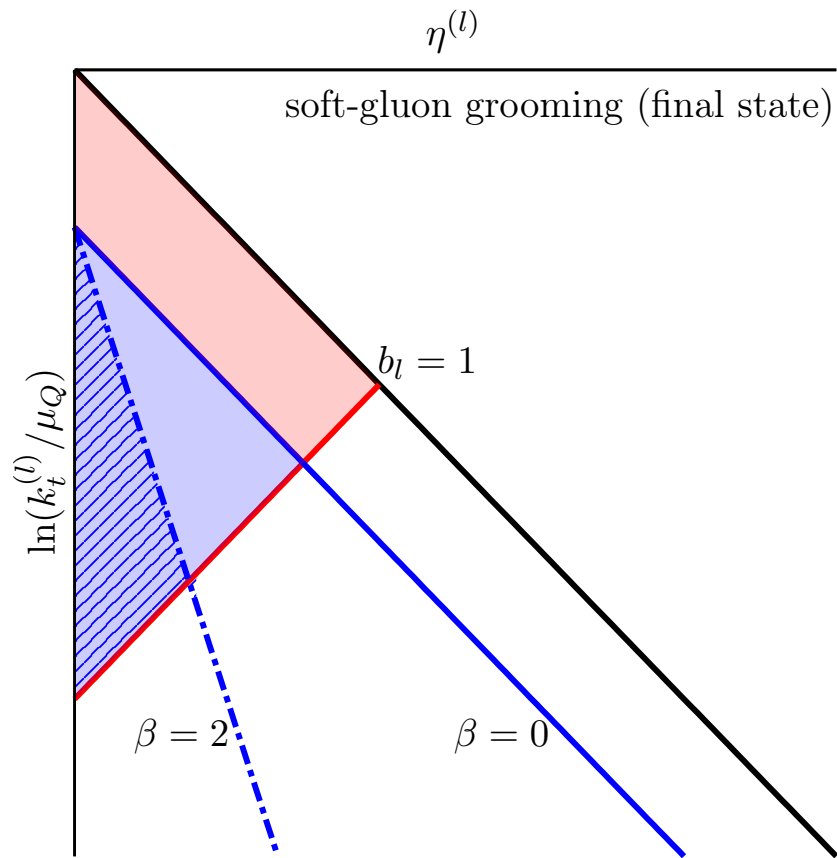
Figure 3.1: The emission phase space in the Lund plane illustrating the kinematic
constraints [...] with grooming [...]. The blue areas [...] mark the
phase-space region removed by grooming with boundaries corresponding
to $\beta = 0$ (solid line and area) and $\beta = 2$ (dashed line, hatched area).
Figure and caption taken from Figure 3 (right) in
Ref. [III]

The above analysis is only requiring the scaling behaviour of the grooming procedure in
the soft and collinear limits, and hence is applicable to both groomed hemispheres and
groomed jets. Though it used the notation and definitions of the hadron collider case,
the arguments in terms of the behaviour in the Lund plane equally apply to the e^+e^-
case.

3.4 One-loop calculations

With a better idea of what kind of observables are of interest, it is now time to discuss the practicalities of performing the relevant calculations. First, consider a fixed order calculation, of a cross section as introduced in Eq. (2.15). For the Born calculation, the contributing final states $\mathcal{C}$ all have the same multiplicity of coloured final state particles n and are distinguished by different numbers of quarks and gluons, $n = n_q + n_g$. The integral over the n-particle phase space ϕ_n is typically done with Monte Carlo methods. For low multiplicity final states, fully analytic results are available, but for the purpose of this discussion the Monte Carlo method will always be assumed as a default. A review of the various Monte Carlo methods used in particle physics is not within the scope of this thesis, Refs. [30, 147] provide an overview.

This creates a difficulty in extending a calculation beyond the Born order. The virtual corrections to a particular n-parton process, at first order, are automated nowadays and are readily available in software with standard interfaces, see below for examples. However, the loop integrals are performed, as in Sec. 2.3, in dimensional regularisation, with the divergencies exposed as poles in ϵ. Those will indeed be cancelling against the singularities in integration of the $n + 1$ particles phase space necessary for the real correction, which however is supposed to be done via Monte Carlo sampling. This requires that the cancellation of the divergencies is local in the real correction $n + 1$ particle phase space.

A very elegant method to achieve this at one-loop accuracy was introduced in [148, 149]. The idea is to introduce an approximation of the real corrections, that has the same singularities but is simple to integrate analytically over the phase space of the soft-collinear parton. The same factorisation as in Sec. 2.3 can be exploited, conceptually

$$\langle \mathcal{B} \cup \{k\} | \mathcal{B} \cup \{k\} \rangle \sim \sum_{I \neq J} \langle \mathcal{B} | \mathcal{S}_{IJ}^{\epsilon}(k) | \mathcal{B} \rangle \; , \tag{3.38}$$

where $\mathcal{S}_{IJ}$ is chosen to correctly reflect the collinear and soft limits with respect to dipole IJ, meaning that the integral

$$\sum_{I \neq J} \mathcal{I}_{IJ} \equiv \int dk_{+1}^{\epsilon} \sum_{I \neq J} \langle \mathcal{B} | \mathcal{S}_{IJ}^{\epsilon}(k) | \mathcal{B} \rangle = \int dk_{+1}^{\epsilon} \langle \mathcal{B} \cup \{k\} | \mathcal{B} \cup \{k\} \rangle + \mathcal{O}(\epsilon^0) \; , \tag{3.39}$$

with the poles in powers of $1/\epsilon$ being equal. The phase space dk_{+1} here denotes the factorised one emission phase space

$$d(\mathcal{B} \cup \{k\}) = d\mathcal{B} \, dk_{+1} \; , \tag{3.40}$$

and the superscript ϵ reiterates that the integration is performed in $D = 4 - 2\epsilon$ dimensions. Overall infrared finiteness means that those poles cancel against the ones produced in the loop integrals. Hence, the two components

$$\mathcal{VI} \equiv \int d\mathcal{B} \left(2\operatorname{Re}\left(\langle \mathcal{B}^{(1)} | \mathcal{B} \rangle \right) + \langle \mathcal{B} | \sum_{I \neq J} \mathcal{I}_{IJ} | \mathcal{B} \rangle \right) \Theta(\mathcal{B}) \tag{3.41}$$

$$\mathcal{RS} \equiv \int d(\mathcal{B} \cup \{k\}) \left(\langle \mathcal{B} \cup \{k\} | \mathcal{B} \cup \{k\} \rangle \Theta(\mathcal{B}, \{k\}) - \langle \mathcal{B} | \mathcal{S}_{IJ}^{\epsilon}(k) | \mathcal{B} \rangle \Theta(\mathcal{B}) \right) \tag{3.42}$$

are IR finite, assuming that Θ is IR safe, and their sum is equal to the total cross section

$$\Sigma^{(1)} = \mathcal{VI} + \mathcal{RS} . \tag{3.43}$$

The phase space integrals for $\mathcal{VI}$ and $\mathcal{RS}$ can then be performed via Monte Carlo methods. They return finite results that can just be added up. The generation of tree level matrix elements for the Born calculation and the real correction is automated in the SHERPA framework [150]. This includes the ingredients to perform the subtraction procedure described above, in particular the subtraction terms $\mathcal{S}$ and their integrated version $\mathcal{I}$. The generation of virtual corrections, as an expansion in ϵ, is automated and the results are available in the form of libraries. Examples include BLACKHAT [151–154], MCFM [155–158], MADGRAPH [159–161], GOSAM [162, 163] and NJET [164]. The main tools used here will be OPENLOOPS [165, 166] which are based on the techniques of [167, 168] and RECOLA [169–171]. Both use the COLLIER library [172–175] as well as other external tools [176, 177]. With that, the calculation of first order corrections can be considered as fully automated[1]. A similar automation is provided in the EVENT2 [148, 178] framework.

In terms of cross sections of the form in Eq. (2.15) that shall mainly be discussed here, this enables the calculation of both $\Sigma^{(0)}$ and $\Sigma^{(1)}$, with an arbitrary cut $V(\mathcal{C}) < v$. It is possible to calculate $\Sigma^{(2)}$ partially. More precisely, the quantity

$$\overline{\Sigma}^{(2)}(v) \equiv \Sigma^{(2)}(1) - \Sigma^{(2)}(v) = \int d\mathcal{C} \frac{d\sigma}{d\mathcal{C}} \Theta(V(\mathcal{C}) - v) , \tag{3.44}$$

i.e. the cross section for events with the observable V *larger* than some cut, can still be calculated. The contribution with two real corrections can be regularised with an additional cut $V(\mathcal{B}, \{k, l\}) > v^{\text{cut}}$. This implies that only one of the momenta k or l can be arbitrarily soft and/or collinear. The divergence related to the limiting behaviour of that single momentum can be treated with the same subtraction methods

---

[1]There are several additional considerations to be made in practice, in particular when including coloured initial states, that have not been discussed here for simplicity.

as described above, cancelling with the poles of the one-loop virtual corrections to the $\mathcal{B} \cup \{k\}$ final state with only one additional particle. The same cut eliminates the two-loop virtual corrections, as those are always at $V = 0$.

This procedure does not reproduce the overall cross section at order α_s^2 relative to the Born process. It does however correctly calculate the normalised differential distribution. This can explicitly be verified by expanding the prescriptions given in Sec. 5.5 in α_s and checking that they correctly reproduce such normalised cross sections.

3.5   General purpose Monte Carlo event generators

A complete understanding of arbitrary hadronic final states at either lepton-lepton, lepton-hadron or hadron-hadron colliders generally requires at least some modelling input. General purpose event generators are tools aimed to simulate and describe all aspects of such collision events. An overview can for example be found in Refs. [179, 180]. The general strategy is to start from a perturbative fixed order calculation of some hard core processes, represented by the red blob in Fig. 3.2. This is dressed with emissions of soft and collinear quarks and gluons, following the general logarithmic structure of QCD matrix element as discussed at the end of the last chapter, in tools called parton showers.

The picture shows a hadronic collision, so the incoming particles of the hard process are partons taken out of the incoming hadrons according to the corresponding PDFs, *cf.* Eq. (2.1). Like the final state partons, the initial state can also radiate before entering the hard interaction. A physical effect not discussed so far is represented by the purple blob in Fig. 3.2. The remaining partons in the hadrons may further interact with each other, causing a secondary interaction. The partons eventually reach energies of the order of the Landau pole, *cf.* Eq. (2.36) and transition to hadrons. Practically, the parton shower evolution will be cut off at a scale of ≈ 1 GeV and dedicated hadronisation models take over. The produced hadrons then further decay to lighter hadrons until stable configurations are reached.

Parton showers operate by obtaining emission probabilities $d\mathcal{P}$ from approximate matrix elements, like the splitting functions in Eq. (2.81). It is subject of the particular parton shower implementation what exactly the probability $\mathcal{P}$ is, here the goal is just to illustrate the general procedure. Integrating between two energy scales t, t', that can be thought of equivalent to the k_t scales involved in Eq. (2.70),

$$\int_{t'}^{t} d\mathcal{P} \tag{3.45}$$

is interpreted as probability to emit a parton between those two scales. The probability that no emission happens is then one minus the probability that any number of emissions happens,

$$\Pi(t, t') = 1 - \sum_{n=1}^{\infty} \int_{t_1}^{t} d\mathcal{P} \int_{t_2}^{t_1} d\mathcal{P} \cdots \int_{t'}^{t_n} d\mathcal{P} \ . \tag{3.46}$$

This can be simplified by modifying the integral limits to cover the full range (t, t') and

divide by the symmetry factor $n!$,

$$\Pi(t, t') = \sum_{n=0}^{\infty} \frac{\left(-\int_{t'}^{t} d\mathcal{P}\right)^n}{n!} = \exp\left[-\int_{t'}^{t} d\mathcal{P}\right] . \tag{3.47}$$

This so called Sudakov form factor [182] corresponds to the probability to obtain no emissions at all between the scales. If $d\mathcal{P}$ was independent of the parton shower scale, the emission would just follow a Poisson distribution. This is clearly not quite the case as is clear from Eq. (2.70). The η boundaries, and realistically also the argument of α_s, will depend on the energy scale. Emissions can still be generated efficiently according to Eq. (3.47) using the Sudakov veto algorithm [183] or variants thereof [184, 185]. Note that, in practice, in initial state evolution, it is necessary to also correct the PDF scale for the emitted parton energy and the interpretation of the Sudakov factor as no-emission probability is not so straightforward [147].

The main generators in use include [179] the ARIADNE program [186], HERWIG in its original form [187–189] as well as the more recent iterations [190–193], PYTHIA being rooted in the JETSET code [194–197] and then being extended to the fully fledged PYTHIA generator [198–204] with its latest variants in [183, 205, 206]. The SHERPA generator [207–209] completes this list. This thesis describes the implementation of semi-analytic resummation as a plugin to SHERPA. Some aspects of it shall hence be explained here in more detail.

The hard process in SHERPA can be calculated using one of two internal matrix element generators, AMEGIC [210] based on the method of [211–213] or COMIX [214] based on Berends-Giele recursion relations [215, 216]. Both can also be used for fixed order calculations at NLO as described in the previous section. The necessary virtual corrections can be obtained by the same tools as mentioned there, or via standardised interfaces [217, 218].

There are two options for parton showers in SHERPA. The CSSHOWER [219] will be treated as the default in the following, and it should be understood that this is used if nothing else is stated explicitly. The Dire [220] parton shower will be used for systematic studies of differences. It is particularly useful in this instance that the shower model can be changed while leaving all other variables the same. Other studies of this kind usually default to using different event generators as whole packages.

The most important effects, for the purpose of this work, in the non-perturbative realm are the hadronisation of final state particles, and the multiple parton interactions due to the underlying event. The latter is modelled in SHERPA by an implementation of the
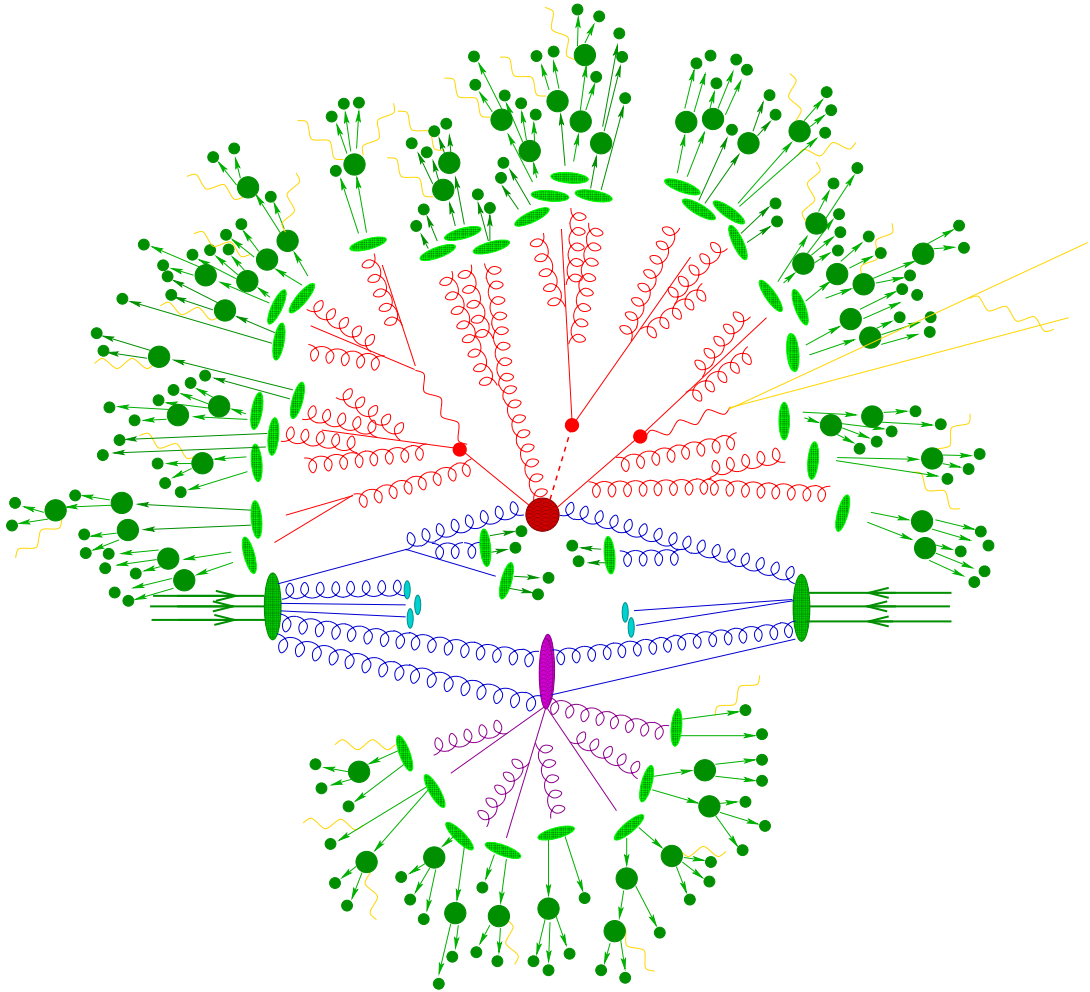
Figure 3.2: Pictorial representation of a tth event produced by an event generator. The hard interaction (big red blob) is followed by the decay of both top quarks and the Higgs boson (small red blobs). Additional hard QCD radiation is produced (red) and a secondary interaction takes place (purple blob) before the final-state partons hadronise (light green blobs) and hadrons decay (dark green blobs). Photon radiation occurs at any stage (yellow).
Figure and caption taken from Figure 1.1 of Ref. [181].

Sjostrand-van-der-Zijl model, named after the authors of Ref. [221].

For hadronisation corrections, there are two main approaches commonly used, the Lund string model [222] and the cluster hadronisation model [223]. A version of the latter is

available as a native implementation in SHERPA [224]. The Lund model is mainly used in PYTHIA, but via an interface to PYTHIA 6.4 perturbative events from SHERPA can be hadronised with the string model as implemented in that PYTHIA version. Similarly to the comments on the two parton showers, this enables a comparison of two different hadronisation models with equivalent perturbative input.

As a final point, SHERPA comes with a wide set of tools to include exact higher order corrections to the hard process. The simplest are matrix element corrections [225–228], applying a weight to the first emission generated by the parton shower to correct it to the corresponding tree level matrix element. Methods to include the full one-loop correction to a particular Born process together with the exact real matrix element are the POWHEG [229] and the MC@NLO methods [230, 231]. SHERPA provides an implementation of the latter [232].

Going beyond that in some aspects is the merging of different multiplicities. The sum over finals states $\mathcal{C}$ in the definition of the cross sections contains final states with different jet multiplicities as defined by a suitable algorithm as described in Sec. 3.2. If these jets are well separated, the amplitudes should be calculated based on the fixed order expressions. If a jet approaches the soft or collinear region however, logarithmic enhancements as seen in Sec. 2.3 are unavoidable. In this region, the parton shower will provide a better description.

The CKKW-L [233, 234] merging prescription, with the acronym abbreviating the author names of the references, introduces an energy scale Q_{cut}. The parton shower is then allowed to fill the phase space below this energy scale, while the phase space above it is filled by a tree level matrix element generator producing the exact amplitudes. The hard matrix element is interpreted as a configuration reached by the parton shower after several emission steps. It can be assigned a core process by a cluster algorithm that inverts the parton shower. The parton shower is then run starting from this core, vetoing emissions that occur before Q_{cut}. This effectively multiplies the matrix element by the correct Sudakov factor according to the shower model.

This procedure suggests a particular scale choice for the evaluation of α_{s} in the hard matrix element. Typically, in a fixed order calculation, all powers of α_{s} would be evaluated at the same scale μ_R. In the shower picture above however, the powers of α_{s} present in the core process would be evaluated at some scale μ_{core}, while the scale of the additional factor of α_{s} associated with the emission of the additional jet are determined from the scale at which this emission occurs in the parton shower approximation. In practice, the scale for the evaluation of the hard matrix element is indeed chosen according to the inverted shower history.

While the shower emissions are vetoed above Q_{cut}, it is allowed to add additional radiation below this scale. The approach can then be iterated, separating that radiation into a range where it is produced by the parton shower and one where it is described by an exact tree level matrix element of yet higher multiplicity. A simulation with this approach as implemented in SHERPA [235] will be referred to as being of MEPS@LO accuracy. The LO indicates that the hard matrix elements are evaluated at tree level. It is however possible to combine this prescription with the MC@NLO method mentioned earlier [236–239]. Simulations using that formalism will be called MEPS@NLO accurate.

For comparison and validation, also Monte Carlo samples from PYTHIA and HERWIG will be used in the following. The latest versions of HERWIG implement two different showers, a dipole based shower [240] similar to the ones in SHERPA and the more traditional angular ordered parton shower [241]. The latter will be used here if not explicitly stated otherwise. The hadronisation model in HERWIG is an implementation of the cluster model [242]. In principle, similar matching and merging schemes are available [243, 244].

PYTHIA also features a dipole based parton shower, with hadronisation traditionally modelled by the Lund fragmentation model [245] . See [234, 246–248] for the work on matching and merging algorithms in this context. In addition, PYTHIA features an alternative parton shower called VINCIA [249, 250] based on antenna functions. Matching to higher order matrix elements in this version is available through iterated matrix element corrections [251]. This approach avoids the introduction of an explicit energy scale to separate the phase space into a hard matrix element region and a shower region as seen for the CKKW prescription above. Still, from a technical point of view it is sensible to regularise high multiplicity matrix elements at a scale Q_{match} [251].

Soft gluon resummation and the CAESAR formalism

A way to obtain all order statements for QCD observables was outlined in Sec. 2.3. There is a long history [99, 252–269][1] of publications performing analyses for particular observables. The emerging structures are usually of a form similar to Eq. (2.89), or can be recast that way.

Other methods include the derivation of formal renormalisation group equations for the jet and soft functions derived for a particular process. Ultimately, the factorisation can already be made explicit at the level of the operators entering the Lagrangian. This leads to the development of effective field theories, in this particular case known as soft-collinear effective theory (SCET) [270–277].

The CAESAR formalism [88, 278–284] represents the generalisations of the first approach, working by essentially directly reorganising the perturbative series for suitable observables. In particular, one needs a general strategy to first formalise the notion of "suitable" observables, and perform the resummation at NLL for them. In this section it shall briefly be explained how the CAESAR formalism addresses those questions. Those developments were summarised in Ref. [88], and this first section will mostly be paraphrasing the arguments given there for completeness.

The development leads to a relatively simple "master formula" that will be briefly discussed. The following sections will then introduce some additional points, adding observables that are not directly within the original CAESAR formalism, but whose NLL resummation takes a very similar structure and can be obtained by making simple changes to the master formula and its components.

---

[1]Despite the large size of the list, it is not claimed to be exhaustive, even for the time period $\approx$ late 1970's - early 2000's it covers.

4.1 Prerequisites

The CAESAR formalism applies to observables fulfilling the requirement of recursive IRC (rIRC) safety, which requires that adding more soft gluons to a given ensemble of soft gluons emitted from the dipoles formed by the hard legs of the process does not significantly change the behaviour of the observable. It can formally be stated as follows [88]:

First, introduce the notation of a momentum $\kappa_i(\zeta_i)$ defined by[2]

$$V(\mathcal{B}, \kappa_i(\zeta_i)) \equiv \zeta_i \tag{4.1}$$

with the requirement that its azimuth with respect to the relevant dipole is independent of ζ_i. It is also convenient to introduce the notation

$$v_i \equiv V(\mathcal{B}, k_i) \tag{4.2}$$

for the individual contribution of a momentum k_i taken out of a set of momenta $\{k_j\}$. An observable V is rIRC safe if the following limits are well defined, for any set of momenta $\{\kappa_i(\bar{v}\zeta_i)\}$:

$$(i) \quad \lim_{\bar{v}\to 0} \frac{V(\mathcal{B} \cup \{\kappa_i(\bar{v}\zeta_i)\})}{\bar{v}} \tag{4.3}$$

$$(ii) \quad \lim_{\zeta\to 0} \lim_{\bar{v}\to 0} \frac{V(\mathcal{B} \cup \{\kappa_i(\bar{v}\zeta_i)\} \cup \{\kappa(\bar{v}\zeta)\})}{\bar{v}} = \lim_{\bar{v}\to 0} \frac{V(\mathcal{B} \cup \{\kappa_i(\bar{v}\zeta_i)\})}{\bar{v}} \tag{4.4}$$

$$(iii) \quad \lim_{\kappa_a\to x\kappa_b} \frac{V(\mathcal{B} \cup \{\kappa_i(\bar{v}\zeta_i)\} \cup \{\kappa_a(\bar{v}\zeta), \kappa_b(\bar{v}\zeta)\})}{\bar{v}} =$$
$$\lim_{\bar{v}\to 0} \frac{V(\mathcal{B} \cup \{\kappa_i(\bar{v}\zeta_i)\} \cup \{\kappa_a(\bar{v}\zeta) + \kappa_b(\bar{v}\zeta)\})}{\bar{v}} \ . \tag{4.5}$$

Note that the equality between the limits is meant as a further requirement on the observable V. The first limit in the second to last line denotes collinear limit between κ_a and κ_b.

Further, the scaling behaviour of the observable in the soft and collinear limit with respect to any external momentum is assumed to be of the general form of Eq. (2.64). More precisely, to accommodate a non-trivial dependence on the azimuthal angle ϕ, the assumed scaling will be

$$V(\mathcal{B}, k) = g_l(\phi) d_l \left(\frac{k_t^{(l)}}{\mu_Q}\right)^a e^{-b_l \eta^{(l)}} \ . \tag{4.6}$$

---

[2]The requirement does not, in fact, uniquely specify the momentum. See Ref. [88] for a concrete representation.

The full CAESAR formalism also requires the conditions of globalness, eliminating any regions of phases space where the observable is 0 away from the limit of arbitrary soft gluons, and continuous globalness. The latter is stated in Ref. [88] as follows:

$$\left. \frac{\partial V(\mathcal{B}, \{k\})}{\partial \ln k_t^{(l)}} \right|_{\text{fixed } \eta^{(l)}, \phi^{(l)}} = a \tag{4.7}$$

$$\left. \frac{\partial V(\mathcal{B}, \{k\})}{\partial \ln k_t^{(l)}} \right|_{\text{fixed } \ln k_t^{(l)} + \eta^{(l)}, \phi^{(l)}} = a + b_l \; . \tag{4.8}$$

Note that a is not indexed with the leg l as the scaling in the soft limit is assumed to be universal over the full phase space. This was already reflected in the notation before.

Together, this is sufficient to guarantee that the cross sections at NLL accuracy take the form of Eq. (2.89). The formalism relies on the property of coherence exhibited by QCD amplitudes with several soft gluon emissions. Whenever those are at largely different rapidity ranges, their emission factorises and can be treated as independent.

The above conditions are needed to deal with the effect of correlated emission of gluons close in rapidity. An observable that is global in the sense specified here will not be able to resolve such emissions and can approximately be computed on the overall momentum of such a cluster. Thus, only the weight of such an emission is modified, in a way that can be absorbed into the running of the strong coupling. This leads to the physical coupling scheme, often named after the authors of Ref. [285], Catani-Marchesini-Webber (CMW) scheme. It implies a shift

$$\alpha_s(\mu^2) \rightarrow \alpha_s(\mu^2) \left(1 + \alpha_s(\mu^2) \left(\beta_0 \ln \frac{k_t^2}{\mu^2} + \frac{K}{2\pi} \right) \right) \; , \tag{4.9}$$

where, in the $\overline{\text{MS}}$ scheme, K is given by

$$K = \left(\frac{67}{18} - \frac{\pi^2}{6} \right) C_A - \frac{10}{9} T_R n_f. \tag{4.10}$$

Next, the effect of emissions at much smaller scales $v_i < \epsilon v$ can be neglected in the calculation of

$$\Theta \left(v - V \left(\mathcal{B}, \{\kappa_a(v_a > \epsilon v)\}, \{\kappa_i(v_i < \epsilon v)\} \right) \right) \sim \tag{4.11}$$

$$\Theta \left(v - V \left(\mathcal{B}, \{\kappa_a(v_a > \epsilon v)\} \right) \right)$$

for some value of $\epsilon > 0$. This statement is supposed to hold in the sense that corrections only lead to contributions to $\Sigma(v)$ that are at most NNLL. This means that the phase space integral for every emission can be separated into three parts, the one where $v_i > v$, one where $v > v_i > \epsilon v$ and the one where $\epsilon v > v_i$. In the first and last region, there is no combined effect of the θ function containing all momenta at once, and the contribution of n emissions is just proportional to the nth power of the single emission result. Summing over the number of emissions leads to exponentiation of the single emission result, in the same way as the no-splitting probability, Eq. (3.47), emerged in Sec. 3.5. Then, the sum over the emissions integrated over the region where they contribute together, can be collected in a function, *cf.* Eq. (2.37) in Ref. [88],

$$
\mathcal{F} = e^{-R' \ln \frac{v}{\epsilon v_1}} \int dk_1 \, \frac{\langle \mathcal{B} \cup k_1 | \mathcal{B} \cup k_1 \rangle}{\langle \mathcal{B} | \mathcal{B} \rangle} \sum_{m=0}^{\infty} \frac{1}{m!} \prod_{i=2}^{m+1} \int_{\epsilon v_1}^{v_1} dk_i \, \frac{\langle \mathcal{B} \cup k_i | \mathcal{B} \cup k_i \rangle}{\langle \mathcal{B} | \mathcal{B} \rangle} \tag{4.12}
$$
$$
\times \, \theta \left(v - V(\mathcal{B}, k_1, \{k_i\}) \right) \ .
$$

Here $v_1 > v_i$ is assumed to be the largest contribution of the momenta in the ensemble. Eq. (4.12) still contains subleading contributions that need to be eliminated in order to arrive at a pure NLL formula. This can of course be done easily if it is possible to treat the observable calculation $V(\{k_i\})$ analytically. Ref. [88] showed a way to achieve this also in a numerical evaluation of Eq. (4.12). The resummation framework in SHERPA has options for both analytically calculated $\mathcal{F}$ functions, as well as to read in and interpolate numerically evaluated integrals. In the context of Ref. [II], also an internal code implementing a version of the procedure used in Ref. [88] was set up. This will briefly be commented on later.

4.2 The master formula

The final result for the resummed cross section to NLL accuracy for an rIRC safe observable can be expressed in a relatively simple master formula. In full generality, it can be stated as

$$\Sigma_{\mathsf{res}}(v) = \sum_{\delta} \Sigma_{\mathsf{res}}^{\delta}(v) \; , \tag{4.13}$$

$$\Sigma_{\mathsf{res}}^{\delta}(v) = \int d\mathcal{B}^{\delta} \frac{d\sigma^{\delta}}{d\mathcal{B}} \exp\left[-\sum_{l \in \mathcal{B}^{\delta}} R_l^{\mathcal{B}^{\delta}}(L) \right] \mathcal{S}^{\mathcal{B}^{\delta}}(L) \mathcal{P}^{\mathcal{B}^{\delta}}(L) \mathcal{F}^{\mathcal{B}^{\delta}}(L) \Theta_{\mathsf{hard}}^{\mathcal{B}^{\delta}} \; . \tag{4.14}$$

Here Θ_{hard} regularises the Born cross section and ensures that the legs $l \in \mathcal{B}^{\delta}$ are all well separated. The full Θ applied to all possible final states $\mathcal{C}$ is

$$\Theta = \Theta_{\mathsf{hard}}(\mathcal{C})\theta(V(\mathcal{C}) - v) \; . \tag{4.15}$$

Of course, the restrictions of IRC safety apply to Θ_{hard} as well. To include the effect of initial state emission, the scales used in the PDFs have to be corrected. This is achieved by multiplying by the PDF fraction

$$\mathcal{P}^{\mathcal{B}^{\delta}}(L) = \frac{f_a(x_a, e^{-2L/(a_a+b_a)}\mu_F^2)}{f_a(x_a, \mu_F^2)} \frac{f_b(x_b, e^{-2L/(a_b+b_b)}\mu_F^2)}{f_b(x_b, \mu_F^2)} \; . \tag{4.16}$$

The soft function corresponds to the exponentiation of the single logarithmic terms proportional to the colour insertion operators. It has the general structure

$$S^{\mathcal{B}^{\delta}}(L)(t) = \frac{\langle \mathcal{B}^{\delta} | e^{-\frac{t}{2}\Gamma^{\dagger}} e^{-\frac{t}{2}\Gamma} | \mathcal{B}^{\delta}\rangle}{\langle \mathcal{B}^{\delta} | \mathcal{B}^{\delta}\rangle} \; . \tag{4.17}$$

The exponent Γ also contains the dependence on Coulomb gluons [286–288] in the case of coloured initial states, and is in general given by [289]

$$\Gamma = -2\sum_{I<J} \mathbf{T}_I \mathbf{T}_J \ln \frac{Q_{IJ}}{Q_{\mathsf{soft}}} + i\pi \sum_{\substack{IJ=\mathsf{final\text{-}final}\\IJ=\mathsf{initial\text{-}initial}}} \mathbf{T}_I \mathbf{T}_J \; . \tag{4.18}$$

The dependence of $\mathcal{S}$ on the relevant logarithm L is via

$$\mathcal{S}(L) \equiv S(T(\alpha_{\mathsf{s}}\beta_0 L/a)) \; , \tag{4.19}$$

and T needs to be calculated using the running coupling at one loop order. The result depends on a generic combination of L, α_{s} and β_0, and it is conventional to introduce

$$\lambda \equiv \alpha_{\mathsf{s}}(\mu^2)\beta_0 L \; . \tag{4.20}$$

To achieve NLL accuracy it is sufficient to calculate T with one-loop running of the strong coupling,

$$T(\lambda) = \int_{\mu^2 e^{-\frac{2\lambda}{\alpha_s \beta_0}}}^{\mu^2} \frac{dk_t^2}{k_t^2} \frac{\alpha_s(k_t^2)}{\pi} = \frac{-\ln(1 - 2\lambda)}{\pi \beta_0} \; . \tag{4.21}$$

Likewise, the radiators are to be calculated taking into account the running of the strong coupling, in the form of Eq. (4.9). Note that the terms associated with K are of order α_s^2 and hence at most lead to NLL terms, which is why this was not important in the evaluation of $\mathcal{S}$ since it only starts at NLL order itself. At this accuracy, it is permissible to average over the azimuthal angle ϕ of the soft momentum with respect to the radiating dipole [88]. The only remaining dependence is proportional to

$$\ln \bar{d} \equiv \ln d + \int \frac{d\phi}{2\pi} g(\phi) \; . \tag{4.22}$$

The final results can for example be found in App. A of Ref. [88] and will be reported here for completeness. The radiator for leg l has the form

$$R_l(L) = C_l \left[r_l(L) + r_l'(L) \left(\ln \bar{d}_l - b_l \ln \frac{2E_l}{\mu_Q} + B_l T \left(\frac{L}{a + b_l} \right) \right) \right. \tag{4.23}$$

$$\left. + T \left(\frac{L}{a} \right) \ln \frac{Q_{\text{soft}}}{\mu_Q} - C_l \left(\eta_{\text{min}}^{(l)} - \ln \frac{2E_l}{Q_{\text{soft}}} \right) T \left(\frac{L}{a} \right) \right] \; .$$

Note that, deviating from Ref. [88], it was allowed here explicitly that the boundary η_{min} is non-zero. Of course, the correct result is only obtained if the full phase space is covered. For the global observable case it will always be assumed also here that the dipoles are split at

$$\eta_{\text{min}} = 0 \qquad \Rightarrow \qquad \eta_{\text{min}}^{(l)} = \ln \frac{2E_l}{Q_{\text{soft}}} \; . \tag{4.24}$$

The function r_l' is the logarithmic derivative of r_l. To NLL accuracy it can be calculated as

$$r_l'(L) = \frac{1}{b_l} \left[T \left(\frac{L}{a} \right) - T \left(\frac{L}{a + b_l} \right) \right] \tag{4.25}$$

$$\rightarrow \frac{1}{a \pi \beta_0} \frac{2\lambda/a}{1 - 2\lambda/a} \qquad \text{as} \qquad b_l \rightarrow 0 \; . \tag{4.26}$$

On the one hand it is clear from the integral defining r_l, Eq. (2.70), that r_l' has to take this form. Of course, this result could also be obtained and verified by actually taking

the derivative of the LL part of r_l, to be reported in Eq. (4.30). For completeness, the following abbreviations are also used

$$R'_l(L) = C_l r'_l(L) \,, \qquad R'(L) = \sum_{l \in \mathcal{B}^\delta} R'_l(L) \,, \tag{4.27}$$

$$R(L) = \sum_{l \in \mathcal{B}^\delta} R_l(L) \,. \tag{4.28}$$

Notice that, in all NLL parts one can in principle choose an arbitrary scale for the evaluation of α_{s}, since this will always be associated with an α_{s}^2 correction. Changing the scale in the LL part however one needs to subtract the resulting NLL term. The remaining ingredient, containing the full LL behaviour of the distribution, is[3]

$$r_l(L) = \frac{1}{\alpha_{\mathsf{s}}(\mu^2)} r_{1,l}(L) + r_{2,l}(L) \,. \tag{4.29}$$

Performing the integrals while taking the running coupling into account and evaluating it at a scale of k_t^2, the following results are computed, *cf.* App. A of Ref. [88],

$$r_{1,l}(L) = \frac{1}{2\pi\beta_0^2 b_l} \left[a \left(1 - \frac{2\lambda}{a} \right) \ln \left(1 - \frac{2\lambda}{a} \right) \right. \tag{4.30}$$

$$\left. -(a + b_l) \left(1 - \frac{2\lambda}{a + b_l} \right) \ln \left(1 - \frac{2\lambda}{a + b_l} \right) \right]$$

$$\rightarrow -\frac{1}{2\pi\beta_0^2} \left[\frac{2\lambda}{a} + \ln \left(1 - \frac{2\lambda}{a} \right) \right] \qquad \text{as} \qquad b_l \rightarrow 0 \,, \tag{4.31}$$

---

[3]Note that Ref. [88] extracts an explicit factor L instead of $1/\alpha_{\mathsf{s}}$ from $r_{1,l}$. The convention followed here is that of Ref. [III].

$$r_{2,l}(L) = \frac{K + 2\pi\beta_0 \ln\left(\mu^2/\mu_Q^2\right)}{4\pi^2\beta_0^2 b_l} \left[(a + b_l) \ln\left(1 - \frac{2\lambda}{a + b_l}\right) - a \ln\left(1 - \frac{2\lambda}{a}\right) \right]$$

$$+ \frac{\beta_1}{2\pi\beta_0^3 b_l} \left[\frac{a}{2} \ln^2\left(1 - \frac{2\lambda}{a}\right) - \frac{a + b_l}{2} \ln^2\left(1 - \frac{2\lambda}{a + b_l}\right) \right. \tag{4.32}$$

$$\left. + \quad a \ln\left(1 - \frac{2\lambda}{a}\right) - (a + b_l) \ln\left(1 - \frac{2\lambda}{a + b_l}\right) \right] ,$$

$$\rightarrow \frac{K + 2\pi\beta_0 \ln\left(\mu^2/\mu_Q^2\right)}{4\pi^2\beta_0^2} \left[\ln\left(1 - \frac{2\lambda}{a}\right) + \frac{2\lambda/a}{1 - 2\lambda/a} \right] \tag{4.33}$$

$$- \frac{\beta_1}{2\pi\beta_0^3} \left[\frac{1}{2} \ln^2\left(1 - \frac{2\lambda}{a}\right) + \frac{\ln\left(1 - 2\lambda/a\right) + 2\lambda/a}{1 - 2\lambda/a} \right] .$$

The addition of $2\pi\beta_0 \ln\mu^2/\mu_Q^2$ to K in the definition of $r_{2,l}$ corrects the choice of the scale in $\alpha_s(\mu^2)$ to μ_Q^2 at NLL accuracy. It will be the default convention to associate the scale used in the evaluation of α_s with μ_R^2, the scale used in the computation of the hard scattering process. Note that the limits for $b_l \rightarrow 0$ are given explicitly here. Of course the limits are straightforward analytically. However, in a numerical code the $b_l = 0$ case needs to be implemented separately.

The final missing piece is the multiple emission function $\mathcal{F}$. The default in the CAESAR formalism is to extract it numerically. The code for this, *e.g.* used in Ref. [II] is factorised from the remaining pieces within the SHERPA framework. Sec. 5.3 will briefly document the options for numerical evaluation. Here, it shall just be mentioned that for additive observables, defined by the property

$$V(\mathcal{B}, \{k_j\}) = \sum v_j , \tag{4.34}$$

it is relatively simple to calculate $\mathcal{F}$ analytically, since the relevant Θ function factorises in Laplace space,

$$\Theta\left(v - \sum_j v_j\right) = \int \frac{d\nu}{2\pi i\nu} e^{\nu v} e^{-\sum_j v_j \nu} = \prod_j \int \frac{d\nu}{2\pi i\nu} e^{\nu v} e^{-v_j \nu} . \tag{4.35}$$

Inserting this into Eq. (4.12) and evaluating the inverse Laplace transform, the $\mathcal{F}$ function takes the rather simple form

$$\mathcal{F}(L) = \frac{e^{-\gamma_E R'(L)}}{\Gamma\left[1 + R'(L)\right]} . \tag{4.36}$$

Similar results can also be extracted for the observables where fully analytic resummed calculations have been performed.

4.3 Extension to jet observables

The original CAESAR formalism as for example summarised in Ref. [88] is explicitly only applicable to global observables, *i.e.* observables that are sensitive to radiation everywhere in phase space. This property is clearly broken by the jet substructure observables introduced in Sec. 3.2. The only final state particles that contribute are the ones that are clustered by the chosen jet algorithm into the jet on which the measurement is performed. This excludes in particular partons collinear to any of the other hard final state legs, and to the initial states. In addition, the phase space for soft-wide angle radiation is cut off at the jet boundary. Nevertheless, NLL resummed predictions often have a very similar structure to Eq. (4.13). They can hence be treated with few modifications to the framework.

The blue-print for the modifications will be Ref. [108] where the jet mass, *cf.* Eq. (3.27), was resummed at NLL accuracy. The discussion is restricted to anti-k_t jets, with a radius R. This avoids the appearance of cluster logarithms at NLL [290–293]. The analysis will be further restricted to observables that scale like

$$V(\mathcal{B}, k \in \mathcal{J}) \propto \frac{k_t^{(J)}}{\mu_Q} e^{-b_J \eta^{(J)}} \tag{4.37}$$

in the limit where the momentum k is inside the jet $\mathcal{J}$ and the scaling is relative to the hard leg inside the jet. This is true for both the jet mass and the jet angularities, *cf.* Eq. (3.28). Note there always has to be one hard parton to trigger a jet. On the other hand, it is assumed that more than one hard parton inside a jet will already have a significant value $V \sim 1$. Thus, there is only one parton for which the collinear limit of k contributes, assumed to have index J. The radiator corresponding to J is indeed almost that of the usual CAESAR formalism, with parameters $a = 1$ and $b_l = b_J$. The normalisation $g_l d_l$ needs to be derived from the particular definition of the observable. Evidently, nothing changes in the J-collinear limit, if k is inside the jet the observable is supposed to be a smooth function and does not know of the behaviour outside the jet. The only difference is the angular scale where the radiation from J stops contributing. In the previous section, this was assumed to happen at $\eta = 0$ for every dipole, and at that point the other half of that dipole would take over. Now, the contribution needs to be cut off at the jet boundary. That can conveniently be achieved by setting

$$\eta_{\mathsf{min}}^J = \ln\left(2\frac{\cosh(y_J)}{R}\right) \;, \tag{4.38}$$

where R is the radius of the jet and y_J the rapidity of J. The fact that there is no contribution from the collinear limits of the other hard partons is expressed by setting their radiators to zero,

$$R_l \propto \delta_{lJ} \;. \tag{4.39}$$

Similarly, since the contributions to the PDF ratio, Eq. (4.16), are originated by radiation collinear to the initial state, it can be ignored and set to one,

$$\mathcal{P} = 1 \ . \tag{4.40}$$

The multiple emission function similarly only receives contributions from the J collinear limit, but behaves as usual inside the jet. Restricting to additive observables, this means

$$\mathcal{F}(L) = \frac{e^{-\gamma_E R'_J(L)}}{\Gamma\left[1 + R'_J(L)\right]} \ . \tag{4.41}$$

Two effects are entering the soft function $\mathcal{S}$. Soft wide-angle emissions can either directly contribute to the jet J and set an observable value. The radiation from each dipole needs to be integrated over the jet area. The J collinear part of the dipoles involving J is already taken care of due to the radiator R_J. Since the only property of the observable that matters in the soft limit is the scaling with k_t, *i.e.* not the b_J parameter determining the collinear behaviour, the results from Ref. [108] for the jet mass are applicable to all observables that are linear in k_t in that region. This is precisely the restriction made in Eq. (4.37).

The other effect important for $\mathcal{S}$ are so called non-global logarithms. They arise because not all soft, but finite, emissions result in a non-zero value of the observable. This violates the assumption that the observable should be global, which guaranteed that only the different flavour combinations with a given parton multiplicities form the Born events $\mathcal{B}$ around which the resummation is to be performed. Now, in addition to performing the resummation around the n parton final states, it also has to be performed around the $n + 1$ parton final states, at least in the phase space where the additional parton is not inside the jet.

Going through the steps sketched in Sec. 2.3, one would naively obtain a similar structure of exponentiated logarithms inserted into the $\langle \mathcal{B} \cup \{k_i \notin \mathcal{J}\} | \mathcal{B} \cup \{k \notin \mathcal{J}\} \rangle$ matrix element. This might at first seem not that bad since those configurations are of course suppressed with at least one power of α_s with respect to the $\langle \mathcal{B} | \mathcal{B} \rangle$ used in the original resummation. However, the additional emission, even if not inside the jet, can be soft enhanced. This can lead to a final state containing arbitrary many soft gluons, that at some point contribute radiation inside the jet area. Since this is only possible starting at order α_s^2, one emission is outside and one inside the jet, this leads to next-to-leading logarithms only.

This problem was discussed in Ref. [294], and a solution was proposed in the form of a Monte Carlo algorithm. This algorithm works in the $N_c \to \infty$ limit. Ref. [108] used

this technique to resum the non-global logarithms for the jet mass in this approximation. The general form of the soft function exponent Γ used there corresponds to

$$t\Gamma = -2\sum_{I<J}\mathbf{T}_I\mathbf{T}_J\left(tI_{IJ}^{\mathcal{B}^\delta} + f_{IJ}^{\mathcal{B}^\delta}(t)\right) + i\pi\sum_{\substack{IJ=\text{final-final}\\IJ=\text{initial-initial}}}\mathbf{T}_I\mathbf{T}_J t \ , \qquad (4.42)$$

where I_{IJ} are the results of the integration over the global part described earlier, they can be calculated analytically as a power series in the jet radius R [108]. The functions f_{IJ} are obtained from a Monte Carlo algorithm like the one introduced in Ref. [294]. The results of this algorithm are then either fit with a suitable function, or interpolated based on a grid in the parameter t, and evaluated at the corresponding value $T(L)$.

4.4   Extension to soft drop groomed observables

Including the effect of the soft drop procedure outlined in Sec. 3.3 requires a partial re-computation of the radiator functions R_l. This calculation was carried out in Ref. [III]. The context there were resummed predictions for event shapes after soft drop grooming the hemispheres defined by the transverse thrust axis. An explicit expression for the definition of soft drop groomed transverse thrust was given in Eq. (3.33). The calculation of the radiator is more general however, and also applicable to jet observables with the modifications introduced in the last section.

The resummation for soft drop groomed observables is performed in the $v \ll z_{\text{cut}} \ll 1$ limit. In this range, it is appropriate to neglect powers of z_{cut}, *i.e.* terms vanishing as $z_{\text{cut}} \to 0$, and only take into account logarithms of z_{cut} that are enhanced by NLL terms in v. Technically, the relevant argument of the logarithms is z'_{cut} introduced in Eq. (3.37). Analogous to the logarithms of the observable L, those will be denoted by

$$L_z = -\ln z'_{\text{cut}} \, . \tag{4.43}$$

The difference between z_{cut} and z'_{cut} is by a factor $\left(R_{\text{SD}} \sin\theta / 2\right)^{-\beta}$. Note that the hard final state legs are assumed to be well separated from the beam in any case. Assuming specifically central hard jets, *i.e.* $\sin\theta \sim \mathcal{O}(1)$, and choosing $R \sim \mathcal{O}(1)$, one indeed arrives at $z'_{\text{cut}}/z_{\text{cut}} \sim \mathcal{O}(1)$ in the relevant limit collinear to the final state particles. With this assumption the two cases $v \ll z'_{\text{cut}} \ll 1$ and $v \ll z_{\text{cut}} \ll 1$ hence are equivalent. Of course, with any particular choice of grooming parameters and event selection cuts, it should be evaluated how well the full all orders QCD result is expected to be approximated.

As discussed in Sec. 3.3, the effect of grooming is to remove the soft-wide angle corner in the Lund diagram for the radiation from a final state leg. The blue area marked in Fig. 3.1 hence does not need to be integrated over, the integral for the radiator should only cover the red area in that figure. Alternatively, one can subtract the integral of that blue area from the result of integrating over the full phase space, *cf.* Eq. (2.70).

The relevant point where the red line limiting the observable and the blue line limiting the grooming region meet is, in general, given by

$$f\left(v, z'_{\text{cut}}\right) \equiv v^{\frac{2(1+\beta)}{b_l + a_l(1+\beta)}} \left(z'_{\text{cut}}\right)^{\frac{2b_l}{b_l + a_l(1+\beta)}} = v^{2p_l^{(v)}} \left(z'_{\text{cut}}\right)^{2p_l^{(z)}} \, , \tag{4.44}$$

where in the second equality implicitly defines

$$p_l^{(v)} \equiv \frac{1+\beta}{b_l + a_l\left(1+\beta\right)} \quad \text{and} \quad p_l^{(z)} \equiv \frac{b_l}{b_l + a_l\left(1+\beta\right)} \, . \tag{4.45}$$

The new radiator can now be computed to be

$$
R\left(v, z_{\mathsf{cut}}\right) = \sum_l C_l \left[\int_{\mu_Q^2 v^{\frac{2}{a_l+b_l}}}^{\mu_Q^2} \frac{dk_t^2}{k_t^2} \frac{\alpha_\mathsf{s}\left(k_t^2\right)}{\pi} \left(\ln\left(\frac{Q}{k_t}\right) + B_l \right) \right.
\tag{4.46}
$$

$$
+ \int_{\mu_Q^2 v^{\frac{2}{a_l}}}^{\mu_Q^2 v^{\frac{2}{a_l+b_l}}} \frac{dk_t^2}{k_t^2} \frac{\alpha_\mathsf{s}\left(k_t^2\right)}{\pi} \left(\ln\left(\frac{Q}{2E_l}\right) + \frac{1}{b_l} \ln\left[\left(\frac{k_t}{\mu_Q}\right)^{a_l} \frac{d_l g_l}{v} \right] \right)
$$

$$
- \int_{\mu_Q^2 f\left(v, z_{\mathsf{cut}}'\right)}^{\mu_Q^2 \left(z_{\mathsf{cut}}'\right)^2} \frac{dk_t^2}{k_t^2} \frac{\alpha_\mathsf{s}\left(k_t^2\right)}{\pi} \left(\ln\left(\frac{Q}{k_t}\right) - \frac{\beta}{1+\beta} \ln\left(\frac{2E_l}{k_t}\right) \right.
$$

$$
\left. + \frac{1}{1+\beta} \ln\left(z_{\mathsf{cut}}'\right) \right)
$$

$$
\left. - \int_{\mu_Q^2 v^{\frac{2}{a_l}}}^{\mu_Q^2 f\left(v, z_{\mathsf{cut}}'\right)} \frac{dk_t^2}{k_t^2} \frac{\alpha_\mathsf{s}\left(k_t^2\right)}{\pi} \left(\ln\left(\frac{Q}{2E_l}\right) + \frac{1}{b_l} \ln\left[\left(\frac{k_t}{\mu_Q}\right)^{a_l} \frac{d_l g_l}{v} \right] \right) \right],
$$

where the first two lines can be recognised as the original contribution of the full red triangle in Fig. 2.5, while the last two lines subtract the area of the blue triangle in Fig. 3.1. Note that the dipole scale Q_{IJ} has already been replaced by a generic scale Q, which one is free to do as already discussed. In the default CAESAR formalism the dependence on Q is reflected by the soft function $\mathcal{S}$. Here, it leads to a contribution of the form $T(\alpha_\mathsf{s}\beta_0 L_z) \ln Q/\mu_Q$, which can immediately be ignored at the required accuracy, *i.e.* in the $v \ll z_{\mathsf{cut}}$ limit.

The integrals are straightforward, and the result can be cast into a form similar to Eq. (4.23), *i.e.* the ungroomed case, as

$$
R\left(v, z_{\mathsf{cut}}\right) = \sum_l C_l \left[r_l\left(L,\, L_z\right) + r_l'\left(L,\, L_z\right) \left(\ln\left(\bar{d}_l\right) - b_l \ln\left(\frac{2E_l}{\mu_Q}\right) \right) \right.
\tag{4.47}
$$

$$
\left. + \beta\, \dot{r}_l\left(L,\, L_z\right) \ln\left(\frac{2E_l}{\mu_Q}\right) + B_l T\left(\frac{\alpha_\mathsf{s}\beta_0 L}{a_l+b_l}\right) + T\left(\alpha_\mathsf{s}\beta_0 L_z\right) \ln\left(\frac{Q}{\mu_Q}\right) \right].
$$

Here, the additional function $\dot{r}_l$ was introduced, representing the derivative of r_l with respect to L_z, rather than L, as for r_l'. The functions already present in the standard

case are also modified, and the explicit expressions are

$$r_l\left(L, L_z\right) = \frac{1}{\alpha_{\mathsf{s}}} r_{1,l}\left(\alpha_{\mathsf{s}}\beta_0 L, \alpha_{\mathsf{s}}\beta_0 L_z\right) + r_{2,l}\left(\alpha_{\mathsf{s}}\beta_0 L, \alpha_{\mathsf{s}}\beta_0 L_z\right), \tag{4.48}$$

$$r_l'\left(L, L_z\right) = \frac{1}{b_l}\left[T\left(p_l^{(v)}\alpha_{\mathsf{s}}\beta_0 L + p_l^{(z)}\alpha_{\mathsf{s}}\beta_0 L_z\right) - T\left(\frac{\alpha_{\mathsf{s}}\beta_0 L}{a_l + b_l}\right)\right], \tag{4.49}$$

$$\dot{r}_l\left(L, L_z\right) = \frac{1}{1+\beta}\left[T\left(p_l^{(v)}\alpha_{\mathsf{s}}\beta_0 L + p_l^{(z)}\alpha_{\mathsf{s}}\beta_0 L_z\right) - T\left(\alpha_{\mathsf{s}}\beta_0 L_z\right)\right]. \tag{4.50}$$

The functions $r_{1,l}$ and $r_{2,l}$ are analogous to Eq. (4.30) and Eq. (4.32), representing the LL and some of the NLL terms,

$$r_{1,l}\left(\lambda, \lambda_z\right) = \frac{-1}{2\pi\beta_0^2}\left[\frac{a_l + b_l}{b_l}\left(1 - \frac{2\lambda}{a_l + b_l}\right)\ln\left(1 - \frac{2\lambda}{a_l + b_l}\right)\right. \tag{4.51}$$

$$+ \frac{1}{1+\beta}\left(1 - 2\lambda_z\right)\ln\left(1 - 2\lambda_z\right)$$

$$\left. - \frac{a_l(1+\beta) + b_l}{b_l(1+\beta)}\left(1 - 2(p_l^{(v)}\lambda + p_l^{(z)}\lambda_z)\right)\ln\left(1 - 2(p_l^{(v)}\lambda + p_l^{(z)}\lambda_z)\right)\right],$$

$$r_{2,l}\left(\lambda, \lambda_z\right) = \frac{K + 2\pi\beta_0\ln\mu^2/\mu_Q^2}{4\pi^2\beta_0^2}\left[\frac{a_l + b_l}{b_l}\ln\left(1 - \frac{2\lambda}{a_l + b_l}\right) + \frac{1}{1+\beta}\ln\left(1 - 2\lambda_z\right)\right.$$

$$\left. - \frac{a_l(1+\beta) + b_l}{b_l(1+\beta)}\ln\left(1 - 2(p_l^{(v)}\lambda + p_l^{(z)}\lambda_z)\right)\right] \tag{4.52}$$

$$- \frac{\beta_1}{2\pi\beta_0^3}\left[\frac{a_l + b_l}{b_l}\left(\frac{1}{2}\ln^2\left(1 - \frac{2\lambda}{a_l + b_l}\right) + \ln\left(1 - \frac{2\lambda}{a_l + b_l}\right)\right)\right.$$

$$+ \frac{1}{1+\beta}\left(\frac{1}{2}\ln^2\left(1 - 2\lambda_z\right) + \ln\left(1 - 2\lambda_z\right)\right)$$

$$- \frac{a_l(1+\beta) + b_l}{b_l(1+\beta)}\left(\frac{1}{2}\ln^2\left(1 - 2(p_l^{(v)}\lambda + p_l^{(z)}\lambda_z)\right)\right.$$

$$\left.\left. + \ln\left(1 - 2(p_l^{(v)}\lambda + p_l^{(z)}\lambda_z)\right)\right)\right].$$

The initial state radiator need special consideration in the groomed case. The soft drop procedure as introduced in Sec. 3.3 for global event shapes, is such that the evaluation of the soft drop condition, *cf.* Eq. (3.29) if coloured initial stats are present, is always
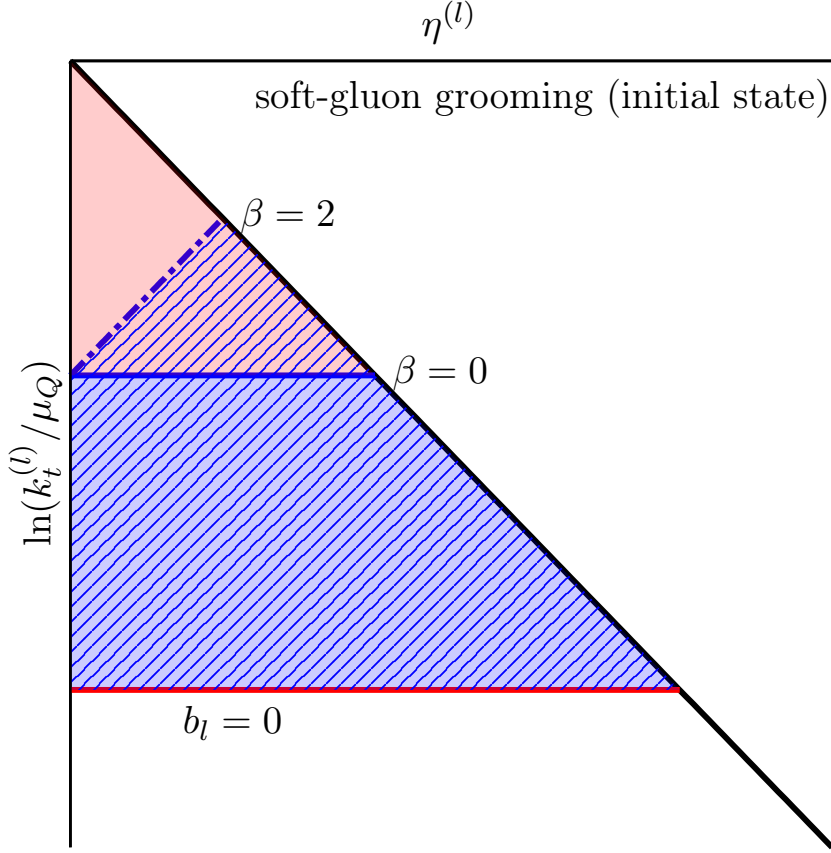
Figure 4.1: The Lund diagram showing the kinematic constraints for soft drop applied to initial-state emissions. As examples $a_l = 1$ with $b_l = 0$ and $\beta = 0$ (solid line and area) and $\beta = 2$ (dashed line, hatched area) are shown. Figure and caption taken from Figure 18 of Ref. [III].

evaluated by comparing two final objects. This leads to the kinematic constraint depicted in the Lund diagram in Fig. 4.1. Evidently, for small enough observable values v there is no contribution at all, *i.e.* the blue area in Fig. 4.1 cuts out the full soft-collinear phase space for the initial state legs. The resulting integrals would hence at most lead to logarithms of z'_{cut}. Those are excluded in the limit $v \ll z_{\mathrm{cut}} \ll 1$ where the calculation is performed. This justifies to ignore the initial state radiators and the PDF ratios,

$$R_l = 0 \qquad \text{for} \qquad l \in \mathcal{B}_{\mathrm{in}} \, , \tag{4.53}$$

$$\mathcal{P} = 1 \, , \tag{4.54}$$

for soft drop groomed observables. Note that those settings are in any case in place

for the jet substructure observables discussed in Sec. 4.3. Since the jet direction is by definition not the initial state direction, Eq. (4.39) enforces Eq. (4.53) anyways.

A similar argument applies to the soft function $\mathcal{S}$ for contributions from both initial and final state legs. An infinitely soft but not collinear emission will always be groomed away. This was already observed in the discussion below Eq. (4.46). Soft emissions only lead to logarithms of z'_{cut}, and the soft function can hence also be set to

$$\mathcal{S}_{\text{SD}}(L) = 1 \ . \tag{4.55}$$

At last, it should be made clear that, since logarithms of z_{cut} that are not enhanced by any logarithms of the observable are regarded as subleading, one can of course also include some of them without changing the formal accuracy. This corresponds to, for example, setting

$$\mathcal{S}_{\text{SD}}(L) = \mathcal{S}(L_z) \tag{4.56}$$

in the groomed distribution. This can be useful, since for $v > z_{\text{cut}}$ grooming is usually assumed to be inactive, and the final prediction is made by using the groomed cross section below and the ungroomed cross section above z_{cut}. This however might lead to discontinuities in the overall prediction, since for example the soft function would approach $\mathcal{S}(L_z)$ for $v \to z_{\text{cut}}$, $v > z_{\text{cut}}$, but be constant $\mathcal{S}(L) = 1$ for $v < z_{\text{cut}}$. This discontinuity can be avoided by using

$$\mathcal{S}(L) \to \mathcal{S}(\min(L, L_z)) \ . \tag{4.57}$$

over the full range. Of course, the discontinuity would be of an order that is neglected in the calculation, and will be resolved at higher orders. In particular in a binned distribution, it might not be visible if the binning around $v \approx z_{\text{cut}}$ is not fine enough. So both options, Eq. (4.55) or Eq. (4.56), might be viable in certain circumstances.

4.5 Analysis of non-perturbative scales

In the limit of very soft gluon momenta, at scales $\sim \Lambda_{\text{QCD}}$, perturbation theory is expected to break down. This is evidenced phenomenologically by the presence of hadrons, fundamentally non-perturbative objects, at those scales. One expects observables to be sensitive to non-perturbative physics whenever the integrals in the Lund plane need to be extended over such scales. This is visible as logarithmic branch cuts, *cf.* also [41], in the individual ingredients of the master formula, resulting from integrating α_s over the Landau Pole. The analysis here will closely follow Ref. [III].

Without grooming, *cf.* Sec. 4.2, the branch cuts are located at

$$2\lambda = a_l + b_l \,, \tag{4.58}$$

$$2\lambda = a_l \,. \tag{4.59}$$

These can easily be expressed in terms of the observable $v = e^{-\lambda/\alpha_s\beta_0}$, which yields

$$v_{\text{Had, collinear}} = \left(e^{-1/2\alpha_s\beta_0}\right)^{a_l+b_l} = \left(\frac{\Lambda_{\text{QCD}}}{\mu_R}\right)^{a_l+b_l} \,, \tag{4.60}$$

$$v_{\text{Had, wide-angle}} = \left(e^{-1/2\alpha_s\beta_0}\right)^{a_l} = \left(\frac{\Lambda_{\text{QCD}}}{\mu_R}\right)^{a_l} \,. \tag{4.61}$$

As the notation suggests, the first one corresponds to the collinear limit while the second one is approached in the soft, wide-angle limit. Non-perturbative effects will become important as v approaches the larger of the two solutions, such that,

$$v_{\text{Had}} = \left(\frac{\Lambda_{\text{QCD}}}{\mu_R}\right)^{a_l+b_l} \,, \qquad \text{for } b_l \leq 0 \,, \tag{4.62}$$

$$v_{\text{Had}} = \left(\frac{\Lambda_{\text{QCD}}}{\mu_R}\right)^{a_l} \,, \qquad \text{for } b_l > 0 \,, \tag{4.63}$$

If grooming is included, *cf.* the equations in Sec. 4.4, the branch cuts are pushed to

$$2\lambda = a_l + b_l \,, \tag{4.64}$$

$$2p_l^{(v)}\lambda = 1 - 2p_l^{(z)}\lambda_z \,. \tag{4.65}$$

Note that it is assumed $\lambda_z < 1/2$. This condition corresponds to $z'_{\text{cut}} > \Lambda_{\text{QCD}}/\mu_R$. If that is not true, the full groomed part of the distribution shifts into the non-perturbative region and the whole discussion in terms of perturbative physics is pointless. Expressing

those in terms of the observable in the same way yields

$$
v_{\text{Had, collinear}} = \left(e^{-1/2\alpha_s\beta_0} \right)^{a_l+b_l} = \left(\frac{\Lambda_{\text{QCD}}}{\mu_R} \right)^{a_l+b_l} , \tag{4.66}
$$

$$
v_{\text{Had, wide-angle}} = \left(e^{-1/2\alpha_s\beta_0} \right)^{a_l+b_l/(1+\beta)} \left(e^{L_z} \right)^{b_l/(1+\beta)} = \left(\frac{\Lambda_{\text{QCD}}}{\mu_R} \right)^{a_l} \left(\frac{\Lambda_{\text{QCD}}}{\mu_R z'_{\text{cut}}} \right)^{b_l/(1+\beta)} . \tag{4.67}
$$

The first solution, emerging from the collinear limit, is unchanged. However, the second solution is approached for the softest wide-angle emissions allowed by grooming now. This pushes the observable value associated with hadronisation corrections to lower values compared to the same observable without grooming. Checking which value is approached first, one obtains

$$
v_{\text{Had}} = \left(\frac{\Lambda_{\text{QCD}}}{\mu_R} \right)^{a_l+b_l} , \qquad \text{for} \ \ b_l \leq 0 , \tag{4.68}
$$

$$
v_{\text{Had}} = \left(\frac{\Lambda_{\text{QCD}}}{\mu_R} \right)^{a_l} \left(\frac{\Lambda_{\text{QCD}}}{\mu_R z'_{\text{cut}}} \right)^{b_l/(1+\beta)} , \qquad \text{for} \ \ b_l > 0 . \tag{4.69}
$$

This can be validated for example by comparing with Ref. [136], which reported results for the energy-energy correlations $e_2^{(\alpha)}$ with $\alpha > 1$. Those are another class of jet substructure observables with parameters $a = 1$, $b_J = \alpha - 1$. Ref. [136] finds,

$$
e_2^{(\alpha)} \Big|_{\text{NP}} \approx \left(\frac{\Lambda_{\text{QCD}}}{z_{\text{cut}}Q} \right)^{\frac{\alpha-1}{1+\beta}} \frac{\Lambda_{\text{QCD}}}{Q}, \qquad \alpha > 1 , \qquad \text{(Ref. [136] Eq. (4.7))}
$$

with Q representing the hard scale in Ref. [136], equivalent to μ_R in the above equations.

The behaviour of v_{Had} for different CAESAR parameter choices and different options for grooming is illustrated in Fig. 4.2. Note that the x-axis is in terms of the dimensionless ration $\mu_R/\Lambda_{\text{QCD}}$. In all cases, the observable scale v_{Had} at which hadronisation corrections are expected to dominate decreases with an increasing hard scale μ_R relative to Λ_{QCD}. The black line represents the most common global observables as a baseline. The angular coefficient is positive, $b_l \leq 0$, and the wide angle emissions are dominating soft physics. All observables are for $a = 1$, but of course a different power would just correspond to a re-scaling of the y-axis in that case. Examples where the black line is applicable are most event shapes, for example thrust, Eq. (3.2), as well as the wide hemisphere broadening Eq. (3.18) and heavy hemisphere mass Eq. (3.16). The dashed line showcases the $b_l < 0$ case at the example of $b_l = -1/2$. This is for example the case for the jet angularities λ_α with $\alpha < 1$, *cf.* Eq. (3.28). The $b_l = -1/2$ case corresponds to $\alpha = 1/2$. Here the sensitivity to soft physics comes from the collinear limit. Hence,
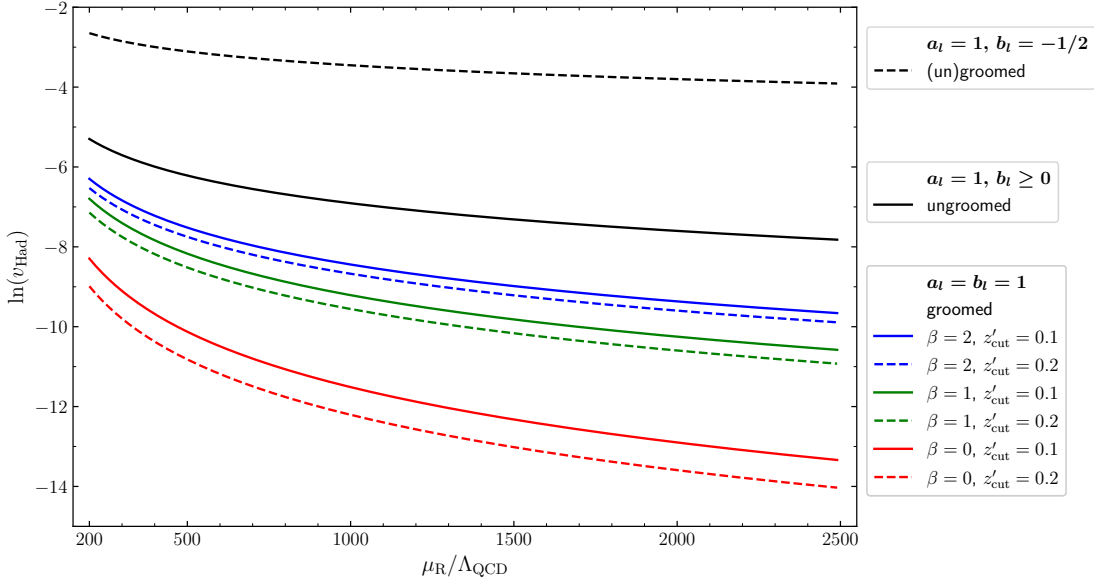
Figure 4.2: Observable value v_{Had} where to expect dominance of non-perturbative corrections, *i.e.* hadronisation effects, as a function of the dimensionless quantity $\mu_{\text{R}}/\Lambda_{\text{QCD}}$. Results are given for different combinations of CAESAR parameters. For the case $a_l = b_l = 1$, relevant for example for the thrust observable, we present results for different grooming parameter combinations.

Figure and caption taken from Figure 4 of Ref. [III].

hadronisation corrections enter at much larger observable values, assuming equal values of the hard scale $\mu_R/\Lambda_{\text{QCD}}$. It is evident that soft drop grooming significantly reduces the value of the observable at which non-perturbative effects are expected to enter for a given hard scale. This is illustrated using the example of $a = 1$, $b_l = 1$, applicable for example to groomed thrust, Eq. (3.31) or Eq. (3.33), and angularities with $\alpha = 2$. The behaviour with the grooming parameters is as expected. More grooming, *i.e.* grooming parameters leading to a larger cut out area in the Lund plane equivalent of the blue area in Fig. 3.1, leads to smaller non-perturbative scales. The largest suppression is observed for the $\beta = 0$ case, and with increasing β, corresponding to the colour codes in Fig. 4.2 the original behaviour without grooming is slowly approached. Increasing the parameter z_{cut} again shifts v_{NP} to lower values for a given hard scale and angular parameter β. This is shown by the dashed lines, which replace $z'_{\text{cut}} = 0.1$ in the solid coloured lines by $z'_{\text{cut}} = 0.2$.

CAESAR resummation within the SHERPA framework

The plugin to the SHERPA framework implementing the computation of the necessary ingredients of the CAESAR formalism was first presented in Ref. [295]. The general idea is that configurations corresponding to the Born process for a particular observable are dressed with the ingredients of the master formula Eq. (4.13), in the same style as a parton shower would be applied. The phase space integration technology available in SHERPA can be used to sample over the Born processes $\mathcal{B}^\delta$ and sum over the channels δ.

Certain components like the radiators are trivial in principle, and just need to be available as functions in the code. There are however certain subleading choices that can be made, modifying those terms potentially in way that depends on the kinematics of the Born event considered. The options for those choices available will be described in the first of the following sections.

A key feature of resummation in the SHERPA framework is the availability of colour ordered matrix elements from SHERPA's matrix element generator COMIX. This can be exploited to obtain the soft function $\mathcal{S}$ for multijet configurations. It was one of the major motivations for the original implementation in Ref. [295], the current status will also be described here. More advanced options to include the multiple emission $\mathcal{F}$ function were introduced to the plugin in Ref. [II].

The fixed order capabilities of SHERPA are also used to automatically calculate the LO and NLO corrections for the selected observable. The matrix element generators are differential also in the parton flavours, enabling the determination of the C_1^δ coefficients for more complicated final states. Additionally, this requires the use of appropriate matching schemes when combining the resummed and fixed order calculations. The final topic in this chapter will be a practical way to apply non-perturbative corrections obtained from a fully fledged Monte Carlo simulation to the resummed calculation.

5.1 Choices for subleading terms

While the formalism described in Ch. 4 fixes the analytic form of the results to NLL accuracy, there are certain ambiguities left beyond this precision. Those are primarily represented by the choice of the scales μ_R^2, μ_F^2 used for the renormalisation and factorisation of the hard process. They can be varied to estimate the perturbative fixed order uncertainty. This can be done on-the-fly within the SHERPA framework [296].

In addition some choices can modify the resummed distribution by adding terms that vanish in the $v \to 0$ limit. Since the formal accuracy is defined in this limit, it is not altered by such an addition. First, it is common to modify the logarithms L to

$$\ln\left(\frac{1}{v}\right) \to \frac{1}{p} \ln\left(\left(\frac{x_v}{v}\right)^p - \left(\frac{x_v}{v^{\mathrm{max}}}\right)^p + 1\right) = L\,, \qquad (5.1)$$

and subtracting the corresponding change of the leading logarithm. This achieves that $L(v = v_{\mathrm{max}}) = 0$ while still $L \to \ln x_v/v \sim \ln 1/v$ in the limit where $v \ll 1$. The value of v_{max} can then be set to the physical endpoint of the distribution, or to the endpoint of a fixed order calculation carried out at a particular accuracy. If the fixed order calculation is carried out within the plugin, the maximal values for each observable encountered are provided in the output.

The choice of $x_v \sim \mathcal{O}(1)$ reflects the ambiguity to choose the normalisation of the observable. One approach [280] in choosing a value is to set it to

$$\ln x_v = \frac{1}{n} \sum_{l \in \mathcal{B}} \ln \bar{d}_l \,, \qquad (5.2)$$

with n the number of coloured final state legs in $\mathcal{B}$. If $\bar{d}_l$ is the same for all legs, this just divides out the normalisation of the observable. On the other hand, one can of course let $x_v = 1$, but should make sure in this case that the normalisation is chosen appropriately to ensure that logarithms of $\ln \bar{d}_l$ are not artificially enlarged by an arbitrary choice in the normalisation, i.e. make sure that $\bar{d}_l = \mathcal{O}(1)$. Variations of x_v can be used to estimate the size of uncertainties associated with logarithmic subleading contributions.

The value of p modifies the power with which corrections of the form v/v_{max} vanish. The default value is $p = 1$. It can be varied to estimate uncertainties related to power corrections in v.

Finally, while the above procedure ensures that the cross section Σ approaches one at the physical endpoint v_{max}, the derivative at this point might not smoothly approach

zero, leading to artefacts in differential distributions. To fix this, the distribution can be shifted by power corrections obtained from terms in the expansion of Σ to order α_{s} that are linear in L,

$$\Delta\Sigma \equiv 2\pi \left.\frac{\Sigma^{(1)}}{\alpha_{\mathsf{s}} L}\right|_{L=0} . \tag{5.3}$$

The resulting shift in $\ln\Sigma$ is then implemented as

$$\ln\Sigma(L) \to \ln\Sigma(L) - \frac{\alpha_{\mathsf{s}}}{2\pi} L \left(\frac{v}{v_{\mathsf{max}}}\right)^{p} \Delta\Sigma \tag{5.4}$$

In the same way, one can modify where exactly the transition between groomed and ungroomed distributions occur for observables with grooming. Naively, the transition takes place at $v \sim z_{\mathsf{cut}}$, however this is modified by fixed order corrections. As documented in Ref. [III], the argument of L_z can be shifted,

$$L_z = -\ln\left(z'_{\mathsf{cut}}\right) \to -\frac{\ln\left(\tilde{z}^a_{\mathsf{cut}}/x_v\right)}{a} , \tag{5.5}$$

by taking into account the correction

$$R \to R + \frac{1}{a_l} \dot{r}_l\left(L, \, L_z\right) \left[a_l \ln\left(\frac{2E_l}{\mu_Q}\right) \right. \tag{5.6}$$

$$\left. + \left(a_l\left(1+\beta\right) + b_l\right)\ln\left(\frac{Q}{2E_l}\right) + \ln\left(\bar{d}_l\right) \right] .$$

The shift in L can be performed as in Eq. (5.1). When choosing x_v, the reasoning leading to Eq. (5.2) would lead to a similar formula but only include a sum over the final state legs in the groomed case. Finally, a shift

$$\exp\left[\tilde{R}\left(L, \, L_z\right)\right] \to \exp\left[\tilde{R}\left(L, \, L_z\right) - \tilde{R}\left(0, \, L_z\right) - \left(\frac{v}{v^{\mathsf{max}}}\right)^p \tilde{R}'\left(0, \, L_z\right) L\right], \quad (5.7)$$

is implemented, with $\tilde{R}$ including the multiple-emission function $\mathcal{F}$ next to the usual radiator R, and $\tilde{R}'$ denoting its derivative with respect to L. Subtracting $\tilde{R}(0, L_z)$ removes all pure logarithms L_z, leaving only those that are also associated with logarithms L of the observable.

5.2   The soft function

The soft function $\mathcal{S}$ has the form given in Eq. (4.17). To make practical use of it, one first needs to obtain an explicit expression for the insertion operators $\mathbf{T}_I\mathbf{T}_J$ in some basis for the colour space of the process. A simple example is the so called trace basis. To construct it, the identity in Eq. (2.6) is used to express all structure constants in terms of generators t_{ij}^a. Similar to the examples in Eq. (2.8) and Eq. (2.9), the colour structure will be decomposed into traces

$$t_{il}^a \dots t_{ki}^a \propto |b^{\text{trace}}\rangle \ , \tag{5.8}$$

where the exact structures appearing depend on the process under consideration. The Born amplitude can then be written as

$$|\mathcal{B}\rangle = \sum_\alpha \mathcal{A}^\alpha |b_\alpha\rangle \ . \tag{5.9}$$

Note that the "trace" superscript was removed in Eq. (5.9) relative to Eq. (5.8), since other bases can be used in general, and an index α was added to label the different colour structures. The coefficients $\mathcal{A}_\alpha$ are the corresponding amplitudes stripped of the colour structure, containing all the information on the kinematics of the Born process. Next, one introduces the matrices

$$c_{\alpha\beta} = \langle b_\alpha | b_\beta \rangle \tag{5.10}$$

$$H^{\alpha\beta} = \overline{A}^\alpha A^\beta \ . \tag{5.11}$$

With this at hand, the matrix element squared for the Born process, which on the colour space takes the form of a product between vectors, can be expressed as a trace over the c and H matrices

$$\langle \mathcal{B}|\mathcal{B}\rangle = c_{\alpha\beta}H^{\alpha\beta} \ . \tag{5.12}$$

Note that the elements of the matrices, $c_{\alpha\beta}$ and $H^{\alpha\beta}$, are indeed just numbers so can immediately be implemented programmatic by computing the product between two real valued matrices and then taking the trace of the result. Similarly, the insertion operators are expressed as matrices

$$T_{\alpha\beta} = \langle b_\alpha | \mathbf{T}_I\mathbf{T}_J | b_\beta \rangle \tag{5.13}$$

$$\Gamma_{\alpha\beta} = \langle b_\alpha | \Gamma | b_\beta \rangle \ , \tag{5.14}$$

with Γ defined in Eq. (4.18). In order to obtain the correct structure in the exponential, *cf.* Ref. [295] it has to be defined according to

$$\exp[x\Gamma] \equiv c_{\alpha\gamma} \exp\left[xc^{\gamma\delta}\Gamma_{\delta\beta} \right] \tag{5.15}$$

where c with raised indices is determined by

$$c_{\alpha\gamma}c^{\gamma\beta}|b_{\beta}\rangle \equiv |b_{\alpha}\rangle \ . \tag{5.16}$$

This implicitly defines $c^{\gamma\beta}$ as the generalised inverse on the set $\{|b_{\alpha}\rangle\}$. Ref. [295] explicitly derived this for the QCD case by working in $N_c = 3 + \epsilon$ dimensions and taking the $\epsilon \to 0$ limit at the end. If the basis set was minimal, it would hold that $c_{\alpha\gamma}c^{\gamma\beta} = \delta^{\beta}_{\alpha}$ and the two matrices would truly be inverse to each other. In general the basis sets are however allowed to be overcomplete. The most commonly used, including the trace basis exemplified here, are overcomplete at least for high enough multiplicities. The calculation of the matrices $T_{\alpha\beta}$ and $c_{\alpha\beta}$ in a variety of bases for arbitrary processes has been automated in Ref. [297] in the context of the SHERPA resummation framework. Other approaches include [298–301].

The relevant inputs for most processes needed in practice are available as input files and do not need a dedicated re-computation. Likewise, the hard matrix $H^{\alpha\beta}$ can be obtained from COMIX as described in Ref. [295]. The plugin then only needs to implement the algebra to calculate the inverses, exponentials and traces of matrices and products of matrices, to arrive at the final function

$$S(t) = \frac{Tr\left[He^{-\frac{t}{2}\Gamma^{\dagger}}ce^{-\frac{t}{2}\Gamma}\right]}{Tr\left[cH\right]} \ . \tag{5.17}$$

For the more delicate of those tasks, external software packages are used. In particular, Ref. [302] is used to calculate the generalised inverse of matrices, and Ref. [303] for the matrix exponential.

In order to validate this part of the calculation, several tests can be automatically performed within the SHERPA implementation. The first is to check the generalised inversion procedure. Since a generalised inverse c^{-1} of a matrix c is not unique, one can shift

$$c^{-1} \to c^{-1} + \left[\mathbf{1} - cc^{-1}\right]\mathcal{R} \ , \tag{5.18}$$

where $\mathcal{R}$ is a matrix with random entries of the correct dimensionality and $\mathbf{1}$ is diagonal with entries equal to 1 on the diagonal and zero otherwise. Since the two inverses are equivalent on the relevant space, in the sense that both fulfil the implicit definition in Eq. (5.16), one might perform such a shift and check that the calculation returns the same result. Of course, this is trivial if the basis set is not overcomplete and $cc^{-1} = \mathbf{1}$. Note that, if one indeed chooses a completely random matrix $\mathcal{R}$, numerical inaccuracies in cancellations might still be relatively large. Still, since the cancellation can be checked on the basis of an individual phase space point, this is a powerful consistency test of the implementation. Likewise, the correctness of the colour insertion operators can

be tested by verifying that they obey the relations implied by colour conservation, *cf.* Eq. (2.78).

Finally, one can explicitly check that the insertion operators correctly reproduce the soft limit for a single emission, which is reflected in the eikonal approximation Eq. (2.61). In the notation established in this section, it can be expressed by defining the current

$$\gamma = -2g^2 \sum_{i<j} \frac{p_i \cdot p_j}{(p_i \cdot k_s)(p_j \cdot k_s)} T_{\alpha\beta} c^{\alpha\beta} \ . \tag{5.19}$$

The quantity of interest is then the ratio

$$R_s = \frac{Tr\left[\gamma c_n H_n\right]}{Tr\left[\gamma c_{n+1} H_{n+1}\right]} \ . \tag{5.20}$$

Here the subscripts label the Born multiplicity, *i.e.* the denominator is the matrix element squared for the $(n+1)$ parton matrix element, while the numerator is the one for n partons with the eikonal current inserted. This ratio should then approach 1 in the limit where $k_s = \lambda_s k$, $\lambda_s \to 0$. This test was performed in the original Ref. [295] as well as in the context of Ref. [II]. The results of the latter are shown in Fig. 5.1 for various Born final states. The test is performed in jet final states in electron positron annihilation at $\sqrt{s} = 91.2$ GeV. The different lines in Fig. 5.1 correspond to individual $(n+1)$ parton configurations. Those are drawn randomly, in a phase space regularised by requiring that the Durham resolution scale, *cf.* Eq. (3.25), is $y_{n,n+1} > 0.02$. One of the gluons is then picked and its momentum scaled down.

The upper row of plots in Fig. 5.1 displays the soft limit of a 5 parton matrix element, containing in addition to the gluon that approaches the soft limit either two quark-antiquark pairs on the right, or an quark-antiquark pair and two more gluons on the left. Since the production mode for the jets here is the decay of a Z boson, there is no channel that would contain only gluons. The bottom row of plots shows the same test with an additional hard gluon in the matrix element. In all cases, unity is approached for small λ_s, confirming the validity of the current implementation.

In order to systematically asses the effect of subleading colour, an option is implemented to consider the full resummed calculation in the strict $N_c \to \infty$ limit with $\alpha_s N_c = \alpha_{s,0} = \text{const.}$ fixed, known as the t'Hooft limit [304]. In terms of the usual QCD parameters, this implies

$$\frac{C_F}{2\pi\beta_0} \to \frac{3}{11} \ , \qquad\qquad \frac{C_A}{2\pi\beta_0} \to \frac{6}{11} \ , \qquad \alpha_s\beta_0 \to \frac{11}{12\pi}\alpha_{s,0} \ , \tag{5.21}$$

$$\frac{K}{2\pi\beta_0} \to \frac{67/3 - \pi^2}{11} \ , \qquad\qquad \frac{\beta_1}{\beta_0^2} \to \frac{102}{121} \ . \tag{5.22}$$
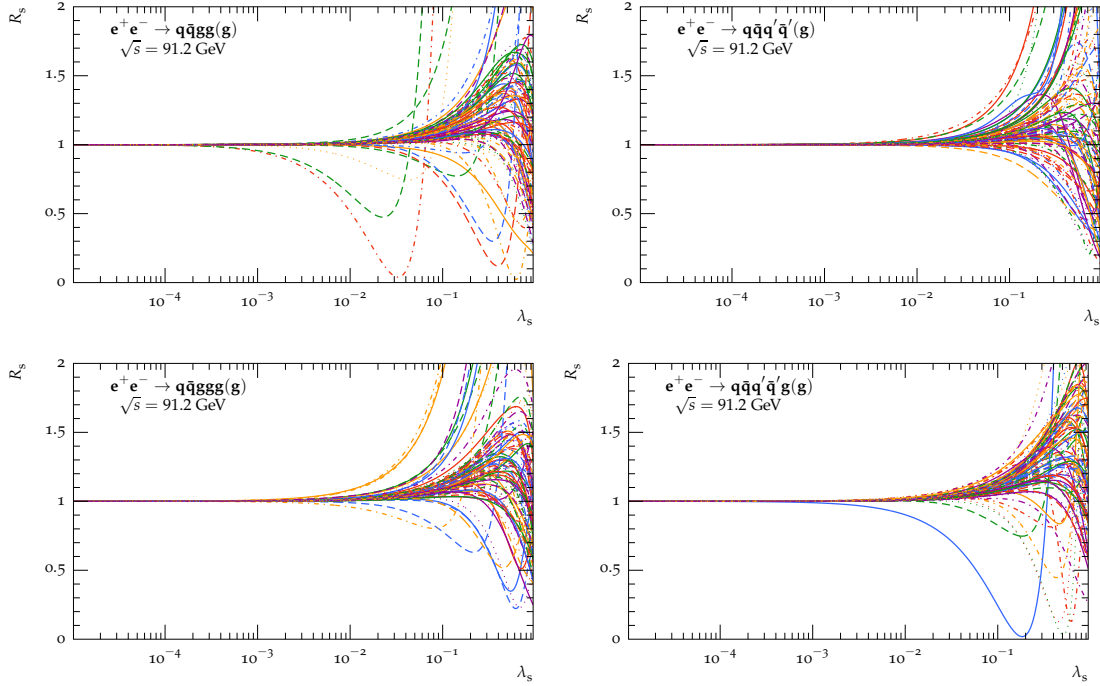
Figure 5.1: Ratio of the eikonal approximation to the exact $e^+e^- \to 5\text{-}, 6\text{-parton}$ tree-level matrix element versus the softness parameter λ_s.

Figure and caption taken from Figure 1 in Ref. [II].

To evaluate the colour insertion operators in the large-N_c limit, one needs to calculate

$$\alpha_{\mathsf{s}} \frac{\langle b_\alpha | \, \boldsymbol{T}_i \boldsymbol{T}_j \, | b_\beta \rangle}{|b_\alpha||b_\beta|} \to \alpha_{\mathsf{s},0} \, \langle b_\alpha | \, \boldsymbol{T}_i \boldsymbol{T}_j \, | b_\beta \rangle_{\mathrm{LNC}} \tag{5.23}$$

with the identification

$$\langle b_\alpha | \, \boldsymbol{T}_i \boldsymbol{T}_j \, | b_\beta \rangle_{\mathrm{LNC}} = \lim_{N_c \to \infty} \frac{\langle b_\alpha | \, \boldsymbol{T}_i \boldsymbol{T}_j \, | b_\beta \rangle}{N_c |b_\alpha||b_\beta|} \, . \tag{5.24}$$

An additional option is the "improved LC" scheme used in Ref. [II], which consist of making the replacement in Eq. (5.23) but evaluate all other quantities at finite N_c. This means in particular that the correct Casimirs are used in the radiators that are identified with a particular leg and its flavour. Likewise, the β function coefficients, Eq. (2.31) and Eq. (2.32), and collinear anomalous dimensions, Eq. (2.84) and Eq. (2.85), are calculated at $N_c = 3$ in this case. This is closer to the approximations made in practical parton shower implementations, which, while only claiming to be correct in the large N_c limit, would not usually implement a strict limit but attempt to set as many colour factors as possible to the correct values.

5.3 The multiple emission function

The $\mathcal{F}$ function can be calculated from Eq. (4.12) at NLL accuracy. However, the form given there still does contain subleading contributions. If the integrals are supposed to be calculated numerically, this can be done by scaling the gluon momenta to become indeed infinitely soft and probe the behaviour of the observable V in that limit. This is the general strategy taken in Ref. [88]. The final form of the $\mathcal{F}$ function found there, in the notation of Ref. [II], is given by

$$\mathcal{F}^{\mathcal{B}_\delta}(L) = \lim_{\epsilon \to 0} e^{R' \ln \epsilon} \sum_{m=0}^{\infty} \frac{R'^m}{m!} \left(\prod_{i=1}^{m+1} \sum_{l_i \in \delta} \frac{R'_{l_i}}{R'} \int_\epsilon^1 \frac{d\zeta_i}{\zeta_i} \int_0^1 \frac{d\xi_i}{\mathcal{N}_{l_i}} \int_0^{2\pi} \frac{d\phi_i}{2\pi} \right) \delta(\ln\zeta_1)$$

$$\times \exp\left(-R' \ln \lim_{\bar{v} \to 0} \frac{V(\mathcal{B}_\delta; \kappa_1(\zeta_1\bar{v}), ..., \kappa_{m+1}(\zeta_{m+1}\bar{v}))}{\bar{v}} \right), \tag{5.25}$$

with

$$\mathcal{N}_{l_i} = \left(1 + \frac{a + (1 - \xi_i)b_{l_i}}{a(a + b_{l_i})} 2\lambda \right) \int_0^1 d\tilde{\xi}_i \frac{1}{1 + \frac{a + (1 - \tilde{\xi}_i)b_{l_i}}{a(a + b_{l_i})} 2\lambda} . \tag{5.26}$$

Here ξ_i is the fraction of the maximal rapidity for leg l_i, and $V(\kappa_i(\zeta_i\bar{v})) = \zeta_i\bar{v}$ implies $\eta_{i,\max} = \ln(1/\zeta_i\bar{v})/(a + b_{l_i})$. The numerical evaluation of the integrals and limits has been implemented, in the context of the SHERPA plugin discussed here, in Ref. [305]. Fig. 5.2 shows the results of this implementation for the Durham jet resolution scales. The right hand side illustrates how the limit $\bar{v} \to 0$ is approached for several values of R'. The rows correspond to different Born multiplicities n and the corresponding Durham resolution scales $y_{n,n+1}$, *cf.* Eq. (3.25).

The plugin implements the technology needed to extrapolate the functions calculated on a grid, usually in R'. This makes use of cubic Hermite splines to exploit the monotonicity of $\mathcal{F}$ as described in [306, 307]. The left hand side validates the various explicit results for the $\mathcal{F}$ functions corresponding to the white dots, compared to the interpolated function (solid line) that is practically used for the resummation.

Of course, in cases where the $\mathcal{F}$ function is known in analytic form, this is used in the plugin. Likewise, the numerical $\mathcal{F}$ functions provided with the plugin code could easily be exchanged with externally generated values. In the simplest case this could be achieved by saving them in the same format, essentially just as a space separated list of R', $\mathcal{F}$ and optionally the uncertainty $\Delta\mathcal{F}$. To asses the effect of the uncertainty on the final result, the resummed cross section Σ can be recalculated with a variation of $\mathcal{F}$ by $\Delta\mathcal{F}$.
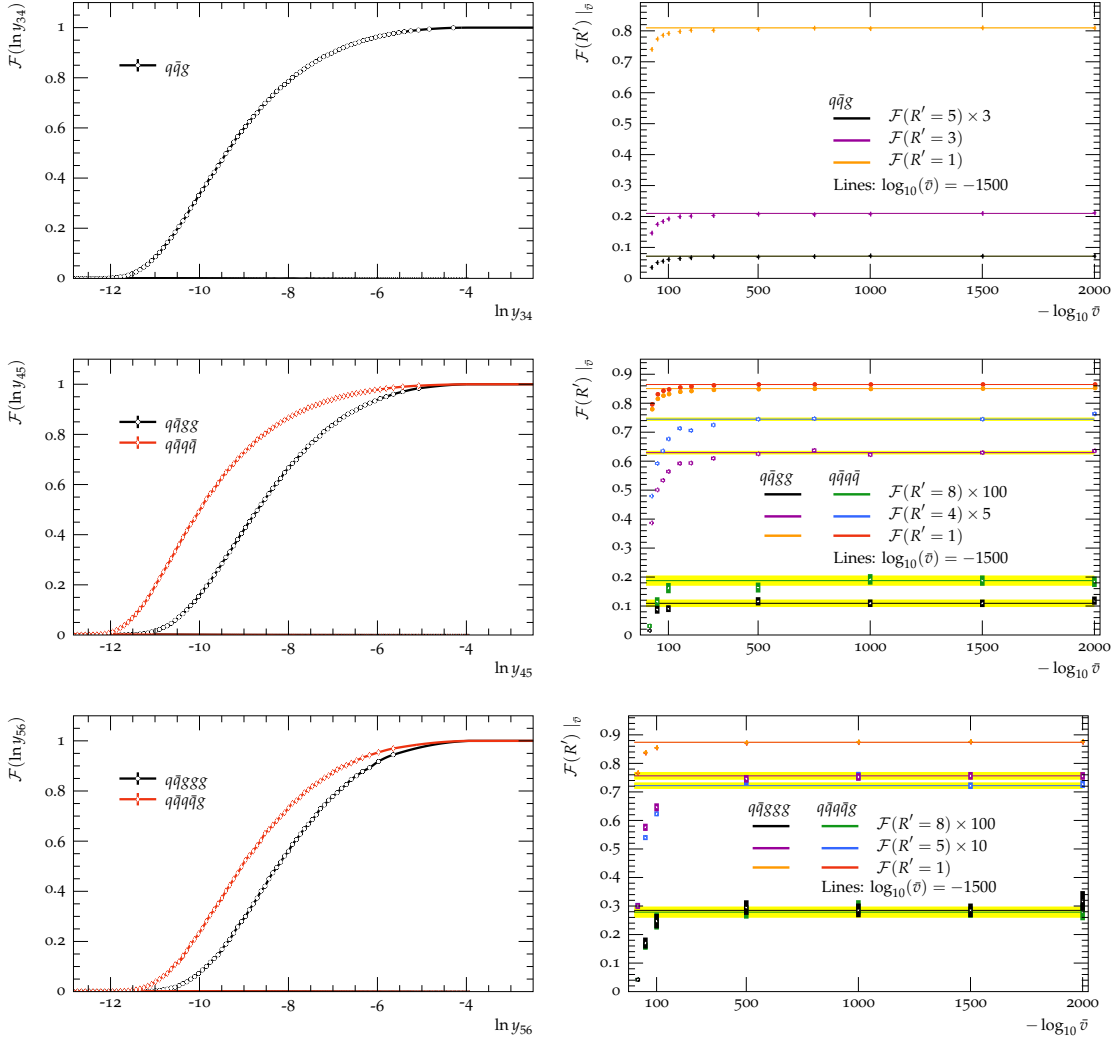
Figure 5.2: Multiple-emission function $\mathcal{F}$ for the different Born channels δ appearing in the resummation of y_{34}, y_{45} and y_{56} respectively. While the left column emphasises the dependence on the large logarithm, i.e., $\ln\left(y_{n,n+1}\right)$, the right column shows the convergence of the numerical evaluation of the limit $\bar{v} \to 0$ for selected values of R'. The lines with error bands mark the value and statistical uncertainty for $\bar{v} = 10^{-1500}$. Note that for y_{34} as well as the other $\mathcal{F}$ functions with $R' = 1$, the dot sizes are larger than the error bar would be.

Figure and caption taken from Figure 1 in Ref. [II].

5.4 Flavour mapping and NLL′ accuracy

As was anticipated at the end of Sec. 2.3, in order to correctly compute the contributions of order $\alpha_s^2 L^2$ to the cross sections Σ, it is necessary to take into account the cross terms between LL contribtions, of order $\alpha_s L^2$, and corrections of order α_s relative to the respective Born process that are constant in the observable, *i.e.* that are not enhanced by logarithms, but also do not vanish in the $v \to 0$ limit. The full $\mathcal{O}(\alpha_s)$ contribution to Σ has the general form, *cf.* Eq. (2.87),

$$\Sigma_{\mathsf{fo}}(v) = \sigma^{(0)} \left(1 + \frac{\alpha_s}{2\pi} L^2 A_1 + \frac{\alpha_s}{2\pi} L B_1 + \frac{\alpha_s}{2\pi} C_1 + \frac{\alpha_s}{2\pi} D_1(v) + \mathcal{O}\left(\left(\frac{\alpha_s}{2\pi} \right)^2 \right) \right)$$

(5.27)

$$\lim_{v\to 0} D_1(v) = 0 \ ,$$

(5.28)

with some coefficients A_1, B_1, C_1, D_1. Here D_1 is itself a function of the observable value that however vanishes in the small observable limit as indicated in the second line. The subscript 1 indicates that those are the coefficients of one power of α_s relative to the Born process. Similarly, the resummed predictions can be expanded in terms of α_s. This expansion will of course only contain the logarithmic terms,

$$\Sigma_{\mathsf{res}}(v) = \sigma^{(0)} \left(1 + \frac{\alpha_s}{2\pi} L^2 A_1 + \frac{\alpha_s}{2\pi} L B_1 + \mathcal{O}\left(\left(\frac{\alpha_s}{2\pi} \right)^2 \right) \right)$$

(5.29)

with the same coefficients A_1 and B_1. For the simplest observables, like 3-jet observables in e^+e^- annihilation, the relevant coefficient C_1 can hence be extracted by simply taking the difference

$$\frac{\alpha_s}{2\pi} C_1 = \lim_{v\to 0} \frac{\Sigma_{\mathsf{fo}}(v) - \Sigma_{\mathsf{res}}(v)}{\sigma^{(0)}} \ .$$

(5.30)

Note that it is not necessary here to further specify the coefficients A, B, C, D, so it is a matter of convention what expansion parameter is used. For example, one could have used α_s instead of $\alpha_s/2\pi$ or absorb $\sigma^{(0)}$ into the coefficients.

The C_1 coefficient is particularly simple in this case. This is because the Born final states in $e^+e^- \to q\bar{q}$ are the same if one ignores the orientation relative to the beam directions. In general, the equivalent structure giving rise to the $\alpha_s^2 L^2$ correction is given by [282]

$$\int d\mathcal{B}^\delta \left(\frac{d\Sigma_{\mathsf{fo}}^{\delta,(1)} - d\Sigma_{\mathsf{res}}^{\delta,(1)}}{d\mathcal{B}} \right) \frac{\Sigma_{\mathcal{B}^\delta}^{(1),LL}}{\sigma^{\delta,(0)}} \ .$$

(5.31)

Here $\Sigma_{\mathcal{B}^\delta}^{(1),LL}$ denotes the LL part of the leading order expansion for the resummed cross section appropriate for the phase space point $\mathcal{B}^\delta$. It should be noted that, at this stage one might equally replace it by the full exponent $\Sigma_{\mathcal{B}}^{LL}$, and include any set of NLL terms without changing anything at the formal NLL′ accuracy. The only thing that is relevant for this is the first order, double logarithmic expansion of whatever is written in this place.

This piece will be determined by radiation that is simultaneously soft and collinear. Because of this, the only way it can depend on the colour structure is through the Casimir factors of the hard legs in $\mathcal{B}$. Likewise, it does not depend on the detailed kinematics of the full final state. This can explicitly be verified by inspecting the LL parts of the explicit results, *cf.* Eq. (4.30). Physically, this should be clear fact that collinear emissions only depend on the hard leg they are emitted from.

Thus, the $\Sigma_{\mathcal{B}^\delta}^{(1),LL}$ does not depend on the integration variables in Eq. (5.31). One might write, splitting the integral over the difference into two integrals

$$\Sigma_{\text{res}}^{(1),LL,\delta} \frac{\int d\mathcal{B}^\delta \frac{d\Sigma_{\text{fo}}^{(1)}}{d\mathcal{B}} - \int d\mathcal{B}^\delta \frac{d\Sigma_{\text{res}}^{(1)}}{d\mathcal{B}}}{\sigma^{\delta,(0)}} = \Sigma_{\text{res}}^{(1),LL,\delta} \frac{\Sigma_{\text{fo}}^{(1),\delta} - \Sigma_{\text{res}}^{(1),\delta}}{\sigma^{(0),\delta}} \ . \tag{5.32}$$

This allows to work effectively with an averaged coefficient given by the difference of the two $\mathcal{O}(\alpha_{\text{s}})$ cross sections on the right hand side. In analogy to Eq. (5.30), the relevant coefficient is defined as:

$$\frac{\alpha_{\text{s}}}{2\pi} C_1^\delta \equiv \lim_{v \to 0} \frac{\Sigma_{\text{fo}}^{\delta,(1)} - \Sigma_{\text{res}}^{\delta,(1)}}{\sigma^{\delta,(0)}} \ . \tag{5.33}$$

The left hand side here should be understood in a symbolic sense; if the renormalisation scale μ_R that is used in the calculation, in particular as an argument to the strong coupling, is determined dynamically based on the kinematics, there would be no unique way to split the right hand side of Eq. (5.33) into a constant times α_{s}.

It is important to note that this version of the C_1 coefficient still depends on the channel δ. There is some freedom in its detailed definition, but it should be such that all final state configurations that are sorted into the same channel δ exhibit the same LL behaviour with respect to the observable in question. This LL behaviour is mostly determined by the Casimir factors associated with the Born legs, *i.e.* how many of the Born partons are quarks and gluons. In order to calculate the difference in Eq. (5.33), one hence needs to associate a given configuration with higher multiplicity to one of the flavour channels present at Born level.

A way to do this in an infrared safe way has been proposed in Ref. [308]. This algorithm will be referred to as BSZ algorithm after the authors of Ref. [308]. The procedure was

used by the same authors in Ref. [282] to achieve what is called NLL$'$ accuracy here[1]. The algorithm is a sequential recombination algorithm similar to the ones described in Sec. 3.2. Instead of just working with the momenta, this time also the flavour of the objects is taken into account however.

The flavour of an object is practically implemented as a list of n_f integers, corresponding to the n_f possible quark flavours. For a quark this list contains zeros, apart from the entry corresponding to the flavour of the quark, which is 1. For an antiquark, the single non-zero entry has a value of -1, whereas for a gluon all entries are zero. If objects are combined, their flavours are added together entry by entry. This means that a quark and antiquark of the same flavour are combined into a flavourless object, *i.e.* with all entries set to zero. A priori, it is however not excluded that objects with multiple flavours, or absolute values larger than 1 for some flavour, emerge in the algorithm.

To be precise, the general procedure of the sequential recombination algorithm is altered as follows, with the changes to Sec. 3.2 marked in bold font:

0. Start with the list $\mathcal{O}$ of all final state objects that enter the clustering, the beams B and $\bar{B}$, and the list of clustered jets $\mathcal{J}$. **An object is described by its four-momentum and flavour.**

1. Check if the stopping criterion is met. If yes, add all remaining objects in $\mathcal{O}$ to $\mathcal{J}$ and terminate the algorithm. The list $\mathcal{J}$ contains the jets.

2. Determine the pair $\{i, j\} \in \mathcal{O}$ that minimise some distance measure d_{ij}, and the objects k **and** m that minimises the beam distance measure d_{kB} **and** $d_{m\bar{B}}$.

3. The next step is determined by $d = \min\left(d_{ij}, d_{kB}, \mathbf{d_{m\bar{B}}}\right)$:

    (a) If $d = d_{ij}$, update $\mathcal{O}$ by removing objects i and j and adding a new object with four momentum $p_i + p_j$ **and the combined flavour of** i **and** j.

    (b) If $d = d_{kB}$ $(d = d_{m\bar{B}})$, update $\mathcal{O}$ **by assigning the combined flavour of** k, B $(m, \bar{B})$ **to beam** B $(\bar{B})$.

    Go back to step 1.

This creates a final list of objects with associated flavours. The natural stopping criterion here is to run the algorithm until the Born configuration for the observable in question is met. For practical purposes, several flavour assignments obtained this

---

[1] The accuracy containing the same terms was referred to as NNLL$_\Sigma$ in Ref. [282].

way might be combined to form a channel δ in the context of extending a resummed result to NLL′ accuracy. Commonly, it is for example sufficient to label a channel by the number of quarks and gluons, *i.e.* single flavoured and flavourless objects in the final list $\mathcal{J}$, sorting any configuration that leads to $\mathcal{J}$ containing objects with multiple flavours to a separate "other" channel. In other cases it might however be desirable to maintain at least the ordering of the types of particles in some hardness measure, or to further split up the channels based on kinematic regions. The implementation within the SHERPA framework is flexible in this regard, first doing the clustering keeping all the flavour information and only at the very end naming the channel.

A main concern Ref. [308] is the question of how to define the distance measures d, in order to achieve an infrared safe flavour assignment. The primary example for how this fails for an arbitrary definition like the ones given in Sec. 3.2, is the case of a gluon splitting into an quark-antiquark pair. In the limit where the intermediate gluon becomes soft, *i.e.* the sum of the quark and antiquark four momenta approach zero, this should not alter the flavour assignment. However, it is in general not guaranteed that the two quarks would end up in the same jet in this case. If they are for example clustered together respectively with two different gluons, this would lead to two objects treated as quark jets, even if the momenta of the quarks are infinitely soft.

To avoid such scenarios, and based on the general structure of QCD matrix element and similar considerations, Ref. [308] argued for the following distance measures in the case of colour neutral initial states:

$$
d_{ij} = \begin{cases} \min\left(E_i^2, E_j^2\right)(1 - \cos\theta_{ij}), & \text{if softer of } i, j \text{ is a gluon} \\ \max\left(E_i^2, E_j^2\right)(1 - \cos\theta_{ij}), & \text{if softer of } i, j \text{ is a quark} \end{cases}, \tag{5.34}
$$

where as in Sec. 3.2 the initial state is ignored in this case. The words "quark" and "gluon" are used here to indicate flavoured and flavourless objects respectively, for the sake of brevity. Further note that Ref. [308] actually defined the y_{ij} equivalents of the measures given here.

In the presence of hadronic initial states, those need to be taken into account and
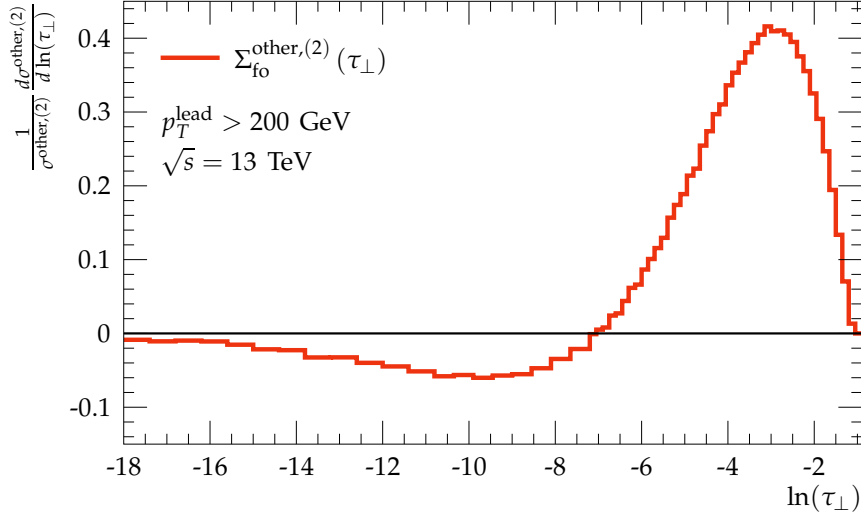
Figure 5.3: The $\mathcal{O}(\alpha_s^2)$ contribution to the 'other' channel in the limit $\tau_\perp \to 0$. Figure and caption taken from Figure 5 of Ref. [III].

distance measures have to be defined for them. Ref. [308] suggests to use

$$
d_{ij} = \begin{cases} \min\left(p_{T,i}^2, p_{T,j}^2\right) \Delta R_{ij}^2 \,, & \text{if softer of } i, j \text{ is a gluon} \\ \max\left(p_{T,i}^2, p_{T,j}^2\right) \Delta R_{ij}^2 \,, & \text{if softer of } i, j \text{ is a quark} \end{cases} \,, \tag{5.35}
$$

$$
d_{iB} = \begin{cases} \min\left(p_{T,i}^2, p_{T,B}^2(y_i)\right) \,, & \text{if } i \text{ is a gluon} \\ \max\left(p_{T,i}^2, p_{T,B}^2(y_i)\right) \,, & \text{if } i \text{ is a quark} \end{cases} \,, \tag{5.36}
$$

$$
d_{i\overline{B}} = \begin{cases} \min\left(p_{T,i}^2, p_{T,\overline{B}}^2(y_i)\right) \,, & \text{if } i \text{ is a gluon} \\ \max\left(p_{T,i}^2, p_{T,\overline{B}}^2(y_i)\right) \,, & \text{if } i \text{ is a quark} \end{cases} \,, \tag{5.37}
$$

$$
\text{where} \quad \begin{aligned} p_{T,B}(y) &= \sum_j p_{T,j} \left(\Theta\left(y_j - y\right) + \Theta\left(y - y_j\right) e^{y_j - y} \right) \\ p_{T,\overline{B}}(y) &= \sum_j p_{T,j} \left(\Theta\left(y - y_j\right) + \Theta\left(y_j - y\right) e^{y - y_j} \right) \end{aligned} \,. \tag{5.38}
$$

The precise considerations for the choice of the beam distance measure shall not be repeated here, since for the purpose of this work it is only important that it indeed achieves an IRC safe definition of the jet flavour. This was proven also in Ref. [308].

A powerful test of the IRC safety of the flavour assignment is to check that the flavour channels that are not present at Born level indeed vanish. As explained before, those

contributions are collected in one single channel labelled "other". Since the IRC safety issues of generic jet algorithms only start at order α_{s}^2, it is particularly important to check that the NLO contributions to that channel vanish in the infrared limit, in order to validate the implementation of the algorithm. An example for such a test is presented in Fig. 5.3. Here transverse thrust, *cf.* Eq. (3.19), is used to parameterise the soft limit of radiation around dijet configurations in proton-proton collisions. Indeed, that contribution is vanishing in the $\tau_\perp \to 0$ limit.

Having checked this, it is possible to introduce a "bland" variant of the algorithm. It is defined by setting the distance measures between any two object to infinity if their combination would lead to more than one overall flavour. This effectively excludes these combinations and guarantees that one ends up with objects that can be interpreted as quark, antiquark or gluon. It is of course not mandatory to proceed in this way. Since these contributions vanish in the $v \to 0$ limit, the logarithmic accuracy is unaffected by how they are handled. They could be left in the separate "other" channel, be sorted to the physical Born channels by the way corresponding to the "bland" algorithm or even be sorted to channels randomly, as far as the logarithmic accuracy is concerned.

Considerations for groomed event shapes

There are some subtleties arising in the application of the above algorithm in the case of soft drop grooming. In short, everything works out at the end, but some additional arguments are required. They are laid out here in the same way as presented in Ref. [III]. The main cause of trouble is that for groomed observables, the limit $v^{\mathrm{SD}} \to 0$ does not uniquely impose the soft limit for all particles beyond the Born multiplicity. This implies that the $\Sigma_{\mathrm{fo}}^{\delta,(1)}$ receives several contributions.

As in the ungroomed case, at $v^{\mathrm{SD}} = 0$ the virtual+real corrections contribute with a constant. For the real correction, there is a part of phase space where nothing is groomed. In this region everything works as in the ungroomed case, contributing a finite remainder between the integral of this fixed order phase space and $\Sigma_{\mathrm{res}}^{\delta,(1)}$.

Due to grooming, there is an addition part of the real correction that results in $v^{\mathrm{SD}} = 0$ because one particle is groomed away. The proper treatment for those would be to multiply with the Sudakov factors for the corresponding $(n + 1)$-particle final state. However, as explained previously, the only important term as far as NLL′ accuracy is concerned are the cross terms with the LL part of the Sudakov factors. Those are the same as for the $2 \to 2$ configuration obtained by ignoring the groomed parton.
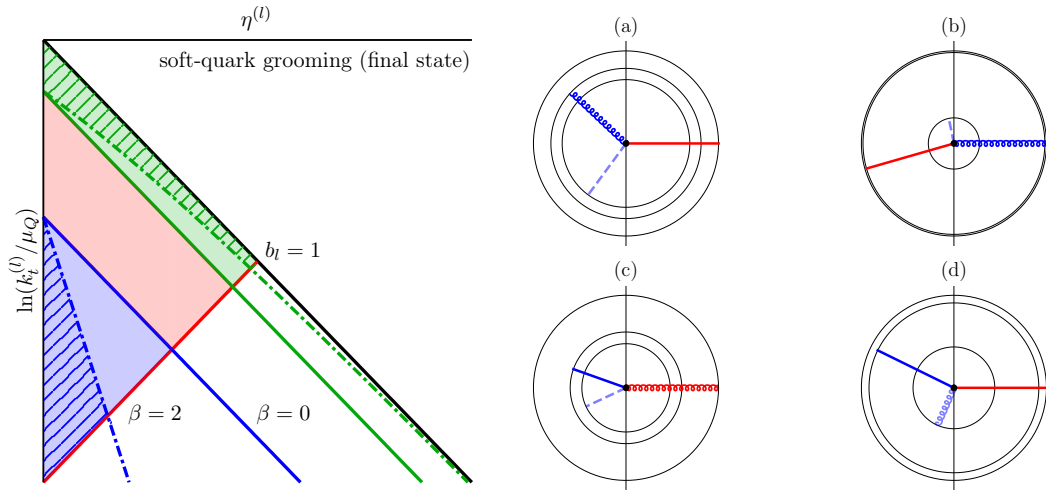
Figure 5.4: Left: The emission phase space in the Lund plane with the CAESAR parameters $a_l = 1$ and $b_l = 1$ (valid for thrust). The green area marks the phase-space region where the emitting particle will be removed by grooming with boundaries corresponding to $\beta = 0$ (solid line and area) and $\beta = 2$ (dashed line, hatched area). The blue area marks the region where the emitted gluon is removed, *cf.* Fig. 3.1. Right: Displays of the transverse plane of several LO final-state configurations. The colour codes indicate jet association according to the BSZ algorithm, groomed particles are in light shade and dashed in the case of quarks. (a) Sample event from the green area, where the quark is groomed instead of the gluon. (b), (c) Sample events with two quarks in one hemisphere, with the softer one getting groomed, for different jet clusterings. (d) Sample event from the blue area, a soft gluon is groomed.

Figure and caption taken from Figure 6 of Ref. [III].

This means that it is still valid to just cluster all fixed order events according to the BSZ algorithm. The different configurations that can be encountered in LO $2 \to 3$ events are illustrated in Fig. 5.4. Panel (d) shows the "usual" case, where a soft gluon is groomed. In this case the gluon always has the smallest of the three transverse momenta. Momentum conservation also excludes the case where the other two particles are collinear. The gluon will hence always be clustered first. Clustering a gluon does not change the flavour assignment of the other two objects, so this is the same as if the gluon was discarded. The same reasoning applies if a quark is groomed but clustered to the beam. Since the soft drop observables do not receive contributions from initial state radiation at NLL accuracy, the flavour assignment of the beams does not matter in the end.

A more careful analysis is required if a groomed quark is clustered together with a final state particle. The relevant cases where two quarks are in the same hemisphere are panels (b) and (c) of Fig. 5.4, which the BSZ algorithm classifies as quark-quark (b) and gluon-gluon (c) like final states. In a fourth case, the quark can be in the same hemisphere as a gluon, and clustered together with that gluon. In the soft gluon limit, only the gluon can be groomed. However, at fixed order there is also the case shown in panel (a) of Fig. 5.4 where the quark is actually groomed. The relevant phase space region for this is marked in green in the Lund diagram on the left of Fig. 5.4. The cases (a), (b) and (c) are all suppressed with powers of z_{cut}, and can hence be neglected in the $z_{\mathrm{cut}} \ll 1$ limit in which the calculations in Sec. 4.4 were performed. They are enhanced by logarithms of L in the $\beta = 0$ case and need to be considered if the goal is to claim NLL accuracy including finite z_{cut} effects, *cf.* [142, 309]. With $\beta > 0$, they would enter at NLL' accuracy only, and still be suppressed by z_{cut}. Finite z_{cut} effects are not implemented in the SHERPA resummation framework currently, and their discussion is beyond the scope of this work.

Considerations for jet observables

For observables defined on anti-k_t jets, that can be resummed as described in Sec. 4.3, there are some modifications necessary to achieve the proper structure at NLL' accuracy. The discussion here will follow that already presented in Ref. [IV]. The reason modifications are necessary is in the non-global structure of such observables, *i.e.* the fact that they can be zero at any perturbative order if no additional particle is inside the jet on which the observable is defined. This requires in principle a resummation to be performed on arbitrary multi-jet configurations.

The considerations are similar to the groomed observables above. To achieve NLL' accuracy, it is enough to dress the LO configurations with the appropriate LL Sudakov factor. This can effectively be achieved by multiplying those events with the full NLL $\Sigma_{\mathrm{res}}^{\delta}$, corresponding to the channel δ obtained after dropping all other jets. This will contain the correct LL factor, since this only depends on the jet flavour and not the other details of the configuration.

Consider the situation depicted in Fig. 5.5 (b) for example. Their flavour channel need to be defined by the single object inside the measured jet alone. On the other hand, in the example shown in Fig. 5.5 (a), the quarks need to be clustered, at least in the collinear limit. The jet will then be identified as a gluon jet. IRC safety guides the correct prescription for the situations shown in Fig. 5.5 (c) and (d). As discussed before, The $g \to q\bar{q}$ splitting is undone first in the soft gluon limit.
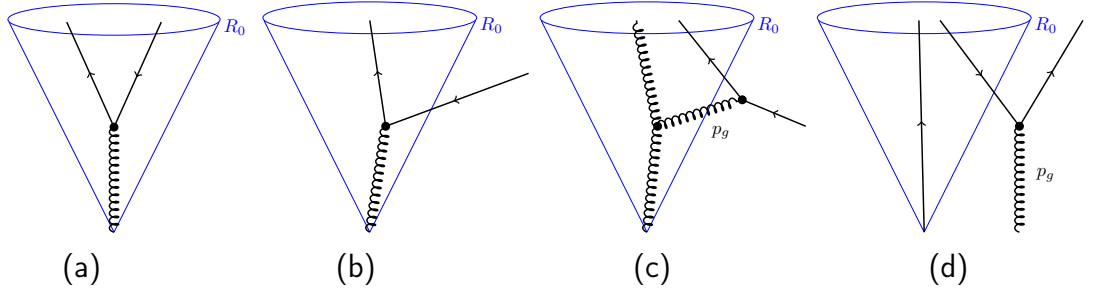
Figure 5.5: Examples for partonic input configurations to the flavour assignment algorithm. Configuration (a) needs to be identified as a gluon jet in the collinear limit, whereas for (b) we need to perform the LL resummation for a quark jet. IR safety requires that configurations (c) and (d) in the limit where $p_g \to 0$ are identified as gluon and quark jet, respectively. Figure and caption taken from Figure 5 of Ref. [IV]

Ref. [IV] proposed the following algorithm, that shall be directly quoted here

0. Start with the list $\mathcal{O}$ of all coloured final-state objects, containing particle four-momenta and flavour labels, and the beams $B, \bar{B}$ with their respective flavours.

1. Run the standard anti-k_t algorithm with radius parameter R_0 on $\mathcal{O}$, and obtain the objects in the leading, *i.e.* highest p_T, jet $J \subset \mathcal{O}$.

2. If J consists of only one object, $J = \{j \in \mathcal{O}\}$, terminate the algorithm. The flavour of j defines the flavour channel δ.

3. Otherwise, determine the pair $\{i, k\} \subset \mathcal{O}$ that minimises the BSZ measure d_{ik}^{BSZ} and the objects l, m that have minimal BSZ distances to the beams $d_{lB}^{\mathsf{BSZ}}, d_{m\bar{B}}^{\mathsf{BSZ}}$. Perform a cluster step according to $d^{\mathsf{BSZ}} = \min(d_{ik}^{\mathsf{BSZ}}, d_{lB}^{\mathsf{BSZ}}, d_{m\bar{B}}^{\mathsf{BSZ}})$:

    (a) If $d^{\mathsf{BSZ}} = d_{ik}^{\mathsf{BSZ}}$, update $\mathcal{O}$ by removing i and k and adding a new object with momentum $p_i + p_k$ and the combined flavour of objects i and k.

    (b) If $d^{\mathsf{BSZ}} = d_{lB}^{\mathsf{BSZ}}$ ($d^{\mathsf{BSZ}} = d_{m\bar{B}}^{\mathsf{BSZ}}$), update $\mathcal{O}$ by removing l (m) and assign the combined flavour of l and B (m and $\bar{B}$) to the beam B ($\bar{B}$).

    Go to step 1 and repeat.

Note that, while the prescription refers to the leading jet this can trivially be extended to other IRC safe identifications of the measured jet.

5.5 Matching to fixed order

With the flavour channel assignment in place, schemes can be devised that actually achieve NLL′ accuracy by combining the fixed order calculation in an appropriate way with the resummation. The general idea is to add the fixed order calculation Σ_{fo} and the resummed cross section Σ_{res}, and subtract the overlap. This should be enough to obtain a distribution that is correct up to the order in α_{s} at which the fixed order calculation was performed, and at the same time contains all logarithms at NLL accuracy.

As a second requirement, also the C_1 coefficient dealt with in Sec. 5.4 should be included. Ideally, this should happen without having to extract it explicitly. To this end, the following matched cross section is defined, for each Born channel δ based on the resummed cross section Σ_{res} and the fixed order result Σ_{fo}:

$$\Sigma_{\text{mult}}^{\delta} = \Sigma_{\text{res}}^{\delta} \left[1 + \frac{\left(\Sigma_{\text{fo}}^{\delta,(1)} - \Sigma_{\text{res}}^{\delta,(1)} \right)}{\sigma^{\delta,(0)}} \right. \tag{5.39}$$

$$\left. + \frac{1}{\sigma^{\delta,(0)}} \left(-\overline{\Sigma}_{\text{fo}}^{\delta,(2)} - \Sigma_{\text{res}}^{\delta,(2)} - \frac{\Sigma_{\text{res}}^{\delta,(1)}}{\sigma^{\delta,(0)}} \left(\Sigma_{\text{fo}}^{\delta,(1)} - \Sigma_{\text{res}}^{\delta,(1)} \right) \right) \right] .$$

The quantity $\overline{\Sigma}$ was introduced in Eq. (3.44). The counting of powers of α_{s} follows Eq. (2.57), *i.e.*

$$\Sigma^{(i)} \propto \alpha_{\text{s}}^{n_{\text{Born}}} \alpha_{\text{s}}^{i} . \tag{5.40}$$

At order α_{s}^2 relative to the Born accuracy, Eq. (5.39) equals the NLO cumulative distribution, apart from a missing additive constant $\sigma_{\text{fo}}^{\delta,(2)}$. For the logarithmic accuracy, one needs to investigate the limit $v \to 0$. Eq. (5.39) reduces to

$$\Sigma_{\text{mult}}^{\delta} \to \left(1 + \frac{\alpha_{\text{s}}}{2\pi} C_1^{\delta} + \mathcal{O}(\alpha_{\text{s}}^2) \right) \Sigma_{\text{res}}^{\delta} , \tag{5.41}$$

with C_1 given by Eq. (5.33),

$$\frac{\alpha_{\text{s}}}{2\pi} C_1^{\delta} \equiv \lim_{v \to 0} \frac{\Sigma_{\text{fo}}^{\delta,(1)} - \Sigma_{\text{res}}^{\delta,(1)}}{\sigma^{\delta,(0)}} . \tag{repeats 5.33}$$

Hence, the correct NLL′ terms are effectively included by this matching scheme. Since the resummed and fixed order cross section are multiplied rather than added, this matching scheme is referred to as "multiplicative matching".

An alternative is the matching scheme that in the literature [258, 282] is often referred

to as LogR matching scheme for historical reasons[2]. Here, the precise definition of it shall be

$$\Sigma_{\text{LogR}}^{\delta} = \Sigma_{\text{res}}^{\delta} \exp\left(\frac{\Sigma_{\text{fo}}^{\delta,(1)} - \Sigma_{\text{res}}^{\delta,(1)}}{\sigma^{\delta,(0)}}\right) \exp\left[\frac{-\overline{\Sigma}_{\text{fo}}^{\delta,(2)} - \Sigma_{\text{res}}^{\delta,(2)} - \frac{\left(\Sigma_{\text{fo}}^{\delta,(1)}\right)^2 - \left(\Sigma_{\text{res}}^{\delta,(1)}\right)^2}{2\sigma^{\delta,(0)}}}{\sigma^{\delta,(0)}}\right] .$$

$$(5.42)$$

After expanding the $\exp$ functions, to first order one recovers the multiplicative matching scheme, and the equivalent arguments regarding the accuracy apply. The final distributions are then obtained by adding the different channels

$$\Sigma_{\text{match}} = \sum_{\delta \in \mathcal{B}} \Sigma_{\text{match}}^{\delta} + \sum_{\delta \notin \mathcal{B}} \Sigma_{\text{fo}}^{\delta} , \qquad (5.43)$$

where the second sum accounts for channels not corresponding to any structure found in the physical Born process, but permitted by the jet-clustering algorithm, *e.g.* the "other" channel in Sec. 5.4.

An important validation step is the comparison of the expansion of the resummed cross section to the fixed order result at equal orders in α_{s}. The example given for this in Fig. 5.6 is again for Durham jet scales with various multiplicities, with the Born events regulated as before,

$$y_{n,n-1} > y_{\text{cut}} = 0.02 .$$

The figure first illustrates the derivatives of the cross sections at order α_{s}. The distribution $\Sigma_{\text{res}}^{(1)}$ itself is quadratic in L, so its derivative (blue) is linear. Fig. 5.6 shows that the difference to the fixed order result (red) vanishes. The fixed order result at the next higher order is shown in green. It contains logarithms to fourth, third and second power as well as terms linear in L, *cf.* Eq. (2.87). Only the first two are completely contained in the second order expansion of the resummed result (orange). This leads to a linear difference in the derivatives with respect to L . After including the C_1 coefficient (purple line), in the same way it is implicitly included in the matching schemes described above, the $\alpha_{\text{s}}^2 L^2$ terms are reproduced. This is confirmed by observing only a constant offset in the derivatives, *e.g.* the purple and green lines in the top panels in Fig. 5.6. The difference between these two is shown in purple in the respective bottom panels and can be confirmed to approach a constant in the soft limit. This confirms that the matching includes the correct coefficient and indeed achieves NLL$'$ accuracy.

---

[2]Those references use R to refer to the cross sections that are called Σ here. Following this, the matching scheme should be called LogΣ scheme. Here the convention from Ref. [II] to use "LogR" will be used.

The same test can be done for observables evaluated after soft drop grooming and for jet observables. The results that have been presented in Ref. [III] and Ref. [IV] to validate the implementation in those cases are shows in App. A for completeness. Fig. A.1 illustrates the case of soft drop groomed global event shapes. The analysis for jet observables is explicitly split up into the gluon channel in Fig. A.2 and the quark jet contribution in Fig. A.3. They exhibit the same general behaviour as Fig. 5.6, hence the discussion given above also applies to them.
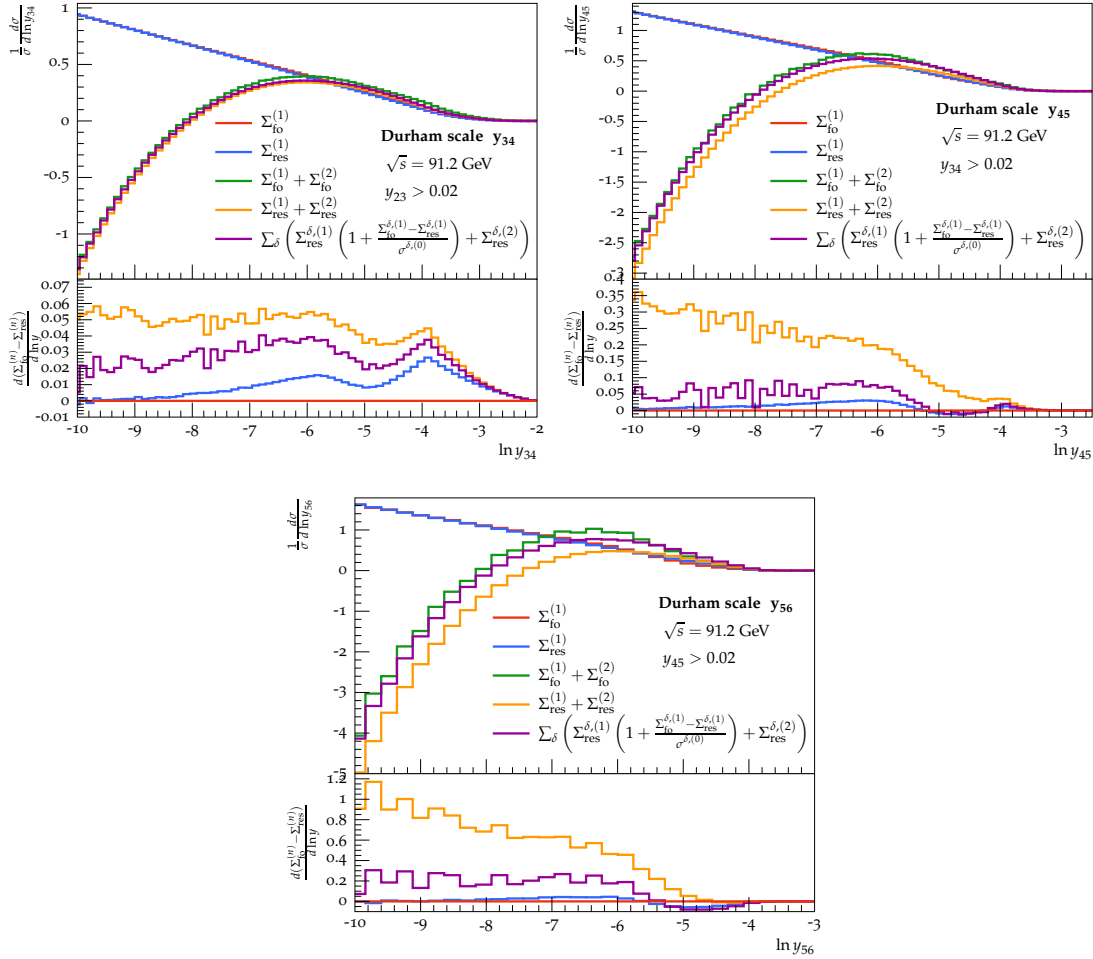
Figure 5.6: Fixed-order predictions for y_{34}, y_{45}, and y_{56}. We show the expansion of Σ_{res} to the relevant orders, and the expansion to second order including the expression approaching the C_1 coefficient in the soft limit. The lower panels show the total difference between fixed order and expansion. Figure and caption taken from Figure 5 of Ref. [II].

5.6   Extraction of non-perturbative corrections

There are several ways used in the literature to correct resummed calculations for non-perturbative effects. Next to dedicated models, *cf.* for example [141, 309–328], for specific processes and observables, such corrections can be estimated from Monte Carlo simulations, *cf.* Sec. 3.5 for an overview of the relevant models and tools. This usually involves taking the perturbative input, after the parton shower stage, and comparing it to the full simulation, including the effects of hadronisation and underlying event and multiple parton interaction effects.

Applying a correction in this way involves making some implicit assumptions about the relation between the perturbative stage of the event generator and the resummed calculation. If they are assumed to be equivalent, the simplest way forward is to take the ratio between parton level (PL) stage and the hadron level (HL) corresponding to the full simulation,

$$\mathcal{R}(v) = \frac{d\sigma_{\mathsf{HL}}^{\mathsf{MC}} / dv}{d\sigma_{\mathsf{PL}}^{\mathsf{MC}} / dv} \ . \tag{5.44}$$

If resummation and parton shower would be exactly equivalent, the hadron level for the resummed or matched cross section $\Sigma_{\mathsf{res/match}}$ can be obtained by calculating

$$\frac{d\Sigma_{\mathsf{HL}}}{dv} = \mathcal{R}(v)\frac{d\Sigma_{\mathsf{res/match}}}{dv} \ . \tag{5.45}$$

Of course, practically the parton level and the resummation will not be exactly equal. Otherwise, the parton shower prediction could just be used instead of the analytical resummed prediction. If they are sufficiently similar, one might however still hope that applying a ratio of this kind captures the dominant non-perturbative effects.

The above approach has a few weaknesses. First, it assumes that the parton shower and resummation are relatively closely related. Practically, this leads in particular to problems related to the region of the observable sensitive to energy scales close to the parton shower cutoff $t_{\mathsf{cut}} \approx 1$ GeV. In this region the two formalism will vary significantly, since the parton shower stops filling the full phase space. The hadronisation model however will be tuned to the particular shower with the cutoff, and will tend to fill that missing phase space. This can lead to an artificially enlarged ratio $\mathcal{R}$ between parton and hadron level.

This can be mitigated by defining a transition operator, corresponding to the conditional probability for the observable to equal v^{HL} at the hadron level configuration $\mathcal{H}(\mathcal{P})$,

given that it equals v^{PL} at the parton level configuration $\mathcal{P}$

$$
\mathcal{T}(v^{\mathsf{PL}}, v^{\mathsf{HL}}) = \frac{\int d\mathcal{P} \, \frac{d\sigma}{d\mathcal{P}} \delta \left(v^{\mathsf{PL}} - V(\mathcal{P}) \right) \delta \left(v^{\mathsf{HL}} - V(\mathcal{H}(\mathcal{P})) \right)}{\int d\mathcal{P} \, \frac{d\sigma}{d\mathcal{P}} \delta \left(v^{\mathsf{PL}} - V(\mathcal{P}) \right)} \ . \tag{5.46}
$$

Note that it is not necessarily specified here what exact phase space the parton level $\mathcal{P}$ is integrated over, and how the hadron level $\mathcal{H}$ is related to it. Any given implementation of a parton shower interfaced to a model of non-perturbative effects implicitly defines them though. The final result is then obtained as

$$
\frac{d\Sigma_{\mathsf{HL}}}{dv} = \int du \, \mathcal{T}(u, v) \frac{d\Sigma_{\mathsf{res/match}}}{du} \ . \tag{5.47}
$$

If one works with binned distributions, this operator can be made discrete. To obtain the cross section $\Delta\Sigma^b$ of a certain bin b with upper edge $v_{b,\mathsf{max}}$ and lower edge $v_{b,\mathsf{min}}$, the integrals would be performed over the region defined by

$$
\Theta_b(\mathcal{C}) = \theta(V(\mathcal{C}) - v_{b,\mathsf{min}})\theta(v_{b,\mathsf{max}} - V(\mathcal{C})) \ . \tag{5.48}
$$

$$
\Delta\Sigma^b = \int d\mathcal{C} \, \frac{d\sigma}{d\mathcal{C}} \Theta_b(\mathcal{C}) \ . \tag{5.49}
$$

The probability that an event is at parton level in bin p and at hadron level in bin h is then given by the transition matrix

$$
\mathcal{T}_{ph} = \frac{\int d\mathcal{P} \, \frac{d\sigma}{d\mathcal{P}} \Theta_p(\mathcal{P}) \Theta_h(\mathcal{H}(\mathcal{P}))}{\int d\mathcal{P} \, \frac{d\sigma}{d\mathcal{P}} \Theta_p(\mathcal{P})} \ . \tag{5.50}
$$

Consequently, the binned hadron level distribution is obtained from the corresponding parton level via

$$
\Delta\Sigma^b_{\mathsf{HL}} = \sum_p \mathcal{T}_{pb} \, \Delta\Sigma^p_{\mathsf{res/match}} \ . \tag{5.51}
$$

A second complication is the implicit assumption that the event selection implemented via Θ_{hard}, *cf.* Eq. (4.15), does not require any non-perturbative correction, *i.e.* that any event that passes this cut at parton level also passes it at hadron level, and the other way around, if an event is outside the considered region at parton level in can not contribute to the hadron level. An example might be to measure an observable based on jets in a certain range of the jets transverse momentum p_T. This could be implemented by setting Θ_{hard} to

$$
\Theta_{\mathsf{hard}}(\mathcal{J} \subset \mathcal{B}) = \theta(p_{T,\mathcal{J}} - p_{T,\mathsf{min}})\theta(p_{T,\mathsf{max}} - p_{T,\mathcal{J}}) \ . \tag{5.52}
$$

A jet at a transverse momentum slightly lower than $p_{T,\mathrm{min}}$ might however pick up additional energy for example from the underlying event, proportional to its jet radius. Thus it might end up in the measured range of jets and contribute to the distribution of the observable considered. The approach using a simple ratio could only take this into account by modifying the cross section by a constant factor.

It is suggested to use a higher dimensional transition matrix to take this effect into account. In a first step, the resummation is performed over a larger region $\Theta_{\mathrm{inclusive}}$ of Born events. This range should be inclusive enough such that there is a negligible probability for Born events that are outside of it at parton level to migrate into the original measurement region given by Θ_{hard}. This might be separated into n regions,

$$\Theta_{\mathrm{inclusive}} = \sum_{r=1}^{n} \Theta_{\mathrm{hard}}^{r} \; , \tag{5.53}$$

with the requirement that there is a subset of these regions that form the original measurement region. For simplicity it will be assumed that those correspond to the first n_{hard} regions,

$$\Theta_{\mathrm{hard}} = \sum_{r=1}^{n_{\mathrm{hard}}} \Theta_{\mathrm{hard}}^{r} \; . \tag{5.54}$$

The transition matrix approach can then be extended by defining the probability to transition from the bin p in region i at parton level to bin h in region j at hadron level.

$$\mathcal{T}_{ph}^{ij} = \frac{\int d\mathcal{P} \, \frac{d\sigma}{d\mathcal{P}} \Theta_p\left(\mathcal{P}\right) \Theta_h\left(\mathcal{H}\left(\mathcal{P}\right)\right) \Theta_{\mathrm{hard}}^{i}\left(\mathcal{P}\right) \Theta_{\mathrm{hard}}^{j}\left(\mathcal{H}\left(\mathcal{P}\right)\right)}{\int d\mathcal{P} \, \frac{d\sigma}{d\mathcal{P}} \Theta_p\left(\mathcal{P}\right) \Theta_{\mathrm{hard}}^{i}\left(\mathcal{P}\right)} \; . \tag{5.55}$$

The binned distribution in the region given by Θ_{hard} can then be calculated as

$$\Delta\Sigma_{\mathrm{HL}}^{b} = \sum_{r=1}^{n_{\mathrm{hard}}} \sum_{i=1}^{n} \sum_{p} \mathcal{T}_{pb}^{ir} \, \Delta\Sigma_{\mathrm{res/match}}^{p,i} \; , \tag{5.56}$$

where $\Delta\Sigma_{\mathrm{res/match}}^{p,i}$ denotes the resummed or matched result for bin b in region i.

The transition matrices can easily be calculated from Monte Carlo simulations if events are accessible at different stages of the simulation. It should be noted that they of course still depend on the model used to derive them, however in a milder way than the ratios. The matrices are based on the conditional probabilities for transitions between bins, and only depend on the parton shower insofar as it determines what exact phase space those probabilities are averaged over.

Case studies

In this final chapter, several studies shall be presented to illustrate the use of the tools developed in the previous sections. Most of the results have been published, in Refs. [I-V]. The phenomenological studies in those references were accompanied by theoretical and technological advancements of the tools described in the previous sections. The focus in this chapter will be on the methods used in the particular cases, like the concrete choices of phase space cuts, scales and other ambiguities, and the final phenomenological results and conclusions. This will naturally to a large extend be paraphrasing the descriptions and summaries of the relevant sections in Refs. [I-V]. However, particular emphasis will be given to the details that are directly connected to the developments within this thesis. The typical structure of the analyses performed in those studies is a division between an analytical calculation and a Monte Carlo study based on general purpose event generators. Comparisons to Monte Carlo studies form an important step in the interpretation of the results obtained, in particular in the cases where no measurement exists yet to compare to. Simulations using SHERPA at various levels of accuracy were routinely performed within the work of this thesis. A detailed Monte Carlo study, investigating also the differences to other generators, was contributed to Ref. [I]. Hence, in the corresponding Sec. 6.1 the used generators and performed simulations will be introduced in more detail. Ref. [II] used a similar setup as Ref. [I] for the SHERPA simulation. The other event generator results were usually contributed by collaborators and will only be discussed as far as they are necessary for the interpretation of the resummed and fixed order results or provide motivation or justification for choices made in the semi-analytic calculation. An exception to this is Sec. 6.4, where, deviating from Ref. [IV], hadronisation corrections are extracted from SHERPA using the method described in Sec. 5.6. The results are also extended to the dijet case here. Hence a dedicated simulation was performed in the context of this thesis. If some parts of the studies were contributed solely by the other collaborators, but still need to be included here for context, this is of course indicated, which should however not be taken as a claim that the other parts would not be the result of a collaborative effort.

6.1 Soft drop groomed thrust at the Large Electron Positron collider

Ref. [I] studies an extension of the thrust event shape, as introduced in Sec. 3.1, that includes the effects of the soft drop procedure described in Sec. 3.3. The precise definition of the observable is as in Eq. (3.31). The resummation of soft drop thrust in the $e^+e^- \to$ jets process was already presented in Ref. [138] in this case. The fixed order calculation there was performed using EVENT2[1]. Ref. [I] rather focused on studying the potential of this observable to improve the accuracy of the determination of the strong coupling constant. No measurement of soft drop thrust was performed at LEP, or any earlier collider for that matter since soft drop was only introduced into the literature in [135], well after the last run of LEP. Because of this, the investigation is based on pseudo data generated from SHERPA. This section will focus mainly on the event generator methodology, to also serve as exemplary for the equivalent Monte Carlo studies accompanying the later results.

Motivation

As the previous chapters indicated, the strong coupling constant α_s is a primary input to all theoretical efforts in perturbative QCD. There are various ways to determine its value. The most precise input actually is not entirely from pQCD but is based on lattice QCD calculations [329–334]. Apart from that, fits of event shape distributions measured at e^+e^- colliders play an important role [335–344]. The value recommended by the Particle Data Group (PDG) is $\alpha_s \left(M_Z^2 \right) = 0.1179 \pm 0.0010$ [30]. This result is strongly determined by the above mentioned lattice calculations. Fits to collider data often suffer from larger uncertainties. One of those uncertainties comes from the unknown, or at best estimated, effect of the non-perturbative parton to hadron transition.

The size of this contribution is illustrated in Fig. 6.1, where a measurement of thrust by the ALEPH collaboration [345], performed at LEP at a center of mass energy of 91.2 GeV, is compared to predictions from SHERPA and the analytic calculation. Details on the SHERPA simulation can be found in the next subsection. It is performed once without non-perturbative corrections (Parton Lev.), and with two different hadronisation models, the cluster (Cluster Frag.) and the Lund (Lund Frag.) fragmentation model. The lowest panel illustrates the ratio from the parton level to the two predicted hadron

---

[1]I am grateful to my collaborators on Ref. [I] for handling this, as well as the minor changes implemented with respect to the calculation in Ref. [138]
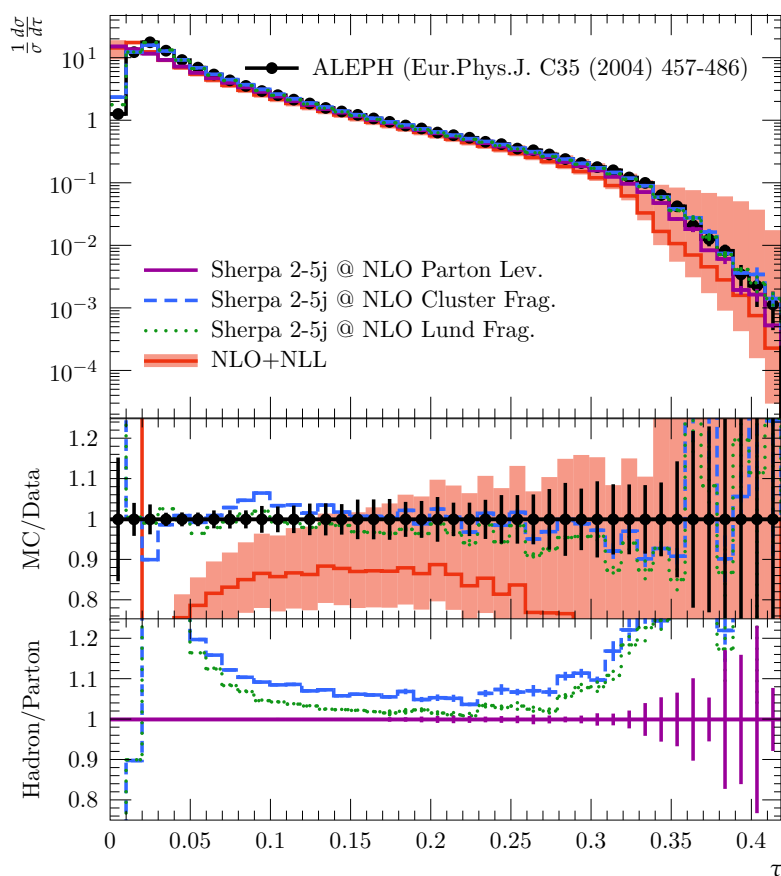
Figure 6.1: Plain thrust distribution as measured by ALEPH compared to SHERPA at parton level and with Cluster and Lund fragmentation, and compared to the nominal resummed distribution matched to NLO. The lower panel shows the hadronisation corrections as obtained from SHERPA with the two fragmentation models MEPS@NLO with up to 5 jets at NLO.
Figure and caption taken from Figure 2 of Ref. [I].

levels, indicating that corrections are $\geq 20\%$ for $\tau < 0.05$, making a fit in this region unpractical. For larger values of thrust, the corrections become smaller and can be as small as $\mathcal{O}(1\%)$ for some bins. This is however with a relatively strong dependence on the hadronisation model used, with the Cluster model generally predicting larger corrections, at best $\mathcal{O}(5\%)$. As the middle panel in Fig. 6.1 clearly shows, the Monte Carlo predictions with either fragmentation model are in good agreement with the ALEPH data over the full range, whereas the central value NLO + NLL calculation is at significantly lower values which would need to be compensated by non-perturbative corrections. As discussed and illustrated in Sec. 3.3 and Sec. 4.5, soft drop grooming has the potential to significantly reduce those corrections. While thrust without soft drop

can and has been computed to high perturbative accuracy, NNLO + N^{3}LL [340, 346], this study is focused on exploring the viability of performing a fit with soft drop thrust and the extend to which non-perturbative uncertainties are indeed reduced.

Methods

The soft drop procedure and the subsequent calculation of the thrust observable was implemented using the RIVET [347] package and relying on FASTJET for the jet clustering, *cf.* Sec. 3.2. A selection of soft drop parameters,

$$z_{\text{cut}} \in \{0.05, 0.1, 0.2, 0.33\}, \tag{6.1}$$

$$\beta \in \{0, 1, 2\} , \tag{6.2}$$

is studied. The soft drop thrust distribution is binned in the same way as the ALEPH thrust measurement [345]. Based on fits performed for plain thrust [340, 346], the range

$$0.06 \leq \tau_{\text{SD}} < 0.25 \tag{6.3}$$

is considered. The upper boundary is chosen relatively low since the analysis is only performed at NLO accuracy instead of NNLO in [340, 346]

To simulate the primary Monte Carlo samples, SHERPA version 2.2.5 was used. As the perturbative input, final states with different parton multiplicities were generated for an e^+e^- collider at a center of mass energy of $\sqrt{s} = 91.2$ GeV, and merged with the MEPS@NLO method in the standard CSSHOWER in SHERPA. The required hard matrix elements were calculated with the matrix element generators provided with SHERPA, AMEGIC and COMIX , and virtual amplitudes obtained from OPENLOOPS version 1.3.1. See Sec. 3.5 for an overview of those methods and tools and the corresponding references.

Hadronisation corrections for the SHERPA samples were modelled with the default cluster hadronisation, and with the Lund fragmentation model from PYTHIA 6.4. To optimally fit the available reference data from LEP, the strong coupling was set to

$$\alpha_{\text{s}}\left(M_Z^2\right) = 0.117 . \tag{6.4}$$

The main parameters of the Lund model were set to values that gave the best description of data from Ref. [345],

$$a = 0.3 \text{ (PARJ(41))}, \qquad b = 0.6 \text{ GeV}^{-2} \text{ (PARJ(42))}, \tag{6.5}$$

$$\sigma = 0.36 \text{ GeV (PARJ(21))} .$$

To validate the size of the hadronisation corrections that are expected for soft drop thrust, several additional Monte Carlo samples were obtained. The angular-ordered parton shower implemented in HERWIG 7.1.4 was used, as well a the default parton shower in PYTHIA 8.235 with the Lund fragmentation model. In addition, the SHERPA implementation of the Dire parton shower was used, with otherwise the same setup as described above for SHERPA. See Sec. 3.5 for a more detailed overview of the various tools.

This test was performed based only on LO $2 \rightarrow 2$ matrix element as input to the various parton showers and fragmentation models. The main reason for this is the large number of different generators studied and the longer computation times required for matched and merged calculations. It is however justified since the goal is mainly to detect differences in the non-perturbative modelling.

It can be verified from Fig. 6.2 that the modelling is consistent within this generator selection. The lower panels of the various plots show the ratios between the full prediction and the parton level of the respective generator. In the central region, they are in all cases of the order of 10%. Another observation is that the difference between the default SHERPA shower with cluster and Lund fragmentation ("Sherpa CS Cluster Frag." and "Sherpa CS Lund Frag.") in most cases, in the central region, covers the full spread of the predictions between the different generators. Based on this observation, the main study is performed using only this shower, and uncertainties associated with hadronisation corrections are obtained by taking an envelope of the predictions based on the cluster and Lund model.

Two different samples were obtained in this SHERPA setup, with a different maximal number of final state partons included in the MEPS@NLO merging. The first sample, with up to 5-jet matrix elements at NLO, intended to be used as pseudo-data for the fits of the analytic calculation. Results from this sample were already previewed in Fig. 6.1, validating its use in this scenario.

While the Monte Carlo can be run relatively quickly to produce basically arbitrary statistical precision, an experimental analysis might not achieve that, in particular not a reanalysis of the existing LEP data. In addition, the systematic uncertainties that might be present due to for example detector effects are not represented in the Monte Carlo at all. In order to obtain a realistic set of pseudo data, the central values were taken from the SHERPA sample mentioned above. They supplied a correlation matrix between bins i and j

$$V_{ij} = \delta_{ij} s_{\text{stat}}^2 + \min\left(s_{\text{sys},i}^2, s_{\text{sys},j}^2\right) \tag{6.6}$$
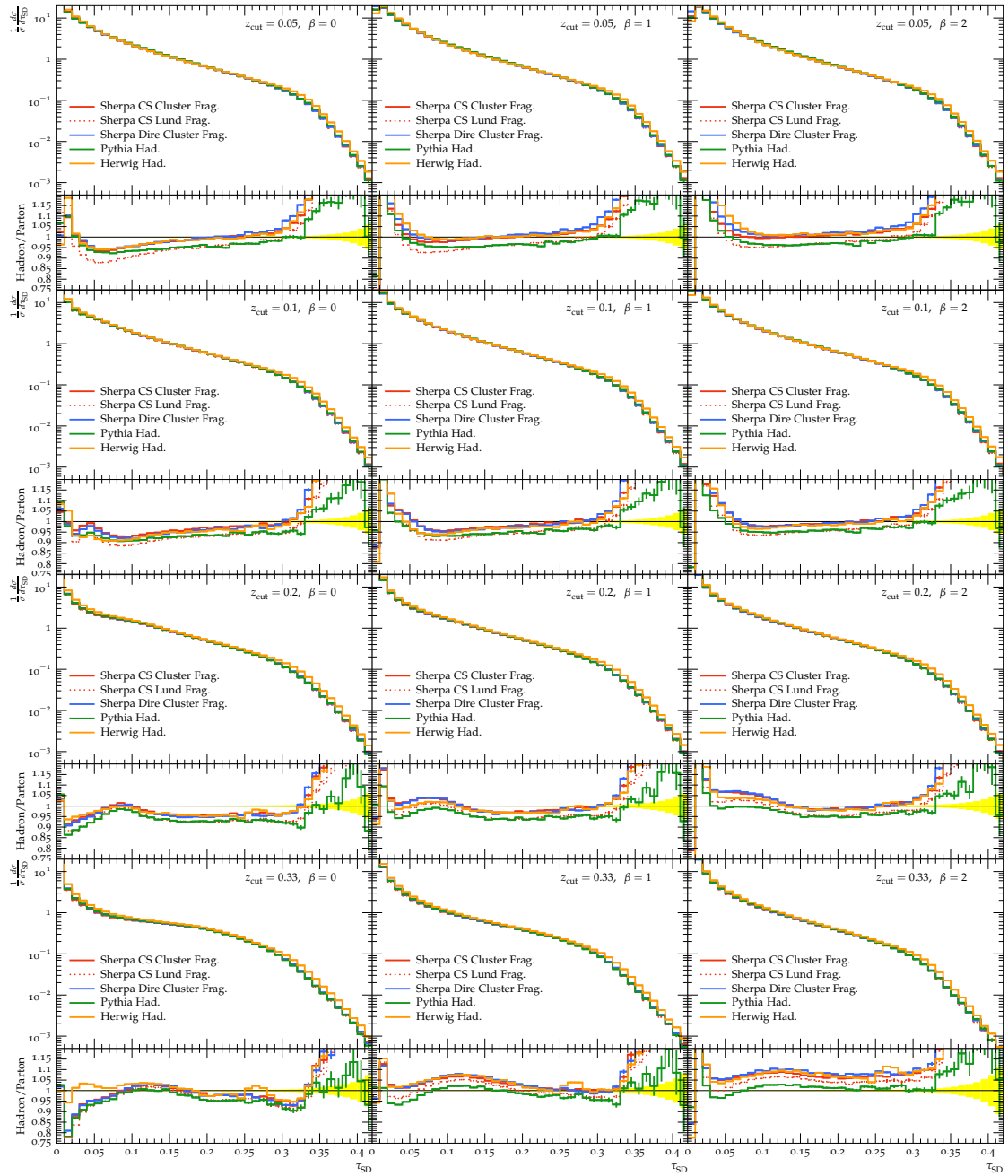
Figure 6.2: Predictions from general-purpose Monte Carlo generators for soft drop thrust with various z_{cut} and β values at parton shower accuracy. Shown are nominal distributions at hadron level and the ratios of hadron level to the respective and underlying parton level predictions.
Figure and caption taken from Figure 11 of Ref. [I].

obtained from the ALEPH measurement of plain thrust, according to

$$s_{\text{stat}} = s_{\text{stat}}^{\text{ALEPH}} \sqrt{\frac{d\sigma^{\text{MC}} / d\tau}{d\sigma^{\text{ALEPH}} / d\tau}} \tag{6.7}$$

$$s_{\text{sys}} = s_{\text{sys}}^{\text{ALEPH}} \,. \tag{6.8}$$

That is, the systematical uncertainties s_{sys} correspond to the ALEPH ones, while the statistical uncertainties s_{stat} are rescaled by the change in bin height, reflecting the changed number of events N in that bin, assuming that the error will scale Poisson-like $s \propto \sqrt{N}$.

The analytic calculation is fit against these pseudo data by minimising the χ^2 function defined by

$$\chi^2 = \sum_{i,j} \Delta_{ij} V_{ij}^{-1} \Delta_{ij} \,, \tag{6.9}$$

where the sum is over the pairs of bins i, j and the difference between (pseudo-)data and theoretical values, normalised to the respective inclusive cross section, given by

$$\Delta_{ij} = \left(\frac{1}{\sigma} \frac{d\sigma}{d\tau} (\tau_i) \right)_{\text{exp}} - \left(\frac{1}{\sigma} \frac{d\sigma}{d\tau} (\tau_i) \right)_{\text{th}} \,. \tag{6.10}$$

The second sample has up to 3 hard matrix element jets. It was used to obtain hadronisation corrections for the analytic calculation. This was in this instance done by simply taking the ratio between hadron and parton level Monte Carlo and multiplying the analytic calculation by that ratio, *cf.* Eq. (5.45). The difference between using the ratios of the cluster and Lund models is entered as an uncertainty into the fit, in addition to the other theoretical uncertainties.

This is significantly simpler than the procedure advertised in Sec. 5.6 using a transition matrix. However, in this case the measurement is relatively inclusive, in the sense that all events contribute to the histogram somewhere and there is no way for hadronisation corrections to push the events out of the measurement region, or into it from the outside. Additionally, in the region where the fit is ultimately performed, the correction in particular for the groomed observables are not that large anyway, and one might expect to get the same result from the two methods, using a transition matrix or a ratio, anyway. That this is indeed the case is illustrated in Fig. 6.3, where those two methods are applied to the analytic calculation using hadronisation corrections from the cluster model. Different values of α_{s} are shown to illustrate that this statement does not depend on its value.
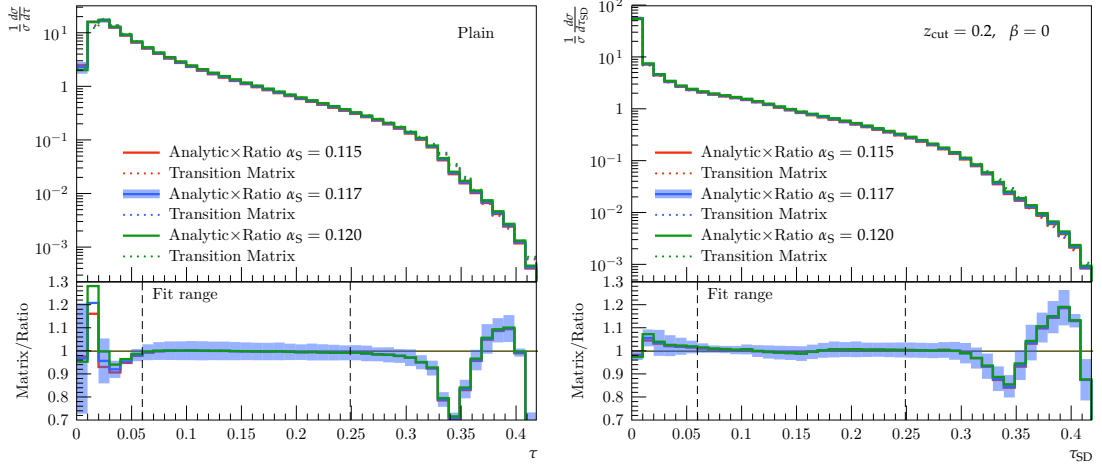
Figure 6.3: Comparison of different methods to apply hadronisation corrections obtained from Monte Carlo to the analytic calculations, for plain thrust (left) and soft-drop thrust (right) with $z_{\text{cut}} = 0.2, \beta = 0$. The corrections are obtained from simulations at parton shower accuracy and are applied either by multiplying the analytic calculation at various α_s values by the ratio from Monte Carlo, as described in the main text (solid) or alternatively by applying a bin-by-bin transition matrix obtained from the same Monte Carlo run (dotted). The cluster hadronisation model is used in all cases, the blue band indicates the uncertainty assigned to the calculation for $\alpha_s = 0.117$ based on the difference to using the Lund model. The bottom panel shows the ratio between the distributions using the two methods for equal values of α_s.
`Figure and caption taken from Figure 12 of Ref. [I].`

An implicit assumption in obtaining hadronisation corrections as ratios from Monte Carlo, as mentioned in Sec. 5.6, is that the analytic calculation and the parton level of the generator should not be too different. Otherwise, one would need to conclude that significantly different effects are missing in the respective perturbative inputs, which would inevitably to some extend be absorbed into different hadronisation corrections. At any rate, the practical performance would likely suffer from too big of a miss match. For this reason, a comparison is presented in Fig. 6.4. The ratio between analytic calculation and Monte Carlo prediction for the parton level is flat for most choices of z_{cut} and β over a large range corresponding to the fit region, *cf.* Eq. (6.3). This validates the use of hadron to parton ratios for the purpose of this study.

In Ref. [I], an additional analytic approach to hadronisation correction was explored, based on earlier work in [141, 309, 322]. This model includes an additional parameter Ω,
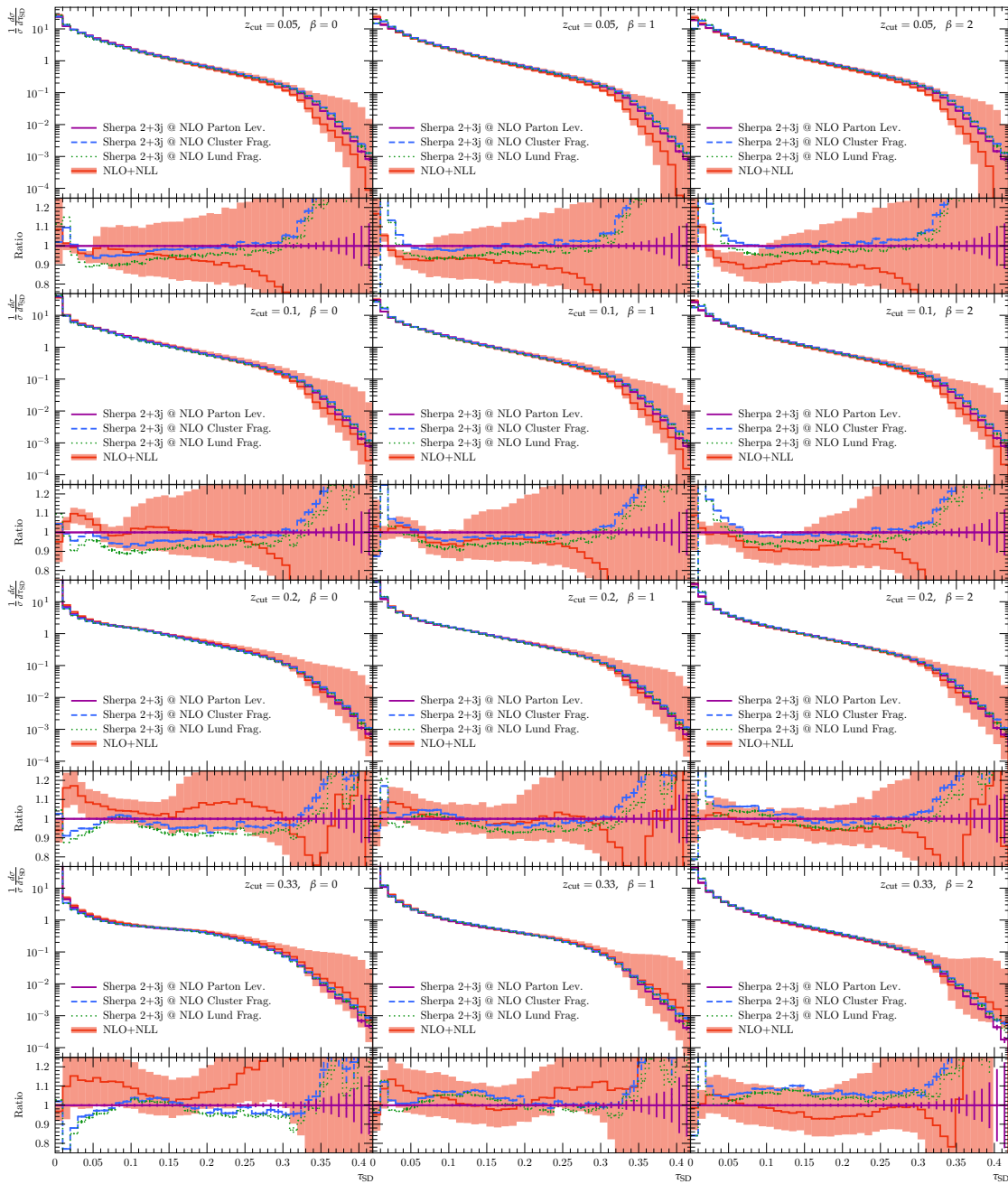
Figure 6.4: Comparison of NLO + NLL matched predictions for soft-drop thrust to SHERPA MEPS@NLO simulations with up to 3 jets at NLO at parton level and with cluster and string fragmentation applied.
Figure and caption taken from Figure 3 of Ref. [I].

representing an energy scale for non-perturbative physics. This was fit simultaneously with α_s, while the Monte Carlo based model only has one free parameter.

Results

The resulting values of α_s from performing fits to the pseudo data are illustrated in Fig. 6.5. In each sub-figure, the points from the left to right correspond to fits based on predictions of increasing accuracy, first only at NLO fixed order (FO), then including the effects of resummation (Res) and finally with the two versions of taking into account non-perturbative corrections (NP (MC) and NP (ana)). The three plots show the different β values and all contain the same result for plain thrust, i.e. thrust without grooming, in black and the result for the respective β value with different z_{cut} according to the coloured legend.

A significant impact is visible from including the resummation, i.e. in going from the "FO" to the "Res" column. This is true for ungroomed and groomed thrust, though somewhat reduced for the most aggressive choices of grooming parameters at $\beta = 0$. In the groomed case, the effect of additionally including non-perturbative corrections is generally reduced compared to the ungroomed case. The uncertainties are however not observed to reduce significantly.

Fitting the plain thrust to the pseudo data leads to a central value of $\alpha_s(M_Z^2) = 0.1248$. The values obtained with smallest z_{cut} value considered here are consistent with that, ranging from $\alpha_s(M_Z^2) = 0.1211$ for $\beta = 0$ to $\alpha_s(M_Z^2) = 0.1305$ for $\beta = 2$. With increasing z_{cut}, the best fit value is generally decreasing for a given value of β. The smallest central value is obtained for $\beta = 0$ with $z_{cut} = 0.2$ and $z_{cut} = 0.33$, where in both cases the best fit is obtained for $\alpha_s(M_Z^2) = 0.111$. As can be read of from Fig. 6.5, the results are all consistent with each other when taking into account the uncertainties.

The overall picture seen for the Monte Carlo based hadronisation corrections is confirmed by the analytic model, however with some exceptions and outliers. Generally, the best fit values tend to be smaller than what is obtained for the equivalent grooming parameters using hadronisation corrections from Monte Carlo. As this model is not the main point of consideration here, it shall just be mentioned that, after Ref. [I] appeared, a different approach to include hadronisation corrections in soft drop groomed observables has been published in Ref. [327]. Developments along those lines might lead to a more consistent picture in the future.
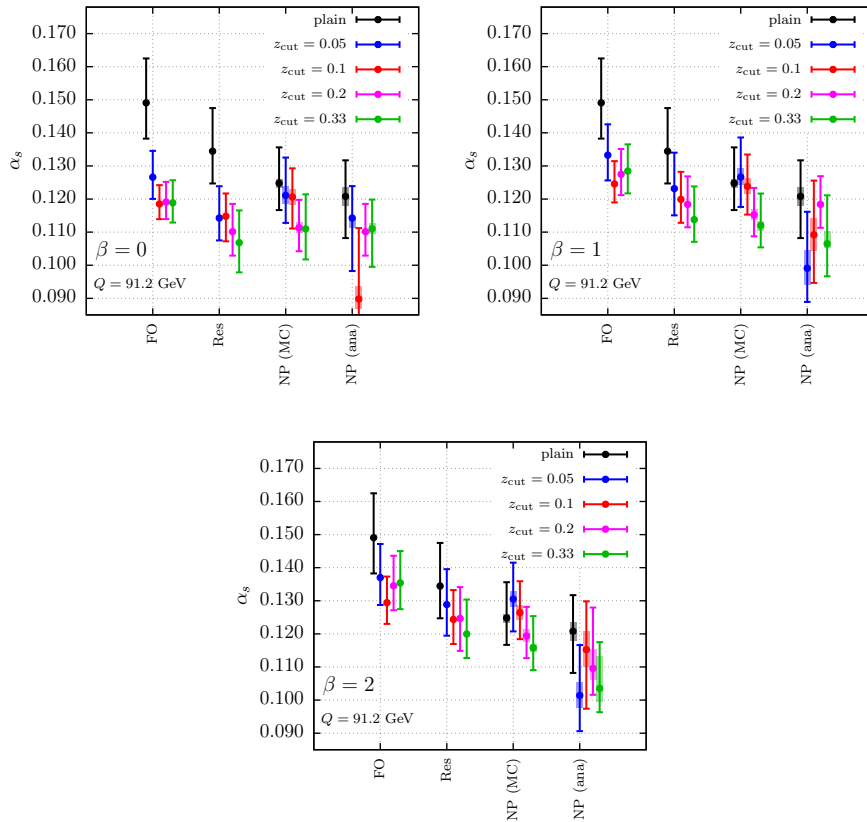
Figure 6.5: Results for fits of $\alpha_s\left(M_Z^2\right)$ to Monte Carlo pseudo data using theoretical predictions at different levels: FO for NLO, Res for NLO+NLL and NP for the inclusion of non-perturbative effects. The non-perturbative effects are modelled based on either the Monte Carlo based hadron-to-parton level rations (NP (MC)) or an analytical model with a single parameter Ω (NP (ana)). The band indicates the total uncertainty, the shaded region displays the hadronisation-related uncertainty.
Figure and caption taken from Figure 6 of Ref. [I].

As a final point, Fig. 6.6 illustrates analytical predictions using the best fit value of α_s for the respective distribution, for the full selection of soft drop parameters β and z_{cut}, compared to the generated pseudo data. It is evident that the best fit predictions are indeed in excellent agreement with the data they are based on, indicating a high quality of the fits. Stronger deviations are visible for larger values of τ_{SD}, where fixed order corrections become important.
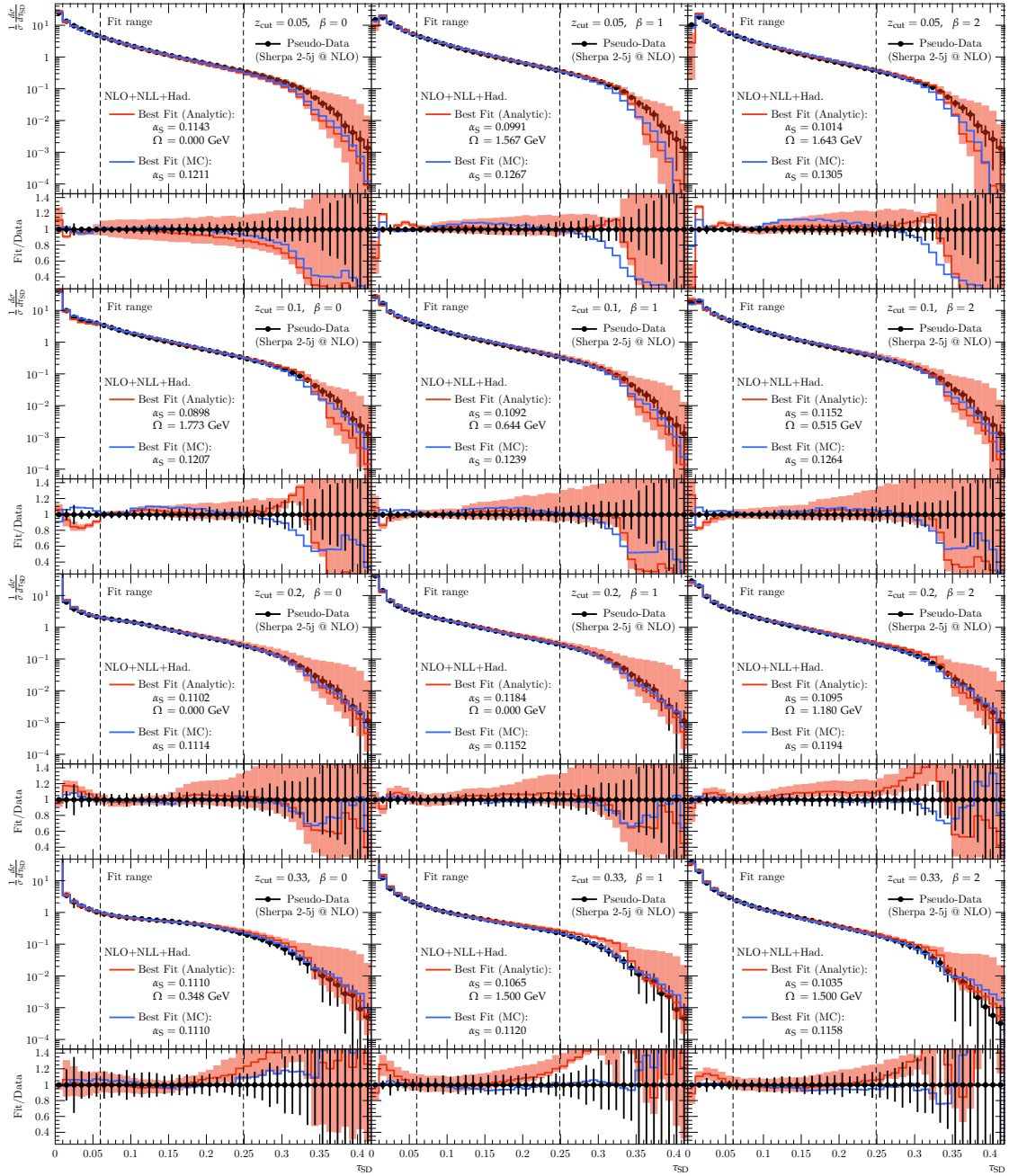
Figure 6.6: Pseudo data (SHERPA MEPS@NLO $2-5$j) and NLO $+$ NLL results with best-fit values for $\alpha_s\left(M_Z^2\right)$ and the analytic (red) and Monte Carlo (blue) hadronisation corrections. Uncertainties of the pseudo data are determined by rescaling of the uncertainties for the ALEPH ungroomed thrust data. Figure and caption taken from Figure 8 of Ref. [I].

6.2 Multi-jet rates at the Large Electron Positron collider

The results in this section are based on Ref. [II]. The goal is to explore the colour structures arising at high jet multiplicities in e^+e^- annihilation. This is achieved by studying the jet resolution scales, y_{ij}, as defined in Eq. (3.25), for the Durham k_t cluster algorithm. The study is performed at a center of mass energy of the collider corresponding approximately to the Z pole mass ≈ 91.2 GeV. They are particularly suited for this, as their definition is easily extended to various multiplicities.

Motivation

Durham jet resolution scales are an important and interesting observable used in QCD phenomenology. They are actively used in event generator tuning and validation [348, 349], and formed an integral part of the LEP program [350, 351]. In particular the three jet resolution scale y_{23}, like thrust in the previous section, is heavily used in the context of α_s extractions [338, 339, 342, 352], likewise are simultaneous fits to higher jet resolution scales [353].

For the three jet scale, calculations are available at high accuracy of NNLO+NNLL [354], achieved in the ARES [355, 356] extension of the CAESAR formalism used in this thesis. The focus here will however be on reaching NLL accuracy for the higher multiplicities, where studies are limited to fixed order calculations at NNLO, while the resummation accuracy is limited [99, 348].

A special motivation to explore higher multiplicities are the presence of non-trivial colour correlations in this case, as compared to the case with 2 partons in the Born process. This is of particular interest in the light of attempts to include such corrections in parton shower algorithms. Those algorithms conventionally work formally by neglecting corrections in $1/N_c$. Recent developments to go beyond that include [357–365] as well as Ref. [VI]. The results presented here can be useful as benchmarks for such improved algorithms and to gauge whether the subleading colour corrections explored in those works can be expected to be the dominant effects missing in conventional parton showers, at least for the jet rates as defined here. A particular emphasis will hence be put on also deriving predictions in the large N_c limit.

Methods

The goal here is to study the n-jet rate as a deviation from a final state with $n-1$ hard jets. To achieve this, the phase space is restricted by requiring

$$y_{n-1,n} > y_{\mathsf{cut}} = 0.02 \ . \tag{6.11}$$

The choice of y_{cut} is a compromise, with a too large cut reducing the cross section significantly, while a too small cut would compromise the stability and validity of the calculation.

A complication relative to the calculation of an observable vanishing in the two jet limit is the fact that there are potentially a lot more different physical scales involved in a multijet process. This is of course somewhat negated by the requirement of y_{cut} above, but still just setting all scales to $Q = \sqrt{s}$ as one would do in $e^+e^- \to q\bar{q}$ seems too simplistic. This is a problem well explored in the context of merging prescriptions for parton showers. The strategy here is to mimic the CKKW prescription as described in Sec. 3.5. The relevant picture is that of a forward evolution from a 2 parton final state, where subsequent emissions happen at scales corresponding to their relative transverse momenta, which are estimated by the Durham jet resolutions of lower multiplicities. This leads to

$$\alpha_{\mathsf{s}} \left(\mu_R^2\right)^{n-2} = \alpha_{\mathsf{s}}\left(y_{23}Q^2\right) \cdot \cdots \cdot \alpha_{\mathsf{s}}(y_{n-1,n}Q^2) \ . \tag{6.12}$$

For the purpose of setting the scale in the resummed calculation, Eq. (6.12) can be solved analytically assuming leading order running. In terms of the scale set by the Landau pole, *cf.* Eq. (2.36), one obtains

$$\mu_R^2 = \Lambda_{\mathsf{QCD}}^2 \exp\left[\frac{\prod_{i=3}^{n}(1-\lambda_i)^{1/(n-2)}}{\alpha_{\mathsf{s}}\beta_0}\right] \ , \tag{6.13}$$

with $\lambda_i = \alpha_{\mathsf{s}}\beta_0 \ln y_{i-1,i}$ corresponding to the various resolution scales present in the hard part of the event. The resummation scale is assumed to be set by the smallest resolution scale of the Born jets, i.e.

$$\mu_Q^2 = y_{n-1,n}Q^2 \ , \tag{6.14}$$

for the resummation of $y_{n,n+1}$. This reflects the picture of subsequent emissions, where a potential evolution would have started with the two parton kinematics and continued until that scale.

The procedure described in Sec. 5.1, in particular Eq. (5.2) is used to set x_v. Since d_l is the same for all legs l, $d_l = d$, this means $x_v = d = y_{n-1,n}$. At last, the endpoint in Eq. (5.1) is set to

$$y_{\mathsf{max}} = \min(y_{\mathsf{kin}}, y_{n-1,n}) \ , \tag{6.15}$$

with y_kin the maximal kinematic value of $y_{n,n+1}$. The second condition requires that the new jet is indeed at a smaller scale the previous ones, $y_{n,n+1} < y_{n-1,n}$, for scale choices where this is not trivially the case.

The results presented, here and in Ref. [II], are for y_{34}, y_{45} and y_{56}, i.e. the 4-, 5- and 6-jet resolution scales, at a center of mass energy of $\sqrt{s} = 91.2$ GeV. Uncertainties are estimated by varying μ_R, μ_Q as well as p from Eq. (5.1), by factors of 0.5 and 2. Those variations are carried out independently and the final uncertainty is obtained by considering the envelope of all predictions. The LogR scheme Eq. (5.42) is used to match the resummed predictions to the fixed order calculation at LO and NLO. The difference to other matching schemes, such as the multiplicative scheme, was found to be negligible relative to the uncertainties considered, hence no specific uncertainty for the matching is included in the final results.

These results are compared against state of the art Monte Carlo predictions at parton level. SHERPA was used to merge simulations both at MEPS@LO and MEPS@NLO accuracy, with the LO calculation including up to 5-parton matrix element. The NLO sample includes one-loop corrections for the 2,3 and 4 parton final state, and additionally the 5 parton matrix element tree level. In both cases, the merging parameter Q_cut, *cf.* Sec. 3.5, is set to

$$\frac{Q_\text{cut}^2}{E_\text{CMS}^2} = 10^{-2} \; . \tag{6.16}$$

Hadronisation corrections in SHERPA were modelled in the default cluster model implemented in SHERPA and via the string fragmentation model as implemented in PYTHIA 6.4. Additional Monte Carlo samples were produced using PYTHIA 8 with the VINCIA antenna shower. It is matched to matrix elements obtained from MADGRAPH including up to 3 final state partons at one-loop accuracy and emissions leading to matrix final states with up to 6 partons are corrected to the exact LO matrix elements via matrix-element corrections. The matching scale regularising the higher multiplicity matrix elements, with 5 and 6 final state particles, was set to

$$\frac{Q_\text{match}}{E_\text{CMS}} = 0.05 \; . \tag{6.17}$$

Non-perturbative corrections in this case are obtained via the standard Lund model in PYTHIA 8.

See Sec. 3.5 for an overview of the event generation methods and the corresponding references.

Results

Fig. 6.7 shows the main outcome of this calculation, at LO + NLL' (greed dashed line) and LO + NLL' (red solid line) accuracies. The yellow band illustrates the theoretical uncertainty, determined from scale variations as described in the previous section, of the LO matched calculation. This is significantly reduced when considering the calculation matched to NLO, as the orange band shows.
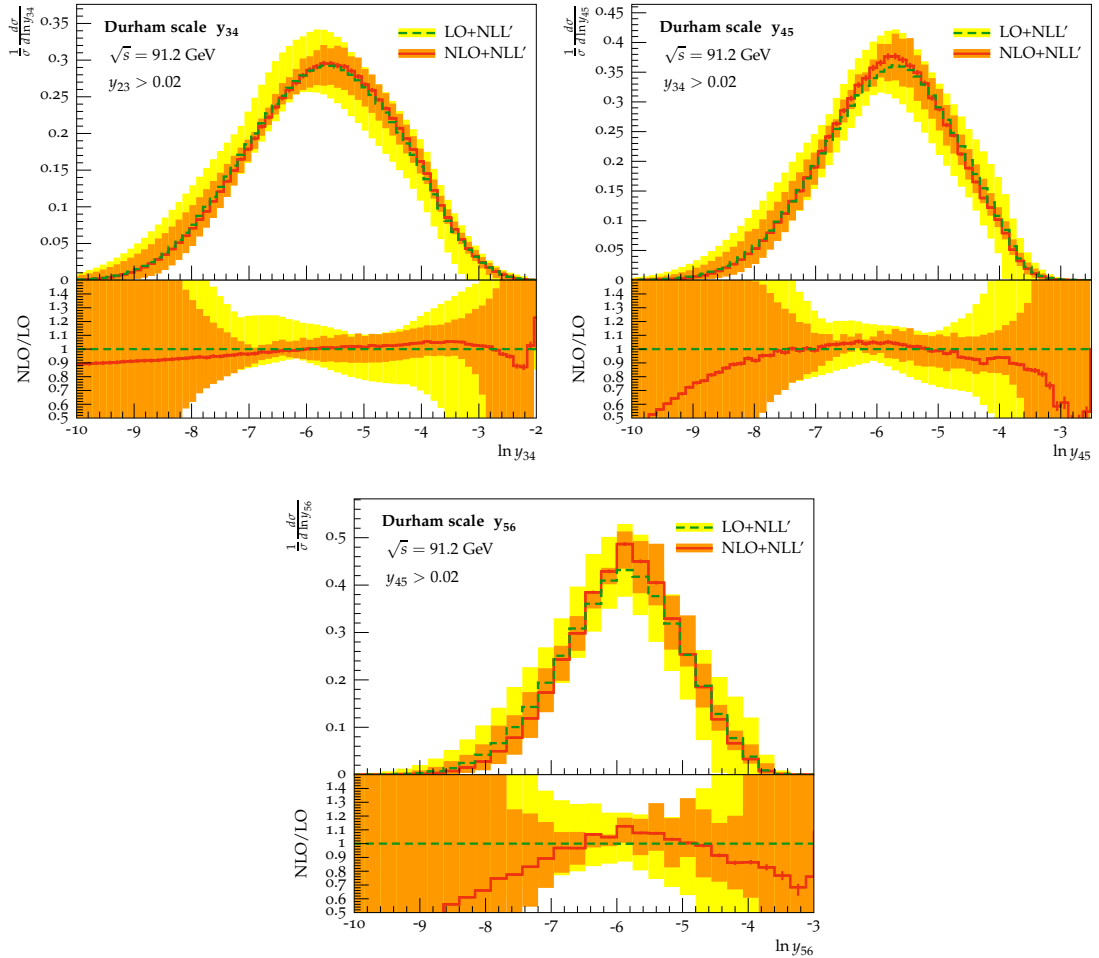
Figure 6.7: Resummed predictions for the Durham jet-resolutions y_{34}, y_{45}, y_{56} in electron-positron annihilations at $\sqrt{s} = 91.2$ GeV. The lower panels show the local NLO K-factor.
Figure and caption taken from Figure 4 of Ref. [II].

This reduction of uncertainties holds for the peak region of all three distributions. In this region, the effect of the NLO corrections on the central value is rather small in all
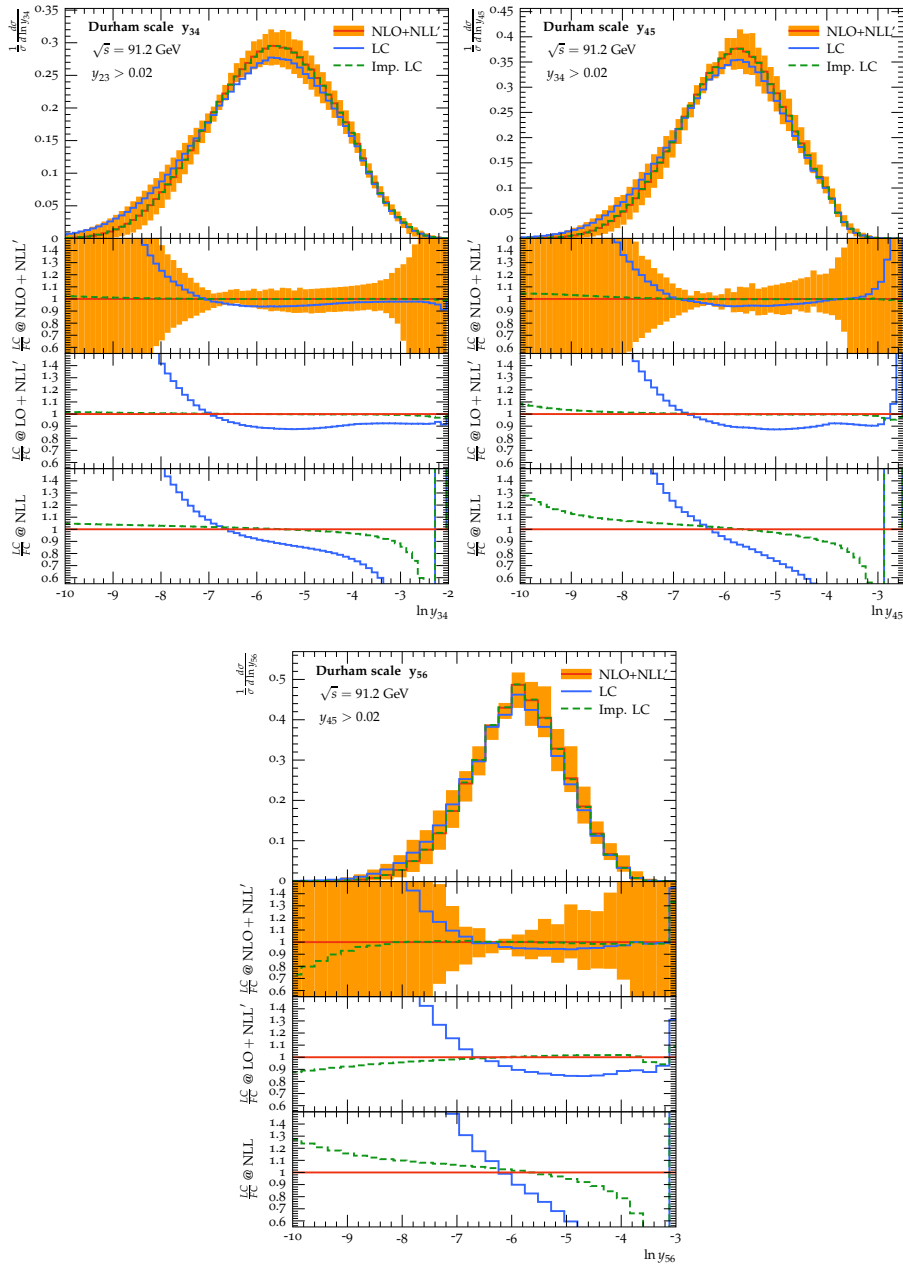
Figure 6.8: Durham splitting scales $y_{n,n+1}$ at NLO + NLL' accuracy, in the $N_C \to \infty$ limit, and in the improved LC scheme. The lowest panels show the corresponding ratios additionally at LO + NLL' accuracy and for the resummation without any matching.

Figure and caption taken from Figure 6 of Ref. [II].

cases, such that the main effect is indeed the reduction in uncertainty. For y_{34}, this statement holds for the whole region where the distribution is appreciably different from zero. For the higher multiplicities, the NLO corrections are larger away from the maximum of the distribution. This is in particular in the region where the kinematic endpoint is approached. In any case, the NLO matched prediction stays within the LO uncertainty band, consistent with overall convergence of the perturbative series.

Fig. 6.8 aims to asses the effect of subleading colour corrections. Apart from the strict t'Hooft large-N_C limit, this includes the improved large-N_C scheme described in Sec. 5.1. The three ratio plots are calculated for the two different colour approximations, with respect to the full prediction, at different levels of perturbative accuracy. The strict $N_C \to \infty$ limit indeed appears to imply a rather strong effect on the NLL result, illustrated in the lowest panels in Fig. 6.8. Already here however, the deviation between the full colour and improved leading colour results is rather small, in particular for y_{34} away from the endpoint region. For the higher multiplicity jet rates, larger effects are still visible at this accuracy.

After including LO and NLO matching in the middle two panels however, the improved leading colour scheme agrees with the full colour calculation for all multiplicities considered here to within a few percent. The only exception to this statement is the very soft tail of the y_{56} Durham scale. The large effects of taking the full large N_C limit however remain at least with LO matching, only at NLO is the agreement between full colour and strict leading colour within the uncertainty of the full calculation.

As described in the motivating paragraph, one might hope that those observations can guide the further development of parton showers, that traditionally operate in some version of a leading colour approximation. Usually, those approximations are closer to the improved leading colour prescription used here than to the strict t'Hooft $N_C \to \infty$ limit. This indicates that the gain of potentially including subleading colour corrections, and eventually reaching full colour accuracy, might be relatively small for this kind of observable. This is in particular the case since matching and merging in parton showers, as done in the samples used here, is a standard technique, and correspondingly the matched comparisons in Fig. 6.8 are perhaps the more relevant ones.

In any case, the resummed result is shown again together with the results from the SHERPA samples, with merging at LO and NLO, in Fig. 6.9. With regards to the observations in the last paragraph, one notes that the deviations between parton shower and resummed result are neither quantitatively nor qualitatively similar to the full colour corrections. In general, the predictions are in good agreement, considering that no specific uncertainties are determined for the shower but those would have to be assumed
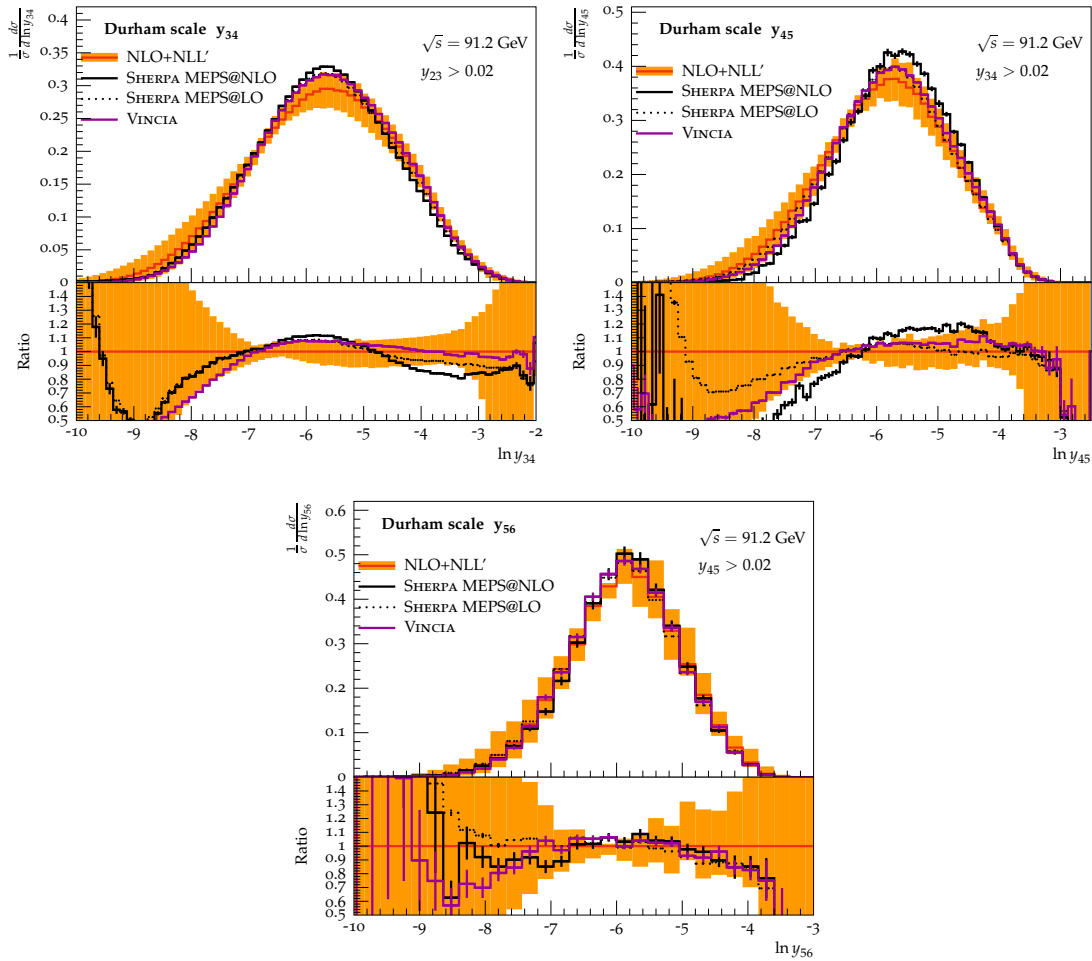
Figure 6.9: Comparison of resummed NLO + NLL′ predictions for y_{34}, y_{45} and y_{56} to parton-level parton-shower simulations from SHERPA and VINCIA [. . .]. Figure and caption taken from Figure 7 (left) of Ref. [II].

to be of a similar size to the uncertainties of the resummation. The additional results from VINCIA support those conclusions.

Since no actual data are available for this particular variation of the Durham jet scales, no hadronisation corrections were obtained in a form that could be applied to the resummed calculation directly. Nevertheless, the qualitative behaviour and general size that can be expected for them can be gauged by comparing the parton and hadron levels of the Monte Carlo samples introduced before. This comparison is shown in Fig. 6.10, with the two options for the hadronisation model in SHERPA as described
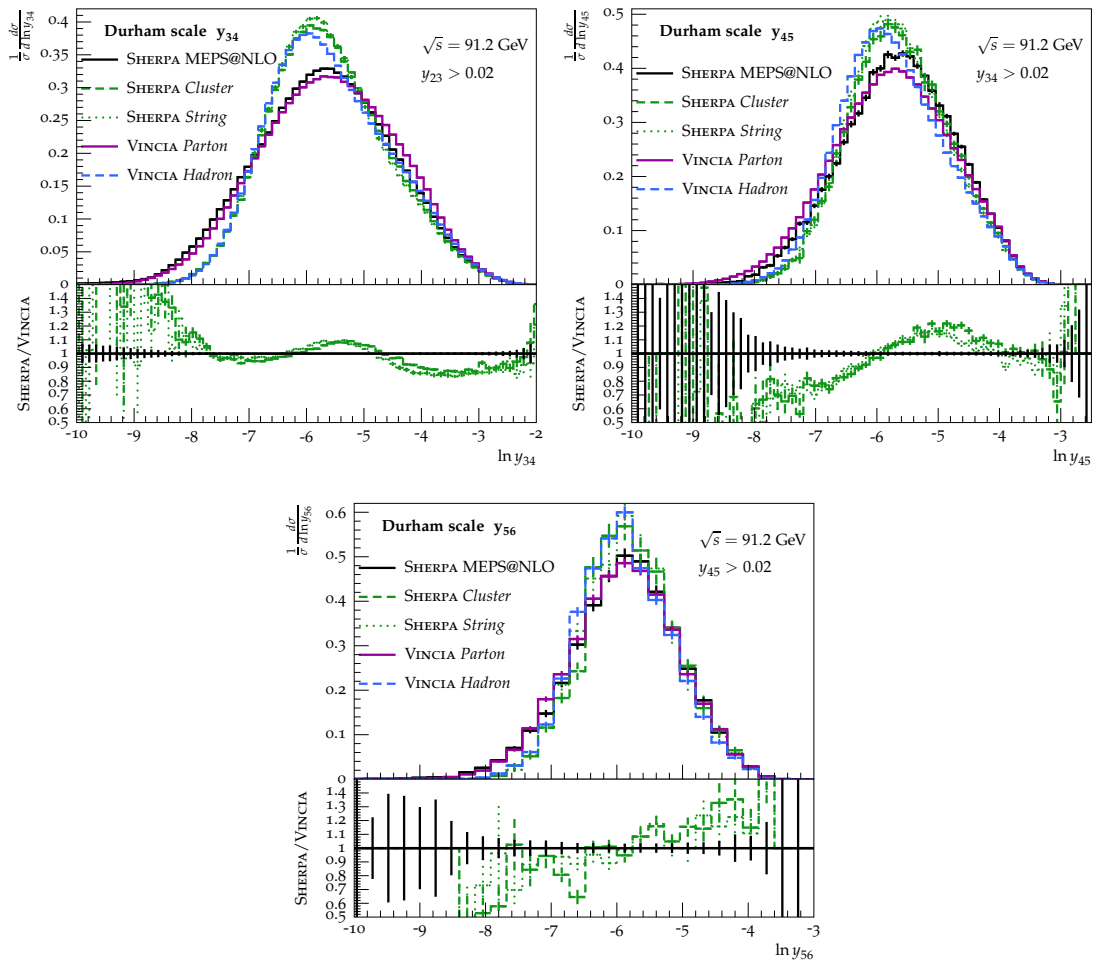
Figure 6.10: Parton shower predictions from SHERPA and VINCIA at parton level compared to the corresponding hadron level results. See text for details. Figure taken from Figure 7 (right) of Ref. [II].

before.

The non-perturbative corrections are certainly non negligible for any of the multiplicities. The modelling is qualitatively similar between SHERPA and VINCIA, although the two models within SHERPA are significantly more similar to each other than to VINCIA. The soft end of the distributions is in all cases significantly suppressed. As one might expect, no large corrections are visible in the hard tail. Overall, this leads to substantially narrower distributions. While there are quantitative differences between SHERPA and VINCIA of the order of 10% up to 20% depending on the region considered, they agree reasonably considering that no uncertainty is estimated in this case.

6.3 Soft drop groomed event shapes at the Large Hadron Collider

The goal of Ref. [III] was to promote the use of soft drop grooming in the study of global event shapes at hadron colliders. This is particularly relevant in the context of potentially measuring those event shapes based on particle tracks. It can be noted that most analyses of event shapes by the LHC experiments, CMS [366, 367] and ATLAS [368, 369], are based on jet momenta. This prescription differs quite a lot from what is assumed in a resummed calculation as it is performed here, making it inapplicable. The treatment of systematic uncertainties is however simplified with jets that just cover a known area in the $\eta - \phi$ plane of the detector. Analyses based on particle tracks are however more susceptible to uncorrelated soft corrections that would be parametrised by the multiple parton interactions (MPI) or underlying event (UE) models in event generators. The idea behind the study in Ref. [III] was to indeed use particle tracks in the definition of the observables but combat those corrections by soft drop grooming.

Motivation

The suffering of global event shapes measured on particle tracks from large non-perturbative corrections is illustrated in Fig. 6.11. The figure shows the transverse thrust, as introduced in Eq. (3.19), obtained from SHERPA at MEPS@NLO accuracy. As before, see Sec. 3.5 for the generator details and references.

The two plots correspond to two different hard energy scales, set by the minimal transverse momentum of the leading jet $p_T^{\text{lead}} > 200$ GeV and $p_T^{\text{lead}} > 500$ GeV. The full phase space is the same as specified later, *cf.* Eq. (6.18) and Eq. (6.19) and the explanation given to them in the text. Naively, the expectation is that events associated with higher energy scales would be affected by non-perturbative corrections less, in accordance with asymptotic freedom. To investigate those effects, the SHERPA sample was analysed at three different levels. At parton level (PL, shown in blue) only the effects of the parton shower are included. The second level also includes the additional particles produced by the underlying event model, this is referred to as PL+UE (red). The full prediction (HL+UE, shown in green) also models the transition from partons to hadrons.

It is clearly visible from Fig. 6.11 that there is a large impact of including the underlying event in addition to the parton shower effects. The distribution receives a significant
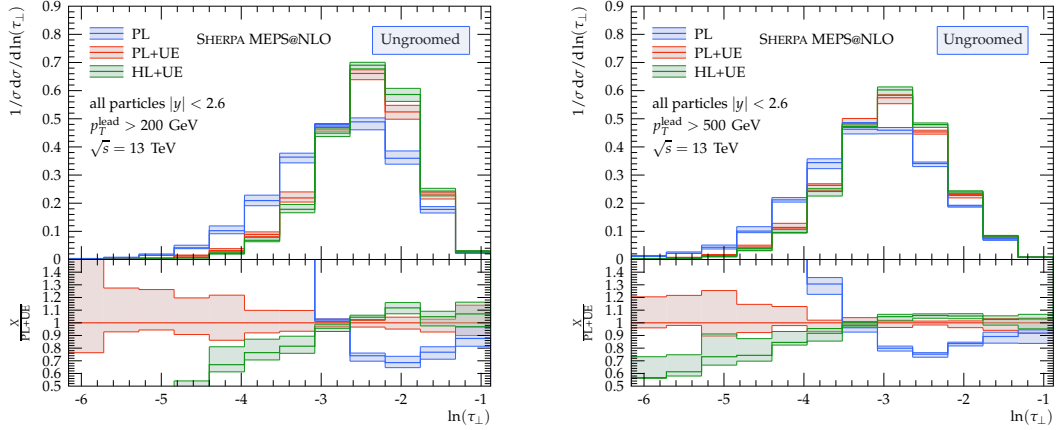
Figure 6.11: The transverse-thrust distributions for events with a leading-jet transverse momentum $p_T^{\text{lead}} > 200$ GeV (left) and $p_T^{\text{lead}} > 500$ GeV (right). [...] Shown are MEPS@NLO predictions obtained with SHERPA at parton level (PL), with the underlying event included (PL+UE), and at full hadron level (HL+UE). The lower panels show the ratios with respect to the PL+UE prediction.
`Figure and caption taken from Figure 1 of Ref. [III].`

shift towards larger values of τ_{SD}. This observation is true for both choices of transverse momentum. The numerical size appears somewhat reduced for the $p_T^{\text{lead}} > 500$ GeV selection. If for example measured by the relative change in the peak height it is reduced from $\approx 30\%$ in the lower transverse momentum selection to $\approx 25\%$. In any case, the underlying event effects can in no sense be treated as a minor correction or uncertainty. Additionally including hadronisation corrections has a much smaller, yet noticeable effect. In the region where most of the overall cross section is distributed, it is limited to $\approx 10\%$, but can be much larger in the soft tail region. Again, the effect is somewhat smaller for the distribution with larger physical scale, but not appreciably different in terms of the qualitative behaviour.

It is clear from this that, if one intends to measure global event shapes on charged particle tracks, non-perturbative corrections and in particular the underlying event need to be either very well understood or mitigated. As a way to avoid them, global event shapes are studied here with the inclusion of soft drop grooming, *cf.* Sec. 3.3 for the method and Sec. 4.4 for the details on the resummation of such observables. A pre-study considered a larger variety of event shapes[2], confirmed that grooming

---

[2]I am grateful to my collaborators on Ref. [III] for conducting this pre-study, that also considered

generally achieves the goal of reducing the impact of the underlying event corrections for sensible choices of the grooming parameters, and settled on transverse thrust, *cf.* Eq. (3.19) and Eq. (3.33) for the version after soft drop, as the main example.

Transverse thrust is one of the standard event shapes studied in hadron-hadron collisions, by both the Tevatron [370] and LHC experiments [366–369]. On the theoretical side, it has been studied as part of automated calculations at NLO [371] and $\mathrm{NLO} + \mathrm{NLL}'$ [279]. Dedicated analyses in soft-collinear effective field theory have reached NNLL accuracy [372, 373]. The extension to a calculation based on a soft drop groomed final state for transverse thrust however is one of the new results, to be presented here and published in Ref. [III].

Methods

The analysis is based on studying event shapes measured in an inclusive dijet selection in proton-proton collisions at a center of mass energy of $\sqrt{s} = 13$ TeV. The phase space is specified by selecting two anti-k_t jets with a radius of $R = 0.4$, *cf.* Sec. 3.2. They are required to be in a central rapidity range,

$$|y_j| < 1 \ . \tag{6.18}$$

The Born type events for the dijet process are severely restricted in their kinematics due to energy and momentum conservation. In particular, the two final state partons that form the jets are back-to-back, *i.e.* have opposite momenta. This strict requirement is broken by any kind of radiation outside of those jets that could contribute to momentum conservation, leading to instabilities if this kind of process is considered beyond fixed leading order. To avoid these instabilities, the transverse momentum requirement is formulated as an asymmetric cut,

$$p_T^{\text{lead}} \geq p_{T,\text{min}} \ , \tag{6.19}$$

$$p_T^{\text{2nd}} \geq \frac{p_{T,\text{min}}}{2} \ . \tag{6.20}$$

In order to cover a range of physical scales, the two choices $p_{T,\text{min}} = 200$ GeV and $p_{T,\text{min}} = 500$ GeV are considered. It should be noted again at this point that the observable calculation is ultimately performed on all final-state particles, as long as the final state contains jets fulfilling those requirements. The soft drop procedure, *cf.* Sec. 3.3, is applied to the hemispheres defined by the original thrust axis, *cf.* Sec. 3.1.

---

different technical details in the application of soft drop grooming to the full final state in hadron-hadron collisions and the exact definition of the observable in this case.

The radius parameter appearing in Eq. (3.29) is fixed at $R_{\mathrm{SD}} = 1$, and the other parameters of the groomer are considered in representative ranges

$$z_{\mathrm{cut}} \in \{0.1, 0.2, 0.3\} \,, \tag{6.21}$$

$$\beta \in \{0, 1, 2\} \,. \tag{6.22}$$

For the fixed order calculation and the resummation, the scales are chosen to be identical. They are identified with half of the scalar sum of the transverse momenta of all partons in the final state

$$\mu = \frac{1}{2} H_T \equiv \frac{1}{2} \sum_i p_{t,i} \,. \tag{6.23}$$

The resummation is performed with the usual treatment of the endpoint- and transition point corrections, *cf.* Sec. 5.1. The value of the endpoint is numerically extracted from the NLO calculation. The value of x_v in Eq. (5.1) is chosen according to Eq. (5.2), but as explained in Sec. 5.1 only including the final state legs in the sum. This is appropriate since, as argued in Sec. 4.4, the groomed observables are insensitive to initial state radiation.

The perturbative uncertainties are estimated by taking the envelope of a standard 7-point variation of the renormalisation and factorisation scales

$$(\mu_R^{\mathrm{var}}/\mu_R, \mu_F^{\mathrm{var}}/\mu_F) \in \{(0.5, 0.5), (0.5, 1), (1, 0.5), (1, 1), (1, 2), (2, 1), (2, 2)\}. \tag{6.24}$$

The resummation scale is also varied by a factor of 0.5 and 2 with the central choice of the μ_R and μ_F. An additional variation is obtained by changing the parameter p in Eq. (5.1) from the default 1 to $p = 2$. The overall envelope of all variations is shown as uncertainty band in the following.

Results

The main results that shall be discussed within this thesis are the resummed predictions for transverse thrust after soft drop grooming. Ref. [III] also presents an extensive discussion of Monte Carlo results and a corresponding comparison. Some examples of this comparison will be followed up on at the end of this section.

The results for the somewhat softer $p_T > 200$ GeV selection are compiled in Fig. 6.12. It summarises the predictions made at NLO, NLL and the matched $\mathrm{NLO} + \mathrm{NLL}'$ accurate predictions. The various plots correspond to different choices of grooming parameters.
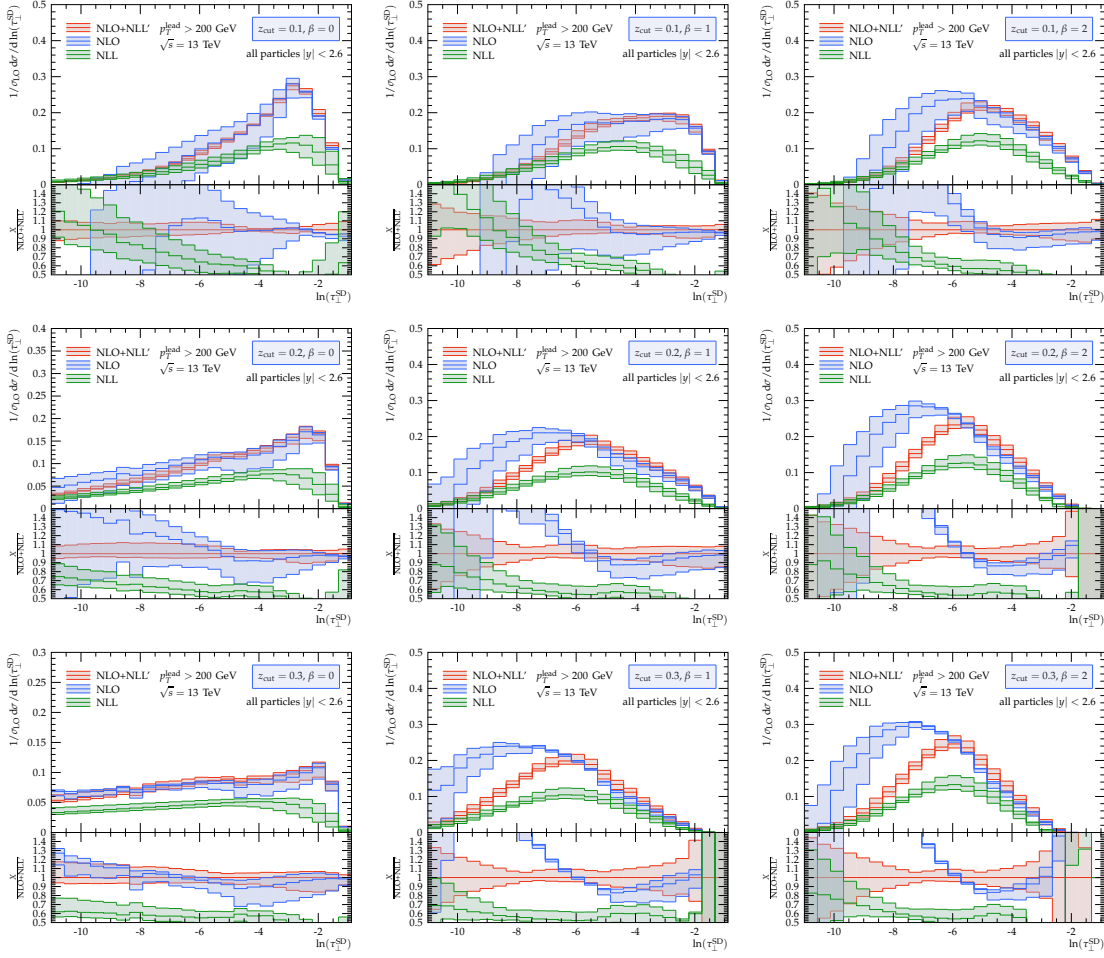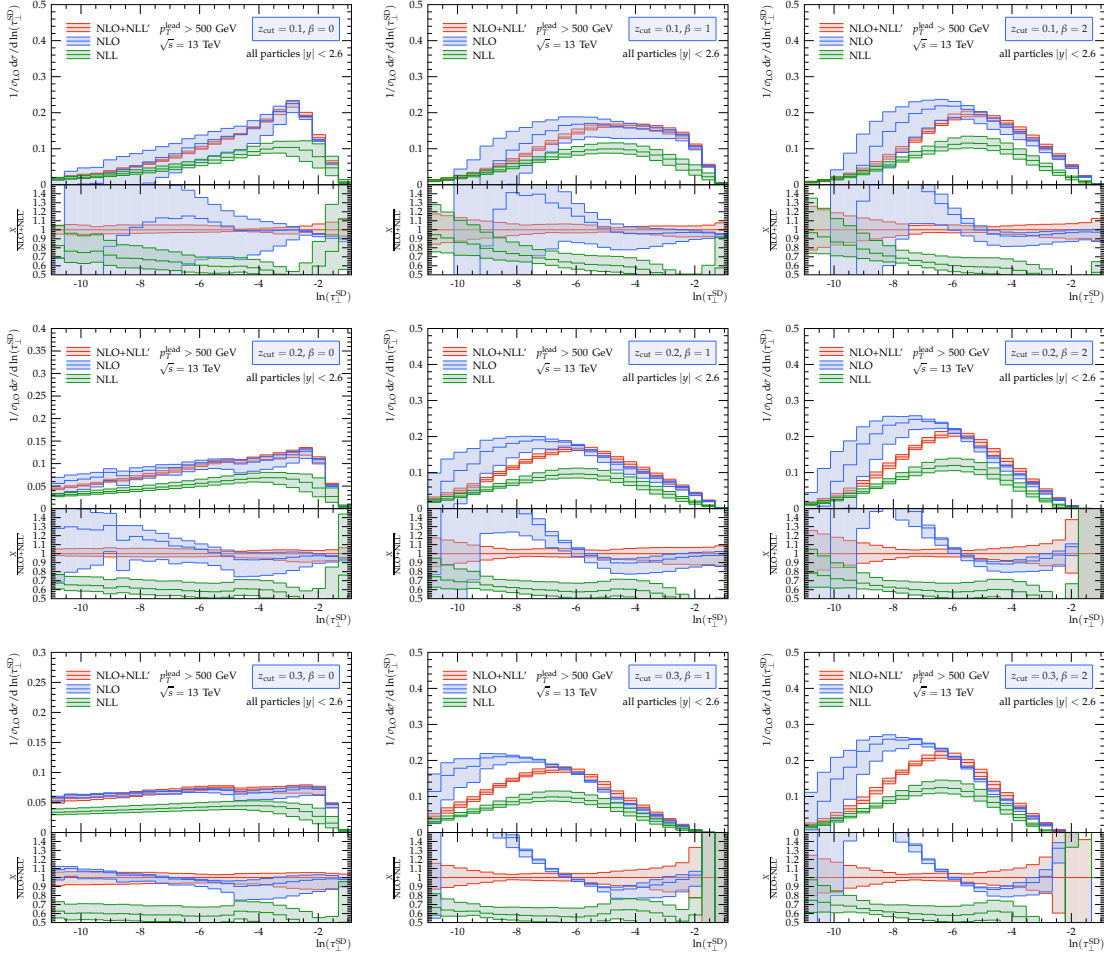
Figure 6.12: $\text{NLO} + \text{NLL}'$ predictions for groomed transverse thrust for $\beta \in \{0, 1, 2\}$ (columns) and $z_{\mathsf{cut}} \in \{0.1, 0.2, 0.3\}$ (rows) for the $p_{T,\mathsf{min}} = 200$ GeV event selection in comparison to the NLO result and the pure NLL resummation.

```
Figure and caption taken from Figure 8 in Ref. [III].
```

Note that all predictions are scaled by the leading order cross section $\sigma_{\mathsf{LO}} = \sigma^{(0)} + \sigma^{(1)}$, rather than their respective cross sections. With this choice the NLL and NLL' cross section are expected to approach the same value in the soft limit, which would not be the case if the NLL cross section was scales by $\sigma^{(0)}$. Note this does not apply to the $\text{NLO} + \text{NLL}'$ cross section, due to the additional logarithms $\propto \alpha_{\mathsf{s}}^2 L$ present at NLO but not at NLL or NLL'.

The left column of Fig. 6.12 collects the results for $\beta = 0$, with increasing values of $z_{\mathrm{cut}} \in \{0.1, 0.2, 0.3\}$. All distributions show marked features when grooming starts to take effect at the transition point $\tau_{\mathrm{SD}} \approx z_{\mathrm{cut}}$. This produces a significant peak with the cross section dropping of suddenly to the left of the transition, followed by an almost flat distribution towards smaller observable values. Note that the LO expectation in this range is indeed a constant. The matched distribution is rather close to the fixed order NLO calculation it is matched to, with only very little effect of the resummed calculation. This parameter choice might therefore be preferred in exploring precision fixed order calculations, *cf.* [374] for example.

In the middle column, β is increased to $\beta = 1$. The features around the transition point are significantly reduced. There is still a pronounced edge visible in the $z_{\mathrm{cut}} = 0.1$ case, while the $z_{\mathrm{cut}} = 0.2$ and $z_{\mathrm{cut}} = 0.3$ distributions are rather smooth. Towards the endpoint region, the matched result is dominated by the fixed order calculation and both approach the same value. In the soft tail however, there is a clear deviation to the NLO calculation, and the NLL resummed prediction is rather mimicked by the matched distribution. Note that, as discussed before, the matched calculation contains additional logarithms from the NLO calculation.

The $\beta = 2$ case is represented by the third column in Fig. 6.12. The trend observed when going from $\beta = 0$ to $\beta = 1$ continues, the features around the transition point are washed out even more, also for the smallest $z_{\mathrm{cut}} = 0.1$ considered here. As required, the soft and hard regions of the matched distribution are dominated by the fixed order and resummed calculation similar to the $\beta = 1$ case. Note that the y-axes are limited to positive values. The NLO calculation is here visibly approaching negative values in the soft limit and resummation is clearly needed to even obtain a physical distribution.

Fig. 6.13 contains the same plots as discussed above, but for the $p_T > 500$ GeV selection. In principle the same qualitative comments apply to the calculation with this somewhat harder scale. It should be noted however that the same numerical soft drop parameters are not equivalent across different scales in terms of the expected phenomenology and the ability to suppress non-perturbative corrections. In terms of the anatomy of the perturbative calculation as discussed here, it is however appropriate to consider equal values.

Comparing to Fig. 6.12, the maximum height of the distributions is lower for the $p_T > 500$ GeV than the one with the same parameter choice for $p_T > 200$ GeV. The effect is the strongest in the $\beta = 0$ case, which exhibits the most pronounced peak structures. In particular the $\beta = 0$, $z_{\mathrm{cut}} = 0.3$ distribution, corresponding to the most aggressive choice of grooming parameters made here, is significantly suppressed

Figure 6.13: NLO + NLL′ predictions for groomed transverse thrust for $\beta \in \{0, 1, 2\}$ (columns) and $z_{\text{cut}} \in \{0.1, 0.2, 0.3\}$ (rows) for the $p_{T,\text{min}} = 500$ GeV event selection in comparison to the NLO result and the pure NLL resummation.
Figure taken from Figure 9 and caption adapted from Figure 8 in Ref. [III].

and shows almost no remaining features. Otherwise, it still applies that the $\beta = 0$ matched cross sections in the leftmost column are almost entirely determined by the fixed order calculation at NLO, in the range of transverse thrust considered here. In the distributions corresponding to $\beta > 0$, the matched distribution interpolates again between the fixed order result and the resummed cross section within the visible range. The need for resummation to obtain a physical distribution is similarly demonstrated

for the two larger β choices.

To summarise the findings of Ref. [III], Fig. 6.14 shows the comparison of a selection of the resummed results to Monte Carlo simulations made with SHERPA at MEPS@NLO accuracy. The simulation is analysed at parton level and at full hadron level including the underlying event. The analysis of the hadron level is restricted to charged particles that would be visible as tracks in a particle detector.
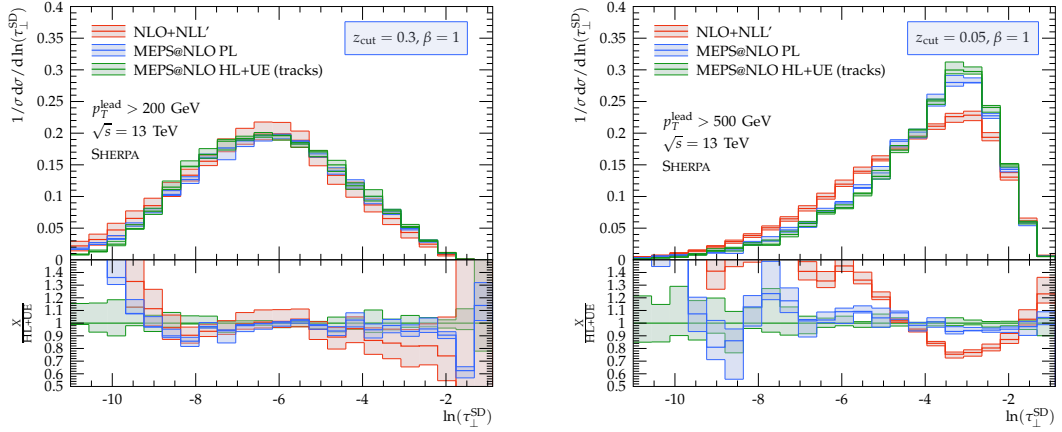
Figure 6.14: The groomed transverse-thrust distributions for events with a leading-jet transverse momentum $p_T^{\text{lead}} > 200$ GeV, with $z_{\text{cut}} = 0.3$ and $\beta = 1$ (left) and $p_T^{\text{lead}} > 500$ GeV, with $z_{\text{cut}} = 0.05$ and $\beta = 1$ (right). Shown are results at NLO + NLL$'$ accuracy as well as MEPS@NLO predictions obtained with SHERPA at parton level (PL), full hadron level (HL+UE), the latter based on charged tracks with $p_T^{\text{track}} > 500$ MeV. In all cases we only include final-state particles with $|y| < 2.6$ in the observable evaluation. The lower panels show the ratios with respect to the HL+UE prediction.
Figure and caption taken from Figure 17 in Ref. [III].

The distributions shown here correspond to the $p_T > 200$ GeV selection with $\beta = 1$ and $z_{\text{cut}} = 0.3$ on the left. The $p_T > 500$ GeV selection is represented by the $\beta = 1$, $z_{\text{cut}} = 0.05$ parameter choice on the right. The soft drop procedure here allows for an almost complete removal of the transition from parton level to even the charged hadron level. One might thus hope to be able to directly compare the resummed calculations to data measured on charged particle tracks. In the first case shown in Fig. 6.14 one then could validate both shower and analytic predictions. The right hand plot in the same figure illustrates a case where sufficiently precise data could discriminate between the two predictions, potentially guiding further developments in either case.

6.4   Jet substructure at the Large Hadron Collider

In this section the study of jet substructure observables will be explored at the example of the jet angularities introduced in Eq. (3.28). Observables of this kind are measured at the various LHC experiments, *cf.* [144, 145, 375]. This study will follow the precise measurement prescription used by the CMS collaboration in the preliminary measurement documented in Ref. [145]. The results can hence directly be compared to those data. Ref. [145] measured the angularities in events with two jets (dijet) and in events with a Z boson and an additional jet (Z+jet). The theoretical prediction in the Z+jet case were already presented in Ref. [IV].

Motivation

Jet angularities are a standard way to probe the internal structure of jets. With the adjustable parameter α they conveniently allow one to probe different regions of phase space with similar definition of observables. They are routinely used as benchmark points in studies on the differences between quark and gluon jets, *cf.* the relevant sections in [376–378] for example. Improving the understanding of this both in theoretical calculations and modelling [379–383], *cf.* also Refs. [VIII,IX], are ongoing research efforts. To test tools in regards to this, one needs to obtain experimental samples that are actually expected to be enhanced in either quark or gluon jets. The process where a jet is produced in association with an electroweak Z boson at Born level receives a larger contribution from diagrams where the final state jet is a quark jet. For two jet production, at the LHC, the larger contributions tend to come from gluon jets. This statement is somewhat dependent on the phase space point considered however. In general, more central jets tend to be more strongly dominated by gluons. To study the differences of quark and gluon jets, it is hence a useful notion to treat the Z+j process as a proxy for quark jets and the more central dijet process as a proxy for gluon jets. The differences between the more central and more forward dijet can contain additional information. The basis of such studies are precise predictions for the various jet selections, that will be the topic of this study. A potential use case in the context of PDF fits was outlined in [378]. This idea is further explored in Ref. [V]. The general idea here is that, at LO in the Z+jet case, the final state flavour also determines the initial state. If the jet is a quark jet, the initial state has to contain a gluon, whereas a gluon jet is arising from two quarks in the initial state. Since the distribution of the angularities is different for quark and gluon jets, a cut at a specific value can generate a sample that is additionally enhanced in quark jets. This sample, at LO, would then

receive a larger contribution from the gluon PDF and would allow to determine it more stringent. The analysis presented in the following contributes to the thorough theoretical understanding that is needed for a practical application of this idea.

Methods

As mentioned earlier, the event selection will follow Ref. [145] (and Ref. [IV] in the Z+jet analysis, which in turn used Ref. [145]). For the Z+jet case, the Z bosons is assumed to decay into muons. They are required to have a minimal transverse momentum $p_{T,\mu}$ and be sufficiently central in terms of their rapidity η_μ,

$$p_{T,\mu} > 26 \text{ GeV} , \qquad \left|\eta_\mu\right| < 2.4 . \tag{6.25}$$

To select muon pairs from Z decays, the invariant mass of the combined momentum is required to be in a window around the Z mass,

$$70 \text{ GeV} < m_{\mu^+\mu^-} < 110 \text{ GeV} . \tag{6.26}$$

Like the individual momenta, also the combined momentum of the muons should pass a certain threshold,

$$p_{T,\mu^+\mu^-} > 30 \text{ GeV} . \tag{6.27}$$

The jet is obtained via anti-k_t clustering, *cf.* Sec. 3.2, with radius parameter $R = 0.4$ and $R = 0.8$. The leading jet, *i.e.* the one with the largest transverse momentum, is the one on which the measurement is performed. It is also required be relatively central,

$$\left|y_{\text{jet}}\right| < 1.7 . \tag{6.28}$$

The Z boson and the jet are required to have a large angular separation in the transverse plane,

$$\left|\phi_Z - \phi_{\text{jet}}\right| > 2 . \tag{6.29}$$

In addition, it is required that they are of similar transverse momentum, by imposing a cut on the asymmetry

$$\left|\frac{p_{T,\text{jet}} - p_{T,\mu^+\mu^-}}{p_{T,\text{jet}} + p_{T,\mu^+\mu^-}}\right| < 0.3 . \tag{6.30}$$

Note that this is trivial for Born events, where due to momentum conservation $p_{T,\text{jet}} = p_{T,\mu^+\mu^-}$. The cut controls the size of NLO QCD corrections and justifies the picture of a leading jet balancing against the Z boson at higher orders. The measurement is performed inclusive regarding other jets of lower transverse momentum.

In the dijet case, the cuts are very similar. Jets are again clustered with the anti-k_t algorithm with $R = 0.4$ and $R = 0.8$. The measurement is performed on the two jets with the largest transverse momentum. They are required to meet the centrality requirements as the jet in the Z+jet case, Eq. (6.28). Additionally, their transverse momenta should satisfy

$$p_{T,\text{jet}} > 30 \text{ GeV} . \tag{6.31}$$

The two jets are ordered by their rapidity y, and referred to as the "central" and "forward" jet, with

$$\left| y_{\text{central}} \right| < \left| y_{\text{forward}} \right| . \tag{6.32}$$

They are required to be separated with respect to each other similar to the separation cuts between Z and jet, *cf.* Eq. (6.29) and Eq. (6.30),

$$\left| \phi_{\text{central}} - \phi_{\text{forward}} \right| > 2 , \tag{6.33}$$

$$\left| \frac{p_{T,\text{central}} - p_{T,\text{forward}}}{p_{T,\text{central}} + p_{T,\text{forward}}} \right| < 0.3 . \tag{6.34}$$

In total, data are hence available for two jet radii ($R = 0.4$ and $R = 0.8$) times three types of jets, those from the Z+jet selection and the central and forward jets from the dijet selection. Each measurement is averaged over a range in p_T of the measured jet. The edges of the ranges considered here are

$$\{88, 120, 150, 186, 254, 326, 408, 481, 614, 800, 1000, 4000\} \qquad \text{for dijet,} \tag{6.35}$$

$$\{88, 120, 150, 186, 254, 326, 408, 1500\} \qquad \text{for } Z\text{+jet .} \tag{6.36}$$

In each range, the angularity of the jet is calculated as defined in Eq. (3.28), for three values of α. The choices are commonly named as jet thrust $\alpha = 2$, jet width $\alpha = 1$ and "Les Houches angularity" $\alpha = 0.5$. Additionally, each jet is groomed with soft drop grooming, *cf.* Sec. 3.3, with parameters $z_{\text{cut}} = 0.1$ and $\beta = 0$.

The focus here will be on the comparison of the NLO + NLL$'$ results to those data. The scales in the calculation are chosen as

$$\mu_R^2 = \mu_F^2 = p_{T,\mu^+\mu^-}^2 , \tag{6.37}$$

$$\mu_Q^2 = R^2 p_{T,\mu^+\mu^-}^2 , \tag{6.38}$$

in the Z+jet and

$$\mu_R^2 = \mu_F^2 = H_T^2/4 , \tag{6.39}$$

$$\mu_Q^2 = R^2 p_{T,\text{jet}}^2 , \tag{6.40}$$

in the dijet case. Note that the scalar sum of the transverse momenta H_T equals twice the transverse momentum of one of the jets for born events, so the scale for dijets is just the p_T^2 in that case. Likewise, the transverse momentum of the Z boson is equal to that of the jet in the event around which the resummation is performed.

The parameter x_v in Eq. (5.1) is per default set to 1, and varied up and down by a factor of 2 with the default choice of μ_R^2 and μ_F^2 to estimate the logarithmic uncertainties. Likewise, renormalisation and factorisation scales are varied independently excluding the most extreme combinations, *i.e.*

$$(\mu_R^{\text{var}}/\mu_R, \mu_F^{\text{var}}/\mu_F) \in \{(0.5, 0.5), (0.5, 1), (1, 0.5), (1, 1), (1, 2), (2, 1), (2, 2)\}. \quad (6.41)$$

The envelope of all these combinations is regarded as perturbative uncertainty.

Non-perturbative corrections are applied via the transition matrix method described in Sec. 5.6. The necessary input is derived from SHERPA simulations at MC@NLO accuracy, *cf.* Sec. 3.5. The same binning in terms of the measured jet p_T is used to define the regions outside the measured phase space. Fig. 6.15 illustrates the migration between different p_T bins. Note that this is technically dependent on the observable considered, the illustration is done for $\alpha = 2$.

There is a clear effect of event migration to the neighbouring bins from parton to hadron level. The black line corresponds, for each bin, to the cross section for events to be in that bin at parton level and *not* be shifted to a different p_T region at hadron level. This is the largest contribution in all cases. The blue area represents events that are in one of the neighbouring bins at parton level, but are shifted to the bin in question by non-perturbative effects. While there is a relatively large effect from this, the additional contribution including up to four neighbouring bins, shown in green, is already much smaller. It should be mentioned that the calculation includes two more bins below 88 GeV, including p_T as low as 50 GeV. Apart from those, bins are not included if they are outside the range on either side, *i.e.* including up to 4 bins for the highest p_T bin only includes the 4 bins with lower transverse momentum. Due to the quick decrease in cross section with larger p_T this should be well justified. Virtually no additional effect is gained by including up to 8 neighbouring bins, this is represented by the red area that is barely visible however. It is concluded that including the 4 neighbouring bins is sufficient in all cases to capture the physical effects.

In principle, there is no problem in including all possible bins once the calculation is done. However, the Monte Carlo calculation of the migration matrices corresponding to bins very far away from the target one tends to be unstable. Hence, only the 4 closest bins will be used with the justification given above. It has been checked explicitly that including more bins has no practical effect on the resulting distributions, unless
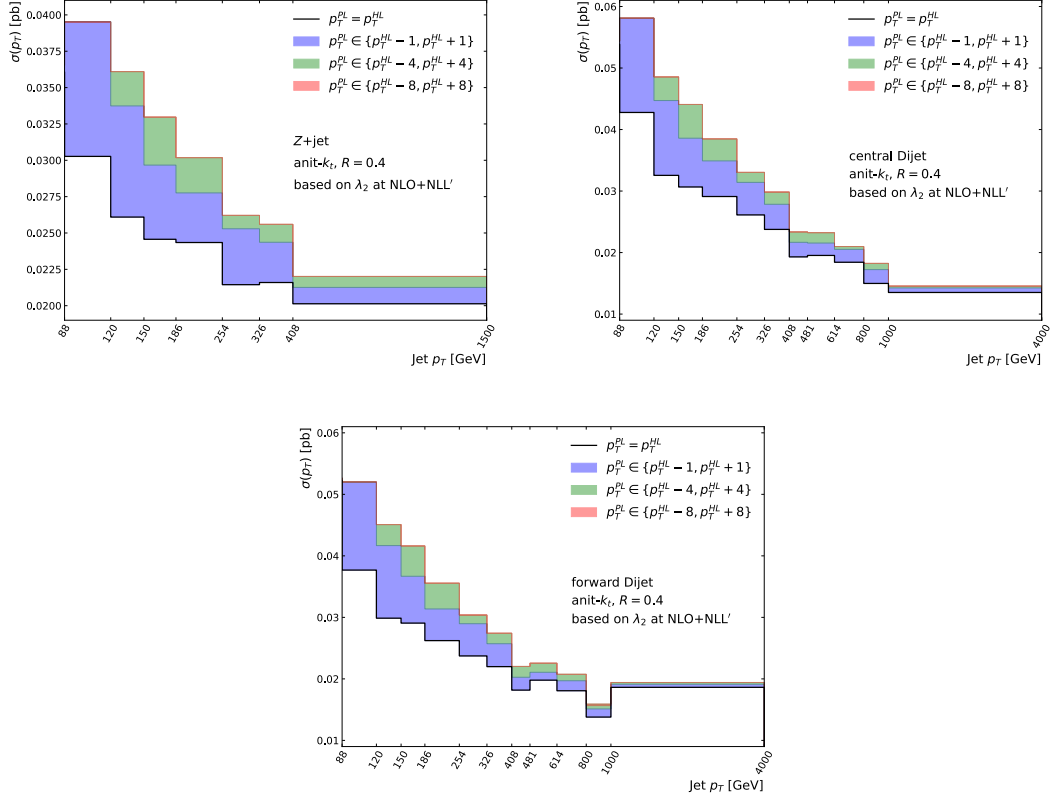
Figure 6.15: Cross section in various jet p_T bins for the leading jet in the Z+jet selection (top left), the central (top right) and the forward (bottom) dijet, obtained by applying transition matrices obtained from SHERPA at MC@NLO accuracy, to the NLO + NLL′ distribution of λ_2. The colour coding represents the cross section where the transverse momentum is equal at hadron and parton level (white), where the hadron level p_T corresponds to migration by at most a single bin (blue), by up to 4 bins (green) and by up to 8 bins (red) relative to the parton level. See text for details.

statistical artefacts become important. The equivalent of Fig. 6.15 for the larger jet radius $R = 0.8$ can be found in Fig. B.1 in App. B. The same conclusions hold in that case.

Variations for the non-perturbative corrections are determined solely using SHERPA in this study. Note that Ref. [IV] also studied other generators and did not find any major differences. The parameter that is used for this is the RESCALE_EXPONENT, *cf.*

Ref. [209][3], that stirs the evolution of the underlying event tune between different energy scales. This way, the tune can be considered as fixed at lower energies, for example the scales where it can be determined from Tevatron data. The central value considered is

$$\text{RESCALE\_EXPONENT} = 0.16 \, , \tag{6.42}$$

with a symmetrical variation corresponding to $\text{RESCALE\_EXPONENT} = 0.08$ and $\text{RESCALE\_EXPONENT} = 0.24$. This hence produces three different versions of the transition matrices that can be applied to the variations obtained from the scale choices in the resummed calculation independently. The overall envelope is used as an estimate of the total theoretical uncertainty. Ref. [145] also performed measurements based on charged particles instead of all hadrons inside the jet. Non-perturbative corrections for this case can likewise be produced and applied to the resummed result in the fashion described above.

The global soft wide-angle contribution $I_{IJ}^{\mathcal{B}^\delta}$ entering Eq. (4.42) can be taken from the appendix of Ref. [108], as power series in the jet radius R. Note the differing conventions to define the function called T here, Eq. (4.21), leading to differences by constant factors in the functions reported here. With the initial states labelled as a and b, the measured jet as J and the auxiliary final state jet as f, they are given by

$$I_{ab}^{\mathcal{B}} = \frac{R^2}{4} \, , \tag{6.43}$$

$$I_{aJ}^{\mathcal{B}} = I_{bJ}^{\mathcal{B}} = \frac{R^2}{16} + \mathcal{O}(R^4) \, , \tag{6.44}$$

$$I_{af}^{\mathcal{B}} = \frac{R^2}{8} \frac{\exp(y_J - y_f)}{1 + \cosh(y_J - y_f)} + \mathcal{O}(R^4) \, , \tag{6.45}$$

$$I_{bf}^{\mathcal{B}} = \frac{R^2}{8} \frac{\exp(y_f - y_J)}{1 + \cosh(y_f - y_J)} + \mathcal{O}(R^4) \, , \tag{6.46}$$

$$I_{fJ}^{\mathcal{B}} = \frac{R^2}{16} \tanh(y_J - y_f) + \mathcal{O}(R^4) \, . \tag{6.47}$$

Here y_i denotes the distance in rapidity between the respective jet axes. This is the only part that actually depends on the Born configuration $\mathcal{B}$ in this case. The nonglobal logarithms are taken into account by the functions $f_{IJ}^{\mathcal{B}}$ in Eq. (4.42). As explained in Sec. 4.3, their calculation proceeds via an external Monte Carlo algorithm that is not subject of this thesis. The results in the Z+jet case were reported in Ref. [IV]. Details on the additional complications in the dijet case, will be discussed in an upcoming publication[4] [384].

---

[3]A more detailed manual with explanations of the parameters is available online at `https://sherpa.hepforge.org/doc/SHERPA-MC-2.2.10.html`

[4]I am grateful to Gregory Soyez for supplying the corresponding results for $f_{IJ}^{\mathcal{B}}$ in for the Z+jet

Results

With groomed and ungroomed distributions measured on all as well only charged hadrons for three different values of α, two jet radii R in 8 (Z+jet) and two times 12 (dijet) p_T bins, in principle there would in total be $2 \times 2 \times 3 \times 2 \times (8 + 12 + 12) = 768$ plots to be described. The discussion here will hence be limited to the analysis with no restrictions on the charge of the particles. The focus will further be on the distributions for the smaller jet radius $R = 0.4$. A selection of additional results can be found in App. B.

Distribution of averages. To gain an overview of the full range of transverse jet momentum, Ref. [145] calculated the averages of the angularity distributions in the various p_T bins. The average is calculated based on the binned distribution, so the corresponding predictions can easily be obtained from the resummed calculation for the appropriate binning. This section will describe the results of this for the ungroomed angularities, for the different kinds of jet selections described in the previous section.

The distribution of the average angularity depending on the jet p_T in the Z+jet selection is shown in Fig. 6.16. With increasing transverse momentum, the value of the average is observed to be decreasing. The largest averages are obtained for the $\alpha = 0.5$ Les Houches angularity, with the data ranging from ≈ 0.22 in the highest p_T bin to ≈ 0.32 in for the lowest p_T range. For larger α the average is significantly smaller, only reaching ≈ 0.18 and ≈ 0.091 respectively. In the largest p_T bin, the average drops to ≈ 0.115 and ≈ 0.058 for $\alpha = 1$ and $\alpha = 2$.

As a general observation, the central values for the predicted averages are smaller than that of the CMS data. The deviation is of the order of $10\% - 20\%$. However, in many cases the average agrees with the data within the respective theoretical uncertainty. The agreement is on the same level that Ref. [145] found for a large selection of general purpose Monte Carlo generators.

The sub-figures of Fig. 6.16 compare the predictions for the three values of α to the data. In the $\alpha = 0.5$ case the agreement appears to be somewhat better at low p_T. The uncertainty band covers the data up to $p_T > 408$ GeV, but the ratio appears to be systematically decreasing even before that. The predictions for $\alpha = 1$ and $\alpha = 2$ behave different with respect to the data, with the ratio starting out below 90% for the first bin. However, the ratio is then approaching 1 with increasing transverse momentum. This is most pronounced for $\alpha = 2$, while the ratio of the $\alpha = 1$ prediction relative to

---

case in Ref. [IV] as well as the additional contributions for the dijet case.
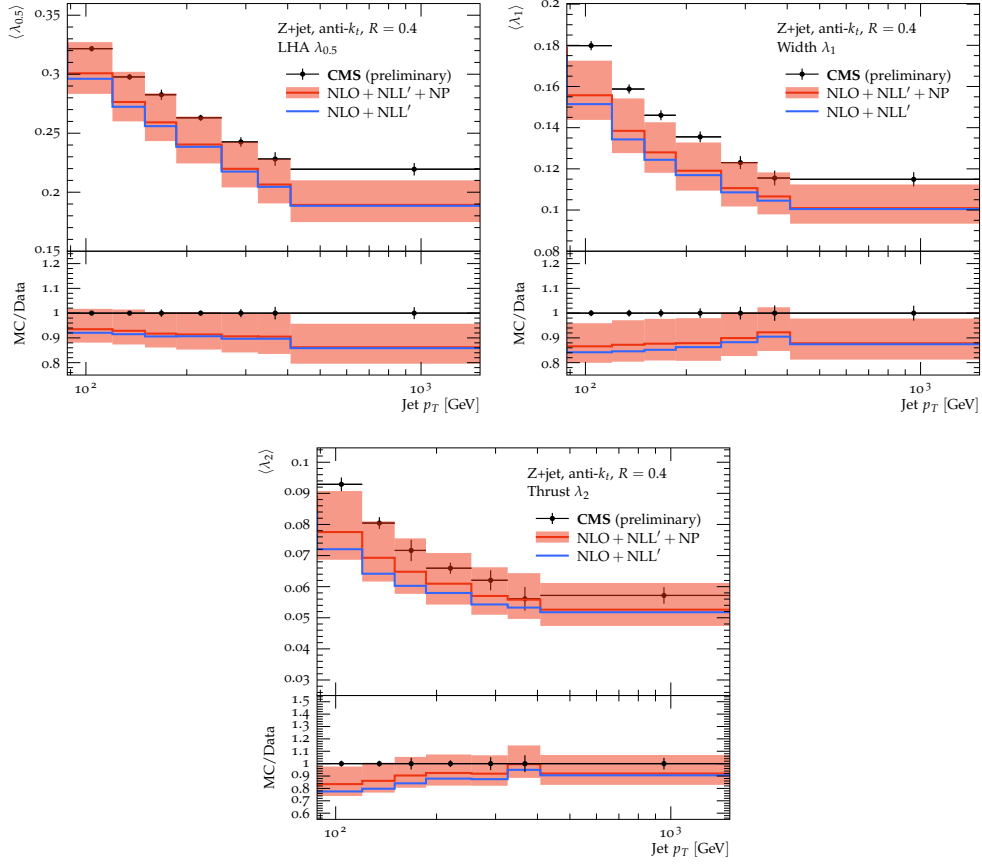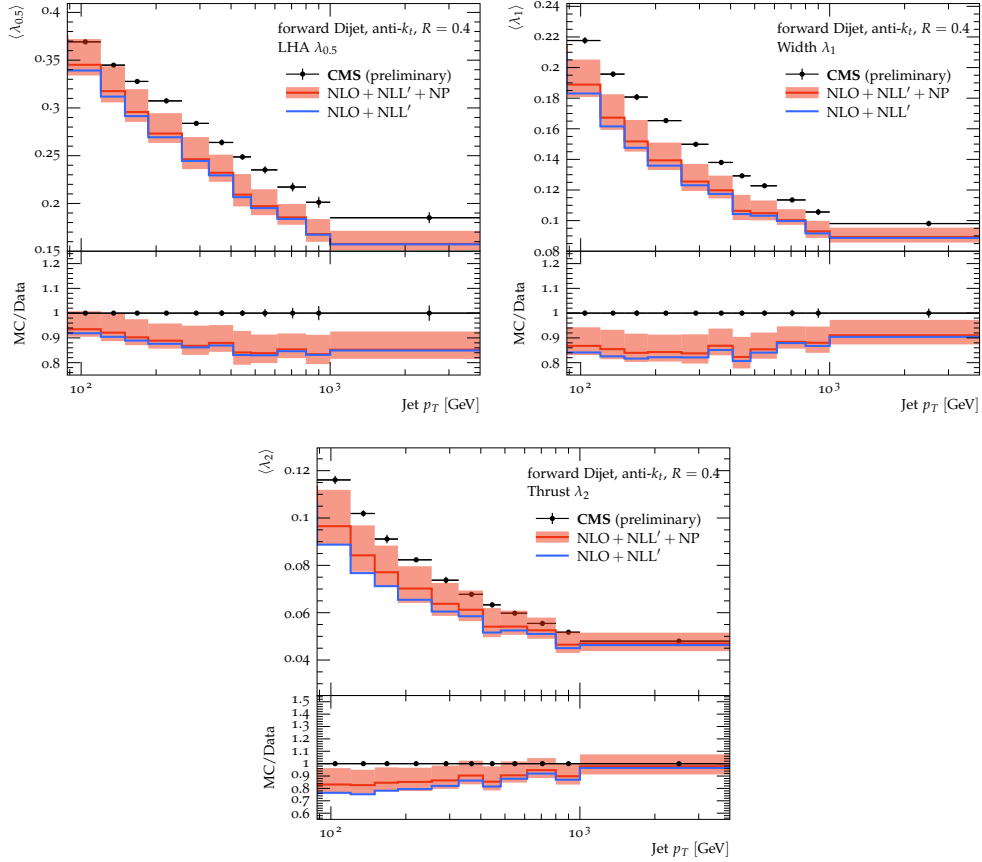
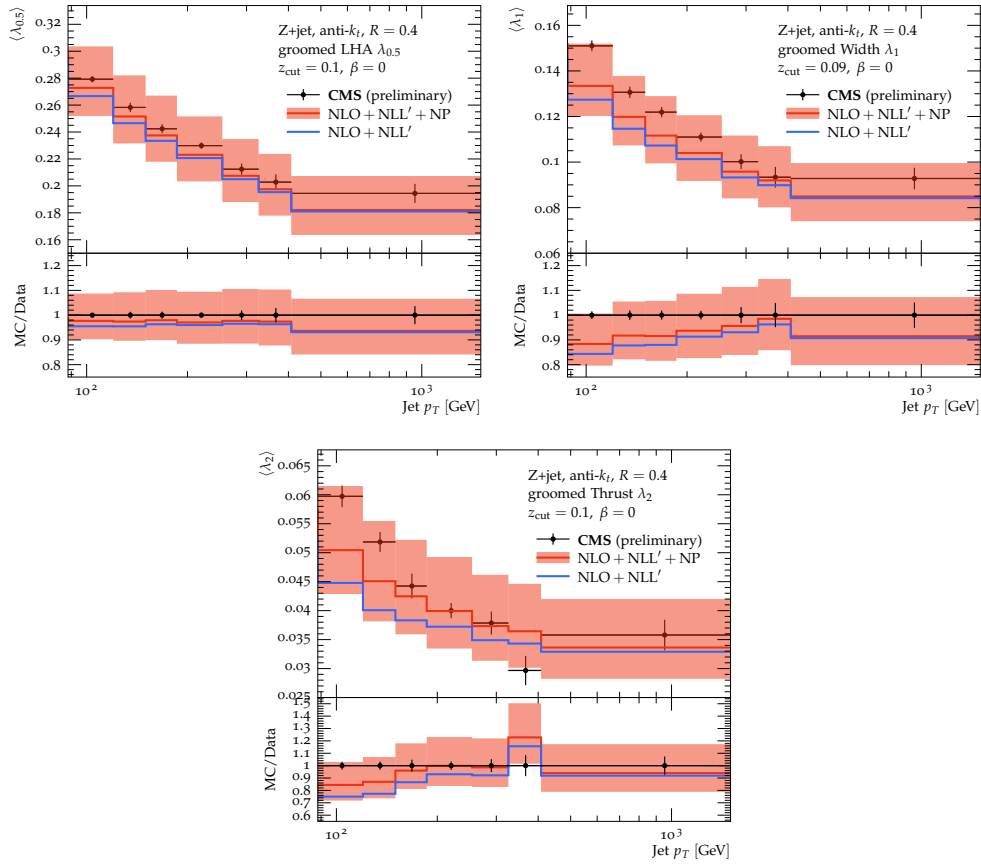**Figure 6.16:** Average distribution of the Les Houches angularity (top left), width (top right) and thrust (bottom) of the leading $R = 0.4$ jet in the Z+jet selection. The blue curve excludes the non-perturbative migration between different p_T bins from the full calculation shown in red.

the measured values almost remains flat. Taking into account uncertainties, the best overall agreement is found for the high p_T region in the $\alpha = 2$ case.

Fig. 6.16 also includes the averages of the perturbative prediction without the non-perturbative shift between p_T bins applied. The effect does not appear to be overly large. As one might expect, it reduces even more with increasing jet p_T. This can in particular be observed for $\alpha = 1$ and $\alpha = 2$, whereas the correction on the average for $\alpha = 0.5$ is almost invisible over the full range. The observations made also hold for $R = 0.8$ jets, *cf.* Fig. B.2, with the non-perturbative correction having a somewhat larger effect at small p_T for all values of α. This might be expected due to the increased susceptibility to underlying event corrections $\propto R^2$.
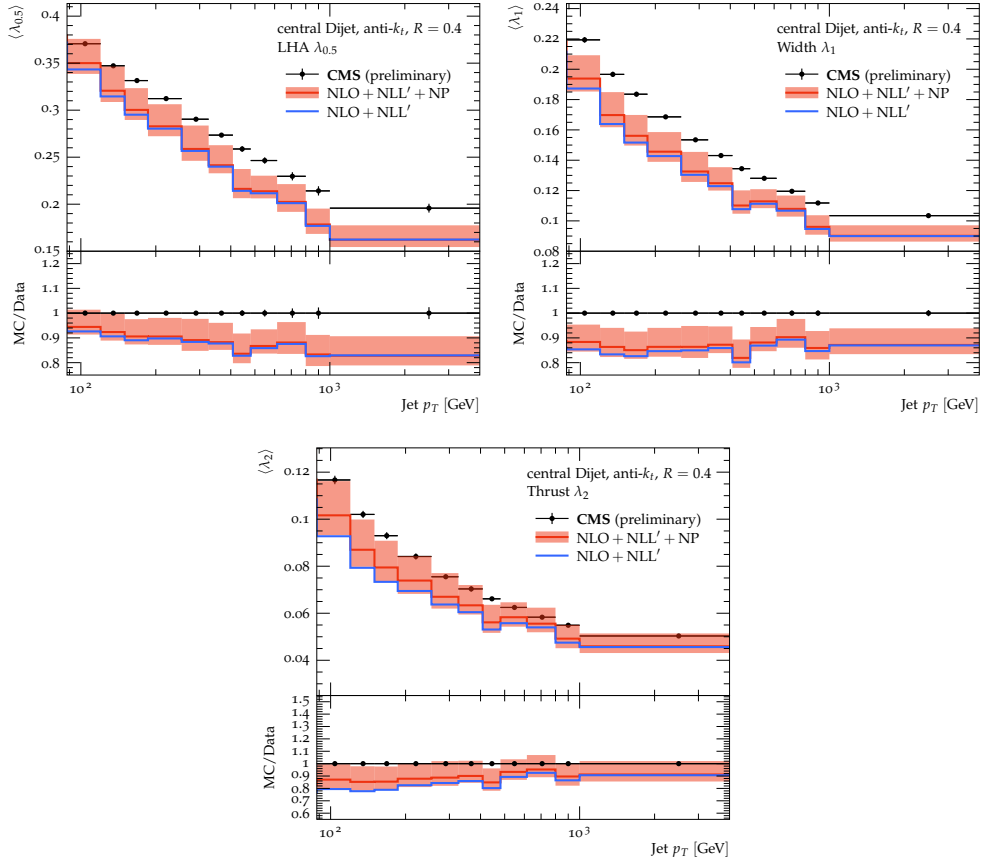
Figure 6.17: Average distribution of the Les Houches angularity (top left), width (top right) and thrust (bottom) of the leading $R = 0.4$ jet in the central dijet selection. The blue curve excludes the non-perturbative migration between different p_T bins from the full calculation shown in red.

The calculation for the central jet in the dijet selection can be found compared to the data in Fig. 6.17. The absolute values measured by CMS tend to be larger than observed for Z+jet, but are still roughly in the same ranges. The averages for $\alpha = 0.5$ for example now reach ≈ 0.37 instead of the ≈ 0.32 observed before. This is for equivalent jet p_T. The region with the largest transverse momentum considered corresponds to a larger scale in the dijet case. Nevertheless, the averages are of similar size in those regions.

The same conclusions as in the Z+jet case stand for the overall agreement, of the order of 80% to 90% depending on the value of α and the transverse momentum range considered. The regions where the theory agrees with the data within uncertainties

Figure 6.18: Average distribution of the Les Houches angularity (top left), width (top right) and thrust (bottom) of the leading $R = 0.4$ jet in the forward dijet selection. The blue curve excludes the non-perturbative migration between different p_T bins from the full calculation shown in red.

appears to be slightly smaller however.

The dependence on the angularity parameter α is qualitatively the same as in the Z+jet case. For $\alpha = 0.5$, the distribution of the average starts out at similar values as the data at low p_T, but then drops of significantly faster. In this case, the deviation exceeds the theoretical uncertainty already starting at 150 GeV. It should however be noted that the same systematic deviation is visible in the Z+jet case, and the deviation is still of the order of the uncertainty. The agreement within uncertainties for the range between 150 GeV and 408 GeV in Fig. 6.16 is probably also not very stable under variations of the procedure to estimate the uncertainties.
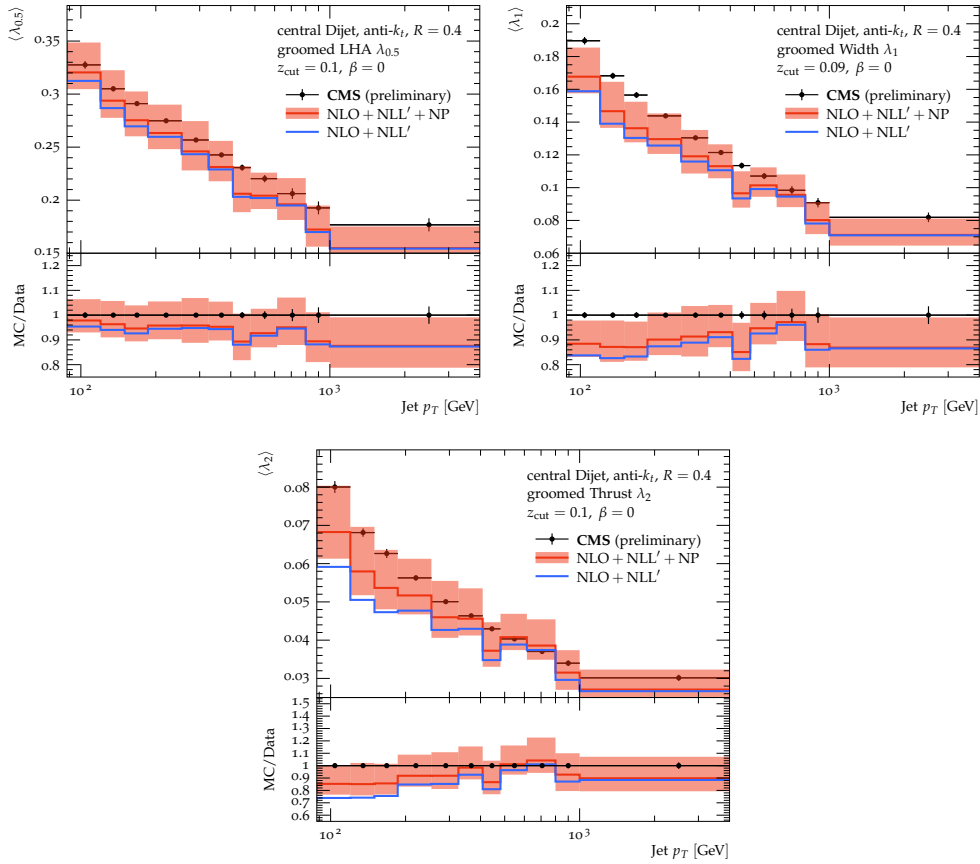
Figure 6.19: Average distribution of the groomed Les Houches angularity (top left), groomed width (top right) and groomed thrust (bottom) of the leading $R = 0.4$ jet in the Z+jet selection. The blue curve excludes the non-perturbative migration between different p_T bins from the full calculation shown in red.

Likewise, for $\alpha = 1$ the ratio to data is almost flat at $\approx 90\%$, with a somewhat smaller error than in the Z+jet case. The $\alpha = 2$ prediction again exhibits the best agreement to data, at least in the large transverse momentum region. The corrections due to non-perturbative p_T migration appear also to be of the same (small) order of magnitude in the dijet case. Again, the same figure for $R = 0.8$ jets is Fig. B.3 and confirms the above findings with increased non-perturbative effects.

Finally, Fig. 6.18 shows the same comparison for the more forward jet of the two leading dijets. It should be noted that the resummation for this is essentially the same as for the more central dijet, if considered event by event. The main difference is

due to the different contribution of quark and gluon jets in those regions. They are however relatively similar in the lower p_T region, at least when both are compared to the composition in the $Z+$jet case. Of course, fixed order corrections can also potentially be slightly different. One should therefore expect a very similar behaviour of the calculation.

This expectation is confirmed by the findings in Fig. 6.18. It holds in both data and theory prediction. The overall agreement is on the same level as in the central dijet selection. The systematic behaviour with α is also mimicked. If anything, the agreement in the high p_T tail for $\alpha = 2$ might be somewhat better for the more forward dijet, however the difference is so small that it might very well be due to statistical fluctuations. The corresponding figure for the $R = 0.8$ case is Fig. B.4.

Effect of grooming. Next to the angularities calculated on all jet constituents, Ref. [145] also measured the angularities based on the particles left after soft drop grooming as described before. The effect is again illustrated based on the averages of the binned distributions in the various transverse momentum regions.

The results for the $Z+$jet selection are shown in Fig. 6.19 and can be compared to the ungroomed case in Fig. 6.16. The value of the average groomed angularity appears to be slightly reduced relative to the ungroomed case. The largest value obtained is now $\langle \lambda_{0.5} \rangle \approx 0.28$ in the lowest transverse momentum bin, with the average in the highest p_T bin below ≈ 0.2 now even for $\alpha = 0.5$. For $\alpha = 2$, the average is at most 0.06 in the range considered here, and is at ≈ 0.036 in the last transverse momentum bin.

The reduction in the averages can also be observed in the predicted values. The effect is however smaller and even decreasing with increasing jet p_T. As a net result, the agreement between NLO $+$ NLL$'$ results and the CMS data is significantly increased, with almost all p_T bins compatible within the estimated theoretical uncertainty.

Maybe somewhat surprising, no significant reduction in the size of the effects of non-perturbative p_T migration is observed. Of course, it was rather small for the averages to begin with. It should also be noted that the averages are computed over the full range of the observable. As discussed in Sec. 4.5, soft drop grooming systematically reduces the value where a given observable is dominated by hadronisation corrections. The averages however represent integrals over the full observable range starting from $\lambda_\alpha = 0$, so the hadronisation dominated region will always be included at some point, even with grooming applied.

For $\alpha = 0.5$, the top left sub-figure in Fig. 6.19, the central values agree within 5%,
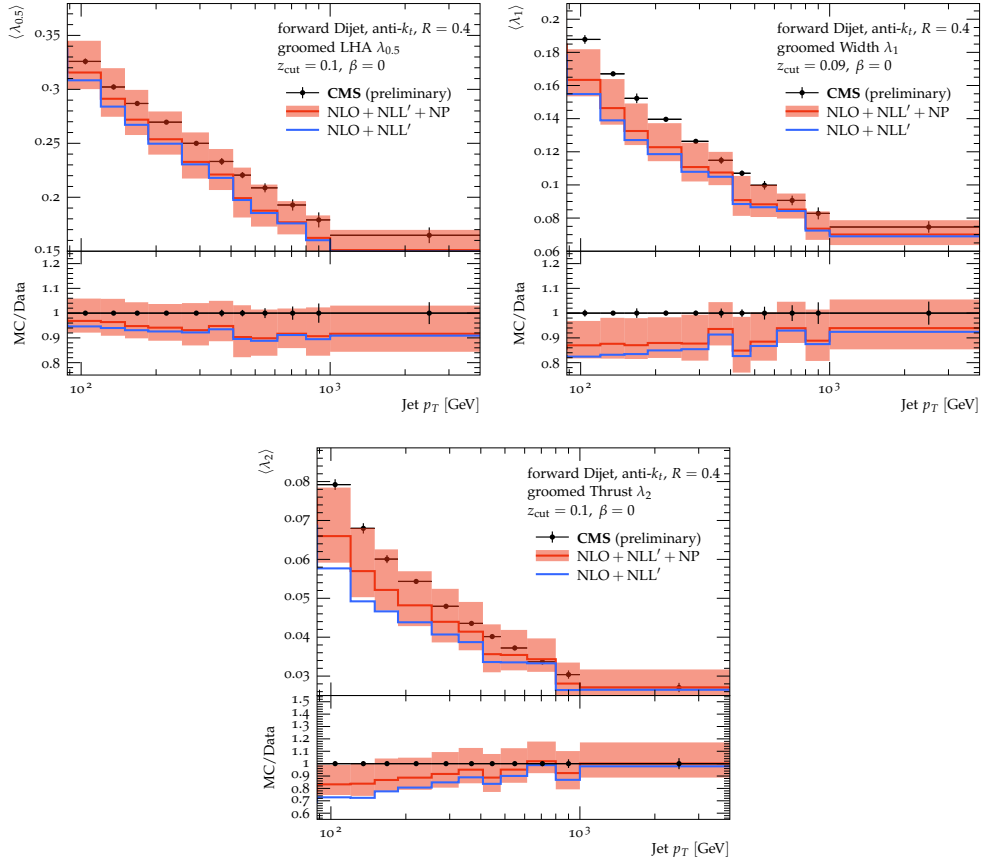
Figure 6.20: Average distribution of the groomed Les Houches angularity (top left), groomed width (top right) and groomed thrust (bottom) of the leading $R = 0.4$ jet in the central dijet selection. The blue curve excludes the non-perturbative migration between different p_T bins from the full calculation shown in red.

apart from maybe the last p_T bin. In any case, all bins are compatible with the data within the uncertainties. Despite the improved agreement, the same systematic effect as before can be observed for the central values, which all tend to be at lower values than the averages of the measured distributions. The ratio is however flat compared to that in the top left plot of Fig. 6.16, with only a slight decrease of the ratio with increasing jet p_T.

The averages for the larger values of α show the same systematic behaviour at low transverse momentum, tending to be small compared to the data. Taking into account uncertainties they are also compatible in the groomed case however. The improvement

Figure 6.21: Average distribution of the groomed Les Houches angularity (top left), groomed width (top right) and groomed thrust (bottom) of the leading $R = 0.4$ jet in the forward dijet selection. The blue curve excludes the non-perturbative migration between different p_T bins from the full calculation shown in red.

with increasing p_T also appears to be somewhat more pronounced for $\alpha = 1$ when compared to the same angularity parameter in Fig. 6.16. In both cases, the uncertainties are increased by a small amount compared to the ungroomed case. This might be expected, since the calculation for the groomed observables is performed in the $v \ll z_{\text{cut}}$ limit, while the average integrates over the full distribution including the transition point. The corresponding figures for a jet radius of $R = 0.8$ can be found in Fig. B.5.

Fig. 6.20 contains the data to theory comparison based on the more central of the leading dijets. Similar conclusions as in the Z+jet case apply when comparing to Fig. 6.17. The absolute values of the averages are reduced in a similar manner, with the
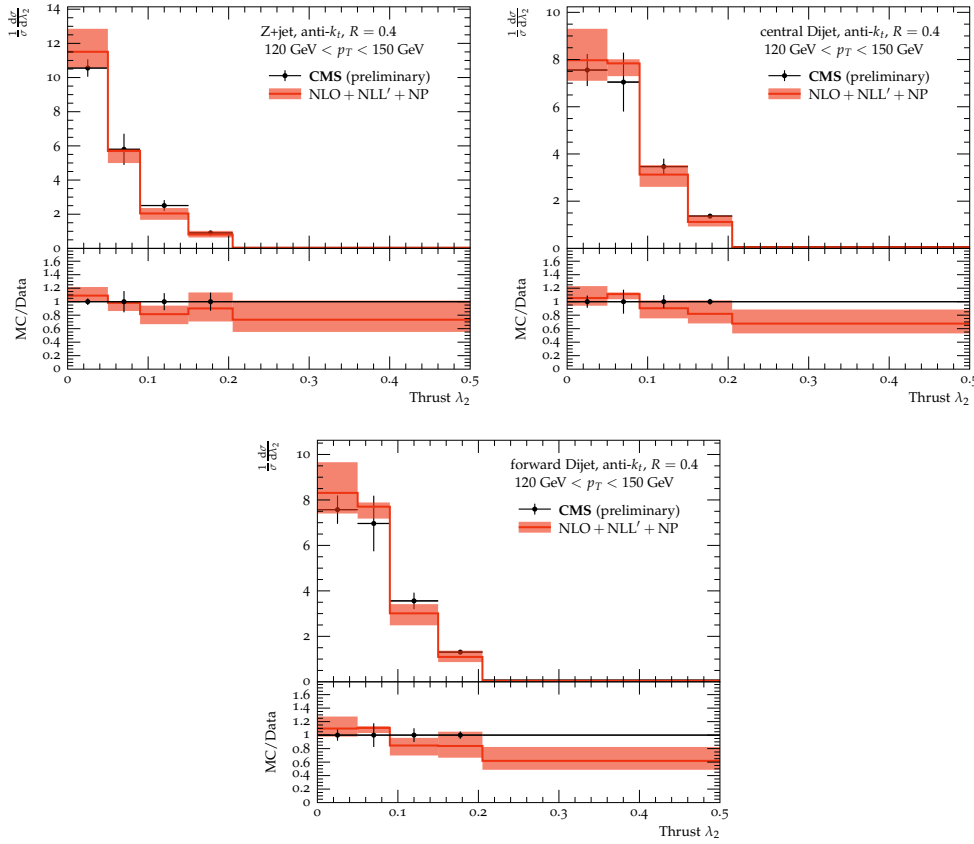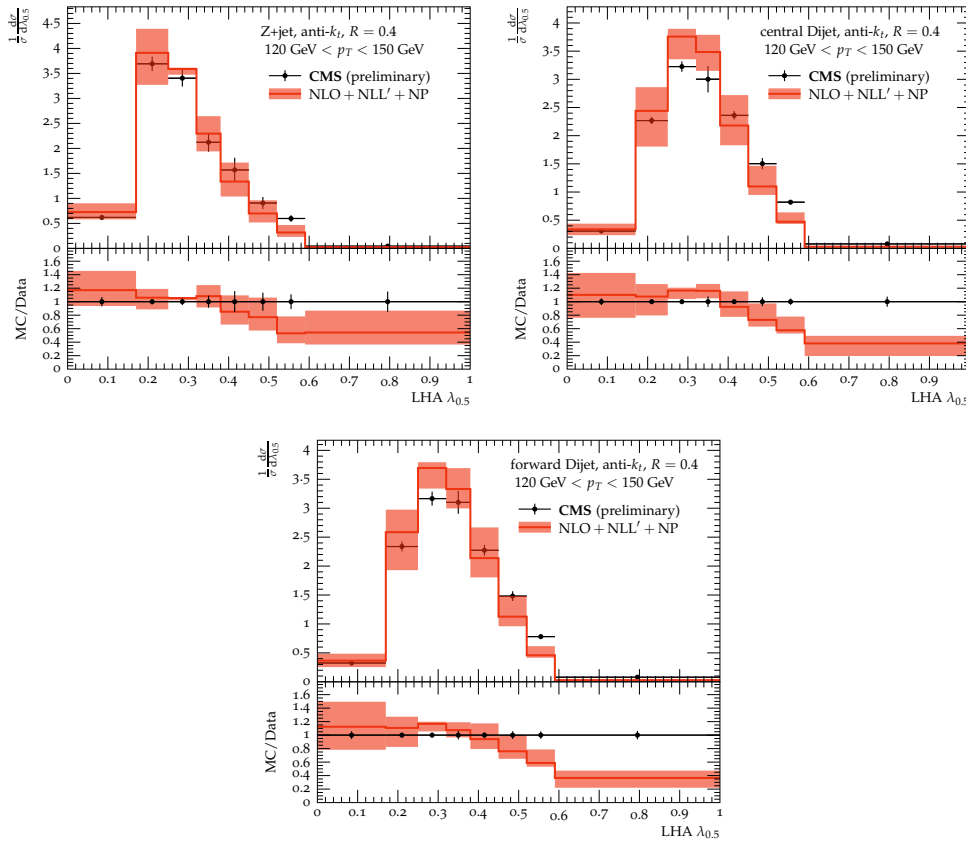
Figure 6.22: Jet thrust λ_2, for the jet in Z+jet (top left), the central (top right) and the forward (bottom) of the dijets.

largest value being now ≈ 0.33 for the $\alpha = 0.5$ case in the first p_T bin. Consistently, this is a reduction with respect to the ungroomed case, but corresponds to a larger value than observed in the groomed Z+jet case. The averages for $\alpha = 2$ reach $\langle \lambda_2 \rangle \approx 0.08$ in the dijet case. They are as low as 0.035 for the highest p_T bin.

As before, the agreement between theory and data is generally improved with grooming. The central values in the $\alpha = 0.5$ case however maintain a visible slope over the full range of the observable. The theoretical prediction in the first few bins for $\alpha = 1$ and $\alpha = 2$ is likewise visibly lower when compared to the measured values for the averages. The deviation appears to be somewhat larger compared to the theoretical uncertainty than what was observed in the Z+jet case.

The last set of averages are the ones for the groomed observables in the forward selection of the dijet phase space. They can be found in Fig. 6.21. As in the ungroomed
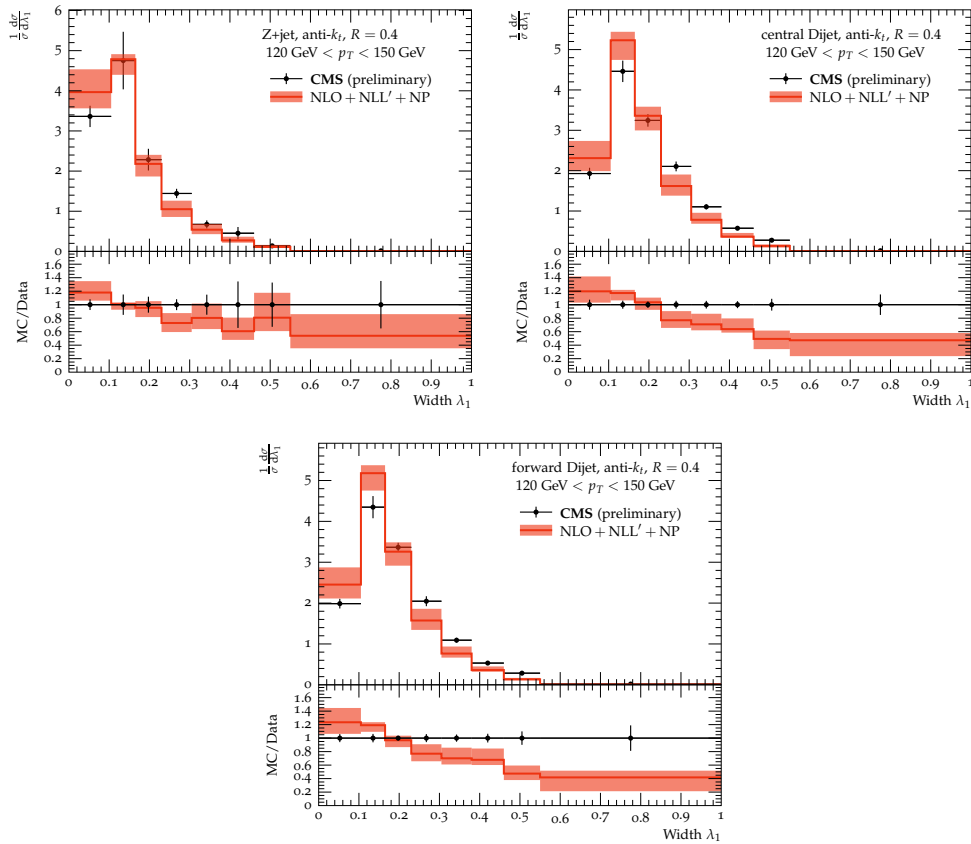
Figure 6.23: Jet width λ_1, for the jet in Z+jet (top left), the central (top right) and the forward (bottom) of the dijets.

case, the picture is very similar to the more central jets. The central value in the highest transverse momentum bins again shows minor improvements in the data comparison relative to Fig. 6.20, but similar comments as in the ungroomed case apply. The $R = 0.8$ versions of Fig. 6.20 and Fig. 6.21 are in Fig. B.6 and Fig. B.7.

Differential distributions for ungroomed angularities. While the averages are a convenient way to summarise the behaviour with varying jet p_T, there is clearly more information contained in the binned differential distributions for a given transverse momentum range. In making a selection of the p_T range, one has to compromise between the reliability of the perturbative prediction and statistical precision that the experimental measurement achieves. The first is improved by going to higher energy scales, while the cross section and hence the events available in experiment decrease for larger p_T. Both Ref. [145] and Ref. [IV] partially focused on the range 120 GeV $< p_T < 150$ GeV.

Figure 6.24: Les Houches angularity $\lambda_{0.5}$, for the jet in Z+jet (top left), the central (top right) and the forward (bottom) of the dijets.

The $\alpha = 2$ angularity is similar to the well studied jet mass, and might hence be expected to be understood the best. Fig. 6.22 shows the distribution of that observable, at the usual NLO + NLL' accuracy with non-perturbative corrections in the transverse momentum range mentioned above. The plots correspond to the leading jet in the Z+jet selection in the top left, and the central in the top right and forward dijet in the bottom sub-figure.

Comparing the three distributions, the two dijet variants look very similar, with almost no visible difference that could not be attributed to statistics. The histogram for the Z+jet selection is peaked somewhat stronger towards low values of λ_2 and then falls off quicker than in the dijet case as the angularity increases. In the dijet case on the other hand, the first and second bin are still compatible with each other, within the uncertainties of both data and theoretical prediction.

Overall the data follow the distribution predicted by the resummed calculation, at least within the uncertainties. The only exception is the very last bin. This corresponds to the endpoint region, *i.e.* the part of phase space that is only filled by extreme configurations. Those are often only possible kinematically at higher orders, where more particles are involved and hence the individual momenta are less restricted by conservation laws. In addition, since the cross section in this bin is very small, even a minor absolute change can have a significant relative effect.

Despite the good agreement between data and theory, a systematic trend is visible for the central value, which tends to overestimate the data in the small λ_2 region and underestimate it on the opposite end. This is visible for all three distributions to a certain degree. This results in the tentatively smaller average of the distribution observed before.

In this context it should be noted that the error band in Fig. 6.22 does not indicate any correlation between variations of the different bins. It is obtained by just taking all different scale variations and forming an envelope. There is however not necessarily a consistent choice of scales that produces an arbitrary combination of bin heights even within that envelope, since certain changes in the bin heights are correlated. This is particularly true for normalised distributions. The uncertainties of the averages are obtained by calculating them based on the final distribution corresponding to each variations considered. The spread of those results then defines the uncertainty of the average. This hence takes into account the correlation between different bins. It is therefore possible that the average appears to be inconsistent with the data, despite the comparison between data and theory being consistent for each individual bin according to the uncertainty envelope. Of course, since the differential distributions contain more information the opposite is also an option, vastly different distributions can lead to the same averages.

Equivalent plots for the $R = 0.8$ case can be found in Fig. B.8. Similar conclusions can be drawn in this case, however the uncertainties tend to be larger.

The results for the $\alpha = 1$ angularity in the same p_T range are shown in Fig. 6.23. Towards larger λ_1 values it can be observed that the distribution in the jet of the Z+jet selection falls off more quickly compared to the dijet case, as was the case for λ_2. The peak height is on similar levels for λ_1. In this case however the soft region is resolved better and it is visible that the differential cross section approaches zero in this range. This is happening slower in the Z+jet version, where the decrease is barely significant whereas it is dramatic for the two dijet distributions.
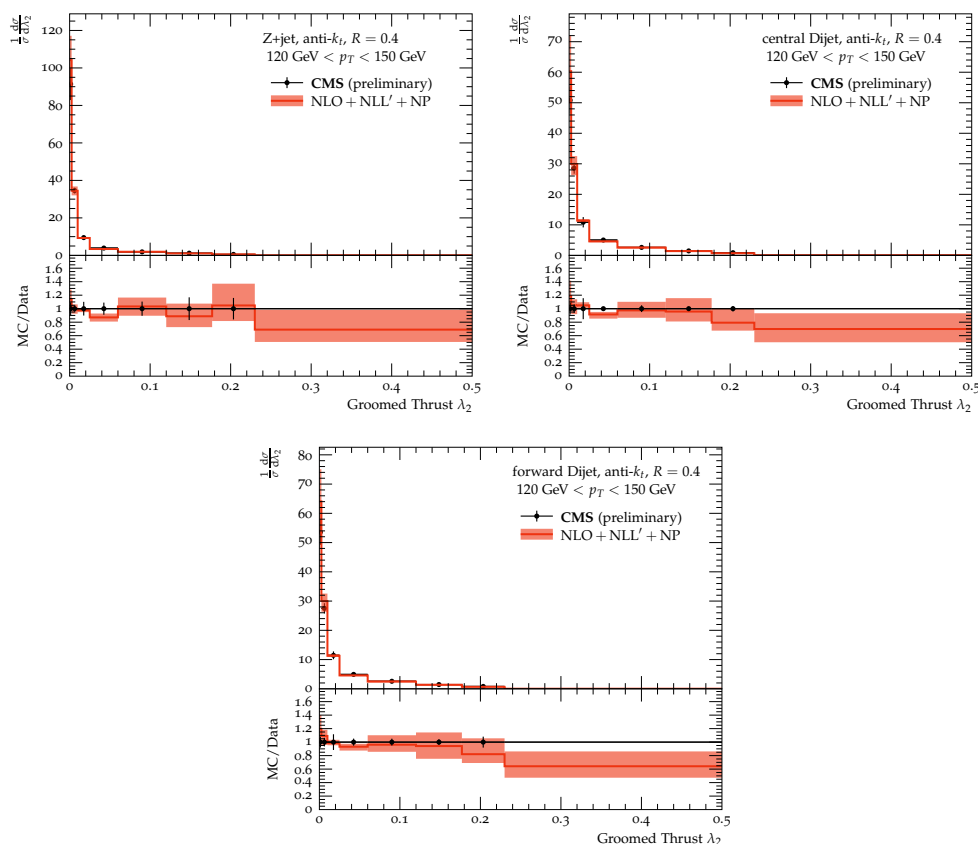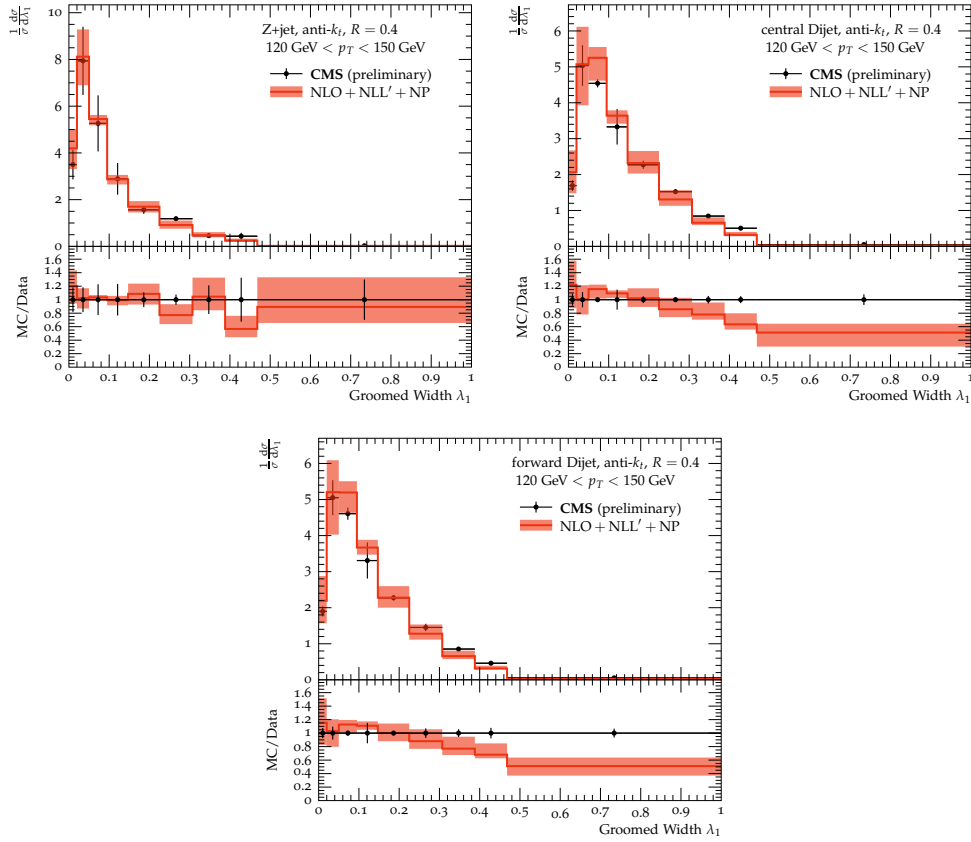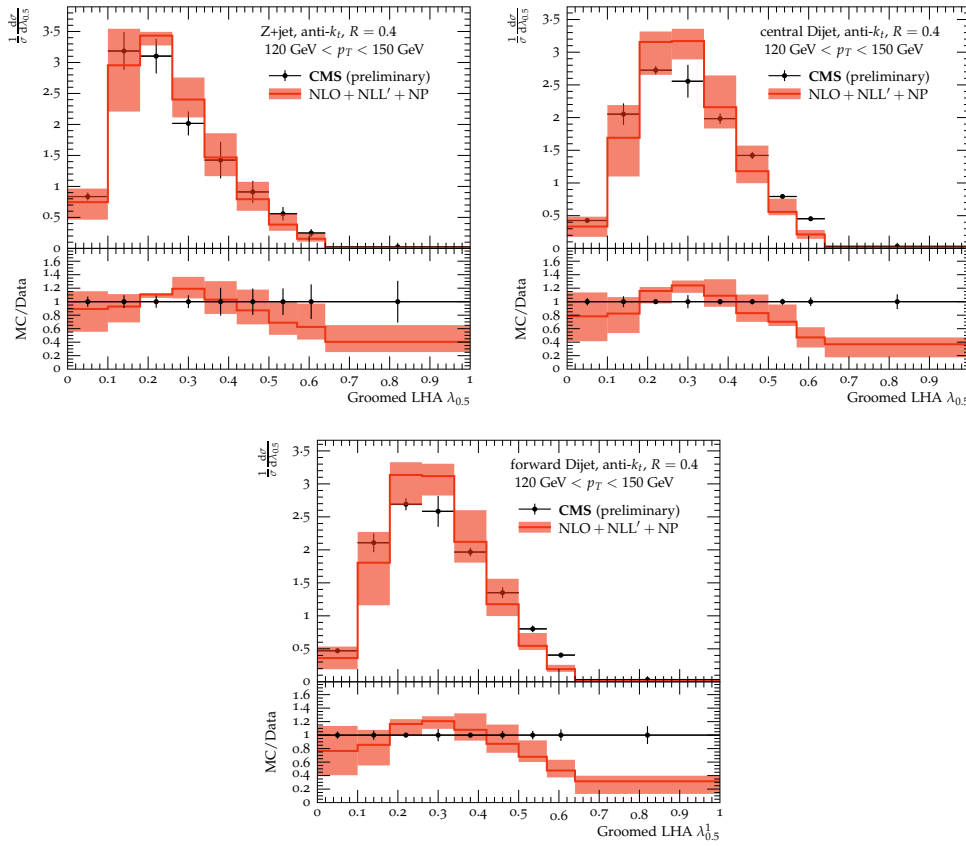
Figure 6.25: Groomed jet thrust λ_2, for the jet in Z+jet (top left), the central (top right) and the forward (bottom) of the dijets.

The data is consistent with the calculation in the Z+jet case, shown in the top left plot. The trend of the prediction being screwed towards smaller angularity values observed for the jet thrust is however even more pronounced. This is yet more the case for the two dijet options. Overall, this leads to $\approx 50\%$ deviations even if excluding the last bin, to which a similar discussion as in the $\lambda = 2$ case applies. The $R = 0.8$ distributions are collected in Fig. B.9.

Finally, there is the $\lambda = 0.5$ Les Houches angularity. The results for the three jet selections are presented in Fig. 6.24. The distribution measured in the Z+jet process raises steeply from the first to the second bin, which corresponds to the maximum for this example. The raise is somewhat slower in the dijet case where the maximum is correspondingly shifted to the right. The trend in the data to theory comparison continues and is more extreme. This is somewhat masked by the large relative uncertainty in the first bin present in all three cases. Towards large $\lambda_{0.5}$, the decrease in the cross

Figure 6.26: Groomed jet width λ_1, for the jet in Z+jet (top left), the central (top right) and the forward (bottom) of the dijets.

section is significantly faster in the resummed calculation compared to the data this times. This leads to significant differences in the last few bins even in the Z+jet case. The equivalent results for jet radius of $R = 0.8$ are in Fig. B.10.

Differential distributions for groomed angularities. In the case of the distribution of the averages, grooming lead to a general improvement of the data to theory comparison. The groomed versions of the angularities in the same 120 GeV < 150 GeV range as above are presented below. Note that the bin widths in terms of λ_α used in Ref. [145] for groomed observables differ compared to the histograms for the ungroomed angularities. A direct comparison of groomed against ungroomed distributions is thus not quite straightforward.

First, Fig. 6.25 illustrates the results for λ_2 after grooming. In the binning used, the data distribution is peaking very strongly in the first bin. This is reproduced in the

Figure 6.27: Groomed Les Houches angularity $\lambda_{0.5}$, for the jet in Z+jet (top left), the central (top right) and the forward (bottom) of the dijets.

theory prediction. In general, a similar agreement as in the ungroomed version is observed, which might be interpreted stronger due to the finer binning. The groomed jet thrust for the three jet versions can be found in Fig. B.11.

For the $\alpha = 1$ angularity corresponding to the jet width, the measurement on the groomed jets again allows for a finer resolution of the peak region. Still, the agreement between data and theory in this area is on the same level as before. The deficiencies in the large λ_1 tail is not resolved however. Since grooming is not active in that region, this should not really be expected in any case. Still, it should be noted that the agreement in the Z+jet case is almost perfect within the uncertainty of both data and theory.

Lastly, the predictions for $\lambda_{0.5}$ after grooming are compared to the CMS data in Fig. 6.27. Similar to the $\alpha = 1$ case, no significant improvement is observed in the region of large angularities. The finer resolution in the peak and soft tail region here however allows

for a different observation than before. In all other distributions considered so far the resummed calculation was overestimating the data for small λ_α, and underestimating the hard tail. In this case however, the central values tend to in fact underestimate the data in the soft and hard tail, while overestimating it in the peak region. Instead of a simple shift, the predicted distributions appear to be narrower than the measured ones. This might motivated the investigation of higher moments than just the average.

This effect is visible in all three versions of jet selections as well as in the measurement based on the $R = 0.8$ jets in Fig. B.13. A shift as observes before is in fact relatively easy to produce by an appropriate scale choice, so one might hope that this could relatively easily be resolved through insights into higher order corrections that might indicate more appropriate scale choices. This not the case for an increase of the width of the distributions as it would be required here. It should be noted that the Monte Carlo predictions made in Ref. [IV] differ in some cases significantly from the resummed distributions. Insights into the differences between parton shower algorithms and resummed calculations at similar accuracy might thus also contribute to the understanding next to genuine higher order calculations.

Summary and Outlook

This thesis reported on the implementation of automated resummation using the CAESAR formalism in the SHERPA framework, continuing the work started in Ref. [295]. Key developments presented here are

- the automated application of flavour sensitive matching schemes to achieve NLL′ accuracy, including the implementation of infrared safe flavour clustering algorithms and their validation,

- the extension of the framework towards soft drop groomed observables, including the calculation and implementation of the modified radiators and a discussion of the subtleties involved in the flavour assignment to the groomed final states,

- the inclusion of jet substructure observables, necessitating a more flexible calculation of the soft function, as well as additional developments in the flavour sensitive clustering algorithms necessary to separate different flavour channels,

- improvements in the standard to apply non-perturbative corrections obtained from hadron level Monte Carlo simulations to the resummed and matched calculations, using an approach based on transition matrices instead of simple ratios between parton and hadron levels,

- the first application of the framework to high multiplicity final states in e^+e^- annihilation, including studies on the effects of subleading colour corrections in Durham jet rates.

- the application of calculations to phenomenology at the LHC and comparison to data measured by the CMS experiment.

The other developments are also illustrated in concrete phenomenological studies. The presented analyses of QCD observables in electron positron collisions are not directly

applicable to measured data for various reasons. It should be noted however that this simpler collider setup is a common testing ground for parton shower developments, with systematic comparisons to resummed calculations being a recent driver of the community, see for example [385–389] as well as Ref. [VII], where the framework presented here could be used to produce additional benchmark results for example for higher multiplicity observables. The same applies to the development of showers taking into account subleading colour corrections, e.g. [357–365] and Ref. [VI]. On the other hand, re-analyses of LEP data might explore those observables. In that context the recent analysis of jet substructure using ALEPH data [390], including the soft drop groomed jet mass, is noteworthy.

A direct application towards phenomenology at the LHC was presented in Sec. 6.4. As a direct followup, Ref. [V] explored the application of those calculations to tag initial state flavours in the context of PDF fits. The framework is in principle set up to perform similar studies for other observables or other experimental setups. A possible further development would for example be the extension of the study detailed in Sec. 6.2 to an LHC setup, with the aim to derive predictions for analyses like [391]. Jet resolution scales have also been used in [392] to gauge different parton shower algorithms in the context of Higgs production via vector boson fusion. Providing benchmarks for this comparison is another possible future application of the framework discussed here.

Next to these immediate possible applications, calculations like the ones performed here will continue to play a major role in the future development of the field in general. The LHC is set to continue data taking in the upcoming years, including its high luminosity phase [393]. The planned electron ion collider (EIC) [267] will provide new data on deep inelastic scattering in the future. Despite no examples of this were explored here, the formalism is fully applicable to electron proton collisions, and no major hurdles should prevent a treatment within the SHERPA framework. Possible colliders yet further in the future include new generations of electron positron colliders [394–396], probing higher energy scales than the LEP experiments. This would in particular increase the range where the logarithmic corrections treated in the CAESAR formalism are important and undisturbed by non-perturbative physics. The same holds for possible future hadron colliders. Those will hence benefit from an easy availability of resummed calculations for a large set of observables. Conversely, they will benefit the theoretical calculations by providing precise data to validate them, and hopefully pose exciting challenges to the theory community.

Validation of fixed order results

This appendix collects additional results for the validation of the expansion of the resummed cross section as implemented in the SHERPA framework against fixed order calculations. See Sec. 5.5 for the interpretation and explanation of the comparisons in general.

Fig. A.1 shows the validation plots for the expansion of the cross sections for soft drop groomed observables. See Sec. 3.3 for an explanation of the soft drop parameters, Sec. 4.4 for the expressions entering the expansion, and Sec. 6.3 for the concrete setup of the calculation.

Fig. A.2 and Fig. A.3 show the validation plots for the expansion of the cross sections for jet substructure observables, with and without grooming. See Sec. 3.2 for the observable definition, Sec. 4.3 for the expression entering the expansion and Sec. 6.4 for the concrete setup of the calculation. The validation is performed for the $Z+$jet final state. Fig. A.2 shows the results for gluon jets, Fig. A.3 contains the same plots for quark jets. See Sec. 5.4 for the algorithm used to define quark and gluon jets in the higher order fixed order calculations.

Figure A.1: Comparison of the expansion of the NLL resummation and fixed-order results for soft-drop groomed thrust at LO and NLO accuracy. The lower panels show the difference between expansion and fixed order at LO and NLO.
Figure and caption taken from Figure 7 in Ref. [III].
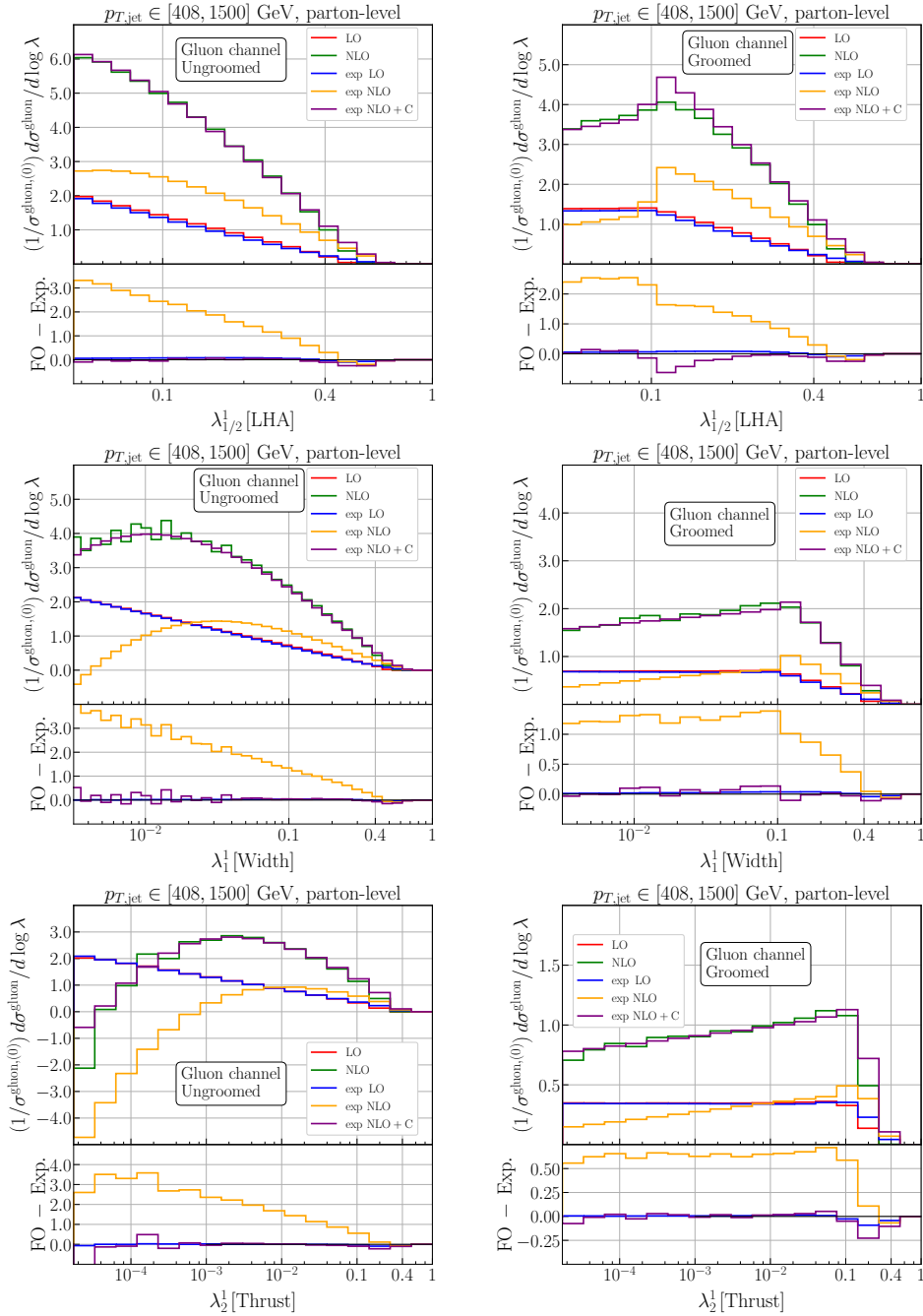
Figure A.2: Fixed-order predictions for the gluon channel, identified with the BSZ algorithm, for ungroomed (left column) and groomed (right column) angularities λ^1_α, for $\alpha \in \{1/2, 1, 2\}$, compared to the expansion of the resummation at the corresponding order of α_s, see text for details. The jet transverse momentum is constrained to $p_{T,\mathrm{jet}} \in [408, 1500]$ GeV. Figure and caption taken from Figure 6 of Ref. [IV].
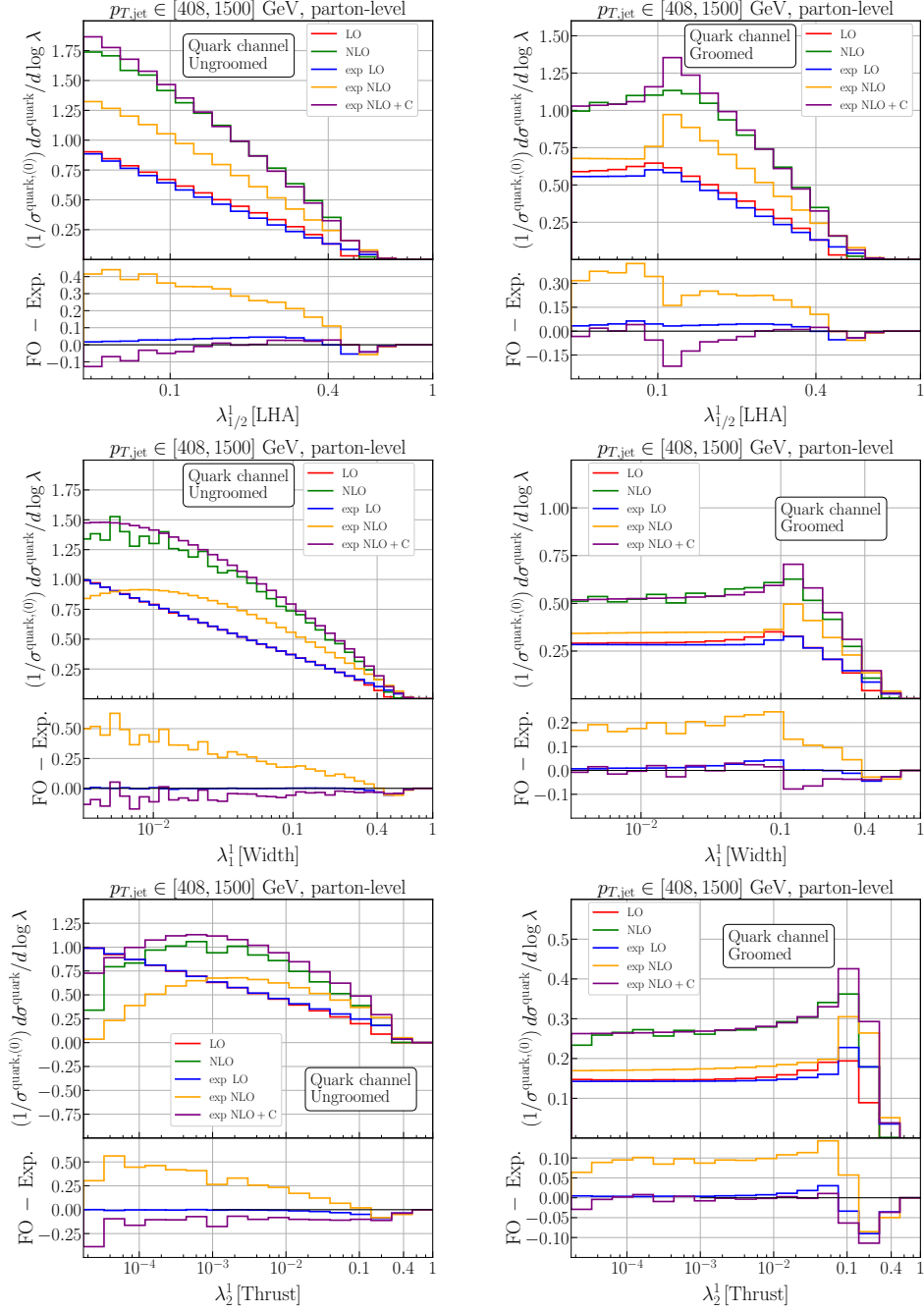
Figure A.3: Fixed-order predictions for the quark channel, identified with the BSZ algorithm, for ungroomed (left column) and groomed (right column) angularities λ^1_α, for $\alpha \in \{1/2, 1, 2\}$, compared to the expansion of the resummation at the corresponding order of α_s, see text for details. The jet transverse momentum is constrained to $p_{T,\text{jet}} \in [408, 1500]$ GeV. `Figure and caption taken from Figure 7 of Ref. [IV].`

Additional results for jet angularities

The following results for jet angularities are also available as referred to in the main text. See Sec. 6.4 for details of the setup.
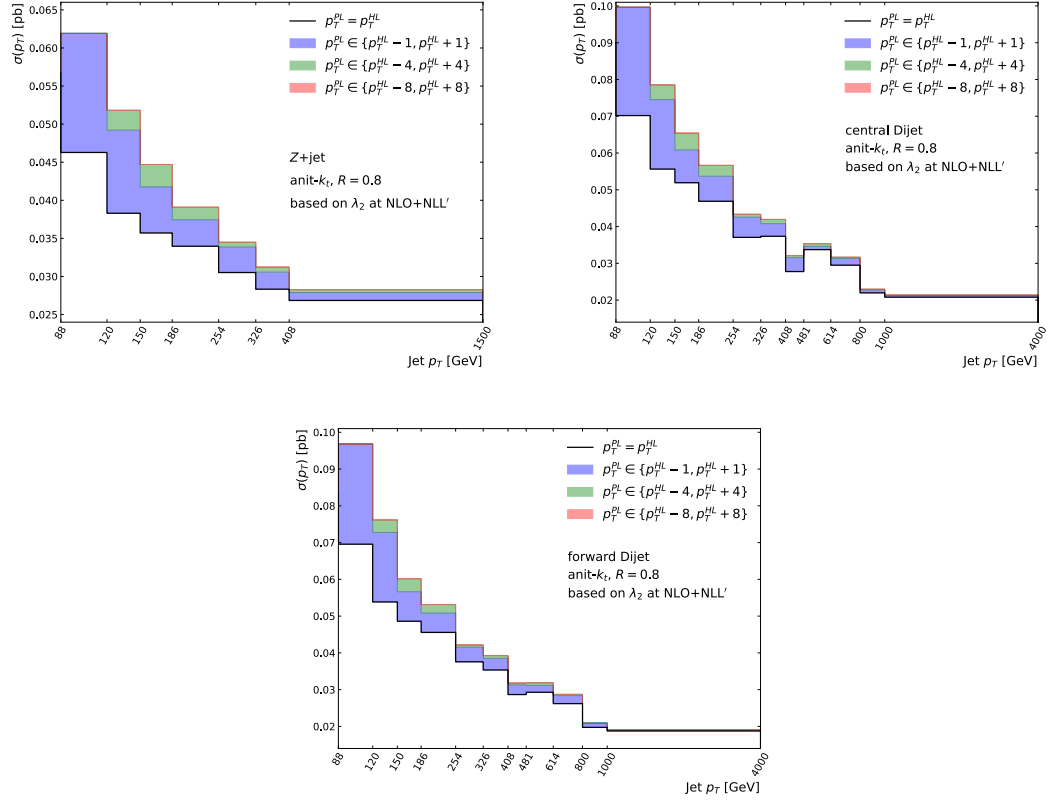
Figure B.1: Cross section in various p_T bins for the leading Z+jet, the central and the forward dijet (from left to right), obtained by applying transition matrices to the NLO + NLL′ distribution of λ_2. The colour coding represents the cross section where the transverse momentum is equal at hadron and parton level (white), where the hadron level p_T corresponds to migration by at most a single bin (blue), by up to 4 bins (green) and by up to 8 bins (red) relative to the parton level.
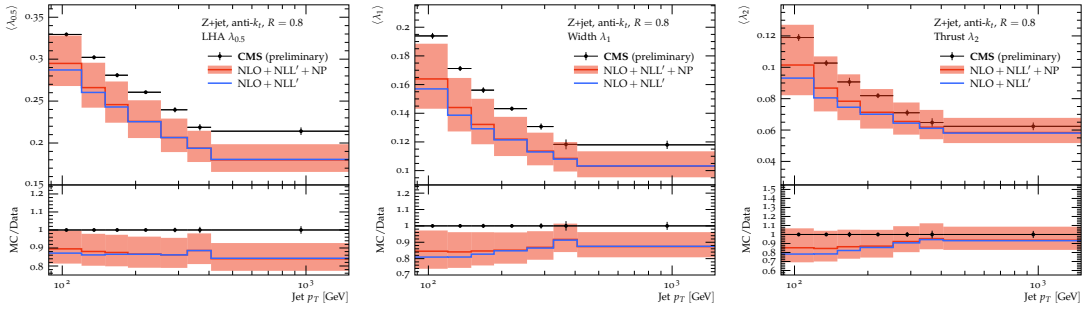
Figure B.2: Average distribution of the Les Houches angularity (left), width (middle) and thrust (right) of the leading $R = 0.8$ jet in the Z+jet selection. The blue curve excludes the non-perturbative migration between different p_T bins from the full calculation shown in red.
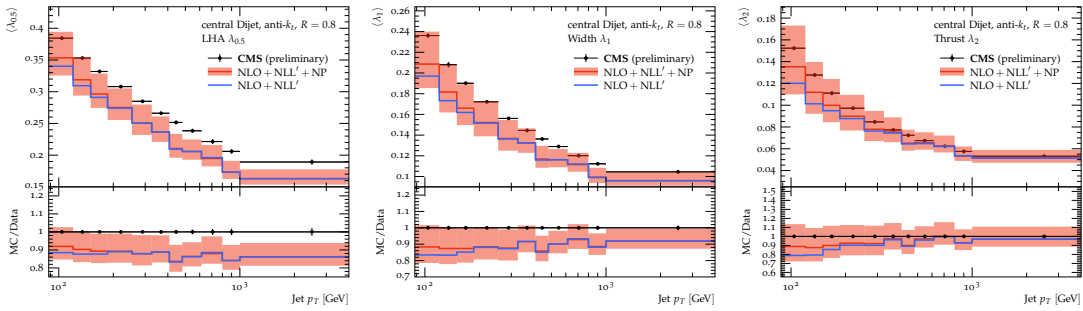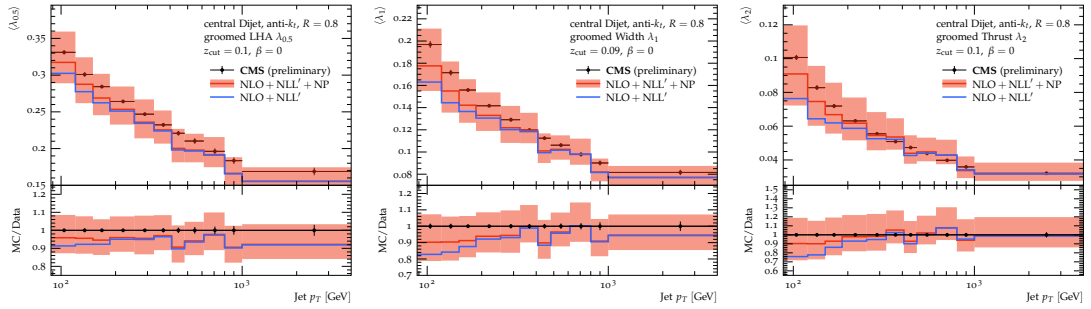

Figure B.3: Average distribution of the Les Houches angularity (left), width (middle) and thrust (right) of the leading $R = 0.8$ jet in the central dijet selection. The blue curve excludes the non-perturbative migration between different p_T bins from the full calculation shown in red.
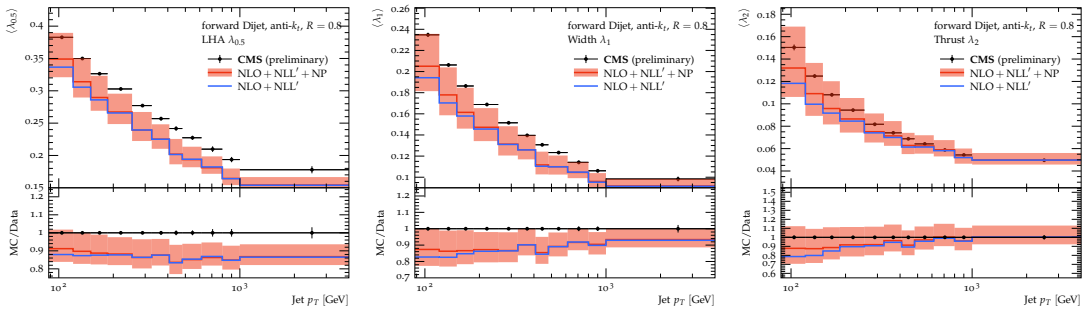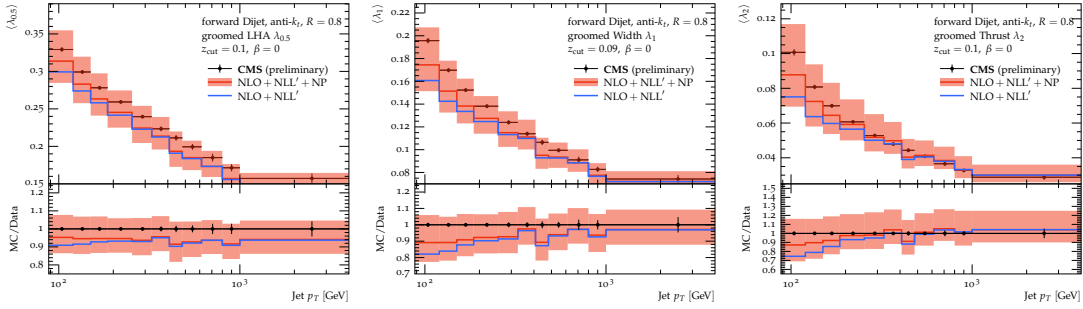

Figure B.4: Average distribution of the Les Houches angularity (left), width (middle) and thrust (right) of the leading $R = 0.8$ jet in the forward dijet selection. The blue curve excludes the non-perturbative migration between different p_T bins from the full calculation shown in red.
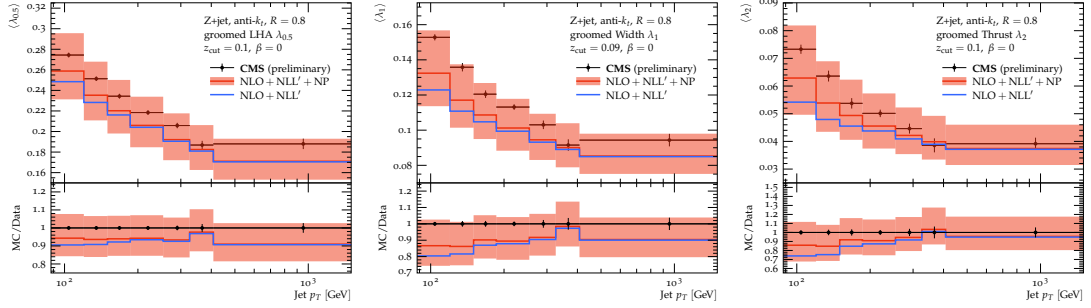
Figure B.5: Average distribution of the groomed Les Houches angularity (left), groomed width (middle) and groomed thrust (right) of the leading $R = 0.8$ jet in the Z+jet selection. The blue curve excludes the non-perturbative migration between different p_T bins from the full calculation shown in red.

Figure B.6: Average distribution of the groomed Les Houches angularity (left), groomed width (middle) and groomed thrust (right) of the leading $R = 0.8$ jet in the central dijet selection. The blue curve excludes the non-perturbative migration between different p_T bins from the full calculation shown in red.

Figure B.7: Average distribution of the groomed Les Houches angularity (left), groomed width (middle) and groomed thrust (right) of the leading $R = 0.8$ jet in the forward dijet selection. The blue curve excludes the non-perturbative migration between different p_T bins from the full calculation shown in red.
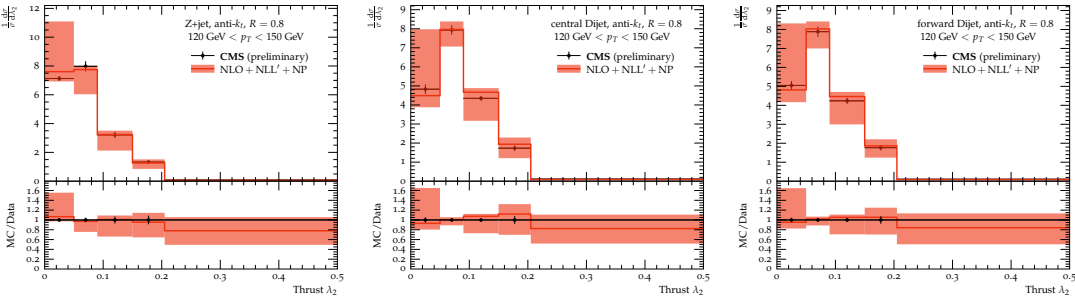
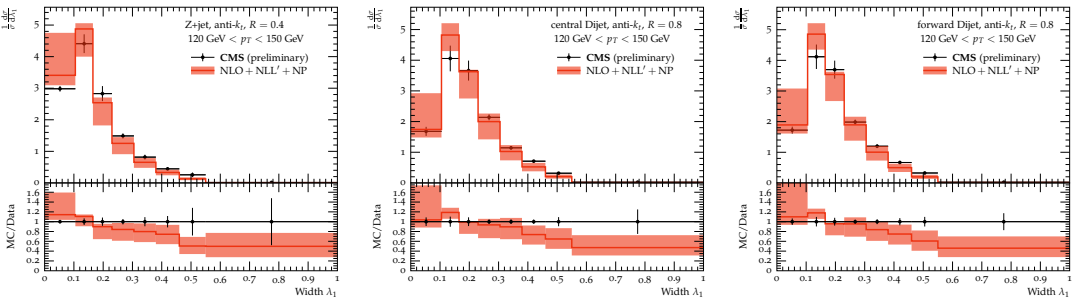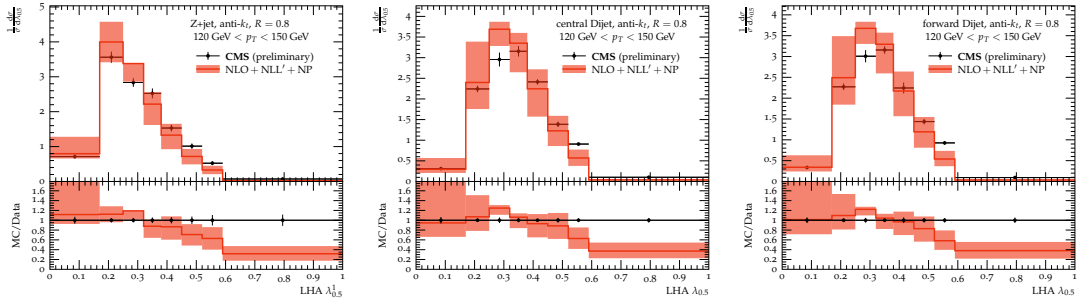**Figure B.8:** Jet thrust λ_2, for the jet in Z+jet (left), the central (middle) and the forward (right) of the dijets.

Figure B.9: Jet width λ_1, for the jet in Z+jet (left), the central (middle) and the forward (right) of the dijets.

Figure B.10: Les Houches angularity $\lambda_{0.5}$, for the jet in Z+jet (left), the central (middle) and the forward (right) of the dijets.
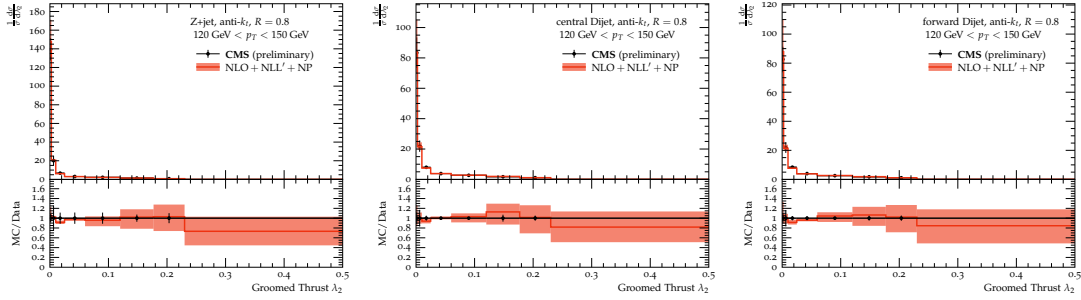

Figure B.11: Groomed jet thrust λ_2, for the jet in Z+jet (left), the central (middle) and the forward (right) of the dijets.
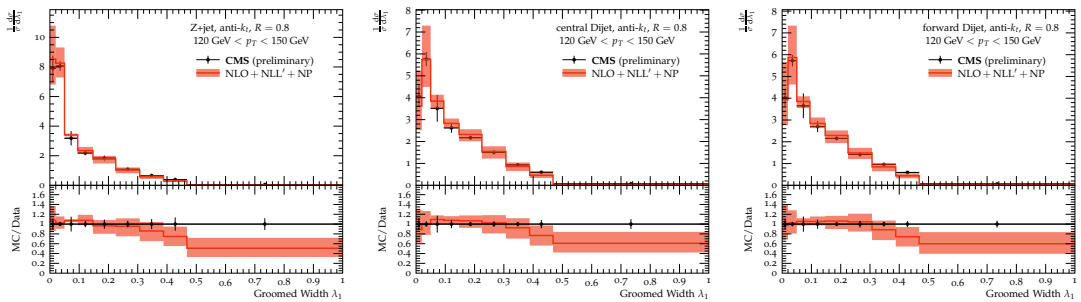

Figure B.12: Groomed jet width λ_1, for the jet in Z+jet (left), the central (middle) and the forward (right) of the dijets.
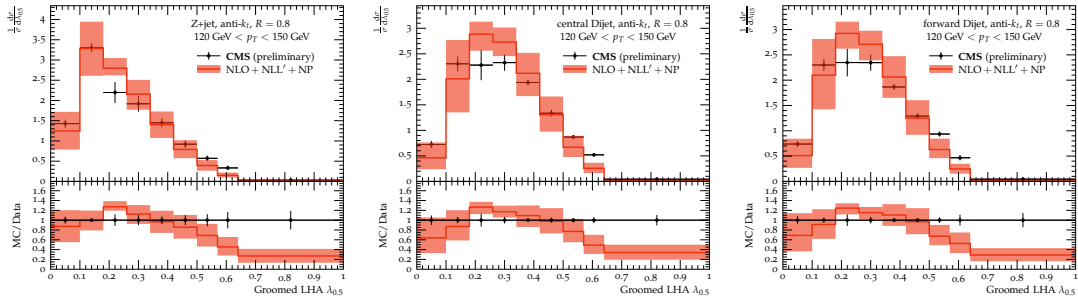
Figure B.13: Groomed Les Houches angularity $\lambda_{0.5}$, for the jet in Z+jet (left), the central (middle) and the forward (right) of the dijets.

References

[I]   S. Marzani, D. Reichelt, S. Schumann, G. Soyez, and V. Theeuwes, *Fitting the Strong Coupling Constant with Soft-Drop Thrust*, JHEP **11** (2019), 179

[II]   N. Baberuxki, C. T. Preuss, D. Reichelt, and S. Schumann, *Resummed predictions for jet-resolution scales in multijet production in e^+e^- annihilation*, JHEP **04** (2020), 112

[III]   by J. Baron, D. Reichelt, S. Schumann, N. Schwanemann, and V. Theeuwes, *Soft-drop grooming for hadronic event shapes*, JHEP **08** (2021), 142

[IV]   S. Caletti, O. Fedkevych, S. Marzani, D. Reichelt, S. Schumann, G. Soyez, and V. Theeuwes, *Jet Angularities in Z+jet production at the LHC*, JHEP **08** (2021), 76

[V]   S. Caletti, O. Fedkevych, S. Marzani and D. Reichelt, *Tagging the initial-state gluon*, [arXiv:2108.10024]

[VI]   S. Höche and D. Reichelt, *Numerical resummation at subleading color in the strongly ordered soft gluon limit*, Phys. Rev. D **104** (2021), 034006

[VII]   S. Höche, D. Reichelt and F. Siegert, *Momentum conservation and unitarity in parton showers and NLL resummation*, JHEP **01** (2018), 118

[VIII]   D. Reichelt, P. Richardson and A. Siodmok, *Improving the Simulation of Quark and Gluon Jets with Herwig 7*, Eur. Phys. J. C **77** (2017), no. 12, 876

[IX]   D. Reichelt, P. Richardson and A. Siodmok, *Colour Reconnections in Quark and Gluon Jets in Herwig 7*, Acta Phys. Polon. B **48** (2017), 1167-1173

[X]   D. Reichelt, *Comparison of analytical and parton-shower approaches to soft-gluon resummation at NLL accuracy*, Master's Thesis, Technische Universität Dresden, 2017

[XI]   D. Reichelt, *Studien zur Überprüfung der vorhergesagten Beziehung zwischen effektiven aQGC Parametern und expliziten Resonanzen*, Bachelor's Thesis, Technische Universität Dresden, 2014

[1] G. K. O'Neill, *Storage-Ring Synchrotron: Device for High-Energy Physics Research*, Phys. Rev. **102** (1956), 1418–1419.

[2] D. W. Kerst, F. T. Cole, H. R. Crane, L. W. Jones, L. J. Laslett, T. Ohkawa, A. M. Sessler, K. R. Symon, K. M. Terwilliger and N. V. Nilsen, *Attainment of very high-energy by means of intersecting beams of particles*, Phys. Rev. **102** (1956), 590–591.

[3] V. D. Shiltsev, *High energy particle colliders: past 20 years, next 20 years and beyond*, Phys. Usp. **55** (2012), 965–976, [`arXiv:1205.3087` [physics.acc-ph]].

[4] G. K. O'Neill, *Storage Rings For Electrons And Protons*, 2nd International Conference on High-Energy Accelerators, 1959.

[5] G. K. O'Neill, *Storage-Ring Work at Stanford*, eConf **C630610** (1963), 209.

[6] C. Bernardini, G. F. Corazza, G. Ghigo and B. Touschek, *The Frascati storage ring*, Nuovo Cim. **18** (1960), no. 6, 1293–1295.

[7] C. Bernardini, U. Bizzarri, G. F. Corazza, G. Ghigo, R. Querzoli and B. Touschek, *A 250-Mev Electron-Positron Storage Ring: The "A D A"*, 3rd International Conference on High-Energy Accelerators, 1961.

[8] C. Bernardini, G. F. Corazza, G. Di Giugno, G. Ghigo, R. Querzoli, J. Haissinski, P. Marin and B. Touschek, *Lifetime and beam size in a storage ring*, Phys. Rev. Lett. **10** (1963), 407–409.

[9] G. I. Budker and A. A. Naumov, *Work on electron - electron, positron - electron, and proton - proton colliding beams at the institute of nuclear physics of the siberian branch of the ussr academy of sciences, conference on high-energy particles, Dubna, 1963*.

[10] C. Bernardini, G. F. Corazza, G. Giugno, J. Haissinski, P. Marin, R. Querzoli and B. Touschek, *Measurements of the rate of interaction between stored electrons and positrons*, Nuovo Cim. **34** (1964), no. 6, 1473–1493.

[11] W. C. Barber, B. J. Gittelman, G. K. O'Neill and B. Richter, *A test of quantum electrodynamics by electron electron scattering*, Phys. Rev. Lett. **16** (1966), 1127–1130.

[12] C. Bernardini, *AdA:The first electron-positron collider*, Phys. Perspect. **6** (2004), 156–183.

[13] *Report on the design study of Intersecting Storage Rings (ISR) for the CERN proton synchrotron*, CERN, Geneva, 1964, French version available.

[14] K. Hubner, *The CERN Intersecting Storage Rings (ISR)*, Eur. Phys. J. H **36** (2012), 509–522.

[15] *SLAC Linear Collider Conceptual Design Report*.

[16] I. Abt et al., The H1 collaboration, *The H1 detector at HERA*.

[17] U. Holm, The ZEUS collaboration, *The ZEUS detector: Status report 1993*.

[18] E. P. Hartouni et al., *HERA-B: An experiment to study CP violation in the B system using an internal target at the HERA proton ring. Design report*.

[19] S. Abachi et al., The D0 collaboration, *The D0 Detector*, Nucl. Instrum. Meth. A **338** (1994), 185–253.

[20] F. Abe et al., The CDF collaboration, *The CDF Detector: An Overview*, Nucl. Instrum. Meth. A **271** (1988), 387–403.

[21] D. Decamp et al., The ALEPH collaboration, *ALEPH: A detector for electron-positron annnihilations at LEP*, Nucl. Instrum. Meth. A **294** (1990), 121–178, [Erratum: Nucl.Instrum.Meth.A 303, 393 (1991)].

[22] P. A. Aarnio et al., The DELPHI collaboration, *The DELPHI detector at LEP*, Nucl. Instrum. Meth. A **303** (1991), 233–276.

[23] K. Ahmet et al., The OPAL collaboration, *The OPAL detector at LEP*, Nucl. Instrum. Meth. A **305** (1991), 275–319.

[24] B. Adeva et al., The L3 collaboration, *The Construction of the L3 Experiment*, Nucl. Instrum. Meth. A **289** (1990), 35–102.

[25] G. Aad et al., The ATLAS collaboration, *The ATLAS Experiment at the CERN Large Hadron Collider*, JINST **3** (2008), S08003.

[26] S. Chatrchyan et al., The CMS collaboration, *The CMS Experiment at the CERN LHC*, JINST **3** (2008), S08004.

[27] A. A. Alves, Jr. et al., The LHCb collaboration, *The LHCb Detector at the LHC*, JINST **3** (2008), S08005.

[28] K. Aamodt et al., The ALICE collaboration, *The ALICE experiment at the CERN LHC*, JINST **3** (2008), S08002.

[29] T. Abe et al., The Belle-II collaboration, *Belle II Technical Design Report*, `arXiv:1011.0352` [physics.ins-det].

[30] P. Zyla et al., The Particle Data Group collaboration, *Review of Particle Physics*, PTEP **2020** (2020), no. 8, 083C01.

[31] R. D. Field, *Applications of perturbative QCD*, Addison-Wesley, Redwood City, USA, 1989, Frontiers in physics, 77.

[32] R. K. Ellis, W. J. Stirling and B. R. Webber, *QCD and collider physics*, ed. 1, vol. 8, Cambridge Monogr. Part. Phys. Nucl. Phys. Cosmol., 1996.

[33] Y. L. Dokshitzer, V. A. Khoze, A. H. Mueller and S. I. Troyan, *Basics of perturbative QCD*, Gif-sur-Yvette, France: Ed. Frontieres, 1991.

[34] G. F. Sterman, *An Introduction to quantum field theory*, Cambridge University Press, 8 1993.

[35] J. Collins, *Foundations of perturbative QCD*, Cambridge University Press, 2013.

[36] M. D. Schwartz, *Quantum Field Theory and the Standard Model*, Cambridge University Press, 3 2014.

[37] T. Schörner-Sadenius (Ed.), *The Large Hadron Collider*, Springer, Berlin, 2015.

[38] J. Campbell, J. Huston and F. Krauss, *The Black Book of Quantum Chromodynamics: A Primer for the LHC Era*, Oxford University Press, 12 2017.

[39] S. Marzani, G. Soyez and M. Spannowsky, *Looking inside jets: an introduction to jet substructure and boosted-object phenomenology*, vol. 958, Springer, 2019.

[40] G. F. Sterman, *Partons, factorization and resummation, TASI 95*, Theoretical Advanced Study Institute in Elementary Particle Physics (TASI 95): QCD and Beyond, 6 1995.

[41] G. Luisoni and S. Marzani, *QCD resummation for hadronic final states*, J. Phys. G **42** (2015), no. 10, 103101, [`arXiv:1505.04084` [hep-ph]].

[42] E. M. Riordan, *The Discovery of quarks*, Science **256** (1992), 1287–1293.

[43] S. Perantonis and C. Michael, *Static potentials and hybrid mesons from pure SU(3) lattice gauge theory*, Nucl. Phys. B **347** (1990), 854–868.

[44] G. S. Bali and K. Schilling, *Static quark - anti-quark potential: Scaling behavior and finite size effects in SU(3) lattice gauge theory*, Phys. Rev. D **46** (1992), 2636–2646.

[45] S. Necco and R. Sommer, *The N(f) = 0 heavy quark potential from short to intermediate distances*, Nucl. Phys. B **622** (2002), 328–346, [`hep-lat/0108008`].

[46] S. Weinberg, *A Model of Leptons*, Phys. Rev. Lett. **19** (1967), 1264–1266.

[47] A. Salam, *Weak and Electromagnetic Interactions*, Conf. Proc. **C680519** (1968), 367–377.

[48] S. L. Glashow, *Partial Symmetries of Weak Interactions*, Nucl. Phys. **22** (1961), 579–588.

[49] F. Englert and R. Brout, *Broken Symmetry and the Mass of Gauge Vector Mesons*, Phys. Rev. Lett. **13** (1964), 321–323.

[50] P. W. Higgs, *Broken Symmetries and the Masses of Gauge Bosons*, Phys. Rev. Lett. **13** (1964), 508–509.

[51] P. W. Higgs, *Broken symmetries, massless particles and gauge fields*, Phys. Lett. **12** (1964), 132–133.

[52] G. S. Guralnik, C. R. Hagen and T. W. B. Kibble, *Global Conservation Laws and Massless Particles*, Phys. Rev. Lett. **13** (1964), 585–587.

[53] P. W. Higgs, *Spontaneous Symmetry Breakdown without Massless Bosons*, Phys. Rev. **145** (1966), 1156–1163.

[54] M. Gell-Mann, *The Eightfold Way: A Theory of strong interaction symmetry*.

[55] Y. Ne'eman, *Derivation of strong interactions from a gauge invariance*, Nucl. Phys. **26** (1961), 222–229.

[56] M. Gell-Mann, *A Schematic Model of Baryons and Mesons*, Phys. Lett. **8** (1964), 214–215.

[57] G. Zweig, *An SU(3) model for strong interaction symmetry and its breaking. Version 2*, DEVELOPMENTS IN THE QUARK THEORY OF HADRONS. VOL. 1. 1964 - 1978 (D. B. Lichtenberg and S. P. Rosen, Eds.), Hadronic Press, 2 1964.

[58] E. Fermi, *Versuch einer Theorie der β-Strahlen. 1.*, Z. Phys. **88** (1934), 161–177.

[59] G. Aad et al., The ATLAS collaboration, *Observation of a new particle in the search for the Standard Model Higgs boson with the ATLAS detector at the LHC*, Phys. Lett. B **716** (2012), 1–29, [arXiv:1207.7214 [hep-ex]].

[60] S. Chatrchyan et al., The CMS collaboration, *Observation of a New Boson at a Mass of 125 GeV with the CMS Experiment at the LHC*, Phys. Lett. B **716** (2012), 30–61, [arXiv:1207.7235 [hep-ex]].

[61] F. Abe et al., The CDF collaboration, *Observation of top quark production in $\bar{p}p$ collisions*, Phys. Rev. Lett. **74** (1995), 2626–2631, [hep-ex/9503002].

[62] S. Abachi et al., The D0 collaboration, *Observation of the top quark*, Phys. Rev. Lett. **74** (1995), 2632–2637, [hep-ex/9503003].

[63] M. Breidenbach, J. I. Friedman, H. W. Kendall, E. D. Bloom, D. H. Coward, H. C. DeStaebler, J. Drees, L. W. Mo and R. E. Taylor, *Observed behavior of highly inelastic electron-proton scattering*, Phys. Rev. Lett. **23** (1969), 935–939.

[64] E. D. Bloom et al., *High-Energy Inelastic e p Scattering at 6-Degrees and 10-Degrees*, Phys. Rev. Lett. **23** (1969), 930–934.

[65] G. Miller et al., *Inelastic electron-Proton Scattering at Large Momentum Transfers*, Phys. Rev. D **5** (1972), 528.

[66] J. D. Bjorken, *Asymptotic Sum Rules at Infinite Momentum*, Phys. Rev. **179** (1969), 1547–1553.

[67] R. P. Feynman, *Photon-hadron interactions*.

[68] J. D. Bjorken and E. A. Paschos, *Inelastic Electron Proton and gamma Proton Scattering, and the Structure of the Nucleon*, Phys. Rev. **185** (1969), 1975–1982.

[69] J. Kuti and V. F. Weisskopf, *Inelastic lepton - nucleon scattering and lepton pair production in the relativistic quark parton model*, Phys. Rev. D **4** (1971), 3418–3439.

[70] E. M. Riordan, A. Bodek, M. Breidenbach, D. L. Dubin, J. E. Elias, J. I. Friedman, H. W. Kendall, J. S. Poucher, M. R. Sogard and D. H. Coward, *Extraction of r = Sigma(L)/ Sigma(T) from Deep Inelastic e p and e d Cross-Sections*, Phys. Rev. Lett. **33** (1974), 561.

[71] A. Bodek et al., *Experimental Studies of the Neutron and Proton Electromagnetic Structure Functions*, Phys. Rev. D **20** (1979), 1471–1552.

[72] C.-N. Yang and R. L. Mills, *Conservation of Isotopic Spin and Isotopic Gauge Invariance*, Phys. Rev. **96** (1954), 191–195.

[73] J. C. Collins, D. E. Soper and G. F. Sterman, *Factorization of Hard Processes in QCD*, Adv. Ser. Direct. High Energy Phys. **5** (1989), 1–91, [hep-ph/0409313].

[74] M. E. Peskin and D. V. Schroeder, *An Introduction to quantum field theory*, Addison-Wesley, Reading, USA, 1995.

[75] H. Lehmann, K. Symanzik and W. Zimmermann, *On the formulation of quantized field theories*, Nuovo Cim. **1** (1955), 205–225.

[76] R. Haag, *Quantum field theories with composite particles and asymptotic conditions*, Phys. Rev. **112** (1958), 669–673.

[77] H. Araki, K. Hepp and D. Ruelle, *On the asymptotic behaviour of Wightman functions in space-like directions*, Helv. Phys. Acta **35** (1962), no. III, 164–174.

[78] G. Passarino and M. J. G. Veltman, *One Loop Corrections for e+ e- Annihilation Into mu+ mu- in the Weinberg Model*, Nucl. Phys. B **160** (1979), 151–207.

[79] D. J. Gross and F. Wilczek, *Ultraviolet Behavior of Nonabelian Gauge Theories*, Phys. Rev. Lett. **30** (1973), 1343–1346.

[80] H. D. Politzer, *Reliable Perturbative Results for Strong Interactions?*, Phys. Rev. Lett. **30** (1973), 1346–1349.

[81] L. D. Landau, *On analytic properties of vertex parts in quantum field theory*, Nucl. Phys. **13** (1959), no. 1, 181–192.

[82] B. Andersson, G. Gustafson, L. Lönnblad and U. Pettersson, *Coherence Effects in Deep Inelastic Scattering*, Z. Phys. C **43** (1989), 625.

[83] G. Gustafson, *Multiplicity distributions in QCD cascades*, Nucl. Phys. B **392** (1993), 251–280.

[84] T. Kinoshita, *Mass singularities of Feynman amplitudes*, J. Math. Phys. **3** (1962), 650–677.

[85] T. D. Lee and M. Nauenberg, *Degenerate Systems and Mass Singularities*, Phys. Rev. **133** (1964), B1549–B1562.

[86] F. Bloch and A. Nordsieck, *Note on the Radiation Field of the electron*, Phys. Rev. **52** (1937), 54–59.

[87] R. E. Cutkosky, *Singularities and discontinuities of Feynman amplitudes*, J. Math. Phys. **1** (1960), 429–433.

[88] A. Banfi, G. P. Salam and G. Zanderighi, *Principles of general final-state resummation and automated implementation*, JHEP **03** (2005), 073, [`hep-ph/0407286`].

[89] G. Altarelli and G. Parisi, *Asymptotic Freedom in Parton Language*, Nucl. Phys. B **126** (1977), 298–318.

[90] V. N. Gribov and L. N. Lipatov, *Deep inelastic e p scattering in perturbation theory*, Sov. J. Nucl. Phys. **15** (1972), 438–450.

[91] L. N. Lipatov, *The parton model and perturbation theory*, Yad. Fiz. **20** (1974), 181–198.

[92] Y. L. Dokshitzer, *Calculation of the Structure Functions for Deep Inelastic Scattering and e+ e- Annihilation by Perturbation Theory in Quantum Chromodynamics.*, Sov. Phys. JETP **46** (1977), 641–653.

[93] E. Farhi, *A QCD Test for Jets*, Phys. Rev. Lett. **39** (1977), 1587–1588.

[94] G. F. Sterman and S. Weinberg, *Jets from Quantum Chromodynamics*, Phys. Rev. Lett. **39** (1977), 1436.

[95] V. Coco, P.-A. Delsart, J. Rojo-Chacon, G. Soyez and C. Sander, *Jets and jet algorithms*, HERA and the LHC: 4th Workshop on the Implications of HERA for LHC Physics, 3 2009.

[96] G. P. Salam and G. Soyez, *A Practical Seedless Infrared-Safe Cone jet algorithm*, JHEP **05** (2007), 086, [`arXiv:0704.0292 [hep-ph]`].

[97] W. Bartel et al., The JADE collaboration, *Experimental Studies on Multi-Jet Production in e+ e- Annihilation at PETRA Energies*, Z. Phys. C **33** (1986), 23.

[98] S. Bethke et al., The JADE collaboration, *Experimental Investigation of the Energy Dependence of the Strong Coupling Strength*, Phys. Lett. B **213** (1988), 235–241.

[99] S. Catani, Y. L. Dokshitzer, M. Olsson, G. Turnock and B. R. Webber, *New clustering algorithm for multi - jet cross-sections in e+ e- annihilation*, Phys. Lett. B **269** (1991), 432–438.

[100] N. Brown and W. J. Stirling, *Finding jets and summing soft gluons: A New algorithm*, Z. Phys. C **53** (1992), 629–636.

[101] S. Bethke, Z. Kunszt, D. E. Soper and W. J. Stirling, *New jet cluster algorithms: Next-to-leading order QCD and hadronization corrections*, Nucl. Phys. B **370** (1992), 310–334, [Erratum: Nucl.Phys.B 523, 681–681 (1998)].

[102] S. Catani, Y. L. Dokshitzer, M. H. Seymour and B. R. Webber, *Longitudinally invariant K_t clustering algorithms for hadron hadron collisions*, Nucl. Phys. B **406** (1993), 187–224.

[103] S. D. Ellis and D. E. Soper, *Successive combination jet algorithm for hadron collisions*, Phys. Rev. D **48** (1993), 3160–3166, [hep-ph/9305266].

[104] Y. L. Dokshitzer, G. D. Leder, S. Moretti and B. R. Webber, *Better jet clustering algorithms*, JHEP **08** (1997), 001, [hep-ph/9707323].

[105] M. Wobisch and T. Wengler, *Hadronization corrections to jet cross-sections in deep inelastic scattering*, Workshop on Monte Carlo Generators for HERA Physics (Plenary Starting Meeting), 4 1998, pp. 270–279.

[106] M. Cacciari, G. P. Salam and G. Soyez, *The anti-k_t jet clustering algorithm*, JHEP **04** (2008), 063, [arXiv:0802.1189 [hep-ph]].

[107] M. Cacciari, G. P. Salam and G. Soyez, *FastJet User Manual*, Eur. Phys. J. C **72** (2012), 1896, [arXiv:1111.6097 [hep-ph]].

[108] M. Dasgupta, K. Khelifa-Kerfa, S. Marzani and M. Spannowsky, *On jet mass distributions in Z+jet and dijet processes at the LHC*, JHEP **10** (2012), 126, [arXiv:1207.1640 [hep-ph]].

[109] Y.-T. Chien, R. Kelley, M. D. Schwartz and H. X. Zhu, *Resummation of Jet Mass at Hadron Colliders*, Phys. Rev. D **87** (2013), no. 1, 014010, [arXiv:1208.0010 [hep-ph]].

[110] T. T. Jouttenus, I. W. Stewart, F. J. Tackmann and W. J. Waalewijn, *Jet mass spectra in Higgs boson plus one jet at next-to-next-to-leading logarithmic order*, Phys. Rev. D **88** (2013), no. 5, 054031, [arXiv:1302.0846 [hep-ph]].

[111] Z. L. Liu, C. S. Li, J. Wang and Y. Wang, *Resummation prediction on the jet mass spectrum in one-jet inclusive production at the LHC*, JHEP **04** (2015), 005, [arXiv:1412.1337 [hep-ph]].

[112] Z.-B. Kang, K. Lee, X. Liu and F. Ringer, *The groomed and ungroomed jet mass distribution for inclusive jet production at the LHC*, JHEP **10** (2018), 137, [arXiv:1803.03645 [hep-ph]].

[113] M. Balsiger, T. Becher and D. Y. Shao, *NLL′ resummation of jet mass*, JHEP **04** (2019), 020, [arXiv:1901.09038 [hep-ph]].

[114] N. Ziani, K. Khelifa-Kerfa and Y. Delenda, *Jet mass distribution in Higgs/vector boson + jet events at hadron colliders with k_t clustering*, Eur. Phys. J. C **81** (2021), 570, [arXiv:2104.11060 [hep-ph]].

[115] T. Aaltonen et al., The CDF collaboration, *Study of Substructure of High Transverse Momentum Jets Produced in Proton-Antiproton Collisions at $\sqrt{s} = 1.96$ TeV*, Phys. Rev. D **85** (2012), 091101, [`arXiv:1106.5952 [hep-ex]`].

[116] G. Aad et al., The ATLAS collaboration, *Jet mass and substructure of inclusive jets in $\sqrt{s} = 7$ TeV pp collisions with the ATLAS experiment*, JHEP **05** (2012), 128, [`arXiv:1203.4606 [hep-ex]`].

[117] S. Chatrchyan et al., The CMS collaboration, *Studies of Jet Mass in Dijet and W/Z + Jet Events*, JHEP **05** (2013), 090, [`arXiv:1303.4811 [hep-ex]`].

[118] A. M. Sirunyan et al., The CMS collaboration, *Measurement of the jet mass in highly boosted $t\bar{t}$ events from pp collisions at $\sqrt{s} = 8$ TeV*, Eur. Phys. J. C **77** (2017), no. 7, 467, [`arXiv:1703.06330 [hep-ex]`].

[119] A. M. Sirunyan et al., The CMS collaboration, *Measurements of the differential jet cross section as a function of the jet mass in dijet events from proton-proton collisions at $\sqrt{s} = 13$ TeV*, JHEP **11** (2018), 113, [`arXiv:1807.05974 [hep-ex]`].

[120] M. Abdallah et al., The STAR collaboration, *Invariant Jet Mass Measurements in pp Collisions at $\sqrt{s} = 200$ GeV at RHIC*, `arXiv:2103.13286 [hep-ex]`.

[121] A. Abdesselam et al., *Boosted Objects: A Probe of Beyond the Standard Model Physics*, Eur. Phys. J. C **71** (2011), 1661, [`arXiv:1012.5412 [hep-ph]`].

[122] A. Altheimer et al., *Boosted Objects and Jet Substructure at the LHC. Report of BOOST2012, held at IFIC Valencia, 23rd-27th of July 2012*, Eur. Phys. J. C **74** (2014), no. 3, 2792, [`arXiv:1311.2708 [hep-ex]`].

[123] D. Adams et al., *Towards an Understanding of the Correlations in Jet Substructure*, Eur. Phys. J. C **75** (2015), no. 9, 409, [`arXiv:1504.00679 [hep-ph]`].

[124] A. J. Larkoski, J. Thaler and W. J. Waalewijn, *Gaining (Mutual) Information about Quark/Gluon Discrimination*, JHEP **11** (2014), 129, [`arXiv:1408.3122 [hep-ph]`].

[125] D. Bertolini, T. Chan and J. Thaler, *Jet Observables Without Jet Algorithms*, JHEP **04** (2014), 013, [`arXiv:1310.7584 [hep-ph]`].

[126] A. J. Larkoski, D. Neill and J. Thaler, *Jet Shapes with the Broadening Axis*, JHEP **04** (2014), 017, [`arXiv:1401.2158 [hep-ph]`].

[127] A. J. Larkoski, G. P. Salam and J. Thaler, *Energy Correlation Functions for Jet Substructure*, JHEP **06** (2013), 108, [`arXiv:1305.0007 [hep-ph]`].

[128] L. G. Almeida, S. J. Lee, G. Perez, G. F. Sterman, I. Sung and J. Virzi, *Substructure of high-p_T Jets at the LHC*, Phys. Rev. D **79** (2009), 074017, [arXiv:0807.0234 [hep-ph]].

[129] S. D. Ellis, C. K. Vermilion, J. R. Walsh, A. Hornig and C. Lee, *Jet Shapes and Jet Algorithms in SCET*, JHEP **11** (2010), 101, [arXiv:1001.0014 [hep-ph]].

[130] A. Hornig, Y. Makris and T. Mehen, *Jet Shapes in Dijet Events at the LHC in SCET*, JHEP **04** (2016), 097, [arXiv:1601.01319 [hep-ph]].

[131] Z.-B. Kang, K. Lee and F. Ringer, *Jet angularity measurements for single inclusive jet production*, JHEP **04** (2018), 110, [arXiv:1801.00790 [hep-ph]].

[132] E.-C. Aschenauer, K. Lee, B. S. Page and F. Ringer, *Jet angularities in photoproduction at the Electron-Ion Collider*, Phys. Rev. D **101** (2020), no. 5, 054028, [arXiv:1910.11460 [hep-ph]].

[133] D. Kang, T. Maji and J. Zhu, *Angularity in DIS at next-to-next-to-leading log accuracy*, arXiv:2106.14429 [hep-ph].

[134] A. J. Larkoski, I. Moult and B. Nachman, *Jet Substructure at the Large Hadron Collider: A Review of Recent Advances in Theory and Machine Learning*, Phys. Rept. **841** (2020), 1–63, [arXiv:1709.04464 [hep-ph]].

[135] A. J. Larkoski, S. Marzani, G. Soyez and J. Thaler, *Soft Drop*, JHEP **05** (2014), 146, [arXiv:1402.2657 [hep-ph]].

[136] C. Frye, A. J. Larkoski, M. D. Schwartz and K. Yan, *Factorization for groomed jet substructure beyond the next-to-leading logarithm*, JHEP **07** (2016), 064, [arXiv:1603.09338 [hep-ph]].

[137] J. M. Butterworth, A. R. Davison, M. Rubin and G. P. Salam, *Jet substructure as a new Higgs search channel at the LHC*, Phys. Rev. Lett. **100** (2008), 242001, [arXiv:0802.2470 [hep-ph]].

[138] J. Baron, S. Marzani and V. Theeuwes, *Soft-Drop Thrust*, JHEP **08** (2018), 105, [arXiv:1803.04719 [hep-ph]], [Erratum: JHEP 05, 056 (2019)].

[139] M. Dasgupta, A. Fregoso, S. Marzani and A. Powling, *Jet substructure with analytical methods*, Eur. Phys. J. C **73** (2013), no. 11, 2623, [arXiv:1307.0013 [hep-ph]].

[140] C. Frye, A. J. Larkoski, M. D. Schwartz and K. Yan, *Precision physics with pile-up insensitive observables*, arXiv:1603.06375 [hep-ph].

[141] S. Marzani, L. Schunk and G. Soyez, *The jet mass distribution after Soft Drop*, Eur. Phys. J. C **78** (2018), no. 2, 96, [arXiv:1712.05105 [hep-ph]].

[142] S. Marzani, L. Schunk and G. Soyez, *A study of jet mass distributions with grooming*, JHEP **07** (2017), 132, [arXiv:1704.02210 [hep-ph]].

[143] G. Aad et al., The ATLAS collaboration, *Measurement of soft-drop jet observables in pp collisions with the ATLAS detector at $\sqrt{s}$ =13 TeV*, Phys. Rev. D **101** (2020), no. 5, 052007, [arXiv:1912.09837 [hep-ex]].

[144] M. Aaboud et al., The ATLAS collaboration, *Measurement of jet-substructure observables in top quark, W boson and light jet production in proton-proton collisions at $\sqrt{s} = 13$ TeV with the ATLAS detector*, JHEP **08** (2019), 033, [arXiv:1903.02942 [hep-ex]].

[145] The CMS collaboration, *Study of quark and gluon jet substructure in dijet and Z+jet events from pp collisions*.

[146] Z.-B. Kang, K. Lee, X. Liu and F. Ringer, *Soft drop groomed jet angularities at the LHC*, Phys. Lett. B **793** (2019), 41–47, [arXiv:1811.06983 [hep-ph]].

[147] S. Höche, *Introduction to parton-shower event generators*, Theoretical Advanced Study Institute in Elementary Particle Physics: Journeys Through the Precision Frontier: Amplitudes for Colliders, 11 2014.

[148] S. Catani and M. H. Seymour, *A General algorithm for calculating jet cross-sections in NLO QCD*, Nucl. Phys. B **485** (1997), 291–419, [hep-ph/9605323], [Erratum: Nucl.Phys.B 510, 503–504 (1998)].

[149] S. Catani, S. Dittmaier, M. H. Seymour and Z. Trocsanyi, *The Dipole formalism for next-to-leading order QCD calculations with massive partons*, Nucl. Phys. B **627** (2002), 189–265, [hep-ph/0201036].

[150] T. Gleisberg and F. Krauss, *Automating dipole subtraction for QCD NLO calculations*, Eur. Phys. J. C **53** (2008), 501–523, [arXiv:0709.2881 [hep-ph]].

[151] C. F. Berger, Z. Bern, L. J. Dixon, F. Febres Cordero, D. Forde, H. Ita, D. A. Kosower and D. Maitre, *An Automated Implementation of On-Shell Methods for One-Loop Amplitudes*, Phys. Rev. D **78** (2008), 036003, [arXiv:0803.4180 [hep-ph]].

[152] C. F. Berger, Z. Bern, L. J. Dixon, F. Febres Cordero, D. Forde, T. Gleisberg, H. Ita, D. A. Kosower and D. Maitre, *Next-to-Leading Order QCD Predictions for W+3-Jet Distributions at Hadron Colliders*, Phys. Rev. D **80** (2009), 074036, [arXiv:0907.1984 [hep-ph]].

[153] C. F. Berger, Z. Bern, L. J. Dixon, F. Febres Cordero, D. Forde, T. Gleisberg, H. Ita, D. A. Kosower and D. Maitre, *Next-to-Leading Order QCD Predictions for $Z, \gamma^* + 3$-Jet Distributions at the Tevatron*, Phys. Rev. D **82** (2010), 074002, [`arXiv:1004.1659 [hep-ph]`].

[154] C. F. Berger, Z. Bern, L. J. Dixon, F. Febres Cordero, D. Forde, T. Gleisberg, H. Ita, D. A. Kosower and D. Maitre, *Precise Predictions for W + 4 Jet Production at the Large Hadron Collider*, Phys. Rev. Lett. **106** (2011), 092001, [`arXiv:1009.2338 [hep-ph]`].

[155] J. M. Campbell and R. K. Ellis, *An Update on vector boson pair production at hadron colliders*, Phys. Rev. D **60** (1999), 113006, [`hep-ph/9905386`].

[156] J. M. Campbell, R. K. Ellis and C. Williams, *Vector boson pair production at the LHC*, JHEP **07** (2011), 018, [`arXiv:1105.0020 [hep-ph]`].

[157] J. Campbell and T. Neumann, *Precision Phenomenology with MCFM*, JHEP **12** (2019), 034, [`arXiv:1909.09117 [hep-ph]`].

[158] J. M. Campbell, S. Höche and C. T. Preuss, *Accelerating LHC phenomenology with analytic one-loop amplitudes: A C++ interface to MCFM*, `arXiv:2107.04472 [hep-ph]`.

[159] J. Alwall, P. Demin, S. de Visscher, R. Frederix, M. Herquet, F. Maltoni, T. Plehn, D. L. Rainwater and T. Stelzer, *MadGraph/MadEvent v4: The New Web Generation*, JHEP **09** (2007), 028, [`arXiv:0706.2334 [hep-ph]`].

[160] V. Hirschi, R. Frederix, S. Frixione, M. V. Garzelli, F. Maltoni and R. Pittau, *Automation of one-loop QCD corrections*, JHEP **05** (2011), 044, [`arXiv:1103.0621 [hep-ph]`].

[161] J. Alwall, R. Frederix, S. Frixione, V. Hirschi, F. Maltoni, O. Mattelaer, H. S. Shao, T. Stelzer, P. Torrielli and M. Zaro, *The automated computation of tree-level and next-to-leading order differential cross sections, and their matching to parton shower simulations*, JHEP **07** (2014), 079, [`arXiv:1405.0301 [hep-ph]`].

[162] G. Cullen, N. Greiner, G. Heinrich, G. Luisoni, P. Mastrolia, G. Ossola, T. Reiter and F. Tramontano, *GoSam: A Program for Automated One-Loop Calculations*, J. Phys. Conf. Ser. **368** (2012), 012056, [`arXiv:1111.6534 [hep-ph]`].

[163] G. Cullen et al., *GOSAM-2.0: a tool for automated one-loop calculations within the Standard Model and beyond*, Eur. Phys. J. C **74** (2014), no. 8, 3001, [`arXiv:1404.7096 [hep-ph]`].

[164] S. Badger, B. Biedermann, P. Uwer and V. Yundin, *Numerical evaluation of virtual corrections to multi-jet production in massless QCD*, Comput. Phys. Commun. **184** (2013), 1981–1998, [`arXiv:1209.0100 [hep-ph]`].

[165] F. Cascioli, P. Maierhofer and S. Pozzorini, *Scattering Amplitudes with Open Loops*, Phys. Rev. Lett. **108** (2012), 111601, [`arXiv:1111.5206 [hep-ph]`].

[166] F. Buccioni, J.-N. Lang, J. M. Lindert, P. Maierhöfer, S. Pozzorini, H. Zhang and M. F. Zoller, *OpenLoops 2*, Eur. Phys. J. C **79** (2019), no. 10, 866, [`arXiv:1907.13071 [hep-ph]`].

[167] S. Kallweit, J. M. Lindert, P. Maierhöfer, S. Pozzorini and M. Schönherr, *NLO electroweak automation and precise predictions for W+multijet production at the LHC*, JHEP **04** (2015), 012, [`arXiv:1412.5157 [hep-ph]`].

[168] F. Buccioni, S. Pozzorini and M. Zoller, *On-the-fly reduction of open loops*, Eur. Phys. J. C **78** (2018), no. 1, 70, [`arXiv:1710.11452 [hep-ph]`].

[169] S. Actis, A. Denner, L. Hofer, A. Scharf and S. Uccirati, *Recursive generation of one-loop amplitudes in the Standard Model*, JHEP **04** (2013), 037, [`arXiv:1211.6316 [hep-ph]`].

[170] S. Actis, A. Denner, L. Hofer, J.-N. Lang, A. Scharf and S. Uccirati, *RECOLA: REcursive Computation of One-Loop Amplitudes*, Comput. Phys. Commun. **214** (2017), 140–173, [`arXiv:1605.01090 [hep-ph]`].

[171] B. Biedermann, S. Bräuer, A. Denner, M. Pellen, S. Schumann and J. M. Thompson, *Automation of NLO QCD and EW corrections with Sherpa and Recola*, Eur. Phys. J. C **77** (2017), 492, [`arXiv:1704.05783 [hep-ph]`].

[172] A. Denner and S. Dittmaier, *Reduction of one loop tensor five point integrals*, Nucl. Phys. B **658** (2003), 175–202, [`hep-ph/0212259`].

[173] A. Denner and S. Dittmaier, *Reduction schemes for one-loop tensor integrals*, Nucl. Phys. B **734** (2006), 62–115, [`hep-ph/0509141`].

[174] A. Denner and S. Dittmaier, *Scalar one-loop 4-point integrals*, Nucl. Phys. B **844** (2011), 199–242, [`arXiv:1005.2076 [hep-ph]`].

[175] A. Denner, S. Dittmaier and L. Hofer, *Collier: a fortran-based Complex One-Loop LIbrary in Extended Regularizations*, Comput. Phys. Commun. **212** (2017), 220–238, [`arXiv:1604.06792 [hep-ph]`].

[176] G. Ossola, C. G. Papadopoulos and R. Pittau, *CutTools: A Program implementing the OPP reduction method to compute one-loop amplitudes*, JHEP **03** (2008), 042, [`arXiv:0711.3596 [hep-ph]`].

[177] A. van Hameren, *OneLOop: For the evaluation of one-loop scalar functions*, Comput. Phys. Commun. **182** (2011), 2427–2438, [`arXiv:1007.4716 [hep-ph]`].

[178] S. Catani and M. H. Seymour, *The Dipole formalism for the calculation of QCD jet cross-sections at next-to-leading order*, Phys. Lett. B **378** (1996), 287–301, [`hep-ph/9602277`].

[179] A. Buckley et al., *General-purpose event generators for LHC physics*, Phys. Rept. **504** (2011), 145–233, [`arXiv:1101.2599 [hep-ph]`].

[180] S. Alioli et al., *Monte Carlo event generators for high energy particle physics event simulation*, `arXiv:1902.01674 [hep-ph]`.

[181] F. Siegert, *Monte-Carlo event generation for the LHC*, Ph.D. thesis, Durham U., 2010.

[182] V. V. Sudakov, *Vertex parts at very high-energies in quantum electrodynamics*, Sov. Phys. JETP **3** (1956), 65–71.

[183] T. Sjöstrand, S. Mrenna and P. Z. Skands, *PYTHIA 6.4 Physics and Manual*, JHEP **05** (2006), 026, [`arXiv:hep-ph/0603175 [hep-ph]`].

[184] S. Platzer and M. Sjödahl, *The Sudakov Veto Algorithm Reloaded*, Eur. Phys. J. Plus **127** (2012), 26, [`arXiv:1108.6180 [hep-ph]`].

[185] L. Lönnblad, *Fooling Around with the Sudakov Veto Algorithm*, Eur. Phys. J. C **73** (2013), no. 3, 2350, [`arXiv:1211.7204 [hep-ph]`].

[186] L. Lönnblad, *ARIADNE version 4: A Program for simulation of QCD cascades implementing the color dipole model*, Comput. Phys. Commun. **71** (1992), 15–31.

[187] G. Marchesini and B. R. Webber, *Monte Carlo Simulation of General Hard Processes with Coherent QCD Radiation*, Nucl. Phys. B **310** (1988), 461–526.

[188] G. Corcella, I. G. Knowles, G. Marchesini, S. Moretti, K. Odagiri, P. Richardson, M. H. Seymour and B. R. Webber, *HERWIG 6.5 release note*, `hep-ph/0210213`.

[189] G. Corcella, I. G. Knowles, G. Marchesini, S. Moretti, K. Odagiri, P. Richardson, M. H. Seymour and B. R. Webber, *HERWIG 6: An Event generator for hadron emission reactions with interfering gluons (including supersymmetric processes)*, JHEP **01** (2001), 010, [`hep-ph/0011363`].

[190] S. Gieseke, A. Ribon, M. H. Seymour, P. Stephens and B. Webber, *Herwig++ 1.0: An Event generator for e+ e- annihilation*, JHEP **02** (2004), 005, [hep-ph/0311208].

[191] M. Bahr, S. Gieseke, M. Gigg, D. Grellscheid, K. Hamilton, S. Platzer, P. Richardson, M. H. Seymour and J. Tully, *Herwig++ 2.3 Release Note*, arXiv:0812.0529 [hep-ph].

[192] M. Bahr et al., *Herwig++ Physics and Manual*, Eur. Phys. J. C **58** (2008), 639–707, [arXiv:0803.0883 [hep-ph]].

[193] J. Bellm et al., *Herwig 7.0/Herwig++ 3.0 release note*, Eur. Phys. J. C **76** (2016), no. 4, 196, [arXiv:1512.01178 [hep-ph]].

[194] T. Sjöstrand, *The Lund Monte Carlo for Jet Fragmentation*, Comput. Phys. Commun. **27** (1982), 243.

[195] T. Sjöstrand, *The Lund Monte Carlo for e+ e- Jet Physics*, Comput. Phys. Commun. **28** (1983), 229.

[196] T. Sjöstrand, *The Lund Monte Carlo for Jet Fragmentation and e+ e- Physics: Jetset Version 6.2*, Comput. Phys. Commun. **39** (1986), 347–407.

[197] T. Sjöstrand and M. Bengtsson, *The Lund Monte Carlo for Jet Fragmentation and e+ e- Physics. Jetset Version 6.3: An Update*, Comput. Phys. Commun. **43** (1987), 367.

[198] H. U. Bengtsson, *The Lund Monte Carlo for High p_T Physics*, Comput. Phys. Commun. **31** (1984), 323.

[199] H. U. Bengtsson and G. Ingelman, *The Lund Monte Carlo for High p_T Physics*, Comput. Phys. Commun. **34** (1985), 251.

[200] H.-U. Bengtsson and T. Sjöstrand, *The Lund Monte Carlo for Hadronic Processes: Pythia Version 4.8*, Comput. Phys. Commun. **46** (1987), 43.

[201] T. Sjöstrand, *High-energy physics event generation with PYTHIA 5.7 and JETSET 7.4*, Comput. Phys. Commun. **82** (1994), 74–90.

[202] T. Sjöstrand, P. Eden, C. Friberg, L. Lönnblad, G. Miu, S. Mrenna and E. Norrbin, *High-energy physics event generation with PYTHIA 6.1*, Comput. Phys. Commun. **135** (2001), 238–259, [hep-ph/0010017].

[203] L. Lönnblad, *Development strategies for PYTHIA version 7*, Comput. Phys. Commun. **118** (1999), 213–228, [hep-ph/9810208].

[204] M. Bertini, L. Lönnblad and T. Sjöstrand, *PYTHIA version 7-0.0: A Proof of concept version*, Comput. Phys. Commun. **134** (2001), 365–391, [`hep-ph/0006152`].

[205] T. Sjöstrand, S. Mrenna and P. Z. Skands, *A Brief Introduction to PYTHIA 8.1*, Comput. Phys. Commun. **178** (2008), 852–867, [`arXiv:0710.3820 [hep-ph]`].

[206] T. Sjöstrand, S. Ask, J. R. Christiansen, R. Corke, N. Desai, P. Ilten, S. Mrenna, S. Prestel, C. O. Rasmussen and P. Z. Skands, *An introduction to PYTHIA 8.2*, Comput. Phys. Commun. **191** (2015), 159–177, [`arXiv:1410.3012 [hep-ph]`].

[207] T. Gleisberg, S. Höche, F. Krauss, A. Schalicke, S. Schumann and J.-C. Winter, *SHERPA 1. alpha: A Proof of concept version*, JHEP **02** (2004), 056, [`hep-ph/0311263`].

[208] T. Gleisberg, S. Höche, F. Krauss, M. Schönherr, S. Schumann, F. Siegert and J. Winter, *Event generation with SHERPA 1.1*, JHEP **02** (2009), 007, [`arXiv:0811.4622 [hep-ph]`].

[209] E. Bothmann et al., The Sherpa collaboration, *Event Generation with Sherpa 2.2*, SciPost Phys. **7** (2019), no. 3, 034, [`arXiv:1905.09127 [hep-ph]`].

[210] F. Krauss, R. Kuhn and G. Soff, *AMEGIC++ 1.0: A Matrix element generator in C++*, JHEP **02** (2002), 044, [`hep-ph/0109036`].

[211] R. Kleiss and W. J. Stirling, *Spinor Techniques for Calculating p anti-p —> W+- / Z0 + Jets*, Nucl. Phys. B **262** (1985), 235–262.

[212] A. Ballestrero, E. Maina and S. Moretti, *Heavy quarks and leptons at e+ e-colliders*, Nucl. Phys. B **415** (1994), 265–292, [`hep-ph/9212246`].

[213] T. Gleisberg, F. Krauss, C. G. Papadopoulos, A. Schaelicke and S. Schumann, *Cross-sections for multiparticle final states at a linear collider*, Eur. Phys. J. C **34** (2004), 173–180, [`hep-ph/0311273`].

[214] T. Gleisberg and S. Höche, *Comix, a new matrix element generator*, JHEP **12** (2008), 039, [`arXiv:0808.3674 [hep-ph]`].

[215] F. A. Berends and W. T. Giele, *Recursive Calculations for Processes with n Gluons*, Nucl. Phys. B **306** (1988), 759–808.

[216] C. Duhr, S. Höche and F. Maltoni, *Color-dressed recursive relations for multi-parton amplitudes*, JHEP **08** (2006), 062, [`hep-ph/0607057`].

[217] T. Binoth et al., *A Proposal for a Standard Interface between Monte Carlo Tools and One-Loop Programs*, Comput. Phys. Commun. **181** (2010), 1612–1622, [`arXiv:1001.1307 [hep-ph]`].

[218] S. Alioli et al., *Update of the Binoth Les Houches Accord for a standard interface between Monte Carlo tools and one-loop programs*, Comput. Phys. Commun. **185** (2014), 560–571, [arXiv:1308.3462 [hep-ph]].

[219] S. Schumann and F. Krauss, *A Parton shower algorithm based on Catani-Seymour dipole factorisation*, JHEP **03** (2008), 038, [arXiv:0709.1027 [hep-ph]].

[220] S. Höche and S. Prestel, *The midpoint between dipole and parton showers*, Eur. Phys. J. **C75** (2015), no. 9, 461, [arXiv:1506.05057 [hep-ph]].

[221] T. Sjöstrand and M. van Zijl, *A Multiple Interaction Model for the Event Structure in Hadron Collisions*, Phys. Rev. D **36** (1987), 2019.

[222] B. Andersson, G. Gustafson and B. Soderberg, *A General Model for Jet Fragmentation*, Z. Phys. C **20** (1983), 317.

[223] B. R. Webber, *A QCD Model for Jet Fragmentation Including Soft Gluon Interference*, Nucl. Phys. B **238** (1984), 492–528.

[224] J.-C. Winter, F. Krauss and G. Soff, *A modified cluster-hadronisation model*, Eur. Phys. J. **C36** (2004), 381–395, [hep-ph/0311085].

[225] M. Bengtsson and T. Sjöstrand, *Coherent Parton Showers Versus Matrix Elements: Implications of PETRA - PEP Data*, Phys. Lett. B **185** (1987), 435.

[226] M. H. Seymour, *A Simple prescription for first order corrections to quark scattering and annihilation processes*, Nucl. Phys. B **436** (1995), 443–460, [hep-ph/9410244].

[227] M. H. Seymour, *Matrix element corrections to parton shower algorithms*, Comput. Phys. Commun. **90** (1995), 95–101, [hep-ph/9410414].

[228] G. Miu and T. Sjöstrand, W *production in an improved parton shower approach*, Phys. Lett. B **449** (1999), 313–320, [hep-ph/9812455].

[229] P. Nason, *A New method for combining NLO QCD with shower Monte Carlo algorithms*, JHEP **11** (2004), 040, [hep-ph/0409146].

[230] S. Frixione and B. R. Webber, *Matching NLO QCD computations and parton shower simulations*, JHEP **06** (2002), 029, [hep-ph/0204244].

[231] S. Frixione and B. R. Webber, *The MC@NLO 3.3 Event Generator*, hep-ph/0612272.

[232] S. Höche, F. Krauss, M. Schönherr and F. Siegert, *A critical appraisal of NLO+PS matching methods*, JHEP **09** (2012), 049, [arXiv:1111.1220 [hep-ph]].

[233] S. Catani, F. Krauss, R. Kuhn and B. R. Webber, *QCD matrix elements + parton showers*, JHEP **11** (2001), 063, [`hep-ph/0109231`].

[234] L. Lönnblad, *Correcting the color dipole cascade model with fixed order matrix elements*, JHEP **05** (2002), 046, [`hep-ph/0112284`].

[235] S. Höche, F. Krauss, S. Schumann and F. Siegert, *QCD matrix elements and truncated showers*, JHEP **05** (2009), 053, [`arXiv:0903.1219 [hep-ph]`].

[236] S. Höche, F. Krauss, M. Schönherr and F. Siegert, *NLO matrix elements and truncated showers*, JHEP **08** (2011), 123, [`arXiv:1009.1127 [hep-ph]`].

[237] S. Höche, F. Krauss, M. Schönherr and F. Siegert, *QCD matrix elements + parton showers: The NLO case*, JHEP **04** (2013), 027, [`arXiv:1207.5030 [hep-ph]`].

[238] T. Gehrmann, S. Höche, F. Krauss, M. Schönherr and F. Siegert, *NLO QCD matrix elements + parton showers in $e^+e^- \longrightarrow$ hadrons*, JHEP **01** (2013), 144, [`arXiv:1207.5031 [hep-ph]`].

[239] S. Höche, F. Krauss, S. Pozzorini, M. Schönherr, J. M. Thompson and K. C. Zapp, *Triple vector boson production through Higgs-Strahlung with NLO multijet merging*, Phys. Rev. D **89** (2014), no. 9, 093015, [`arXiv:1403.7516 [hep-ph]`].

[240] S. Platzer and S. Gieseke, *Coherent Parton Showers with Local Recoils*, JHEP **01** (2011), 024, [`arXiv:0909.5593 [hep-ph]`].

[241] S. Gieseke, P. Stephens and B. Webber, *New formalism for QCD parton showers*, JHEP **12** (2003), 045, [`hep-ph/0310083`].

[242] S. Gieseke, C. Rohr and A. Siódmok, *Colour reconnections in Herwig++*, Eur. Phys. J. **C72** (2012), 2225, [`arXiv:1206.0041 [hep-ph]`].

[243] K. Hamilton, P. Richardson and J. Tully, *A Modified CKKW matrix element merging approach to angular-ordered parton showers*, JHEP **11** (2009), 038, [`arXiv:0905.3072 [hep-ph]`].

[244] K. Hamilton and P. Nason, *Improving NLO-parton shower matched simulations with higher order matrix elements*, JHEP **06** (2010), 039, [`arXiv:1004.1764 [hep-ph]`].

[245] R. Corke and T. Sjöstrand, *Interleaved Parton Showers and Tuning Prospects*, JHEP **03** (2011), 032, [`arXiv:1011.1759 [hep-ph]`].

[246] N. Lavesson and L. Lönnblad, *Merging parton showers and matrix elements: Back to basics*, JHEP **04** (2008), 085, [arXiv:0712.2966 [hep-ph]].

[247] L. Lönnblad and S. Prestel, *Matching Tree-Level Matrix Elements with Interleaved Showers*, JHEP **03** (2012), 019, [arXiv:1109.4829 [hep-ph]].

[248] L. Lönnblad and S. Prestel, *Unitarising Matrix Element + Parton Shower merging*, JHEP **02** (2013), 094, [arXiv:1211.4827 [hep-ph]].

[249] W. T. Giele, D. A. Kosower and P. Z. Skands, *A simple shower and matching algorithm*, Phys. Rev. D **78** (2008), 014026, [arXiv:0707.3652 [hep-ph]].

[250] N. Fischer, S. Prestel, M. Ritzmann and P. Skands, *Vincia for Hadron Colliders*, Eur. Phys. J. C **76** (2016), no. 11, 589, [arXiv:1605.06142 [hep-ph]].

[251] W. T. Giele, D. A. Kosower and P. Z. Skands, *Higher-Order Corrections to Timelike Jets*, Phys. Rev. D **84** (2011), 054003, [arXiv:1102.2126 [hep-ph]].

[252] Y. L. Dokshitzer, D. Diakonov and S. I. Troian, *Hard Processes in Quantum Chromodynamics*, Phys. Rept. **58** (1980), 269–395.

[253] W. Furmanski, *e+ e- JETS: CONES OR TUBES?*, Nucl. Phys. B **158** (1979), 429–451.

[254] J. Wosiek and K. Zalewski, *LEADING LOG VERSION OF THE STERMAN-WEINBERG FORMULA*, Nucl. Phys. B **161** (1979), 294–300.

[255] P. E. L. Rakow and B. R. Webber, *Noncollinearity of Jets in Quantum Chromodynamics*, Phys. Rev. Lett. **43** (1979), 1695, [Erratum: Phys.Rev.Lett. 44, 764 (1980)].

[256] C. T. H. Davies and B. R. Webber, *Transverse Hadronic Energy Emission in Hard Scattering Processes*, Z. Phys. C **24** (1984), 133.

[257] S. Catani, G. Turnock and B. R. Webber, *Jet broadening measures in e^+e^- annihilation*, Phys. Lett. B **295** (1992), 269–276.

[258] S. Catani, L. Trentadue, G. Turnock and B. R. Webber, *Resummation of large logarithms in e+ e- event shape distributions*, Nucl. Phys. B **407** (1993), 3–42.

[259] S. Catani and B. R. Webber, *Resummed C parameter distribution in e+ e- annihilation*, Phys. Lett. B **427** (1998), 377–384, [hep-ph/9801350].

[260] A. Banfi, G. Marchesini, Y. L. Dokshitzer and G. Zanderighi, *QCD analysis of near-to-planar three jet events*, JHEP **07** (2000), 002, [hep-ph/0004027].

[261] A. Banfi and G. Zanderighi, *Perturbative QCD analysis of near-to-planar three jet events*, Nucl. Phys. B Proc. Suppl. **96** (2001), 64–68, [hep-ph/0010052].

[262] A. Banfi, Y. L. Dokshitzer, G. Marchesini and G. Zanderighi, *Near-to-planar three jet events in and beyond QCD perturbation theory*, Phys. Lett. B **508** (2001), 269–278, [hep-ph/0010267].

[263] A. Banfi, Y. L. Dokshitzer, G. Marchesini and G. Zanderighi, *QCD analysis of D parameter in near to planar three jet events*, JHEP **05** (2001), 040, [hep-ph/0104162].

[264] A. Banfi, G. Marchesini, G. Smye and G. Zanderighi, *Multi-jet event shapes in QCD hard processes*, AIP Conf. Proc. **602** (2001), no. 1, 108.

[265] A. Banfi, G. Marchesini, G. Smye and G. Zanderighi, *Out of plane QCD radiation in hadronic Z0 production*, JHEP **08** (2001), 047, [hep-ph/0106278].

[266] A. Banfi, G. Marchesini, G. Smye and G. Zanderighi, *Out-of-plane QCD radiation in DIS with high p(t) jets*, JHEP **11** (2001), 066, [hep-ph/0111157].

[267] S. J. Burby and E. W. N. Glover, *Resumming the light hemisphere mass and narrow jet broadening distributions in e+ e- annihilation*, JHEP **04** (2001), 029, [hep-ph/0101226].

[268] A. Banfi, G. Marchesini and G. Smye, *Azimuthal correlation in DIS*, JHEP **04** (2002), 024, [hep-ph/0203150].

[269] A. Banfi and M. Dasgupta, *Dijet rates with symmetric E(t) cuts*, JHEP **01** (2004), 027, [hep-ph/0312108].

[270] C. W. Bauer, S. Fleming and M. E. Luke, *Summing Sudakov logarithms in B —> X(s gamma) in effective field theory*, Phys. Rev. D **63** (2000), 014006, [hep-ph/0005275].

[271] C. W. Bauer, S. Fleming, D. Pirjol and I. W. Stewart, *An Effective field theory for collinear and soft gluons: Heavy to light decays*, Phys. Rev. D **63** (2001), 114020, [hep-ph/0011336].

[272] C. W. Bauer and I. W. Stewart, *Invariant operators in collinear effective theory*, Phys. Lett. B **516** (2001), 134–142, [hep-ph/0107001].

[273] C. W. Bauer, D. Pirjol and I. W. Stewart, *Soft collinear factorization in effective field theory*, Phys. Rev. D **65** (2002), 054022, [hep-ph/0109045].

[274] M. Beneke, A. P. Chapovsky, M. Diehl and T. Feldmann, *Soft collinear effective theory and heavy to light currents beyond leading power*, Nucl. Phys. B **643** (2002), 431–476, [hep-ph/0206152].

[275] M. Beneke and T. Feldmann, *Multipole expanded soft collinear effective theory with nonAbelian gauge symmetry*, Phys. Lett. B **553** (2003), 267–276, [hep-ph/0211358].

[276] R. J. Hill and M. Neubert, *Spectator interactions in soft collinear effective theory*, Nucl. Phys. B **657** (2003), 229–256, [hep-ph/0211018].

[277] T. Becher, A. Broggio and A. Ferroglia, *Introduction to Soft-Collinear Effective Theory*, vol. 896, Springer, 2015.

[278] A. Banfi, G. P. Salam and G. Zanderighi, *Semi-numerical resummation of event shapes*, JHEP **01** (2002), 018, [hep-ph/0112156].

[279] A. Banfi, G. P. Salam and G. Zanderighi, *Generalized resummation of QCD final state observables*, Phys. Lett. B **584** (2004), 298–305, [hep-ph/0304148].

[280] A. Banfi, G. P. Salam and G. Zanderighi, *Resummed event shapes at hadron - hadron colliders*, JHEP **08** (2004), 062, [hep-ph/0407287].

[281] A. Banfi, G. Corcella, M. Dasgupta, Y. Delenda, G. P. Salam and G. Zanderighi, *Resummation*, HERA and the LHC: A Workshop on the Implications of HERA for LHC Physics: CERN - DESY Workshop 2004/2005 (Midterm Meeting, CERN, 11-13 October 2004; Final Meeting, DESY, 17-21 January 2005) (Geneva), CERN, 8 2005, pp. 160–180.

[282] A. Banfi, G. P. Salam and G. Zanderighi, *Phenomenology of event shapes at hadron colliders*, JHEP **06** (2010), 038, [arXiv:1001.4082 [hep-ph]].

[283] A. Banfi, G. P. Salam and G. Zanderighi, *NLL+NNLO predictions for jet-veto efficiencies in Higgs-boson and Drell-Yan production*, JHEP **06** (2012), 159, [arXiv:1203.5773 [hep-ph]].

[284] A. Banfi, P. F. Monni, G. P. Salam and G. Zanderighi, *Higgs and Z-boson production with a jet veto*, Phys. Rev. Lett. **109** (2012), 202001, [arXiv:1206.4998 [hep-ph]].

[285] S. Catani, B. R. Webber and G. Marchesini, *QCD coherent branching and semiinclusive processes at large x*, Nucl. Phys. B **349** (1991), 635–654.

[286] Y. L. Dokshitzer and G. Marchesini, *Hadron collisions and the fifth form-factor*, Phys. Lett. B **631** (2005), 118–125, [hep-ph/0508130].

[287] Y. L. Dokshitzer and G. Marchesini, *Soft gluons at large angles in hadron collisions*, JHEP **01** (2006), 007, [`hep-ph/0509078`].

[288] N. Kidonakis, G. Oderda and G. F. Sterman, *Evolution of color exchange in QCD hard scattering*, Nucl. Phys. B **531** (1998), 365–402, [`hep-ph/9803241`].

[289] R. Bonciani, S. Catani, M. L. Mangano and P. Nason, *Sudakov resummation of multiparton QCD cross-sections*, Phys. Lett. B **575** (2003), 268–278, [`hep-ph/0307035`].

[290] A. Banfi and M. Dasgupta, *Problems in resumming interjet energy flows with k_t clustering*, Phys. Lett. B **628** (2005), 49–56, [`hep-ph/0508159`].

[291] Y. Delenda, R. Appleby, M. Dasgupta and A. Banfi, *On QCD resummation with k(t) clustering*, JHEP **12** (2006), 044, [`hep-ph/0610242`].

[292] A. Banfi, M. Dasgupta, K. Khelifa-Kerfa and S. Marzani, *Non-global logarithms and jet algorithms in high-pT jet shapes*, JHEP **08** (2010), 064, [`arXiv:1004.3483 [hep-ph]`].

[293] Y. Delenda and K. Khelifa-Kerfa, *On the resummation of clustering logarithms for non-global observables*, JHEP **09** (2012), 109, [`arXiv:1207.4528 [hep-ph]`].

[294] M. Dasgupta and G. P. Salam, *Resummation of nonglobal QCD observables*, Phys. Lett. B **512** (2001), 323–330, [`hep-ph/0104277`].

[295] E. Gerwick, S. Höche, S. Marzani and S. Schumann, *Soft evolution of multi-jet final states*, JHEP **02** (2015), 106, [`arXiv:1411.7325 [hep-ph]`].

[296] E. Bothmann, M. Schönherr and S. Schumann, *Reweighting QCD matrix-element and parton-shower calculations*, Eur. Phys. J. C **76** (2016), no. 11, 590, [`arXiv:1606.08753 [hep-ph]`].

[297] C. T. Preuss, *The Effect of Soft Gluon Radiation on the Colour Structure of Multi-Parton Processes*, Master's thesis, Georg-August-Universität Göttingen, 2018.

[298] S. Keppeler and M. Sjödahl, *Orthogonal multiplet bases in SU(Nc) color space*, JHEP **09** (2012), 124, [`arXiv:1207.0609 [hep-ph]`].

[299] M. Sjödahl, *ColorFull – a C++ library for calculations in SU(Nc) color space*, Eur. Phys. J. C **75** (2015), no. 5, 236, [`arXiv:1412.3967 [hep-ph]`].

[300] M. Sjödahl and J. Thorén, *Decomposing color structure into multiplet bases*, JHEP **09** (2015), 055, [`arXiv:1507.03814 [hep-ph]`].

[301] M. Sjödahl and J. Thorén, *QCD multiplet bases with arbitrary parton ordering*, JHEP **11** (2018), 198, [`arXiv:1809.05002 [hep-ph]`].

[302] M. J. R. Healy, *Algorithm as 7: Inversion of a Positive Semi-Definite Symmetric Matrix*, Journal of the Royal Statistical Society Series C **17** (1968), no. 2, 198–199.

[303] C. Moler and C. V. Loan, *Nineteen Dubious Ways to Compute the Exponential of a Matrix, Twenty-Five Years Later*, SIAM Review **45** (2003), no. 1, 3–49.

[304] G. 't Hooft, *A Two-Dimensional Model for Mesons*, Nucl. Phys. B **75** (1974), 461–470.

[305] N. Baberuxki, *QCD Resummed Predictions for Jet-Resolution Scales*, Master's thesis, Georg-August-Universität Göttingen, 2020.

[306] F. N. Fritsch and R. E. Carlson, *Monotone Piecewise Cubic Interpolation*, SIAM Journal on Numerical Analysis **17** (1980), no. 2, 238–246.

[307] F. N. Fritsch and J. Butland, *A Method for Constructing Local Monotone Piecewise Cubic Interpolants*, SIAM Journal on Scientific and Statistical Computing **5** (1984), no. 2, 300–304.

[308] A. Banfi, G. P. Salam and G. Zanderighi, *Infrared safe definition of jet flavor*, Eur. Phys. J. C **47** (2006), 113–124, [`hep-ph/0601139`].

[309] M. Dasgupta, A. Fregoso, S. Marzani and G. P. Salam, *Towards an understanding of jet substructure*, JHEP **09** (2013), 029, [`arXiv:1307.0007 [hep-ph]`].

[310] A. V. Manohar and M. B. Wise, *Power suppressed corrections to hadronic event shapes*, Phys. Lett. B **344** (1995), 407–412, [`hep-ph/9406392`].

[311] G. P. Korchemsky and G. F. Sterman, *Nonperturbative corrections in resummed cross-sections*, Nucl. Phys. B **437** (1995), 415–432, [`hep-ph/9411211`].

[312] Y. L. Dokshitzer, G. Marchesini and B. R. Webber, *Dispersive approach to power behaved contributions in QCD hard processes*, Nucl. Phys. B **469** (1996), 93–142, [`hep-ph/9512336`].

[313] Y. L. Dokshitzer and B. R. Webber, *Calculation of power corrections to hadronic event shapes*, Phys. Lett. B **352** (1995), 451–455, [`hep-ph/9504219`].

[314] Y. L. Dokshitzer and B. R. Webber, *Power corrections to event shape distributions*, Phys. Lett. B **404** (1997), 321–327, [`hep-ph/9704298`].

[315] G. P. Korchemsky, *Shape functions and power corrections to the event shapes*, 3rd Workshop on Continuous Advances in QCD (QCD 98), 1998, pp. 489–498.

[316] E. Gardi and G. Grunberg, *Power corrections in the single dressed gluon approximation: The Average thrust as a case study*, JHEP **11** (1999), 016, [hep-ph/9908458].

[317] E. Gardi, *Perturbative and nonperturbative aspects of moments of the thrust distribution in e+ e- annihilation*, JHEP **04** (2000), 030, [hep-ph/0003179].

[318] E. Gardi and J. Rathsman, *Renormalon resummation and exponentiation of soft and collinear gluon radiation in the thrust distribution*, Nucl. Phys. B **609** (2001), 123–182, [hep-ph/0103217].

[319] A. Banfi and G. Zanderighi, *Nonperturbative effects in e+e- event shape variables*, Italian Phys. Soc. Proc. **78** (2002), 305–309, [hep-ph/0106231].

[320] A. Banfi, Y. L. Dokshitzer, G. Marchesini and G. Zanderighi, *Nonperturbative QCD analysis of near - to - planar three jet events*, JHEP **03** (2001), 007, [hep-ph/0101205].

[321] A. H. Hoang and I. W. Stewart, *Designing gapped soft functions for jet production*, Phys. Lett. B **660** (2008), 483–493, [arXiv:0709.3519 [hep-ph]].

[322] M. Dasgupta, L. Magnea and G. P. Salam, *Non-perturbative QCD effects in jets at hadron colliders*, JHEP **02** (2008), 055, [arXiv:0712.3014 [hep-ph]].

[323] M. Dasgupta, L. Magnea and G. Salam, *Analytical studies for non-perturbative QCD of jets at hadron colliders*, Frascati Phys. Ser. **47** (2008), 221–228, [arXiv:0805.2267 [hep-ph]].

[324] M. Dasgupta and Y. Delenda, *On the universality of hadronisation corrections to QCD jets*, JHEP **07** (2009), 004, [arXiv:0903.2187 [hep-ph]].

[325] M. Dasgupta and Y. Delenda, *Hadronisation corrections to jets in the k_t algorithm*, 17th International Workshop on Deep-Inelastic Scattering and Related Subjects (Berlin, Germany), Science Wise Publ., 2009, pp. 67–73.

[326] M. Dasgupta, Y. Dokshitzer and G. Salam (Eds.), *First principles non-perturbative QCD of hadron jets. Proceedings, FRIF Workshop, Paris, France, January 12-14, 2006*, 2012.

[327] A. H. Hoang, S. Mantry, A. Pathak and I. W. Stewart, *Nonperturbative Corrections to Soft Drop Jet Mass*, JHEP **12** (2019), 002, [arXiv:1906.11843 [hep-ph]].

[328] G. Luisoni, P. F. Monni and G. P. Salam, C-parameter hadronisation in the symmetric 3-jet limit and impact on α_s fits, Eur. Phys. J. C **81** (2021), no. 2, 158, [arXiv:2012.00622 [hep-ph]].

[329] K. Maltman and T. Yavin, $\alpha_s(M_Z)$ from hadronic tau decays, Phys. Rev. **D78** (2008), 094020, [arXiv:0807.0650 [hep-ph]].

[330] S. Aoki et al., The PACS-CS collaboration, *Precise determination of the strong coupling constant in N_f = 2+1 lattice QCD with the Schrodinger functional scheme*, JHEP **10** (2009), 053, [arXiv:0906.3906 [hep-lat]].

[331] B. Blossier, P. Boucaud, M. Brinet, F. De Soto, X. Du, V. Morenas, O. Pene, K. Petrov and J. Rodriguez-Quintero, *The Strong running coupling at τ and Z_0 mass scales from lattice QCD*, Phys. Rev. Lett. **108** (2012), 262002, [arXiv:1201.5770 [hep-ph]].

[332] C. McNeile, C. T. H. Davies, E. Follana, K. Hornbostel and G. P. Lepage, *High-Precision c and b Masses, and QCD Coupling from Current-Current Correlators in Lattice and Continuum QCD*, Phys. Rev. **D82** (2010), 034512, [arXiv:1004.4285 [hep-lat]].

[333] B. Chakraborty, C. T. H. Davies, B. Galloway, P. Knecht, J. Koponen, G. C. Donald, R. J. Dowdall, G. P. Lepage and C. McNeile, *High-precision quark masses and QCD coupling from $n_f = 4$ lattice QCD*, Phys. Rev. **D91** (2015), no. 5, 054508, [arXiv:1408.4169 [hep-lat]].

[334] A. Bazavov et al., The Fermilab Lattice, MILC collaboration, *Charmed and light pseudoscalar meson decay constants from four-flavor lattice QCD with physical light quarks*, Phys. Rev. **D90** (2014), no. 7, 074509, [arXiv:1407.3772 [hep-lat]].

[335] G. Dissertori et al., *First determination of the strong coupling constant using NNLO predictions for hadronic event shapes in e^+e^- annihilations*, JHEP **02** (2008), 040, [arXiv:0712.0327 [hep-ph]].

[336] S. Bethke, S. Kluth, C. Pahl and J. Schieck, The JADE collaboration, *Determination of the Strong Coupling α_s from hadronic Event Shapes and NNLO QCD predictions using JADE Data*, Eur. Phys. J. **C64** (2009), 351–360, [arXiv:0810.1389 [hep-ex]].

[337] R. A. Davison and B. R. Webber, *Non-Perturbative Contribution to the Thrust Distribution in e^+e^- Annihilation*, Eur. Phys. J. **C59** (2009), 13–25, [arXiv:0809.3326 [hep-ph]].

[338] G. Dissertori et al., *Determination of the strong coupling constant using matched NNLO+NLLA predictions for hadronic event shapes in e+e- annihilations*, JHEP **08** (2009), 036, [arXiv:0906.3436 [hep-ph]].

[339] G. Dissertori, A. Gehrmann-De Ridder, T. Gehrmann, E. W. N. Glover, G. Heinrich and H. Stenzel, *Precise determination of the strong coupling constant at NNLO in QCD from the three-jet rate in electron–positron annihilation at LEP*, Phys. Rev. Lett. **104** (2010), 072002, [arXiv:0910.4283 [hep-ph]].

[340] R. Abbate, M. Fickinger, A. H. Hoang, V. Mateu and I. W. Stewart, *Thrust at N^3LL with Power Corrections and a Precision Global Fit for $\alpha_s(m_Z)$*, Phys. Rev. **D83** (2011), 074021, [1006.3080].

[341] G. Abbiendi et al., The OPAL collaboration, *Determination of $alpha_s$ using OPAL hadronic event shapes at $\sqrt{s} = 91$ - 209 GeV and resummed NNLO calculations*, Eur. Phys. J. **C71** (2011), 1733, [arXiv:1101.1470 [hep-ex]].

[342] J. Schieck, S. Bethke, S. Kluth, C. Pahl and Z. Trócsányi, The JADE collaboration, *Measurement of the strong coupling α_S from the three-jet rate in e^+e^- - annihilation using JADE data*, Eur. Phys. J. **C73** (2013), no. 3, 2332, [arXiv:1205.3714 [hep-ex]].

[343] T. Gehrmann, G. Luisoni and P. F. Monni, *Power corrections in the dispersive model for a determination of the strong coupling constant from the thrust distribution*, Eur. Phys. J. **C73** (2013), no. 1, 2265, [arXiv:1210.6945 [hep-ph]].

[344] A. H. Hoang, D. W. Kolodrubetz, V. Mateu and I. W. Stewart, *C-parameter distribution at N^3LL' including power corrections*, Phys. Rev. **D91** (2015), no. 9, 094017, [arXiv:1411.6633 [hep-ph]].

[345] A. Heister et al., The ALEPH collaboration, *Studies of QCD at e^+e^- centre-of-mass energies between 91-GeV and 209-GeV*, Eur. Phys. J. **C35** (2004), 457–486.

[346] R. Abbate, M. Fickinger, A. H. Hoang, V. Mateu and I. W. Stewart, *Precision Thrust Cumulant Moments at N^3LL*, Phys. Rev. **D86** (2012), 094002, [arXiv:1204.5746 [hep-ph]].

[347] A. Buckley, J. Butterworth, D. Grellscheid, H. Hoeth, L. Lönnblad, J. Monk, H. Schulz and F. Siegert, *Rivet user manual*, Comput. Phys. Commun. **184** (2013), 2803–2819, [arXiv:1003.0694 [hep-ph]].

[348] E. Gerwick, S. Schumann, B. Gripaios and B. Webber, *QCD Jet Rates with the Inclusive Generalized kt Algorithms*, JHEP **04** (2013), 089, [arXiv:1212.5235 [hep-ph]].

[349] B. R. Webber, *QCD Jets and Parton Showers*, Gribov-80 Memorial Workshop on Quantum Chromodynamics and Beyond, 9 2010.

[350] A. Heister et al., The ALEPH collaboration, *Studies of QCD at e+ e- centre-of-mass energies between 91-GeV and 209-GeV*, Eur. Phys. J. C **35** (2004), 457–486.

[351] G. Abbiendi et al., The OPAL collaboration, *Measurement of event shape distributions and moments in e+ e- —> hadrons at 91-GeV - 209-GeV and a determination of alpha(s)*, Eur. Phys. J. C **40** (2005), 287–316, [hep-ex/0503051].

[352] S. Bethke, S. Kluth, C. Pahl and J. Schieck, The JADE collaboration, *Determination of the Strong Coupling alpha(s) from hadronic Event Shapes with O(alpha**3(s)) and resummed QCD predictions using JADE Data*, Eur. Phys. J. C **64** (2009), 351–360, [arXiv:0810.1389 [hep-ex]].

[353] A. Verbytskyi, A. Banfi, A. Kardos, P. F. Monni, S. Kluth, G. Somogyi, Z. Szőr, Z. Trócsányi, Z. Tulipánt and G. Zanderighi, *High precision determination of α_s from a global fit of jet rates*, JHEP **08** (2019), 129, [arXiv:1902.08158 [hep-ph]].

[354] A. Banfi, H. McAslan, P. F. Monni and G. Zanderighi, *The two-jet rate in e^+e^- at next-to-next-to-leading-logarithmic order*, Phys. Rev. Lett. **117** (2016), no. 17, 172001, [arXiv:1607.03111 [hep-ph]].

[355] A. Banfi, H. McAslan, P. F. Monni and G. Zanderighi, *A general method for the resummation of event-shape distributions in e^+e^- annihilation*, JHEP **05** (2015), 102, [arXiv:1412.2126 [hep-ph]].

[356] L. Arpino, A. Banfi and B. K. El-Menoufi, *Near-to-planar three-jet events at NNLL accuracy*, JHEP **07** (2020), 171, [arXiv:1912.09341 [hep-ph]].

[357] S. Platzer and M. Sjödahl, *Subleading N_c improved Parton Showers*, JHEP **07** (2012), 042, [arXiv:1201.0260 [hep-ph]].

[358] S. Plätzer, M. Sjödahl and J. Thorén, *Color matrix element corrections for parton showers*, JHEP **11** (2018), 009, [arXiv:1808.00332 [hep-ph]].

[359] Z. Nagy and D. E. Soper, *Parton shower evolution with subleading color*, JHEP **06** (2012), 044, [arXiv:1202.4496 [hep-ph]].

[360] Z. Nagy and D. E. Soper, *Parton showers with more exact color evolution*, Phys. Rev. D **99** (2019), no. 5, 054009, [`arXiv:1902.02105 [hep-ph]`].

[361] R. Ángeles Martínez, M. De Angelis, J. R. Forshaw, S. Plätzer and M. H. Seymour, *Soft gluon evolution and non-global logarithms*, JHEP **05** (2018), 044, [`arXiv:1802.08531 [hep-ph]`].

[362] J. R. Forshaw, J. Holguin and S. Plätzer, *Parton branching at amplitude level*, JHEP **08** (2019), 145, [`arXiv:1905.08686 [hep-ph]`].

[363] M. De Angelis, J. R. Forshaw and S. Plätzer, *Resummation and Simulation of Soft Gluon Effects beyond Leading Color*, Phys. Rev. Lett. **126** (2021), no. 11, 112001, [`arXiv:2007.09648 [hep-ph]`].

[364] J. Holguin, J. R. Forshaw and S. Plätzer, *Improvements on dipole shower colour*, Eur. Phys. J. C **81** (2021), no. 4, 364, [`arXiv:2011.15087 [hep-ph]`].

[365] S. Plätzer and I. Ruffa, *Towards Colour Flow Evolution at Two Loops*, JHEP **06** (2021), 007, [`arXiv:2012.15215 [hep-ph]`].

[366] V. Khachatryan et al., The CMS collaboration, *Study of Hadronic Event-Shape Variables in Multijet Final States in pp Collisions at $\sqrt{s} = 7$ TeV*, JHEP **10** (2014), 087, [`arXiv:1407.2856 [hep-ex]`].

[367] A. M. Sirunyan et al., The CMS collaboration, *Event shape variables measured using multijet final states in proton-proton collisions at $\sqrt{s} = 13$ TeV*, JHEP **12** (2018), 117, [`arXiv:1811.00588 [hep-ex]`].

[368] G. Aad et al., The ATLAS collaboration, *Measurement of event shapes at large momentum transfer with the ATLAS detector in pp collisions at $\sqrt{s} = 7$ TeV*, Eur. Phys. J. C **72** (2012), 2211, [`arXiv:1206.2135 [hep-ex]`].

[369] G. Aad et al., The ATLAS collaboration, *Measurement of hadronic event shapes in high-p_T multijet final states at $\sqrt{s} = 13$ TeV with the ATLAS detector*, JHEP **01** (2021), 188, [`arXiv:2007.12600 [hep-ex]`].

[370] T. Aaltonen et al., The CDF collaboration, *Measurement of Event Shapes in Proton-Antiproton Collisions at Center-of-Mass Energy 1.96 TeV*, Phys. Rev. D **83** (2011), 112007, [`arXiv:1103.5143 [hep-ex]`].

[371] Z. Nagy, *Next-to-leading order calculation of three jet observables in hadron hadron collision*, Phys. Rev. D **68** (2003), 094002, [`hep-ph/0307268`].

[372] T. Becher and X. Garcia i Tormo, *Factorization and resummation for transverse thrust*, JHEP **06** (2015), 071, [`arXiv:1502.04136 [hep-ph]`].

[373] T. Becher, X. Garcia i Tormo and J. Piclum, *Next-to-next-to-leading logarithmic resummation for transverse thrust*, Phys. Rev. D **93** (2016), no. 5, 054038, [arXiv:1512.00022 [hep-ph]], [Erratum: Phys.Rev.D 93, 079905 (2016)].

[374] A. Kardos, G. Somogyi and Z. Trócsányi, *Soft-drop event shapes in electron–positron annihilation at next-to-next-to-leading order accuracy*, Phys. Lett. B **786** (2018), 313–318, [arXiv:1807.11472 [hep-ph]].

[375] S. Acharya et al., The ALICE collaboration, *Measurements of the groomed and ungroomed jet angularities in pp collisions at $\sqrt{s} = 5.02$ TeV*, arXiv:2107.11303 [nucl-ex].

[376] J. R. Andersen et al., *Les Houches 2015: Physics at TeV Colliders Standard Model Working Group Report*, 9th Les Houches Workshop on Physics at TeV Colliders, 5 2016.

[377] G. Brooijmans et al., *Les Houches 2017: Physics at TeV Colliders New Physics Working Group Report*, 10th Les Houches Workshop on Physics at TeV Colliders, 3 2018.

[378] S. Amoroso et al., *Les Houches 2019: Physics at TeV Colliders: Standard Model Working Group Report*, 11th Les Houches Workshop on Physics at TeV Colliders: PhysTeV Les Houches, 3 2020.

[379] J. Mo, F. J. Tackmann and W. J. Waalewijn, *A case study of quark-gluon discrimination at NNLL' in comparison to parton showers*, Eur. Phys. J. C **77** (2017), no. 11, 770, [arXiv:1708.00867 [hep-ph]].

[380] A. Siódmok, *Quark/Gluon Jets Discrimination and Its Connection to Colour Reconnection*, Acta Phys. Polon. B **48** (2017), 2341.

[381] E. M. Metodiev and J. Thaler, *Jet Topics: Disentangling Quarks and Gluons at Colliders*, Phys. Rev. Lett. **120** (2018), no. 24, 241602, [arXiv:1802.00008 [hep-ph]].

[382] S. Bright-Thonney and B. Nachman, *Investigating the Topology Dependence of Quark and Gluon Jets*, JHEP **03** (2019), 098, [arXiv:1810.05653 [hep-ph]].

[383] Y. Sakaki, *Quark jet rates and quark-gluon discrimination in multijet final states*, Phys. Rev. D **99** (2019), no. 11, 114012, [arXiv:1807.01421 [hep-ph]].

[384] S. Caletti, O. Fedkevych, S. Marzani, D. Reichelt, S. Schumann and G. Soyez, *working title: 'Phenomenology of jet angularities at the LHC', to be published*.

[385] M. Dasgupta, F. A. Dreyer, K. Hamilton, P. F. Monni and G. P. Salam, *Logarithmic accuracy of parton showers: a fixed-order study*, JHEP **09** (2018), 033, [`arXiv:1805.09327 [hep-ph]`], [Erratum: JHEP 03, 083 (2020)].

[386] S. Ferrario Ravasio and G. Bewick, *Impact of the Recoil Scheme on the Accuracy of Angular-Ordered Parton Showers*, Strong dynamics for physics within and beyond the Standard Model at LHC and Future Colliders, 12 2019.

[387] G. Bewick, S. Ferrario Ravasio, P. Richardson and M. H. Seymour, *Logarithmic accuracy of angular-ordered parton showers*, JHEP **04** (2020), 019, [`arXiv:1904.11866 [hep-ph]`].

[388] M. Dasgupta, F. A. Dreyer, K. Hamilton, P. F. Monni, G. P. Salam and G. Soyez, *Parton showers beyond leading logarithmic accuracy*, Phys. Rev. Lett. **125** (2020), no. 5, 052002, [`arXiv:2002.11114 [hep-ph]`].

[389] K. Hamilton, R. Medves, G. P. Salam, L. Scyboz and G. Soyez, *Colour and logarithmic accuracy in final-state parton showers*, `arXiv:2011.10054 [hep-ph]`.

[390] Y. Chen, Y.-J. Lee, M. Maggi, P. Chang, Y.-T. Chien, C. McGinn and D. Perepelitsa, *Analysis note: jet reconstruction, energy spectra, and substructure analyses with archived ALEPH data*, `arXiv:2108.04877 [hep-ex]`.

[391] M. Aaboud et al., The ATLAS collaboration, *Measurement of the k_{t} splitting scales in $Z \to \ell\ell$ events in pp collisions at $\sqrt{s} = 8$ TeV with the ATLAS detector*, JHEP **08** (2017), 026, [`arXiv:1704.01530 [hep-ex]`].

[392] A. Buckley et al., *A comparative study of Higgs boson production from vector-boson fusion*, `arXiv:2105.11399 [hep-ph]`.

[393] I. Bejar Alonso and L. Rossi, *HiLumi LHC Technical Design Report: Deliverable: D1.10*.

[394] C. Adolphsen, The International Study Group, High-Energy Accelerator Organization collaboration, *International study group progress report on linear collider development*.

[395] *A Multi-TeV Linear Collider Based on CLIC Technology: CLIC Conceptual Design Report*.

[396] P. Lebrun, L. Linssen, A. Lucaci-Timoce, D. Schulte, F. Simon, S. Stapnes, N. Toge, H. Weerts and J. Wells, *The CLIC Programme: Towards a Staged e+e- Linear Collider Exploring the Terascale : CLIC Conceptual Design Report*, `arXiv:1209.2543 [physics.ins-det]`.

Acknowledgements

Akademischer Werdegang

1992	Geboren in Dresden
08/1998 - 07/2002	96. Grundschule Dresden
08/2002 - 07/2007	Hans-Erlwein-Gymnasium Dresden
07/2007 - 08/2011	Sportgymnasium Dresden

Abitur

10/2011 - 10/2014	Physikstudium an der Technischen Universität Dresden

Abschlussarbeit
*"Studien zur Überprüfung der vorhergesagten
Beziehung zwischen effektiven aQGC
Parametern und expliziten Resonanzen"*
betreut durch Prof. Dr. Michael Kobel

Bachelor of Science

09/2014 - 09/2015	Erasmusstudent an der Loughborough University (UK)
10/2015 - 02/2018	Physikstudium an der Technischen Universität Dresden

Abschlussarbeit
*"Comparison of analytical and parton-shower
approaches to soft-gluon resummation
at NLL accuracy"*
betreut durch Dr. Frank Siegert

Master of Science

seit 03/2018	Promotionsstudium Physik an der Georg-August-Universität Göttingen